Design and performance analysis of a novel face gas seal

A thesis submitted for the requirements for the degree of Doctor of Philosophy

by

Lev Roberts-Haritonov

Mechanical Engineering Department

School of Engineering and Design

Brunel University

May 2006

ABSTRACT

The scope of this work carried two objectives, each focusing on theoretical model development, performance prediction and experimental evaluation of two concepts, of face type non-contacting gas seals. The theoretical modelling and experimental testing were undertaken across a high duty-operating envelope up to 300 bar, 12000 rpm and 120° C. For both sets of experiments, specialised test equipment and test rig were designed and built.

The first objective was to determine the performance of a slot feed design of non-contacting gas design, by evaluating its performance across the full performance envelope. A set of test seals was made for experimental evaluation. A suitable computer model was developed and validated against experimental data. Results showed good seal performance across the main duty conditions and the model showed good correlation with the experimental test data.

Under the second objective, a totally novel design of non-contacting gas seal was proposed, incorporating a unique lift groove geometry (patent pending). A novel and sophisticated computer model was developed to accurately predict the performance of this design. The model was made fully coupled between the fluid and structural domains of the gas seal.

The model predictions were verified against the experimental data. The correlation between the two was found to be very close and consistent across the entire performance envelope of the seals. The novel design concept performed extremely well under all the test conditions, both real and artificial. The theoretical model developed as part of this research proved itself to be an effective analysis and performance prediction tool.

CONTENTS

TABLE OF FIGURES

NOMENCLATURE

Latin Symbols

A_i	Cross sectional area at radius R_i of the seal face (m)
BF	Seal balance factor (Percent)
C_L	Entrance loss coefficient
C_p	Specific heat capacity at constant pressure ($J.kg^{-1}.K^{-1}$)
C_v	Specific heat capacity at constant volume ($J.kg^{-1}.K^{-1}$)
D	Ring diameter (m
h	Film thickness (m)
h_g	Spiral groove depth (m)
h_i	Film thickness at radius R_i (m)
h_o	Film thickness at radius R_o (m)
H	Rear slot depth (m)
H_{ratio}	Ratio of groove depth to overall film gap
H_{flux}	Heat flux at the seal interface ($W.m^{-2}$)
i	Node number in the x-direction
j	Node number in the y-direction
K	Thermal conductivity ($W.m^{-1}.K^{-1}$)
M	Mach number
$N_{grooves}$	Number of spiral grooves
N_{slots}	Number of feed slots
Nu_D	Nusselt Number
$\dot{m}_{1,2}$	Mass flow rate in the gap h from R_1 to R_2, ($kg.s^{-1}$)
$\dot{m}_{2,3}$	Mass flow rate in the gap h from R_2 to R_3, ($kg.s^{-1}$)
$\dot{m}'_{2,3}$	Mass flow rate in the gap H from R_2 to R_3, ($kg.s^{-1}$)=mass flow through the orifice
$\dot{m}_{orif}$	Mass flow rate through the orifice ($kg.s^{-1}$)
$\dot{m}_x$	Mass flow rate in the x direction ($kg.s^{-1}$)
$\dot{m}_y$	Mass flow rate in the y direction ($kg.s^{-1}$)
$\dot{m}_z$	Mass flow rate in the z direction ($kg.s^{-1}$)
$\dot{m}_\vartheta$	Mass flow rate in the θ direction ($kg.s^{-1}$)

$\dot{m}_r$	Mass flow rate in the radial direction ($kg.s^{-1}$)
P	Pressure (Pa)
P_i	Pressure at radius R_i internal pressure (Pa)
$P_{i,j}$	Pressure at node i,j (Pa)
P_o	Pressure at radius R_o - external pressure (Pa)
P_f	Fluid pressure within the seal interface (Pa)
$P_{interface}$	Power generated at the fluid film interface (W)
P_2	Pressure in the feed groove on location P_2 (Pa)
P^*	Pressure at seal exit when flow is sonic (Pa)
P_{spring}	Spring pressure acting on the face (Pa)
Pr	Prandtl Number
R	Radial position on seal face (m)
R_g	Spiral groove inner radius (m)
$R_{g,eff}$	Effective inner radius of spiral groove (m)
R_b	Balance radius (m)
R_o	Seal face outer radius (m)
R_{spo}	Outer radius of spiral groove (m)
$R_{spo-eff}$	Effective outer radius of spiral grooves (m)
R_i	Seal face inner radius (m)
R_1	Seal face inner radius (m)
R_2	Distribution groove and orifice radius (m) – SF design
R_3	Seal face outer radius (m)
R_{gas}	Gas constant ($J.kg^{-1}.K^{-1}$)
R_{orif}	Orifice radius (m) - SFLS design
Re_D	Reynolds number, based on diameter
Re	Reynolds number, for seal flow
Re_r	Critical rotational Reynolds number
SD	Partial act subtended by the feed slots (degrees)
r, θ,z	Cylindrical coordinates
u,v,w	Components of velocity associated with x,y,z or r, θ,z axes
T	Temperature (K)
T_o	Temperature at radius R_o (K)

T_r	Torque acting on the fluid (N.m)
u_i	Gas velocity at radius R_i ($m.s^{-1}$)
u_*	Gas velocity associated with gas pressure P_* ($m.s^{-1}$)
v_{sonic}	Sonic gas velocity ($m.s^{-1}$)
$\dot{V}$	Volumetric flow rate ($m^3.s^{-1}$)
w_{groove}	Spiral groove width (m)
w_{land}	Spiral groove profile land width (m)
W_o	Seal face opening force (N)
W_c	Seal closing force (N)
W_{slot}	Slot width (m)
W_{sp}	Spring force (N)
Z	Gas compressibility factor
x,y,z	Cartesian coordinates

Greek Symbols

α	Spiral groove angle (rad)
α_{high}	Upper value of surface heat transfer coefficient ($W.m^{-2}.K^{-1}$)
α_{low}	Lower value of surface heat transfer coefficient ($W.m^{-2}.K^{-1}$)
γ	Spiral groove land to spiral groove width ratio
γ_{gas}	Ratio of gas constants C_p/C_v
μ	Viscosity (Pa.s)
ν	Specific volume, ($m^3.kg^{-1}$)
ε	1/(RT) value
ρ	Gas density ($kg.m^{-3}$)
ρ^*	Gas density when flow is sonic ($kg.m^{-3}$)
ρ_i	Fluid density at inner radius ($kg.m^{-3}$)
ρ_o	Fluid density at outer radius ($kg.m^{-3}$)
τ	Tangential stress in the fluid film (Pa)
φ	Ratio of hydrostatic to hydrodynamic action of the seal
ψ	Angular coordinate of the spiral groove (rad)
ω	Angular velocity ($rad.s^{-1}$)
ω_1	Angular velocity of surface 1 ($rad.s^{-1}$)
ω_2	Angular velocity of surface 2 ($rad.s^{-1}$)

AKNOWLEDGEMENTS

Firstly, I would like to thank my wife, Carrie for her continuing support throughout the research program and for final proof reading of the thesis.

I would like to thank Professors Tadeusz Stolarski and Gerry Musgrave for their guidance, encouragement and support at all key stages of the research, and for the opportunity to undertake this work.

I'd like to thank my work colleagues for their support, in particular Dr Ian Bennett.

Finally, I dedicate this work to Carrie, and my children, Isabelle and Daniel, my precious gifts from God.

EXECUTIVE SUMMARY

The scope of this work carried two broad objectives, focussing on two concepts of non-contacting mechanical gas seals.

The first objective was to determine the performance of the slot feed design of non-contacting gas design (referred to as SF design). The performance of the seal was to be evaluated across a high duty-operating envelope: 300 bar, 6000 to 12000 rpm and a maximum operating temperature of 120° C. A suitable computer model was to be developed along with the relevant theory and validated against the experimental data.

The next requirement under the overall objective was to correlate the theory to experimental results. To achieve this detailed theory was to be developed. Based on this theory, a computer model was to be built to predict the performance of the given seal design. An appraisal of the performance was to be given highlighting the major benefits as well as drawbacks.

The second objective was to propose a totally novel design of non-contacting gas seal incorporating a unique hydrodynamic lift feature – The proposed design combines the slot feed feature of the SF design with a partial logarithmic spiral groove geometry, thus creating a hybrid concept (referred to as SFLS design – slot fed logarithmic spiral). A set of test seals were made and their performance determined experimentally across the entire high duty performance envelope of 0 to 300 bar, 6000-12000 rpm and 120° C.

A suitable theoretical model was to be developed to accurately predict the performance of the above design and validate it against the experimental data. An appraisal of the performance was given highlighting the major benefits as well as drawbacks of the two designs. Finally, the performance of the two designs was compared and suitable conclusions were drawn up.

In order to achieve the experimental elements of the above objectives, specialised test equipment and a test rig were designed and built.

The SF seal design was built and effectively incorporated into an industry standard cartridge configuration. A suitable computer based model was developed, based on the solution of thin film gas flow using the compressible flow Reynolds equation. The concept underwent detailed testing and the model predictions were verified

against experimental data. Results showed good seal performance across the main duty conditions and the model showed good correlation with the experimental test data. However, under some artificial conditions, the concept did show a degree of fluid film collapse.

Under the second objective of proposing a novel hybrid gas seal concept, an effective design was produced. To predict its performance a sophisticated computer based model was developed. The fluid film model was based on the numerical solution of the compressible flow Reynolds equation. To solve the Reynolds equation, the model utilised the finite difference (FD) technique applied to a 2-D symmetrical sector of the seal geometry. The model took account of all key factors governing its ultimate accuracy. This included real gas compressibility, inlet inertial losses, choked flow consideration and end effects around the spiral grooves. It was also developed to calculate the necessary power generation and convection coefficients around the seal periphery. For ultimate accuracy and closest representation, a fluid film model was utilised in conjunction with a structural solver (ANSYS based), which was used to calculate the deformations of the seal faces, taking into account all the structural and thermal loading. The model was made fully coupled between the fluid and structural domain, thus enabling it to reach a numerical convergence and solution equilibrium for a given set of operating conditions and seal geometry. An effective algorithm was developed to combine the two lift features within the model as well as an effective means of defining the lift groove geometry.

A set of test seals were made and all the necessary validation testing was completed successfully, across the full pressure and speed range. The model predictions were verified against the experimental data. The correlation between the two was found to be very close and consistent across the entire performance envelope. The SFLS seal concept performed extremely well under all the necessary conditions, both real and artificial. The theoretical model developed as part of this research has proven itself to be an effective analysis and performance prediction tool.

1 INTRODUCTION

Gas seals go back over one hundred years. Whenever, there was a need to accommodate a moving element entering a stationary wall, separating gas at a higher pressure from a gas at a lower pressure, it was necessary to use some kind of gas seal.

Probably the very first applications came into being during the age of steam. Typically, high-pressure steam would be admitted into a suitable chamber (most often cylindrical). There, it would act on a piston in order to displace it and produce useful movement and power. Extremely simple, stationary gas seals sealed that steam in the chamber. Later, as those seals were improved in their design, steam would also be applied to the opposite side of the piston. In this location, a gas seal would have to be applied to the stationary component around the moving piston rod having a reciprocating action, thus requiring the gas seal design to be dynamic. So out of this necessity, gas sealing packing rings, piston rings and bushings were born.

Further along the technological evolutionary line, steam started to be used to generate power using rotary motion, like in steam turbines. For this, yet another type of gas seal had to be developed, one that can tolerate high rotational speeds, such as a labyrinth seal. Thus, in parallel with the development of better power generating machinery, there was and had to be parallel development of better gas sealing technology.

When centrifugal pumps appeared around 150 years ago, another sealing problem had to be solved, but this time involving liquid. Radial packings, bushings and labyrinths were initially used for this (see Figure 1, which shows four types of seals each with progressively smaller operating clearance). In the early 1900's, as the speeds and pressures increased in high performance pumps, another development took place, in the form of axial, face type mechanical seals. In this design, the sealing surface rotated through 90^{o} about the shaft centre line (see axial mechanical seal in Figure 1). Those axial face type seals hand a much higher pressure and speed capability than the radial bushings, packings and labyrinths. The most revolutionary concept behind this seal development was the use of a flat surface to accommodate the relative sliding motion between the stationary and rotating parts.. Prior to this, stationary and rotating parts met at a cylindrical surface.

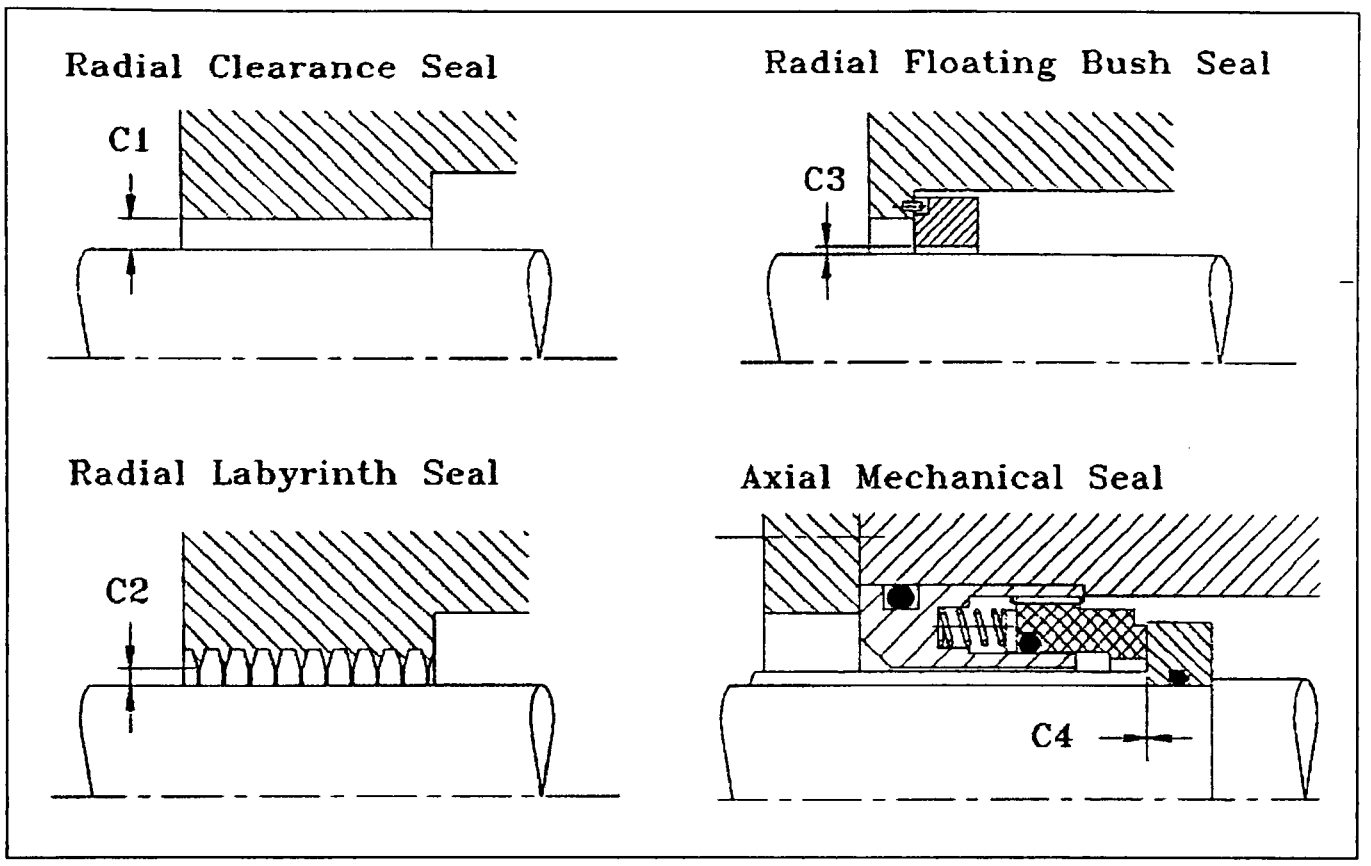

Figure 1:Radial and axial seals [6]

The whole concept of using a flat sealing surface as the interface between a stationary and a rotating part was a crucial development for the modern mechanical seal. The need to seal a fluid with very low viscosity and density, such as a gas, meant that clearances at the interface, or the seal zone, had to be very small in order to achieve low leakages. With cylindrical surfaces, the clearance would be set to accommodate differential thermal movement between these parts, without contact. As a consequence, the clearance cannot be physically lowered beyond a certain point. An axial face type seal does not suffer from this limitation, and if designed for axial adjustability, (which is easily achieved with this concept), results in a better performing seal.

Over the last century, face type mechanical seals were mainly developed for pump sealing applications and their use for gas sealing was limited to very slow moving mixers and agitators. This limitation was primarily because the design relied on relative face sliding contact to restrict the leakage. In pumps, it was possible to do this at high speeds because the process liquid removed the heat generated due to friction and it helped to lubricate the two sliding surfaces. When the sealed medium was gas, it was only possible to remove all the necessary heat from the seal interface

on very slow speed applications. Therefore, when centrifugal compressors arrived on the scene in mid 1900's, there was only one reliable sealing solution available to seal their rotating shafts and it wasn't a gas seal. One had to use a barrier oil seal as a means of sealing high-pressure gas. The seal design was quite simple. But it required a very complex, expensive and what proved to be a very troublesome oil seal support system. Further more, it resulted in seal oil leakage into the process gas stream causing all sorts of problems and complications. A clear need existed for a better seal for those compressors.

Seal manufacturers were becoming aware of these sealing problems on centrifugal compressors because the same companies provided sealing solutions to liquid pumps in the same installations. So in the 1960's some of these manufactures and government supported organisations, such as NASA, started experimental projects aimed at finding a solution where a face type mechanical seal could be made to seal high-pressure gas and operate at a very small clearance. The search was on for a mechanism that would provide lift and separation to the two seal faces, thus eliminating direct frictional contact and the massive heat generation, which the gas could efficiently remove. At the time, suitable theoretical mechanisms were already available and these could be subdivided into two categories: hydrostatic and hydrodynamic. Hydrostatic mechanism relies on the special axis symmetric form of the seal face profile and the way fluid is fed to the seal faces to create an opening pressure profile at the interface. As the name implies, the mechanism is not dependent on the relative rotation. Hydrodynamic mechanism relies solely on rotation for it existence. But some geometry has to be present on the surface of the seal faces in order to create such a mechanism. One such feature already known in the field of tribology was the Rayleigh pad [27].

Both hydrostatic and hydrodynamic mechanisms work by altering the gas pressures between the faces in such a way that if the operating gap decreases, the interface (or opening) pressure increases and vice versa. Thus, a repulsive or opening force is generated that varies inversely with the size of the face operating clearance. Counteracting this opening force is the closing force due to the load being supported, if it is a bearing, or the external pressure being sealed, as in the case of a fluid film seal. The closer the faces come, the larger the repulsive, or opening force. At near contact gaps, the opening force prevails and repels the faces away from each other.

When they move too far away, from each other, the closing force prevails and that brings them closer together. By this means a gap maintaining mechanism is established, based on force equilibrium. The system is normally self-regulating around an average film thickness. Further more, if the film is convergent i.e. the film thickness decreases in the direction of flow, then the average film pressure increases as the film thickness decreases giving a positive stiffness to the film and hence a stable fluid film.

In the mid-late 50's, and on the back of the emergence of jet engine and nuclear power technology, extensive work was taking place in Europe to improve the performance of fluid thrust bearings, for both gas and liquid in those applications. As with the gas seals, the drive was to develop a more effective mechanism to separate the thrust bearing surfaces. So, the end goal was identical in both the seals and the bearings. Both products required adequate separation gap in order to function correctly. In all this, it was clear that what worked for thrust bearings worked equally well for gas seals and vice versa.

Early work was carried out at the Atomic Energy Research Establishment [41] in UK into enhancing the hydrodynamic mechanism in the thrust bearings by adding herringbone type grooves to one of the surfaces.

Later in the 1960s Muijderman [22], a Dutch researcher working for Phillips, made several technical publications on the concept of spiral groove bearings. His work was groundbreaking to the future gas seals from that point on. While the work applied to incompressible fluids and zero pressure drops, and relied on 1-D equations it served as a valuable basis for the development of spiral groove seal technology. Many software codes for spiral groove bearings and seals are based on the Muijderman equations.

The development of computer technology enabled faster computation of computer models. This enabled more efficient and practical solution of the Reynolds equations [28] to predict seal performance both in 1-D and 2-D models. Finite element and finite difference techniques started to applied to model seal flow. In equal measure, more robust material became available in the right combination of properties.

In 1977, for the first time a gas seal was tested on compressed air at 1000 psi on a 4.5" shaft for 1000 hours [29]. It was a face type seal where one of the faces carried

spiral grooves for extra hydrodynamic lift. Some pioneering companies took on the technology and developed gas seal products, mostly using the spiral groove design as proposed by Muijderman [22].

As time progressed, the operating requirements placed on compressors have steadily increased, particularly in terms of pressure. Nevertheless the industry has remaining with what it started off with, the spiral groove seal as well as the calculations originally derived by Muijderman. Alternative ideas and design concepts received little attention in theory and even less under experimentation. What useful research and development work has been done, has concentrated on the spiral groove seal and has largely remained confidential. Meanwhile material and manufacturing technology has marched on together with computational capability. Now one can achieve something, that before could not be done in terms of seal face geometry. So alternate and potentially better designs could now be viable. What was impossible to model before is now possible.

The scope of this work covers two novel of gas seal concepts designed for high duty operation. One design incorporates a novel means of slot feed arrangement, supplying gas to the seal zone.

The second design concept combines the slot fed design of concept 1 with a partial logarithmic spiral groove. This creates a totally novel and unique hydrostatic/hydrodynamic hybrid gas seal concept. To all extents and purposes, this design concept is unique and previously undocumented.

Computer models are to be presented and developed for both designs. The model predictions are to be verified against detailed experimental tests carried out at the highest duty conditions currently expected of the technology, namely in the region of 300 bar. A comparison is then drawn in terms of the respective model accuracy as well as the actual performance of the two design concepts

In considering this work it is worth bearing in mind the complexity associated with accurately predicting the behaviour of a gas seal. A design that runs at an operating gap of just a few microns where the leakage is expected to vary with a cube of that gap. This is particularly so, in this case, where the seal has been designed for high duty operation and optimised for minimum operating gap. Larry Ludwig in a paper

by Shapiro [33] described mechanical seals as "the most unpredictable machine element". That observation is quite true.

2 LITERATURE REVIEW

Non-contacting gas seals emerged directly from gas thrust bearing applications and technology. It seems that as long ago as 1949 this type of bearing had formed the subject of a report by Whipple [41], which remained on the classified list until 1957. His work focussed on a thrust bearing containing herringbone type grooves.. This work was presented in a paper by Ford, et al, published in 1957 [7]. Whipple was on the staff of the Atomic Energy Research Establishment in UK. It is from this research establishment, that the first literature referring to spiral groove thrust bearings seems to have come. No earlier references on this subject have been found. Key summary points stated by Whipple [41] were that geometrically, there are two differences between the theoretical and the practical cases. These were the curvature of the thrust bearing and the end effects caused by the squaring off the spiral grooves. Although recognised as important, neither of the two factors were taken into account. In addition, as pointed out later by Muijderman, [22], Whipple made no use of the continuity equation, nor the Reynolds equation. Instead, boldly and incorrectly assumed that the pressure build up in the grooves would be linear.

In 1966 Muijderman published an excellent textbook [22] where he developed much of the classical theory associated with spiral groove bearings. And although it is focussed on bearing applications, the theory is totally relevant to spiral groove seals, which after all, can be deemed as a variant of the spiral groove thrust bearing. It is also worth reiterating that gas seals as a concept or design did not emerge until the early 1980's. And much of the information was deemed commercially sensitive and thus kept classified. Much of this is still the case now. In his book, Muijderman [22] refers to the very first account of the spiral groove bearings, i.e. flat axial gas lubricated thrust bearings in which one bearing surface is smooth and the other is provided with a recurrent pattern of spiral grooves. The profile of the spiral was defined as being logarithmic in its form. Figure 2 shows such logarithmic spiral groove geometry etched on the running surface of a seal. The profile is also described as a partial logarithmic spiral. That is, the grooves start at the outer radius and terminate part way down the seal face. The ungrooved region below them is termed as the dam.

Muijderman [22], took the work further, first taking on board the important considerations of his previous studies, such as the effect of the radial taper and the end effects of the grooves. In doing this, he was the first to consider the groove form itself. The investigators mentioned in previous references did not consider real spiral grooves, either in their theory or the experiments themselves. Muijderman [22] was the first person to present a theory for logarithmic spiral grooves applied to the running surface of the thrust bearing.

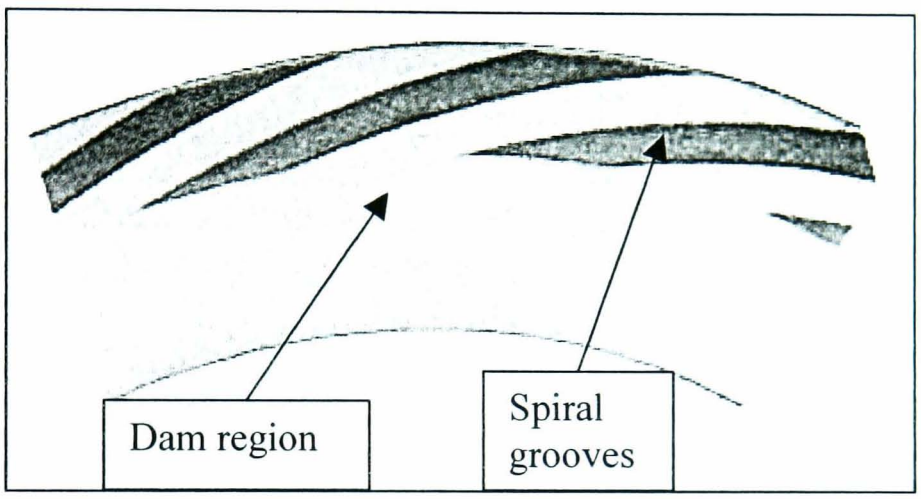

Figure 2: Logarithmic spiral groove

Unlike Whipple[41], Muijderman [22], applied both the Reynolds equation and the mass continuity equation in obtaining a solution to the pressure distribution in the operating gap of the bearing.. He was undoubtedly the first person who developed a set of generalised equations for calculating the pressure across the groove pattern by assuming that the pressure has a linear profile across the grooves. Given this derivation, he then generalised to find the average pressure change per radial increment in terms of flow loss and the pumping effect due to the spirals. The equations are noted here for reference only. While they were originally developed for liquid bearings, the equations are readily modified to include a variable density as required for compressible flow as seen in a gas seal.

$$\frac{dp}{dr} = -\frac{6r\omega}{h_2^2} g_1 - \frac{6\dot{m}\mu(1+\gamma)}{\pi r \rho h_1 h_2^2} g_{99}$$

eqn. 2.1

The first term in the above equation is a pumping term. All the geometry effects of the spiral groove are included in term g_1. The second term is the leakage through the groove and dam regions of the grooved portion of the seal. The geometry effects here are included in the g_{99} term.

The pressure distribution over the dam portion (ungrooved section) is given by the following equation, based on laminar compressible axis symmetric flow.

$$\frac{dp}{dr} = -\frac{6\dot{m}\mu}{\pi r \rho h^3}$$

eqn. 2.2

Muijderman [22], also developed detailed formulations for taking account of the spiral groove end effects in predicting the performance of the spiral groove bearing/seal. The theory has been applied as part of the scope of this current work.

Muijderman [22], developed the theory for predicting the pressure distribution across the face of a spiral groove bearing in 1-D only. The theory produces accurate results for a pure spiral groove bearing. However, they cannot be applied effectively to anything that deviates from a true spiral design as required by the scope of this work. An alternative formulation had to be used. Instead, a generalised two-dimensional numerical solution of the Reynolds equation was taken as a basis for developing a detailed model of the seal performance.

James and Potter [12], presented a detailed description of a two dimensional numerical solution to the problem of the spiral groove bearing. They achieved this by taking the isothermal Reynolds differential equation and writing it in finite difference form for numerical analysis of the pressure distribution within the spiral groove thrust bearing. Then they developed appropriate jump equations, which provide flow continuity at the land-to-groove interfaces. To aid the solution, they apply a co-ordinate transformation to straighten out the grooves. The actual design of the bearing employed full spiral grooves from the OD to the ID of the thrust bearing, etched on one of the running surfaces. Gas flow, load support, static stiffness, power consumption, and compressor efficiency are computed. They conclude that for this particular design, the compressor efficiency increases with decreasing running clearance in the bearing. Also, an optimum spiral angle exists that gives the highest bearing stiffness.

Cheng et al. [5] make a very extensive comparison of the spiral groove to the Rayleigh step profile and the orifice compensated seal. They discuss the pressure generation and static stability of face type seals. They developed an expression to estimate the effectiveness of hydrodynamic action in those seals as well as an

equation for the ratio of hydrostatic to hydrodynamic load. Some design data is presented for the hydrostatic step seal, hydrostatic orifice compensated seal, hybrid spiral-groove seal and the shrouded Rayleigh step seal.

The main conclusions reached were:

- To achieve a stable fluid film in a non-contacting face seal, it is necessary to have positive film stiffness, which can be derived either from hydrostatic or hydrodynamic action.
- The ratio of achievable hydrodynamic or hydrostatic load is a function of fluid viscosity, surface speed, seal width, operating film thickness and the pressure differential.
- The shape of the film gap has a very critical influence on the film stability, stiffness and leakage rate. A convergent film, that is one in which the film gap decreases with the flow, gives rise to a positive stiffness and hence stability. However, an excessively convergence is undesirable because it opens up the gap, reduces the stiffness and increases the leakage rate. A divergent film is unstable, leading to a collapse of the film and surface contact.
- Positive stiffness can also be achieved by the following primary seal configurations: the hydrostatic step face seal, orifice compensated seal, hybrid spiral groove seal or the shrouded Rayleigh step seal. For optimum performance the seal should be designed to operate near maximum stiffness. This is normally achieved by running with the smallest film possible. Comparative analysis suggests that with the hydrostatic seal the maximum stiffness is achieved for a given set of design parameter, beyond which a further reduction in operating gap gives no further stiffness increase. Conversely it is suggested that with the spiral groove seal, negative stiffness is avoided if the grooves are located on the high-pressure side of the seal, thus pumping the fluid to the low-pressure side.
- The paper predicts a progressively increasing stiffness with reducing gap (approximated by an inverse relationship between seal gap and stiffness. However, the predicted curve stops at a film thickness of 12.7 microns, with no information available for smaller film gaps.

Key at al [16] undertook a detailed analysis of a mechanical seal with deep hydropad slots distributed around the circumference of one face. The analysis was purely theoretical. The computational procedure was based on an analytical model utilising the Reynolds equation, which was solved using the finite difference technique. In the model, the hydropads induce the seal face to deform into a circumferential wave pattern leading to a hydrodynamic pressure generation. Their procedure allowed the computation of film thickness, pressure profile and the leakage rates, which are three of the most important performance parameters. The solution of the Reynolds equation using the finite difference technique was very effective. If applied to a soft material such as a carbon, the deep hydropads induce the seal face to deform into a circumferential wave pattern, which hydrodynamically generates elevated film pressure and supplements the hydrostatic load support. Finally, they concluded that if circumferential deformation is expected, it must be fully taken into account in the model if that model is to have any degree of accuracy

Gardner [9] presented a paper on a recent development on non-contacting face seals utilising spiral groove face technology similar to that shown in Figure 2. He described improvements that have been made to the general design of spiral groove seals to improve their pressure deflection characteristics, and the use of alternative face materials such as tungsten carbide and carbon. He also covered some operational characteristics of dry running spiral groove face seals. One such operational characteristic was the apparent effect of sonic flow on expected and actual leakage values. In testing the gas seals he observed an interesting phenomena in the form of sonic flow at the seal exit. He observed this from the seal leakage data, which showed the leakage to be roughly proportional to the pressure squared, up to 600 psi. After that the leakage was observed to be a straight line as a function of pressure. The latter, he concluded was due to the effect of sonic flow at the seal exit. Gardner felt that this feature would be very helpful for designing high-pressure gas seals due to the fact that the leakage would not be as excessive as if it followed a P^2 relationship throughout the whole operating range.

Shapiro et al [33] used the Muijderman model for predicting the performance of a spiral groove seal for a liquid oxygen (LOX) turbo pump, running at 35000 rpm and sealing a pressure of 52 bar. The analysis accounted for fluid turbulence and inertial effects. Shapiro hypothesised that the effects of turbulence upon the fluid film

performance would be the same as if the seal was operating in the laminar regime, but with a greatly increased viscosity. It thus produces greater load carrying capacity and higher viscous power losses than a laminar operating seal.

He argued that because of the large pressure gradients and large operating film thicknesses, the flow through the seal would not be entirely viscous, and thus, inertia forces would be another significant consideration. The effect of inertia is to convert the pressure head into velocity head at sudden contractions. It would do this by producing steep pressure drops at those locations. It was also pointed out as an interesting observation, that a mechanical seal can be described as "the most unpredictable machine element". When one is working with an operating gap in the order of microns, that is not a surprising observation, and a very true one to that.

Sedy [29] published a paper on improved performance of film riding gas seals through enhancement of hydrodynamic effects. This was the first reference to the use of spiral groove bearing lift technology applied to non-contacting gas seals. As with previous references, he utilised the Muijderman [22], derived equations for predicting the pressure distribution across the grooved and dam portions of the gas seal. Referring to past work carried out by NASA on compressible flow regimes in jet engine seals, he concluded that sub-sonic laminar flow which prevails at narrow sealing gaps gives the seal high stiffness and stability. Whereas larger gaps may encounter unstable regimes associated with flow transitions from laminar to turbulent as well as the effects of sonic flow at the exit. His calculations showed that seals indeed developed sonic flow at higher pressures (usually between 1.38 and 2.76 MPa) and, therefore, some of the instability problems may have been caused by insufficient stiffness due a wide operating gap. Also, it seemed that, if it was possible to limit the leakage at high pressures and speeds, the seals could be made to work in a completely laminar subsonic region with none of the above problems.

In equal measure, however, it was also realised that one could not always avoid sonic flow, particularly as the drive was for higher and higher sealing pressures. But if the flow could be made to be laminar many of the above mentioned problems would be overcome. Sedy [29] stated that for optimal performance of the seal, it is important that, if for any reason the gap between the sealing faces suddenly decreases, the opening force should increase sharply to prevent face-to-face contact, and make the faces open back up to the original equilibrium gap. Through detailed computer

based analysis Sedy [29] claimed that a purely hydrostatic lift is not as effective in providing this opening force increase (stiffness), as is the hydrodynamic lift. The analysis pointed basically in the same direction. On the subject of design, Sedy [29] concluded with the following points:

Low leakage was desirable to preserve laminar flow through the seal. To achieve this one needed a narrow operating gap and/or a wider seal dam. Secondly, it was desirable to design a seal with a narrower operating gap or a wider dam to lessen the cooling effect of the expanding gas. Thirdly, the high stiffness requirements also translate into a narrower gap because film stiffness goes up with decreasing film gap. In other words, the core objective must be to have a gas seal with the lowest possible operating gap of all if the abovementioned benefits are to be realised. Based on the above work a set of design rules were put forward for a spiral groove seal. These being:

- Utilise large balance ratios
- Use wide sealing dams.
- Use wider face width.
- Modified face cross-section.

Albeit on the latter, little evidence was offered in the paper.

Sedy [30, 31] also published paper and a patent where he described in detail methods used to compensate for radial taper distortions. The basis of the work was again based on the theory developed by Muijderman [22]. The paper showed that at certain conditions a mechanism is available, which responds to any angular face deflection with a moment, which twists a stationary low-modulus seal ring back towards the parallel position. He claimed that it minimised angular deflections and also almost eliminated fluctuations in gap width. The result is a more stable seal characterised by very little variation in leakage. The paper shows that it is possible to separate hydrostatic and hydrodynamic components of the seal stiffness. The paper's conclusions focus on the importance of seal stability for long life. The concept of high-stiffness operation, together with radial stabilisation is core to this. Another point highlighted is the limitation of attainable hydrostatic stiffness. It is not only the equilibrium film stiffness that is important in the seal design, but also the

stiffness at very narrow film thicknesses when, at some point along the seal circumference, the faces are in danger of contact. Sedy [30, 31] did not quantify what these narrow film thicknesses are, but the current author's more recent experience states those gaps to be in the region of 0.4 to 0.5 μm.

Basu [3] presented a paper on the analysis of a radial groove gas face seal. The design analysed an outside pressurised, bi-directional gas face seal. The seal face was made up of a hydrodynamic section, consisting of alternate regions of land and groove, and a hydrostatic dam area towards the inner diameter.

The compressible Reynolds equation was solved over a radial groove hydrodynamic, by both finite difference and finite element methods. The former algorithm was seen to be about two to three times faster than the latter. Basu [3] argues that both the FD and the FE method give quite agreeable opening force values. The FD method was found to be more than twice the speed of the FE method. Although he also suggests that the FE method is more versatile and can be adapted easily to other hydrodynamic geometries such as spiral groove, circumferential Rayleigh pad and the like. It is worth noting that this observation is contested by more recent publications. For both the FD and FE method, the author used the Newton-Raphson algorithm to linearise the non-linear set of algebraic equations, whereas the SOR (successive over relaxation) type iterative method was chosen to solve the resulting matrix equation. It was noted that SOR was extremely slow and a direct solver, such as Gaussian elimination would have been better. Basu [3] also states that for high-pressure applications radial inertia should be included to allow for choking at the seal outlet. This has been adopted in the model developed as part of this research.

Zuk at al [43] presented analysis for compressible fluid flow across gas film shaft seals and narrow slots. As a basis, Zuk used the classical viscous, isothermal, subsonic compressible flow analysis as per Gross [11]. The flow was analysed using a quasi-one-dimensional integral method, which included fluid inertia, viscous friction and entrance losses. The analysis applied to both turbulent and laminar flow as well as subsonic and choked flow conditions. Results show that a parallel film can have positive film stiffness under choked flow conditions. Zuk at al [43] presented two equations for taking account of the entrance losses and with it, introducing empirically determined entrance loss coefficient C_L

Zuk at al [43] made some important remarks on the physics of compressible seal flow. Static pressure drops to overcome flow friction. The pressure drop increases the specific volume of the fluid. Since the area change is negligible, the mean velocity must increase as the specific volume ($m^3.kg^{-1}$) increases in order to maintain the same mass flow rate at each section of the leakage path. As the velocity increases, the fluid momentum also increases, which requires additional pressure drop. This results in an even greater increase in specific volume. The process will continue until the end of the leakage path or until the fluid reaches the maximum (choking) condition, which will occur, when the Mach number is equal to 1 at the exit (exit velocity being sonic).

Should the Mach number reach a value of 1 somewhere along the leakage path interior, it is expected that behaviour similar to duct flow will occur. For duct flow it can be shown that the flow process will adjust itself until the point at which the Mach number reaches 1 is shifted to the exit of the leakage passage. The mass flow rate of the fluid is the maximum which can be handled for a given inlet density and passage cross-sectional area. This process flow is known classically as Fanno flow line.

The entrance velocity loss may be negligible in subsonic viscous flow compared to the total pressure drop; however, under choked conditions the entrance velocity head loss is no longer negligible. This results in an entrance pressure loss. Also under choked conditions, the exit pressure is larger than the seal downstream pressure and increases with film thickness. The pressure decreases through expansion waves to the seal downstream pressure (normally 1 bar g). However, these expansion waves do not significantly affect the axial force balance on the seal. But they significantly alter the opening pressure profile and the consequential leakage. On some rare occasions, choking can occur at the seal entrance. However, that is not foreseen in the case of this study.

Zuk at al [43] also state that the result of accounting for the entrance loss would result in a decrease in the mass flow rate. It is stated that an entrance loss coefficient equal to 0.6 gave excellent agreement with experiment. This value would be utilised in the subsequent model.

Laurenson et al [19] described preliminary experiments with front slot fed hydrostatic face seals. Here it is important to make a distinction between this and the

rear slot orifice fed design. As per the description, the slot is formed on the running surface of the seal face. The front slot controlled hydrostatic seal has been proposed as an alternative to the capillary controlled and orifice controlled seals. The advantages of slot control lie in simplicity of manufacture and improved reliability in conditions where there is a danger of very small passages being blocked by contaminant particles in the sealed fluid. The main disadvantages are inferior fluid film stiffness, only 50% of that for orifice control and 70% of that for capillary control, and the possibility that if wear takes place on the seal face, the slot depth will be reduced with consequent reduction in clearance. This would not be an acceptable scenario in a non-contacting gas seal that is destined for the marketplace.

Plots of variation of recess pressure in the slots, with clearance were made and they were found to show good agreement with theoretical predictions with a tendency for pressures to be slightly below predicted values. Multiple tests were undertaken with slot depths down to 15μm, with no evidence of contact. As predicted, the leakage dropped with reducing slot depth. Certain hydrodynamic effects were observed, suggesting that the slot may play a role, albeit a small one. It was concluded that the slot controlled hydrostatic seals operate successfully in maintaining low leakage rates with no apparent wear. Although the author did contemplate possible wear over prolonged operating periods due to contact of contaminant particles with the moving faces.

In further work, Laurenson et al [20] studied the hydrostatic design in more detail. They brought to the readers attention the key fact that a hydrostatic seal has much in common with the bearing design. But two factors have more significance for the seal designer: leakage and the existence of a pressure gradient across the seal face. They presented a typical design procedure for a hydrostatic seal. This included a decision on external face dimensions, recess width, desired running clearance and the type of flow control (such as an orifice). Finally they claimed that there existed an optimum radial position of the recess.

Kouga and Fugita [18] presented analysis on a radial taper hydrostatic face seal as often used in high-pressure water applications such as reactor cooling pumps. They took previous work for incompressible flow and adapted it to cover the gas flow dynamics of a hybrid taper flat face seal, and the equivalent annular arrangement. The seal gas stability was discussed, along with various tests to confirm

performance. It is reported that the work has enabled gas seals to achieve sucessful operation in high-speed applications. The flow was assumed to be subsonic, laminar and the gas were assumed to be perfect. The analysis was undertaken in 1-D. Kouga and Fugita [18] utilised entrance loss coefficients, but do not indicate their origin.

In their earlier paper, [17], Kouga and Fugita included inertia losses at the entrance and the discharge. Subsequent discussion and feedback from other persons indicated that the effect of including those inertial effects at the entrance and to a lesser degree at the exit would be to reduce the seal leakage.

Zuk and Ludwig [43] presented a very detailed paper on the analysis of rotational effects on compressible viscous flow across shaft face seals. The flow across a parallel dam of the type that appears in non-contacting shaft face seals was analysed for steady, laminar, subsonic, isothermal compressible flow with relative rotation of the sealing dam surfaces. They considered the effects of rotational effects on the leakage rates, pressure profiles and other physical quantities. Firstly analysis suggests that for laminar flow across the isothermal compressible sealing dam, the change in mass leakage due to relative surface rotation would appear to be important when the surface speed is very high (e.g. 36000 rpm). Analysis suggests that rotational effects appear to be negligible for cases where the radial pressure differential is large, the gap is small and the rotational speed is moderate. This would contrast markedly if the sealed medium was to be a high viscosity liquid. It was also found that the parameter governing the flow regime for radial flow in most seal problems would be the Mach number, rather than the pressure flow Reynolds number. This is true for very small gaps, as calculations would indicate that the flow would become choked in the radial direction before the transition (laminar to turbulent regime) pressure-flow Reynolds number is reached. Choking will of course occur when M=1. The limit of this analysis is valid for $M < 1/\gamma^{1/2}$. The minimum transition Reynolds Re_{2h} (based on the average velocity and hydraulic diameter) will be between 2300 and 6000.

For the case of only circumferential shear flow with no imposed radial pressure gradient, the flow will remain laminar until a certain critical rotational Reynolds number is exceeded; then the flow will become turbulent. For this case, the critical

rotational Reynolds number for transition appears to be the simple Couette flow transition Reynolds number. Thus, $Re_r=Rm\omega h\rho/\mu.=1300$.

The smaller the gap, the longer the transition speed, is delayed. Thus. the wall has a stabilising effect on the flow. So for a 1 foot diameter seal operating at room temperature and pressure, the transition speed would be 71500 rpm for a 25 μm gap and 179000 rpm for a 10 μm gap. The seal design under the scope of this work is designed to operate at gaps of 1/5 of that, speeds of 12000 rpm and a large pressure gradient (>1.5:1). Thus in this case it is the radial flow regime and not the circumferential one that dominates.

So to conclude, based on the work presented by Zuk and Ludwig [43], when one has a seal with high-pressure gradients and very small gaps and speeds, the rotational effects are negligible. Further more, their effect becomes invalid if the seal flow is choked. Thus, the centrifugal force does not have an appreciable effect on gas mass flow for moderate or large pressure ratios (<1.5:1) and moderate rotational speeds.

H S Cheng, C Y Chow, and D F Wilcock [5] presented a paper on the behaviour of hydrostatic and hydrodynamic non-contact face seals. In this paper the pressure generation and static stability of face type seals were discussed and an expression was develop to estimate the effectiveness of hydrodynamic action in this type of seal. The following factors were considered in detail:

Pressure in the fluid film can be generated by two actions. One such action is hydrodynamic, and is generated by the relative motion between the sealing surfaces and the second one is hydrostatic, which is generated by the pressure differential across the seal (see eqn. 2.3 and eqn. 2.4)

The ratio of the hydrostatic to the hydrodynamic load φ can be used to indicate the effectiveness of hydrodynamic action in carrying the load of a face seal

If the fluid film at the seal interface is convergent, i.e. the film thickness decreases in the direction of the flow, then the average film pressure increases giving a positive stiffness and hence a stable film.

Aside from a convergent film, other types of primary seal configuration can also achieve a stable film. These include: hydrostatic step seal, orifice compensated seal, hybrid spiral groove seal and Rayleigh step seal.

To achieve a stable fluid film it is necessary to have a positive film stiffness, which can be derived from either hydrostatic or hydrodynamic action.

The ratio of achievable hydrodynamic or hydrostatic load is a function of the fluid viscosity, surface speed, radial seal width, operating film thickness and the pressure differential.

A convergent flow gives rise to positive film stability. Excessively large convergence will result in a large film thickness, reduced film stiffness and an increase in leakage.

To permit tracker runner motion without diminishing film thickness excessively, the primary seal must have a high stiffness gas film and a low mass.

Load carrying formulae:

Maximum achievable hydrostatic load = $(P_o-P_i)A$

eqn. 2.3

Maximum achievable hydrodynamic load = $f_d 6\mu UbA/h^2$

eqn. 2.4

Ratio of hydrodynamic to hydrostatic: $\varphi = f_d 6\mu Ub/(P_o-P_i)h^2$

eqn. 2.5

Stolarski and Xue [37] presented a paper on the principle of operation and the performance of a back depression hydrostatic gas seal, also taking into account the roughness and deformation effects. To all extents and purposes, this was what is referred to as the Slot Feed design in the subsequent sections of this thesis. The following model considerations were made in this study:

The film thickness incorporates a roughness model proposed by Christensen (eqn. 2.3). The model takes into account the longitudinal and transverse roughness relative to the direction of motion.

Stand alone, uncoupled finite element method was used to find the shape and deformation of the static face under pressure load.

The fluid film pressure was analysed using 1-D orifice flow equations. The pressure profile distribution and the resultant equilibrium gap were calculated using an

iterative routine in converging to an equilibrium condition where the closing forces were equal to the opening force.

The orifice pressure P_2 in the feed slot is calculated by solving a simplified Reynolds equation and then used to calculate the above mentioned pressure profile distribution.

Mass continuity of fluid flow is established between the two inlets to the seal interface and the exit.

For ultimate equilibrium of the fluid film gap, the opening force W_o must equal the closing force W_c. The opening force is derived from the calculated pressure profile in the seal gap. The closing force is the sum of the external seal gas pressure and the spring force, multiplied through by the balance factor B of the seal.

When predicting performance, further variables were considered. These were:

- Interaction between two parallel smooth faces.
- The equilibrium position is when $W_o=W_c$. By changing the closing force, the equilibrium operating gap would change as well.
- Interaction between two parallel rough faces. The roughness will cause the opening force to decrease, thus causing a reduction in film gap h_o.

In closing, the authors reached the following conclusions:

- The hydrostatic seal featuring back depression grooves proved to be a practical proposition when operating at limited pressures up to 15 bar and rotational speeds of 1500 rpm.
- An analytical model must include elastic deformation effects of the stationary face in order to produce more realistic results.
- The main controlling parameters are the balance ratio B, the gap depression ratio h_o/h_v, the radial position of the feed orifice slot R_2 and the depth of the rear feed slot.
- Within the limited operating speeds considered by this study, the design demonstrated negligible hydrodynamic effects.

The work undertaken by Stolarski and Xue [37] formed the starting point and the first of the two research objectives detailed in this thesis. The design was described

as a back depression hydrostatic gas seal. For clarity. in all subsequent chapters this design will be called the slot feed gas seal, abbreviated to SF design.

Tournerie et al [39] presented a paper on optimisation and performance prediction of a grooved face seal, both for liquids and gases. The paper presented a 2-D finite element method to solve the Reynolds equation and obtain a solution to the fluid film domain. The model was very basic and took no account of the influence of the structural domain on the seal equilibrium. The chosen groove geometry was that of a logarithmic spiral, as per Figure 2. A series of experiments were carried out at pressures up to 70 bar and speeds of up to 2400 rpm. The experimental results were then compared with basic model prediction and some optimum values established.

One of the key results showed that there existed an optimum film thickness, which produced a maximum load carrying capacity. This was found to be in the region of 14-16 μm. Further more, it was found that there existed an optimum spiral groove angle α, which gave the seal a maximum stiffness. This was found to be approximately 17^{o}. This ties in extremely well with author's own experience based on commercially classified experimental data. This found the optimum spiral groove angle to be 15^{o}. The results of this published work played a direct influence in the selection of the final design parameters of the novel groove geometry covered by this thesis.

Sneck et al [36] presented a paper where they applied the solution of the 2-D Reynolds equation to predict the performance of a spiral groove seal. The model was much simplified by adopting a "narrow seal" approximation. With this model simplification the radial face width was not discretized into a number of segments. but rather simply taken as an average radial width.

Results of the "narrow-seal" analysis were found to compare favourably with those obtained by Muijderman [22]. Sneck also concluded, somewhat unsurprisingly that the inward pumping effect increased substantially with rotational speed. He also claimed that this inward pumping effect did not change with direction of rotation. However, every other relevant reference, starting with Sedy [29], contradicts that completely. That is, if a spiral groove seal is rotated backwards. the grooves will effectively pump out the gas and lead to a collapse in the fluid film.

Lebeck [21], presented a detailed survey on the best means of solving the Reynolds equation, both for incompressible and compressible flow in 2 dimensions. Two options are available, the finite element and the finite difference method. In considering the solution of the Reynolds equation for laminar and compressible flow, the main difficulty cited has been in finding a solution method that will reliably converge and will not demand excessive computing time. The compressible flow problem results in non-linear finite difference equations for which a direct solution is not possible. Lebeck [21], refers to detailed work undertaken by Szery [38], who presented a survey on the various methods used to solve the Reynolds equation. For compressible flow, the most favoured method due to the simplicity of formulation is the Newton method based. This method was adopted for the solution of the Reynolds equation as part of this research.

As a related body of work, the author undertook an investigation into the feasibility of utilising CFD techniques to model the fluid film domain within a gas seal. This took place at the start of the research program. For this purpose a proprietary CFD package was used as a basis, namely Ansys CFX [2]. A major problem presented itself early on in the exercise. This was encountered when attempting to model the thin film gas film found in a non-contacting gas seal. Those gaps would be in the order of 2-5 μm. However, the seal interface would be in the order of millimetres in size. Hence, in order to effectively mesh such fluid domain, one would have to use elements having extremely large aspect ratios. The element length would have to be in the order of millimetres long in one direction, and sub-micron in length across the fluid film. It proved nearly impossible to reliably mesh and analyse such geometry. Attempts to reduce the aspect ratios to more manageable levels resulted in massive model size computational time. As a consequence of these early problems, the use of CFD as a potential tool for modelling the thin film behaviour in a non-contacting seal was abandoned. Instead, the author focussed on the application of the Reynolds equation for the analysis of the fluid film domain and any associated lift groove geometry.

A number of alternatives to the logarithmic spirals have been developed. However, very little detailed technical publications are available. The vast majority exist in the form of granted patents. One such groove geometry was proposed and patented by the Kaydon ring and Seal Company [14]. The unidirectional and bi-rotational

variants are shown in Figure 3. Both variants feature partial circumferential slots connected to the outside with shallow radial slots. They utilised tapered ramp geometry of the groove.

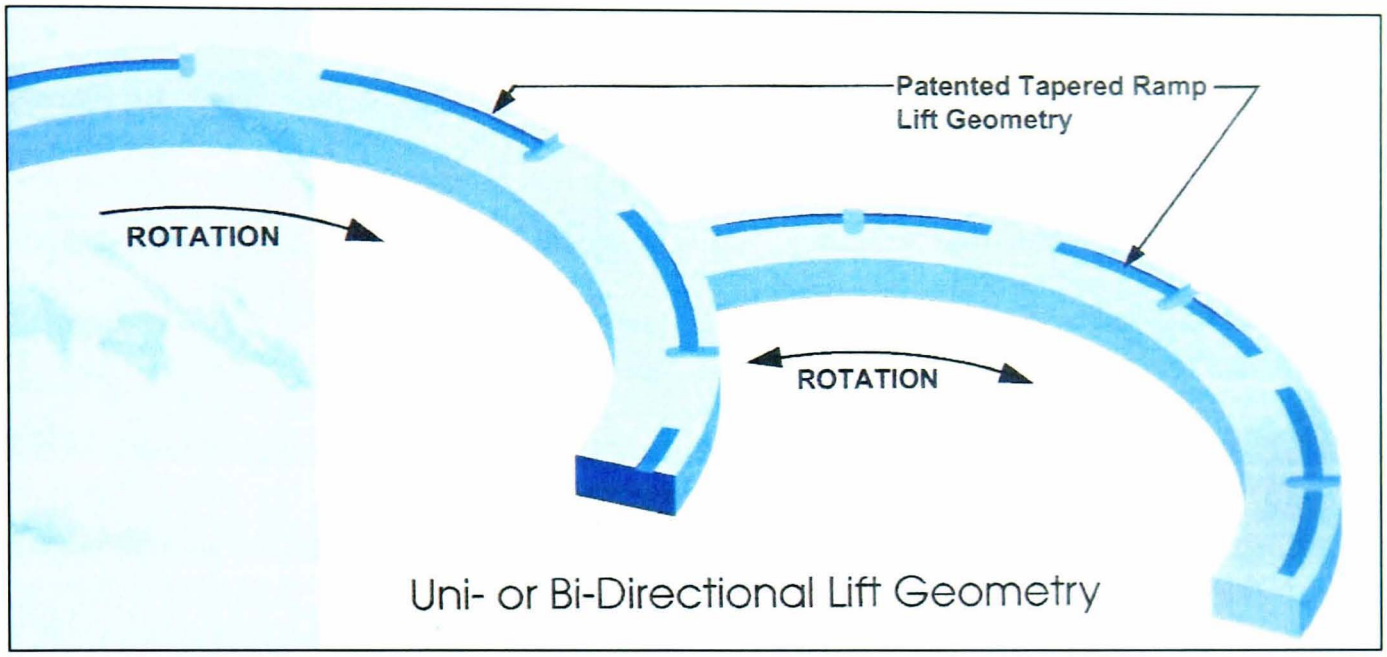

Figure 3: Kaydon tapered ramp groove geometry [14]

The groove concept does not utilise any inward geometric pumping feature. In order to achieve bi directionality, the groove geometry is mirrored about the partial radial feed grooves, which are the circumferential grooves. No information is given about the load carrying capacity of this particular concept. What is probable is that due to the absence of the inward pumping feature, the hydrodynamic effect would probably be limited. Further more, because the radial feed grooves are on the front of running surface, it means that the leakage through them would be a function of two variables: the physical geometry of the groove and the variable depth of that groove due to the viable film gap. No further detailed technical information on the operational characteristic of this concept could be found.

Goldswain via a patent [10] and then Pecht and Goldswain [24] in a technical paper presented alternatives to the established spiral groove lift geometry. They particularly focussed, on a type of hydrodynamic lift geometry, which would offer bidirectional capability. They saw this as an important development requirement given that the unidirectional logarithmic spiral only offered unidirectional capability. In fact it is widely acknowledged, that if a spiral groove seal was to be rotated in the reverse direction for even a few minutes, the grooves would pump all the gas out of the seal interface, resulting in a total collapse of the film, full face contact and catastrophic failure. In order to overcome this major limitation of the unidirectional

logarithmic spiral groove, they proposed the 'Christmas tree' groove design, as shown in Figure 4.

While strongly advocating the true birotational capability, the paper also acknowledged the inferior load carrying capacity of the "Christmas tree" design, compared to the unidirectional logarithmic spiral. The authors do not go into any detail explaining the reasons for this, but from this author's experience, the reduced load carrying capacity of the "Christmas tree" is due to the fluid cascading over the trailing edges of the grooves, rather being pumped directly to the inner circumference and the ungrooved portion, as is the case with the logarithmic spiral. The "Christmas Tree" groove design is in commercial production with John Crane [13].

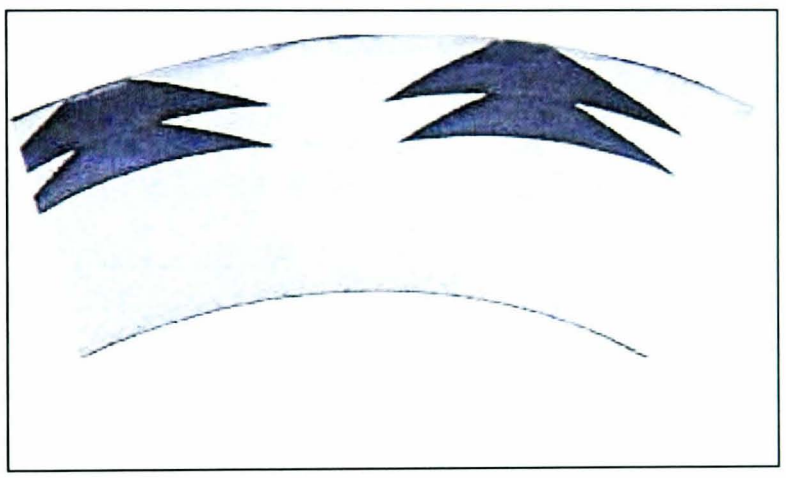

Figure 4: "Christmas tree" lift groove design

Another variant of the bi-rotational hybrid lift design, not utilising the spiral groove was presented in a patent by Victor [40]. And subsequently in a report prepared by Neale Consulting Engineers [23]. The geometry does not utilise any geometry angles, but instead utilises square and rectangular geometry, in the form of a T-slot. It is similar to the Kaydon [14] profile mentioned earlier, but does not employ a tapered groove depth profile. This design of lift groove geometry is in use with the Flow Serve Corporation [8] in their bi-rotational gas seals. This is also the reason why no further technical information on this concept is available in the public domain.

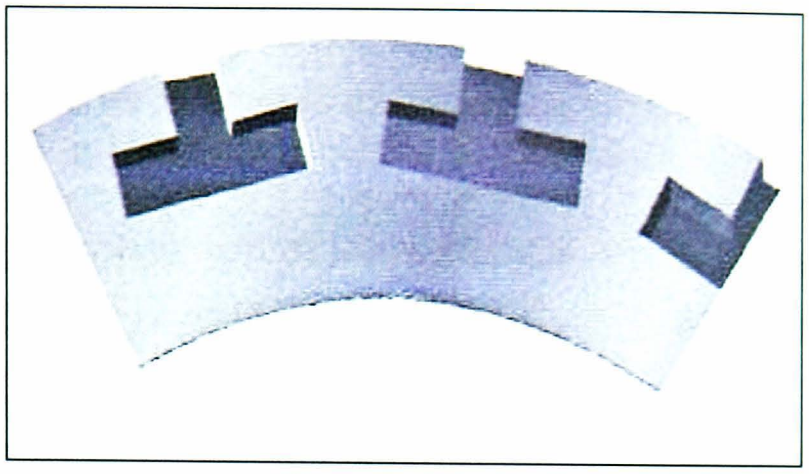

Figure 5: T-slot lift groove geometry

As yet another bi-rotational concept, Victor [40] describes a triangular lift geometry, as shown in Figure 6. In some respects, it is a simplified design of the John Crane "Christmas tree" profile [10]. One interesting feature of this particular profile is the fact that the entrance to the grooves is very small relative to the overall groove geometry. The intent of this design feature is probably to keep the leakages to a minimum. However, the potential disadvantage lies with the fact that the grooves could be starved of gas, thus limiting their load carrying capacity. As with other patents, no further technical information could be found.

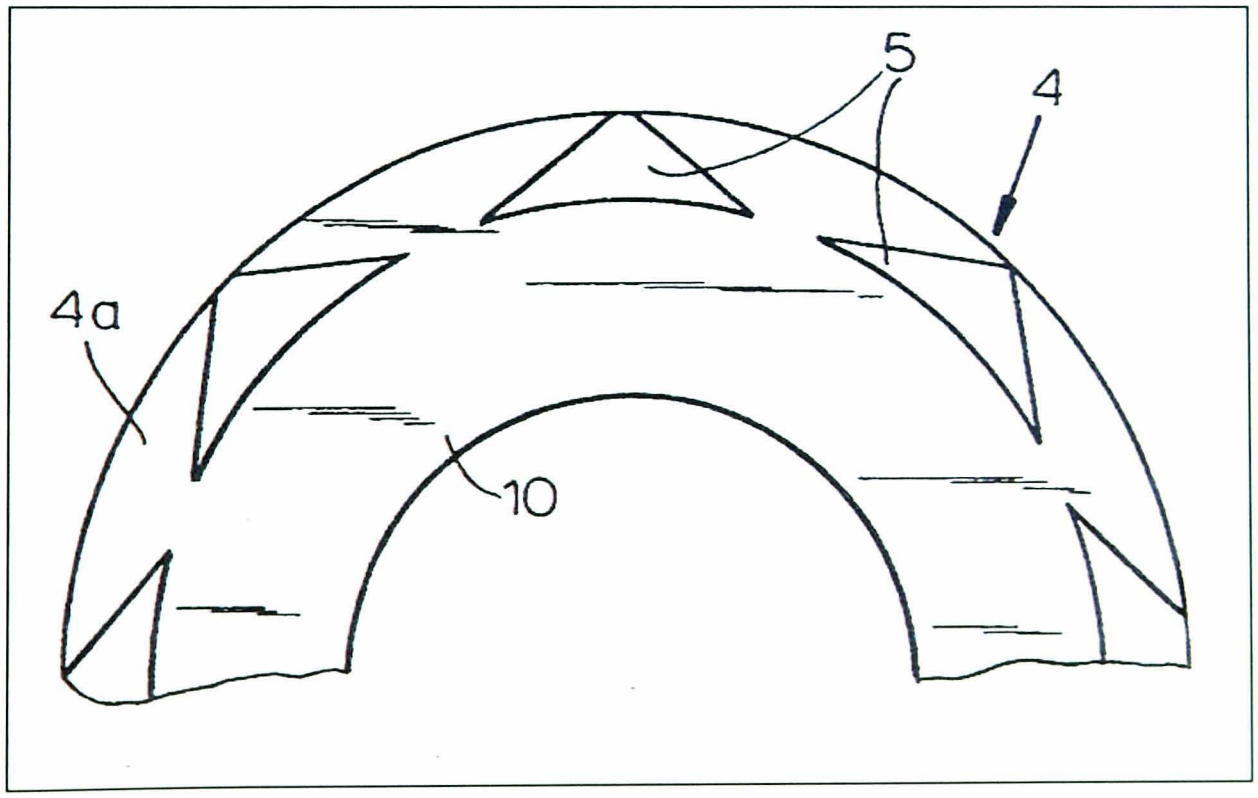

Figure 6: Triangular bi-rotational groove geometry

Sedy [32] put forward a novel variant of the conventional spiral groove face gas seal. In terms of surface profile, the seal utilised a conventional partial logarithmic spiral, identical to the one cited in reference [31]. The uniqueness of the design was in the

fact that the spiral groove depth was not uniform, but stepped, as shown in Figure 7. The deeper groove section is located in the outer half of the groove and the shallower groove section was located at the inner half of the groove. The stepped spiral concept sought to address a key drawback of the logarithmic spiral, namely its very poor static break out torque characteristics. The purpose of the inner shallower section of the spiral was to provide better seal face separation under static conditions (zero speed). The purpose of the deeper outer section of the spiral was to provide the required hydrodynamic operation, which relies on the grooves being relatively short in length, but deep. As is the case with the other referenced patents, there is very little divulgence of technical material.

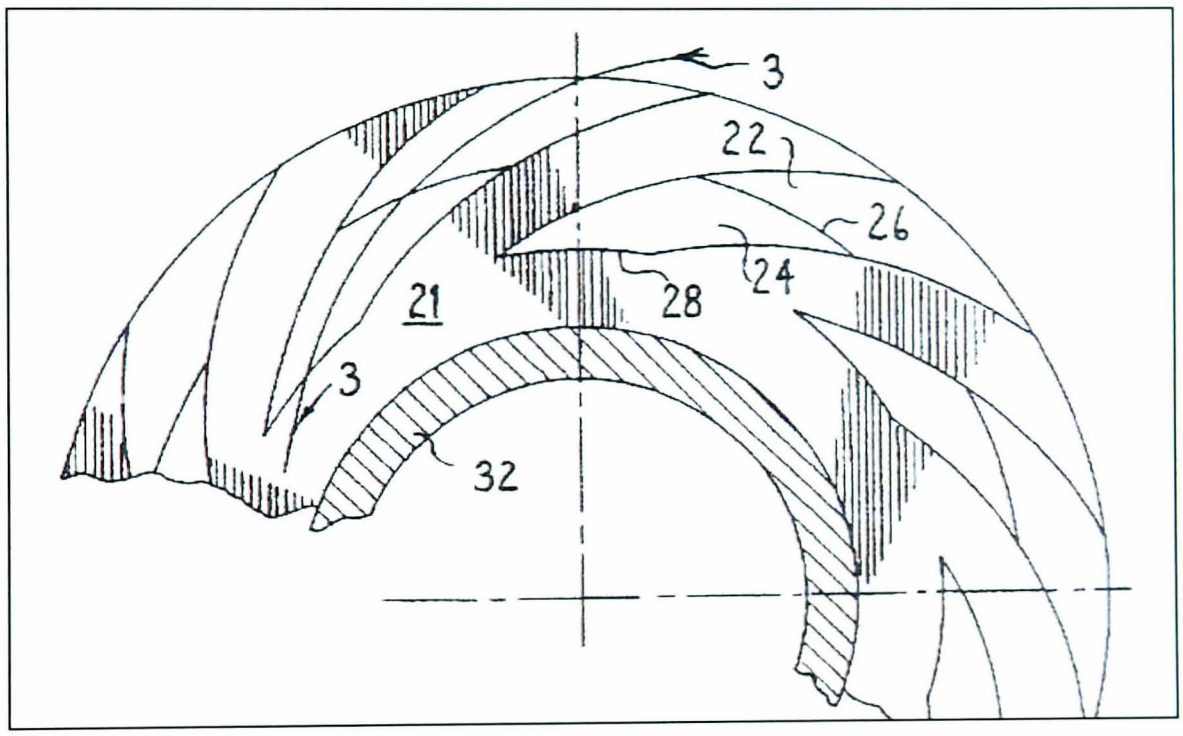

Figure 7: Sedy stepped spiral [32]

Another design variant of the logarithmic spiral was developed and patented by Shimizu [34] and shown in Figure 8. In principle, it is a two part logarithmic spiral. The claimed design intent here is for the first outer part of the logarithmic spiral to generate hydrodynamic lift. The purpose of the backward swept 'tails is to reduce the leakage of the seal due to the pumping effect of the main spiral grooves. However, Shimizu does not give any further description or explanation as to how this is achieved.

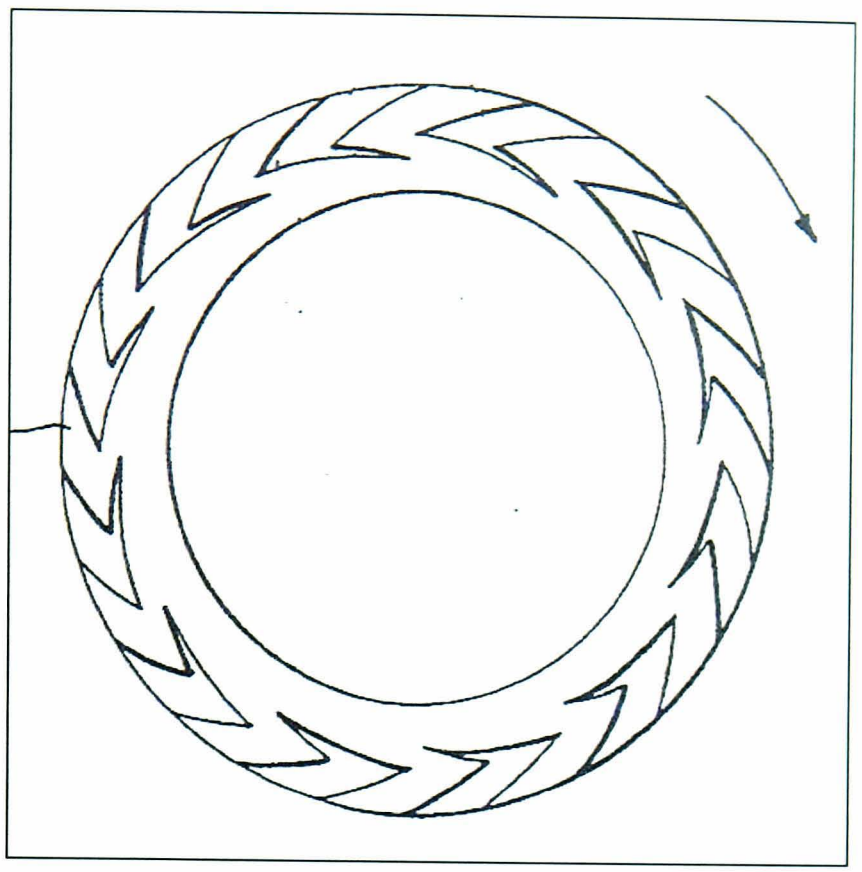

Figure 8: Two part logarithmic spiral groove geometry

A slot fed hydrostatic concept has been cited on a number of occasions and has received extensive attention. However, it is clear that it has never tested to high operational duties and thus, its claimed performance at these and reduced gap conditions have never been proven. In equal measure, the logarithmic spiral groove design has also received detailed attention. Albeit, the more intricate aspects of its performance have still been kept out of public domain. A significant number of alternative groove geometries have been investigated and presented in varying degrees of detail, ranging from technical papers, to patents.

Extensive literature review did not yield a single reference or publication on the concept of a non-contacting gas seal which combines the slot feed element of a hydrostatic gas seal as presented by Stolarski and Xue [37] with a spiral groove geometry, as originally presented by Muijderman, [22] and later by Sedy [29]. No work has been cited on such a proposal and there is no evidence of such a concept in existence anywhere. To all extents and purposes, this is a truly novel and unique design concept for a non-contacting gas seal. The research into this proposal forms the basis of the second objective of the work detailed in this thesis.

3 RESEARCH OBJECTIVES

3.1 OBJECTIVE 1: DETERMINE THE PERFORMANCE OF THE SLOT FEED (SF) DESIGN AT ELEVATED PRESSURES AND SPEEDS. CORRELATE PREDICTIVE THEORY WITH EXPERIMENTAL RESSULTS

The first objective is to determine the performance of the slot feed design of non-contacting gas design (referred to as the SF design). The performance of the seal is to be evaluated across a high duty-operating envelope. The test pressure range is to be 0 to 300 bar, speed range of 6000 to 12000 rpm and a maximum operating temperature of 120°C. In terms of the established technology, the combination of pressure and temperature puts the operating conditions at the very extreme of the performance envelope. To achieve this, a fit for purpose cartridge design of the gas seals is to be designed and made.

The next requirement under this first overall objective is to correlate the theory to experimental results. To achieve this, detailed theory is to be developed. Based on this theory, a computer model is to be built to predict the performance of the given seal design. An appraisal of the performance is to be given highlighting the major benefits as well as drawbacks.

3.2 OBJECTIVE 2: PROPOSE A NOVEL DESIGN OF NON-CONTACTING SEAL. DEVELOP THE PREDICTIVE MODEL AND CORRELATE THEORY WITH EXPERIMENTAL RESULTS

The second objective is to propose a new and totally novel design of non-contacting gas seal incorporating a unique lift geometry – The proposed design is to combine the slot feed feature of the SF design with a partial logarithmic spiral groove geometry, in effect creating a hybrid concept (referred to as the SFLS design – slot fed logarithmic spiral). A set of test seals are to be made and their performance determined experimentally across the entire high duty performance envelope of 0 to 300 bar, 6000-12000 rpm and 120°C.

To validate the performance, a suitable theoretical model is to be developed to accurately predict the performance of the above design and validate the experimental

data. The computer-based model is to be enhanced and developed with the aim of creating an effective analysis and performance evaluation tool. Using the developed theory and the computer-based model, model predictions will be correlated against experimental results. An appraisal of the performance is to be given highlighting the major benefits as well as drawbacks. Finally, the performance of the two designs is to be compared and suitable conclusions to be drawn up

In order to achieve the experimental elements of the above objectives, specialised test equipment is to be designed and built. Also, a dedicated test facility is to be designed and built on the premises of the School of Engineering, to enable the undertaking of all the necessary performance tests.

For effective testing and validation, two tandem cartridge seal designs have been engineered and produced, each one capable of operating within the prescribed performance envelope.

4 DEDICATED GAS SEAL TEST EQUIPMENT AND TEST FACILITY

4.1 RIG SPECIFICATION

A dedicated test facility had to be designed, built and commissioned. The facility had to provide the capability to fully test and measure the performance of the gas seals under investigation, across their entire duty conditions of pressure, speed and temperature.

Detailed research, planning and design by the author, went into the every element and aspect of the test facility. Every key module was conceived, specified, designed and constructed, ground up. This made the facility totally original in every way. One of the biggest limitations for the installation was the available space. Thus, from the outset, the test facility, including the rig was designed to be optimum in terms of compactness, and modular.

Part of the Brunel University Tribology Laboratory was set aside to house, both the test rig as well as the data acquisition and control modules. Figure 9 shows a solid model view of the test facility, as it was finally designed and ultimately constructed and commissioned.

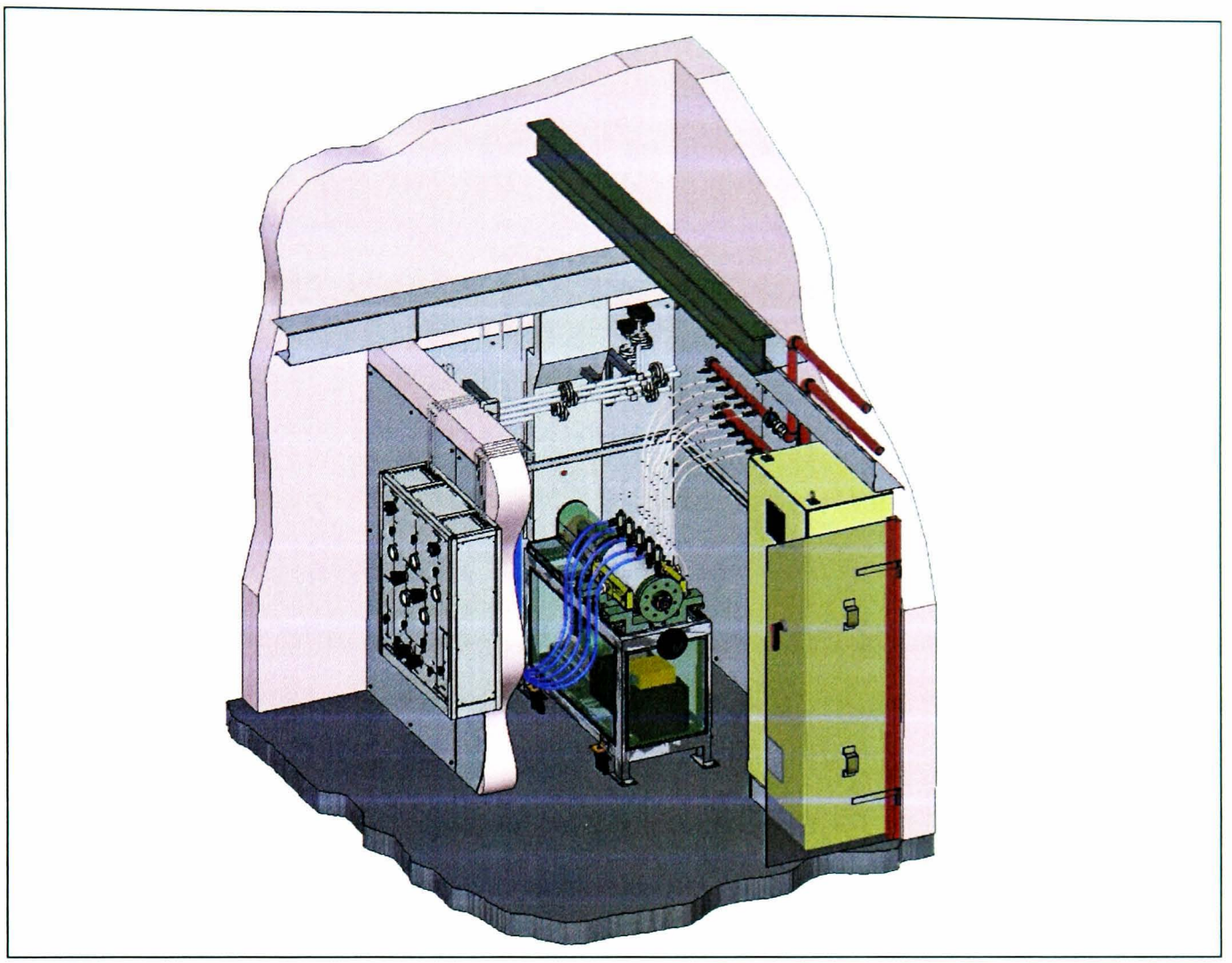

Figure 9: Cutaway isometric view of the gas seals test facility

4.1.1 Summary of test rig operating envelope

Drive speed range: 0-15000 rpm

Pressure capability: 0 - 400 bar

Temperature capability: 20-220°C. (using suitable flexible or rigid hoses)

Cooling system requirements: 45kW

Cooling water supply requirements: water @ 42 l/min @ 1.5 bar at 293 Kelvin.

4.1.2 High pressure test gas (air) supply requirements

Minimum continuous stable pressure: 350 bar

Free air delivery : 800 l/min

A Hamworthy compressor capable of delivering 1550 l/min FAD at maximum pressure of 414 bar was sourced to supply the necessary air for the test facility.

4.1.3 Pipe-work specification:

All rigid high pressure gas supply pipe work was constructed from annealed, seamless 316 stainless steel tubing to ASTM A269, 10mm O.D. x 2 mm wall thickness. Max working pressure 670 Bar. The rigid pipe-work connected to the vessel through a wall mounted manifold and flexible tubing with quick release dry break couplings.

4.1.4 Test rig frame

An engineered test rig frame was designed (Figure 10). This houses the motor, the drive train and is equipped with mounting points to allow for attaching of the test vessel containing the gas seals.

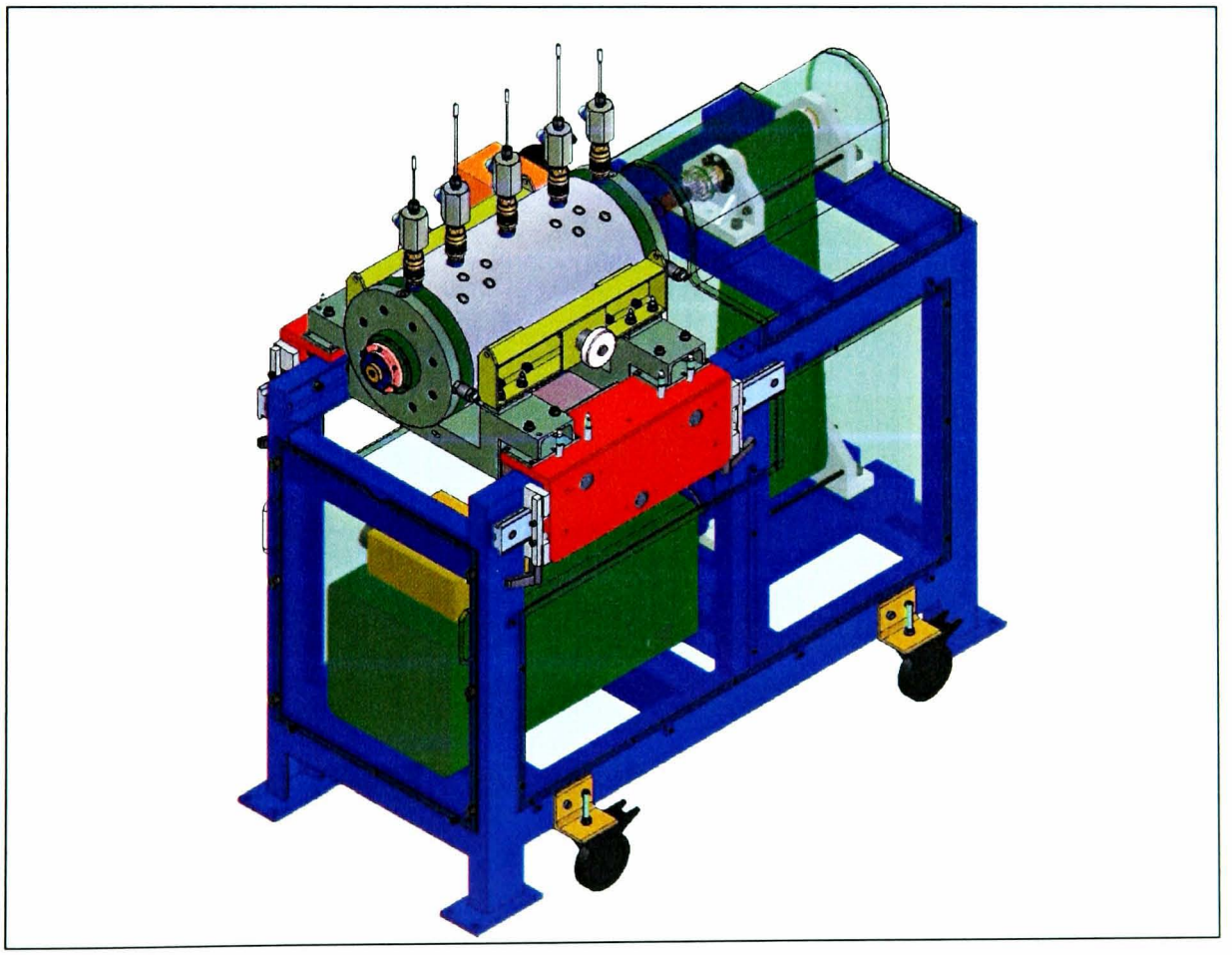

Figure 10: Test rig frame with S129 test vessel in place.

4.1.5 Drive train specification

In order to achieve the necessary operating speed of the gas seals, a dedicated drive train was designed and manufactured. This comprises of the drive motor, step up pulley system and transmission shafts. Details have been given below:

4.1.5.1 Motor

SIEI Ltd Foot mounted Vector Motor and Frame

Rated 105kW

Max. shaft speed 7500 rpm @ 106 Hz.

Full load current, 189 Amps

4.1.5.2 Step-up pulleys

Engineered bearing housings, pulleys and shafts.

Flat belt drive

Step up ratio 2.2 : 1

4.1.6 Motor Controller & Associated Equipment

To house the power electronics, the frequency inverter and control hardware for the drive motor, a separate control unit has been provided. The specification is shown below.

IP54 protected enclosure – 1800 x 800 x 500 mm

Door Isolator & Emergency stop button

RS485 Serial interface to link with RS232 port on PC.

Dynamic braking unit – 85 Amps

Power supply: three Phase 380 – 460 Volt (+/- 10%) 50/60Hz supply. Rated to 300 Amps.

4.1.7 Pressure Control Module

The custom engineered, wall mounted control module (Figure 11 and Figure 12) is designed to allow the operator to manually control the pressurisation of the test vessel and the seals inside it. Figure 13 shows a P&ID diagram for all the components in the module.

The module is designed to test two single or two tandem seals, back to back. It is equipped with fine and coarse pressure control, the former from 0 to 50 bar and the latter from 0 to 350 bar. The interspace location between the inboard and outboard seal cartridges may also be regulated over a similar range, to enable the testing of the OB cartridges. For isolating and testing of the inboard seal pair only, the control module allows the interspace to be vented to atmosphere. All components within the control module are rated to 400 Bar, the pipe work to 670 Bar.

In addition to the above, the control module collects seal leakage from the leakage ports of the test vessel and then directs that to the mass flow meters. The module is also equipped with pressure transducers to measure the system pressure at various points in the test vessel.

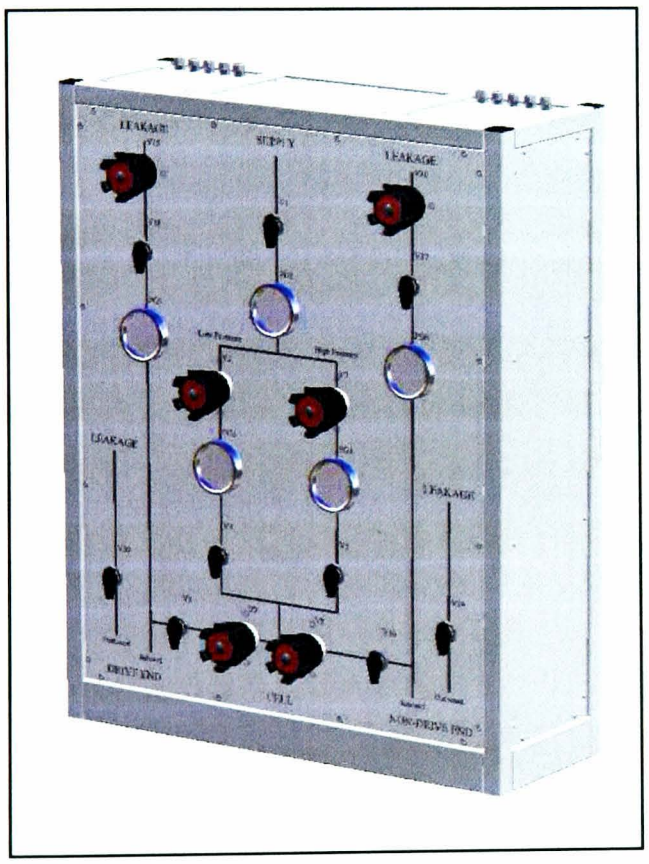

Figure 11: Model of gas seal pressure control module

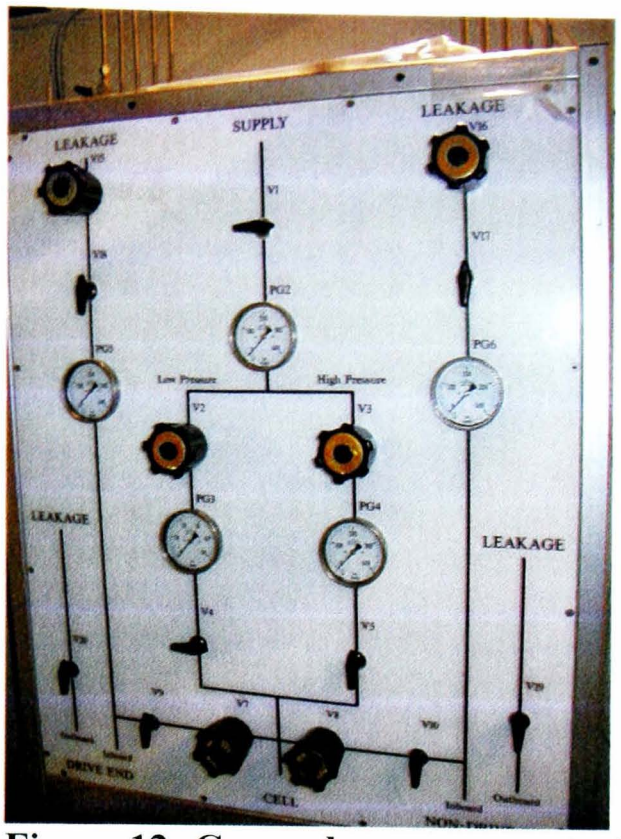

Figure 12: Gas seal pressure control module

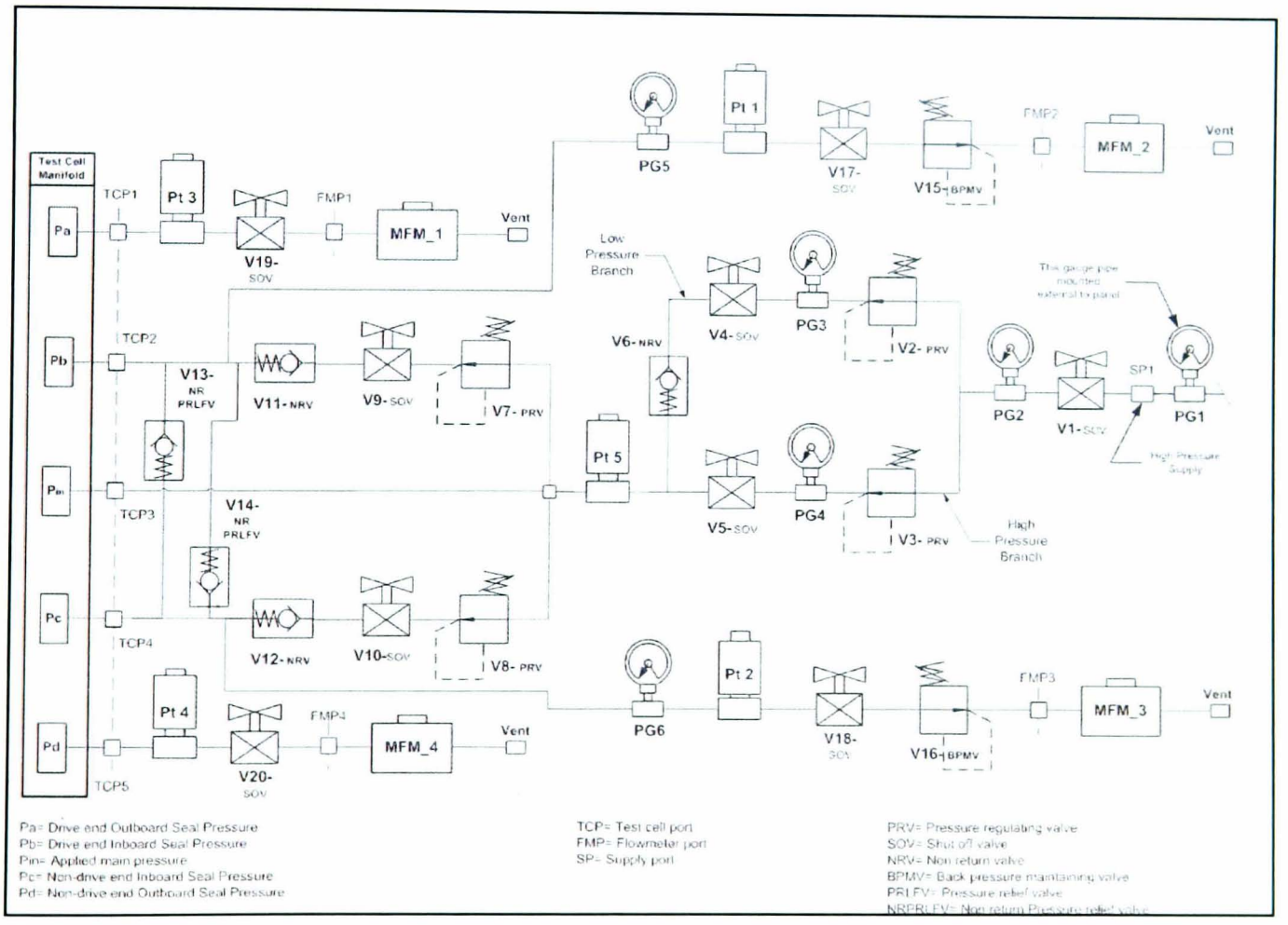

Figure 13: P&ID diagram of the gas control module

4.1.8 Gas Leakage Monitoring & Instrumentation module

One of the most important performance indicators for a mechanical seal is the leakage. To facilitate accurate measurement of leakage the test facility has been

equipped with a bank of dedicated thermal mass flow meters (Figure 14 and Figure 15).

Manufacturer	ABB
Model:	VT-S / V14222
Output:	4 – 20 mA
Pressure range:	0 – 40 bar (gauge)
Volume flow range:	0 – 400 l/min
Temp. range:	248 - 423 Kelvin
Flow meter accuracy:	+/- 1% of full-scale deflection (FSD)

In terms of flow meter accuracy, this is as accurate as one can practically get without then having the compromise on the available flow range.

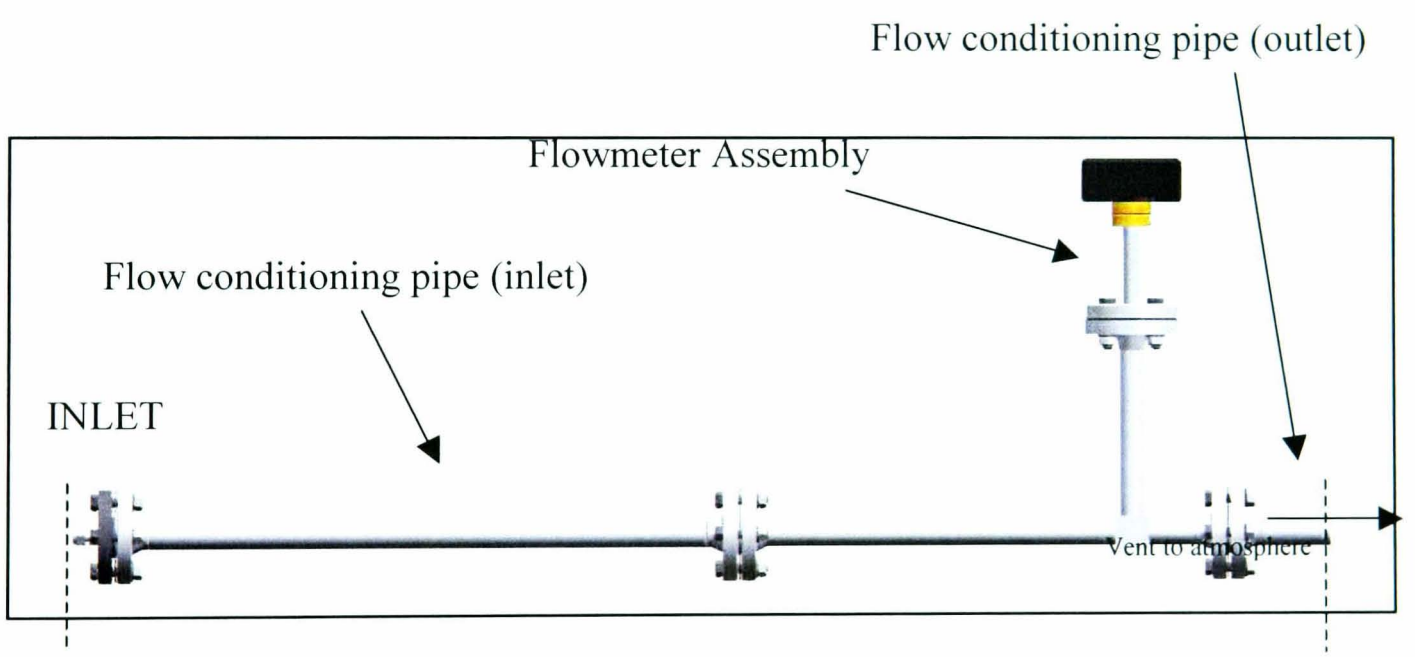

Figure 14: Single Flow-meter assembly – side view

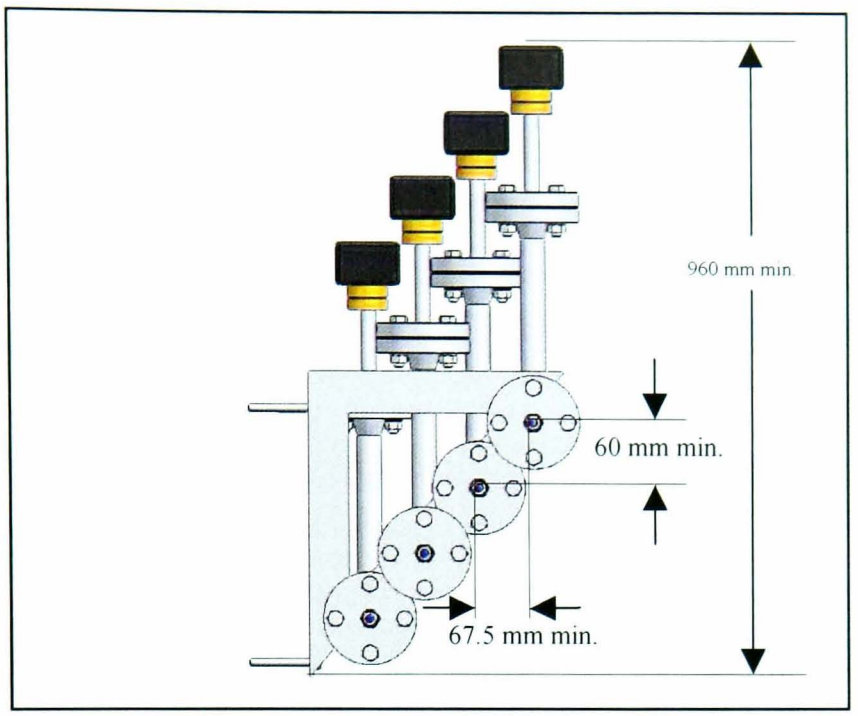

Figure 15: End view of cascaded flow meters - bank of 4 units

4.1.9 Gas Pressure and Temperature Monitoring & Instrumentation

Gas temperature sensing is carried out within the test vessel using Platinum Resistance Thermometers, (PRTs) inserted deep in the vessel through the gas ports using suitable adaptors. These are connected to the data acquisition module using screened cables.

Specification:-

Manufacturer: TC Ltd, type: 16

Diameter: 3 mm sheath

Length: 400 mm

Max. Temp: 350^{O} C

Current: 5mA

Transducer accuracy: +/- 0.5^{o} C.

Pressure transducers mounted within the gas control module measure the pressure in the test vessel pressure at the vessel centre (seal inlet), inter-space (inboard seal discharge) and outboard (outboard seal discharge) locations. The transducers are connected to the data acquisition module using screened cables. The transducer accuracy across the full pressure range is +/- 0.2 bar.

4.1.10 Data Acquisition & monitoring system

The custom designed and manufactured DA module provides the supply voltage to, and receives data from the pressure transducers, flow meters and PRTs. It also controls the motor drive system. The analogue input data is processed and transmitted in digital format via a USB 2.0 link direct to the PC. All the hardware is mounted in a singled box on the wall in the test room.

4.1.11 Software:

For all data acquisition, real time monitoring and data storage, a custom developed control software is used. This is based on the National Instruments LabVIEW$_{TM}$ suite of DA tools and is a stand-alone application, run locally. Test result data is captured and stored in a format recognised by Microsoft Excel$_{TM}$.

Input channels:

Pressure :Cell centre, DE & NDE interspace, DE & NDE Outboard

Temperature: - Cell centre DE & NDE interspace, DE & NDE Outboard

Leakage:- DE & NDE interspace, DE & NDE Outboard

Motor Torque. And motor Speed.

Labview Fieldpoint Software, as supplied by the National Engineering Laboratory was the basis for the data acquisition software. It provides an explorer type environment for set up of the communications (Ethernet) link. It also provides the facility to group and assigns names to the data I/O channels in the system. Finally, it facilitates communication with the embedded Labview Fieldpoint controller module.

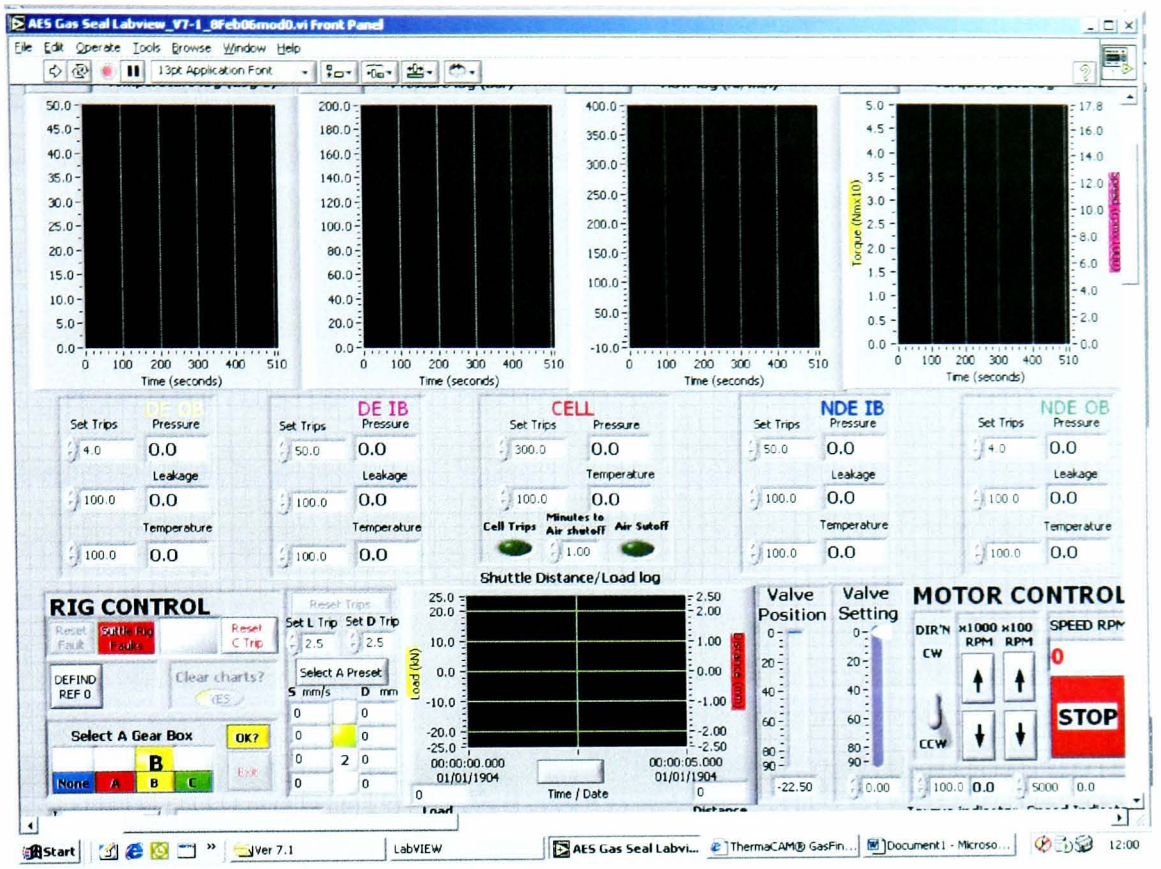

Figure 16: Screen shot of data acquisition system

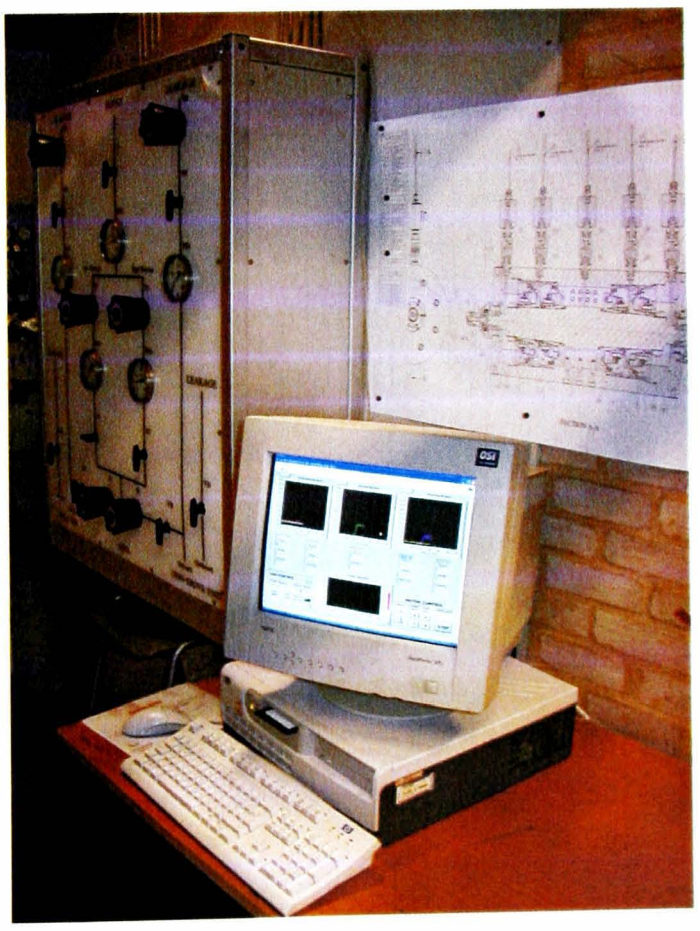

Figure 17: PC based data acquisition system next to the gas seal control module

4.2 THE TEST VESSEL

This is an engineered pressure vessel for testing of gas seals and is at the heart of the test equipment (Figure 18 and Figure 19). The test vessel is designed to simulate the

operational environment of a gas seal, namely the compressor. The test vessel wall simulates the compressor housing and the test vessel shaft simulates the compressor shaft.

The test vessel is a sophisticated assembly engineered to handle the full range of pressures and temperatures required for gas seal testing. It is equipped with a sophisticated cooling system comprising of internal cooling coils and wall scrolls designed to maximize the amount of heat removed from the vessel centre to avoid overheating during testing. Without this system the seal in fact could not be tested. Figure 20 shows the test vessel on the rig frame.

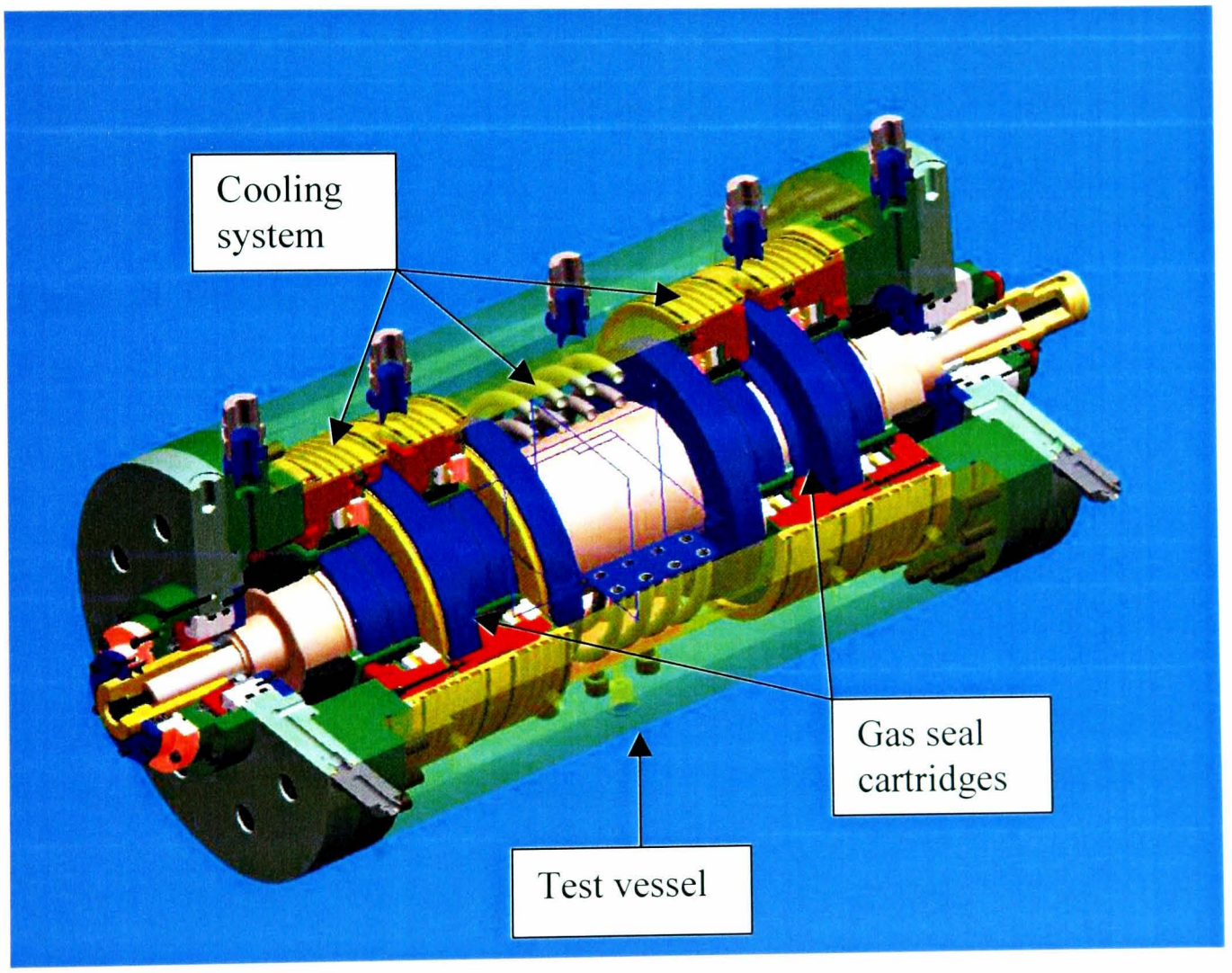

Figure 18: Test vessel model showing the two seal cartridges and an internal cooling system

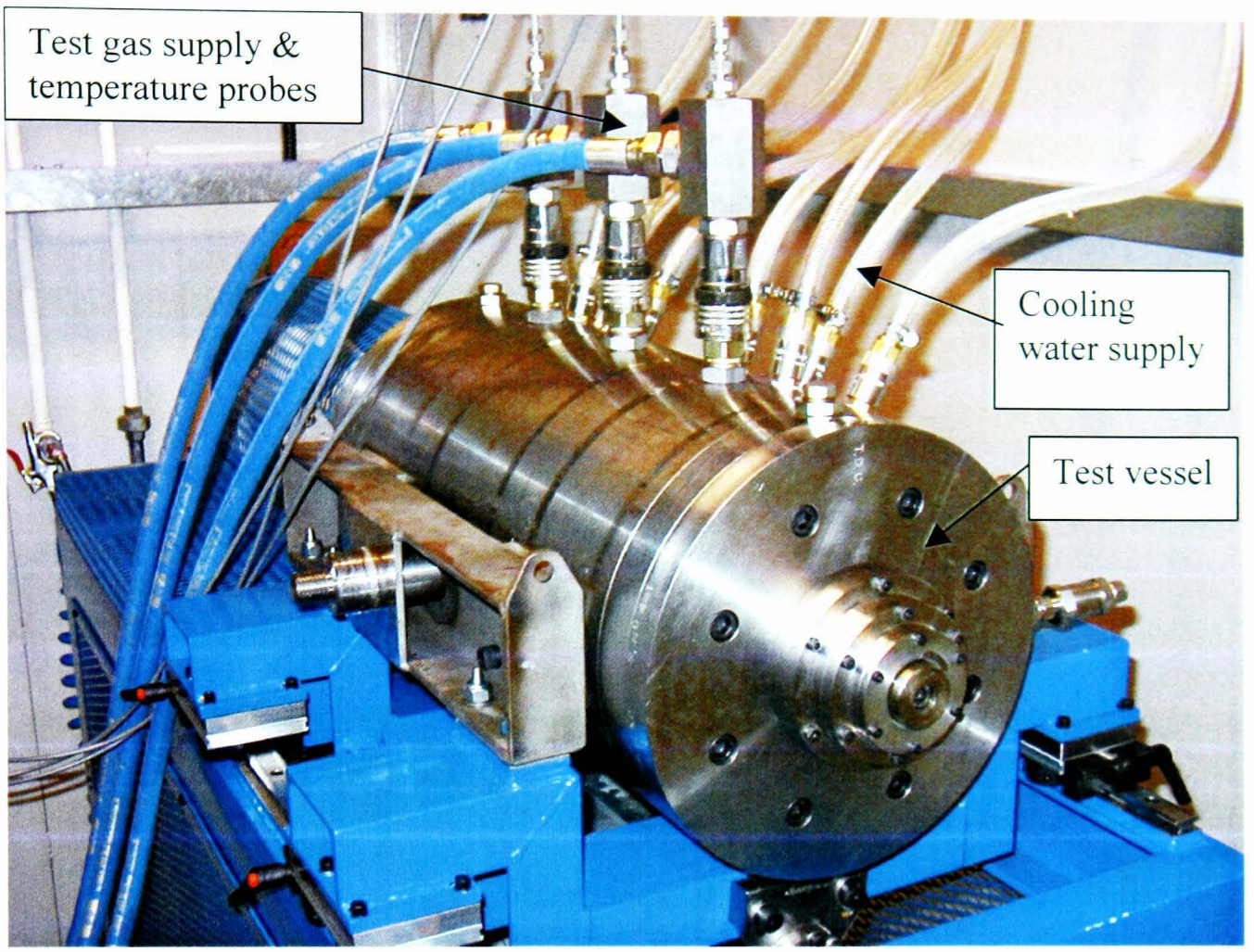

Figure 19: Gas seals test vessel on the rig

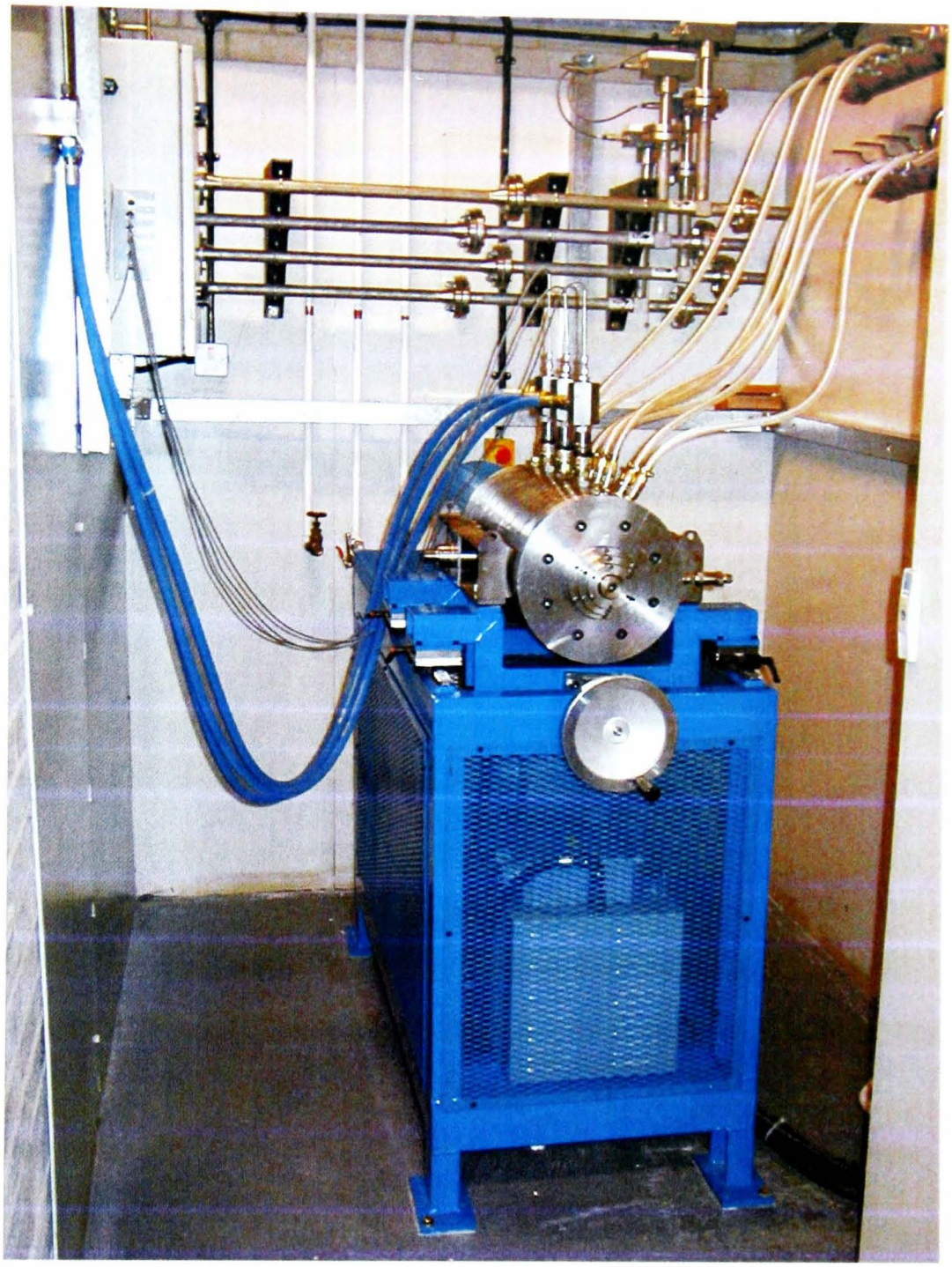

Figure 20: Test rig frame and test vessel in position

4.3 DESCRIPTION OF EXPERIMENTAL PROCEDURES

4.3.1 Ambient static experimental procedures

The objective is to measure static leakages and breakout torque at various pressures from zero to maximum operating conditions of 300 bar.

The starting point is to measure the breakout torque of the seals at zero pressure: At this condition, a calibrated torque meter is attached to the non-drive end of the test vessel shaft, using a suitable fitting. The meter is used to measure the torque at which the shaft just starts to turn under manual rotation. This effectively becomes the datum break out torque for zero pressure.

Test gas is then introduced into the vessel and the test seals using a pressure control module (Figure 11) to raise the sealing pressure to 1 bar. The torque measurement is then repeated, typically 2-3 times, and an average value recorded. The pressure is then increased by a further 1 to 2 bar and the torque measurement repeated. The whole torque measurement procedure is repeated at 1-bar increments until the maximum break out torque drops to a minimum asymptote. From this point on the pressure increments are increased to 20-50 bar, and the torque measurements are measured at each of those increments up to 300 bar. Finally, to record the hysteresis of the system, the above procedure is repeated in reverse, with break out torque figures recorded at decreasing pressure increments, back down to zero bar.

At the same pressure increments, when the torque measurements are taken, the leakage values are also recorded via the PC based data acquisition system. The procedure involves the increase in pressure to a given value. The seals are then held at that pressure for a period of time, to allow them to stabilise, before the leakage value is recorded. This is typically 2-3 minutes. The pressure is then increased to the next pressure increment. The whole procedure is repeated up to and including the maximum pressure. It is then reversed and the leakages are recorded at the same pressure increments, heading back down to zero pressure. The data acquisition system records all the output parameters several times per second.

4.3.2 Dynamic experimental procedures

The performance of the seals is evaluated across the entire pressure and temperature envelope at discrete pressure and speed points in the form of a 'mapped' matrix test. The test is started with a warm up run. The inboard seals are pressurised to 20 bar, and the outboard seals to 10 bar. The drive motor is then started and the seals accelerated to 6000-8000 rpm. The pressure is then raised to 100 bar and the seals are allowed to run for a period of time at those conditions, with no test vessel cooling, to raise their operating temperature to approximately 80-100^{o} C.

To commence the actual mapping test, the speed is first adjusted to 6000 rpm, and the supply pressure is set to 50 bar. This being the first point in the mapping test. The seals are kept at that condition, for a period of anything from 10 min to 1 hour. The data acquisition system measures the performance outputs several times per

second continuously throughout the test. To move onto the next point, the supply pressure is then increased to 100 bar, while the speed is maintained at 6000 rpm. The seals are then again held at that point to allow them to stabilise, while the leakages and other measurements are recorded. This section of the test is repeated at the remaining 50 bar increments up to the maximum operating pressure of 300 bar. This effectively completes the 6000-rpm speed element of the mapping test.

Proceeding onto the next stage, the pressure is then reduced back down to 50 bar and the operating speed increased up to the next speed increment, which would be 8000 rpm. While maintaining this speed, the pressure mapping procedure described above is repeated at 50 bar increments up to and including 300 bar. To complete the full mapping test, the same steps are further repeated at 10000 and 12000 rpm. During dynamic mapping, the temperature of the test seals is controlled to be below the maximum operating temperature, using the integral test vessel cooling system and a remotely operated cooling flow control valve

5 THE SLOT FEED GAS SEAL DESIGN

5.1 INTRODUCTION

The starting point was the work that was completed by Stolarski and Xue [37]. The operating limits under which the seal was studied are summarised below.

- Maximum operating speed: 3000 rpm
- Maximum operating pressure: 15-bar g
- Maximum test duration: 2-3 hours
- Test gas: bottled nitrogen
- Primary ring material (face): antimony impregnated carbon
- Mating ring material (seat): Cobalt bonded tungsten carbide

The design was basic, and not intended for operation at high pressures and speeds. The material choice of the primary ring precluded potential operation at high duties (pressure and temperature). The design of the metal parts also imposed limitations in terms of excessive deflections and high stress levels. Finally, the design was not of a cartridge configuration, i.e., a self-contained module comprised of the rotor parts, stator parts and including the primary seal zone parts.

The slot fed gas seal design, as was evaluated by Stolarski and Xue [37] is shown in Figure 21.

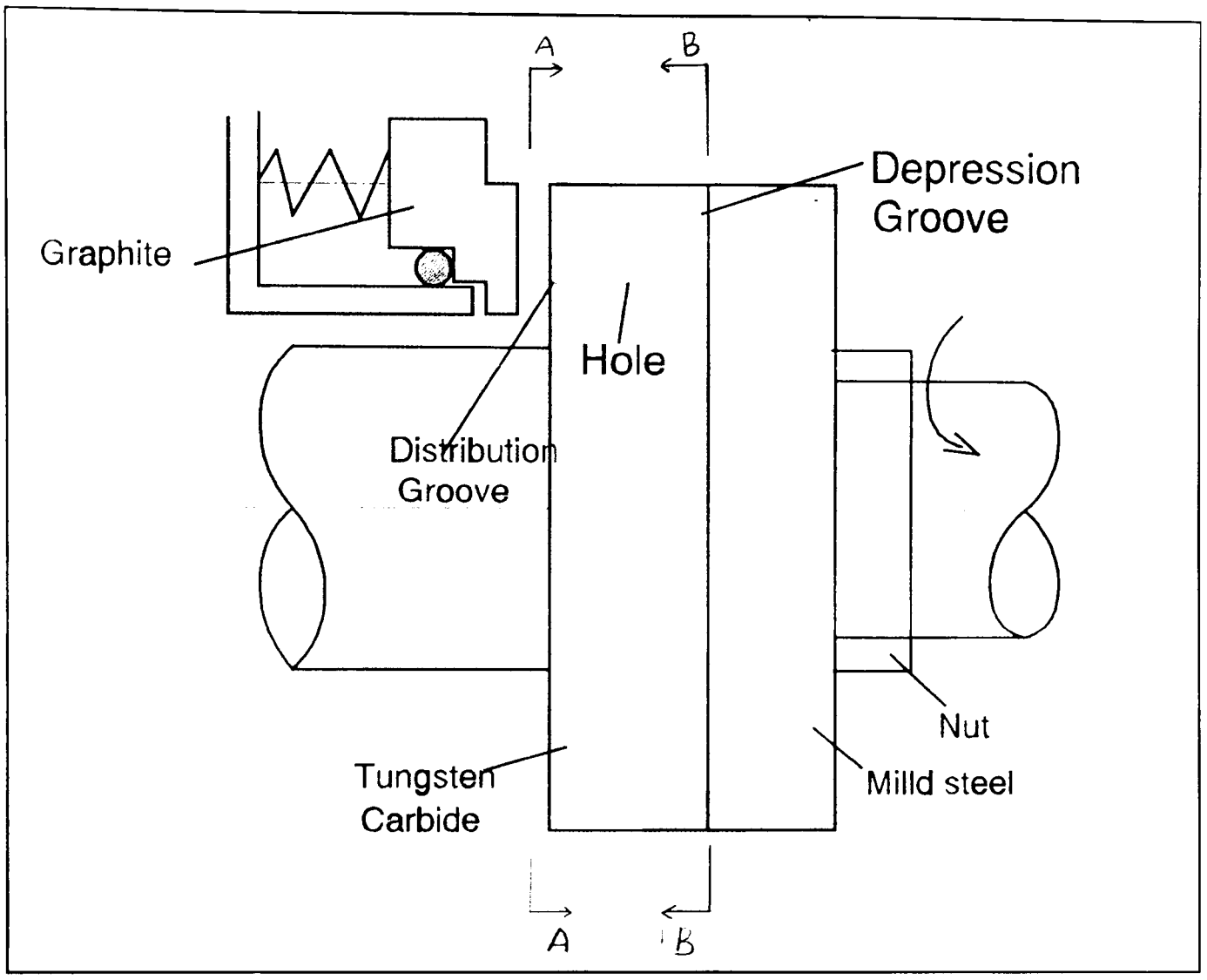

Figure 21: The slot fed dry gas seal concept [37]

5.2 PRINCIPLE OF OPERATION

The seal is of a balanced design, meaning that the balance ratio is less than 100%. In a balanced seal design, the closing force generated by the seal gas pressure is balanced at all times by the opening force generated at the sealing interface of the seal.

The design is non-contacting in its principle of operation. The balance of opening and closing forces mentioned above creates an operating gap between the primary (stationary face) and the mating (rotating seat) rings. The closing force is made up of the spring force and the pressure force from the sealing gas acting on the seal face. The opening force is generated by the opening pressure profile generated at the interface of the seal. When the opening force equals the closing force, which occurs

at a given operating gap, then equilibrium gap is achieved. This force equilibrium condition is shown in Figure 22.

The seal is pressurised from the outside, which means the outer radius has the fluid being sealed and the inner radius is at atmospheric pressure. The seal gas is supplied to the interface via two separate paths. One path is via the feed slots (or depression grooves) and the feed holes in the mating ring (seat). The second path is from the high-pressure side of the seal at the outer radius through the actual seal interface.

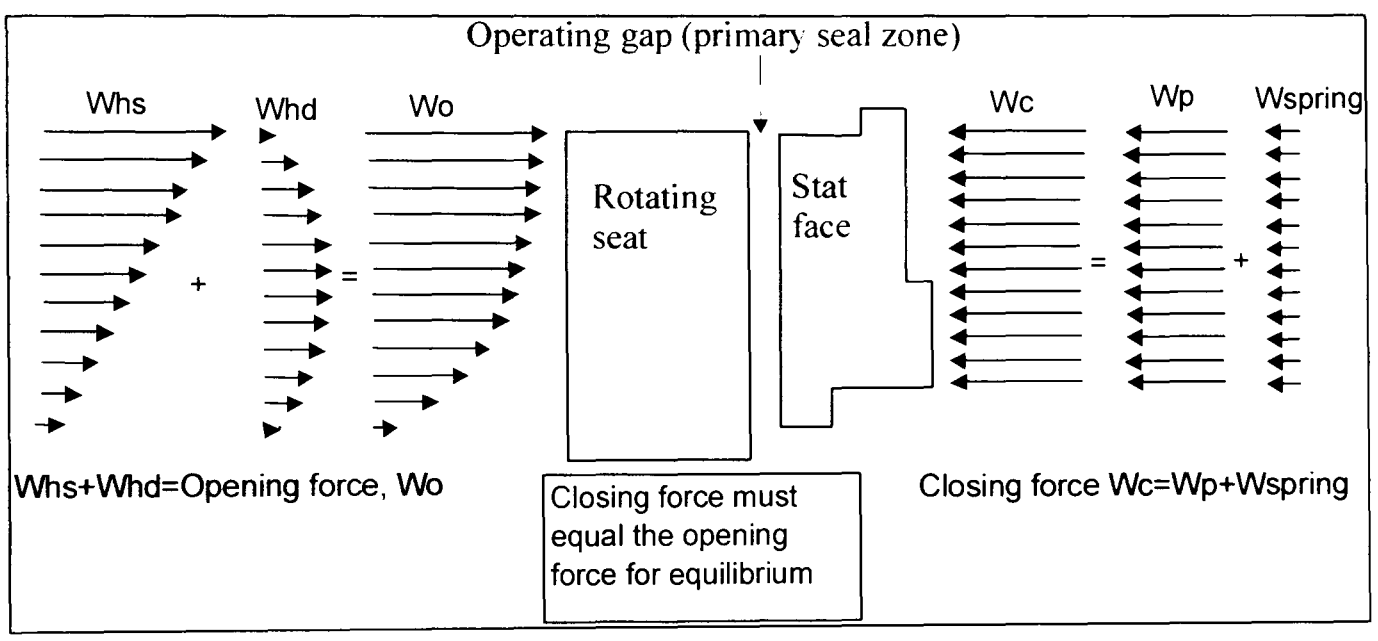

Figure 22: Force equilibrium diagram for a balanced seal

5.2.1 Basic construction

As mentioned above, the primary seal zone is made up of the rotating seat and the stationary face. These two components are enclosed in a self-contained cartridge as shown in Figure 23. The cartridge is designed to provide an effective seal housing between the rotating shaft and the stationary housing of the compressor. To facilitate this, the rotating seat is held in place in a rotor assembly, (depicted red and yellow in Figure 23). The rotor assembly is located on the shaft. Similarly, the stationary face is located within the stationary retainer assembly, located inside and against the inner wall of the housing. Thus, all the rotating parts are in some direct or indirect contact with the rotating shaft, and all the stationary parts are in some direct or indirect contact with the compressor housing. The non-contacting seal gap is thus maintained between the rotating seat and the stationary face.

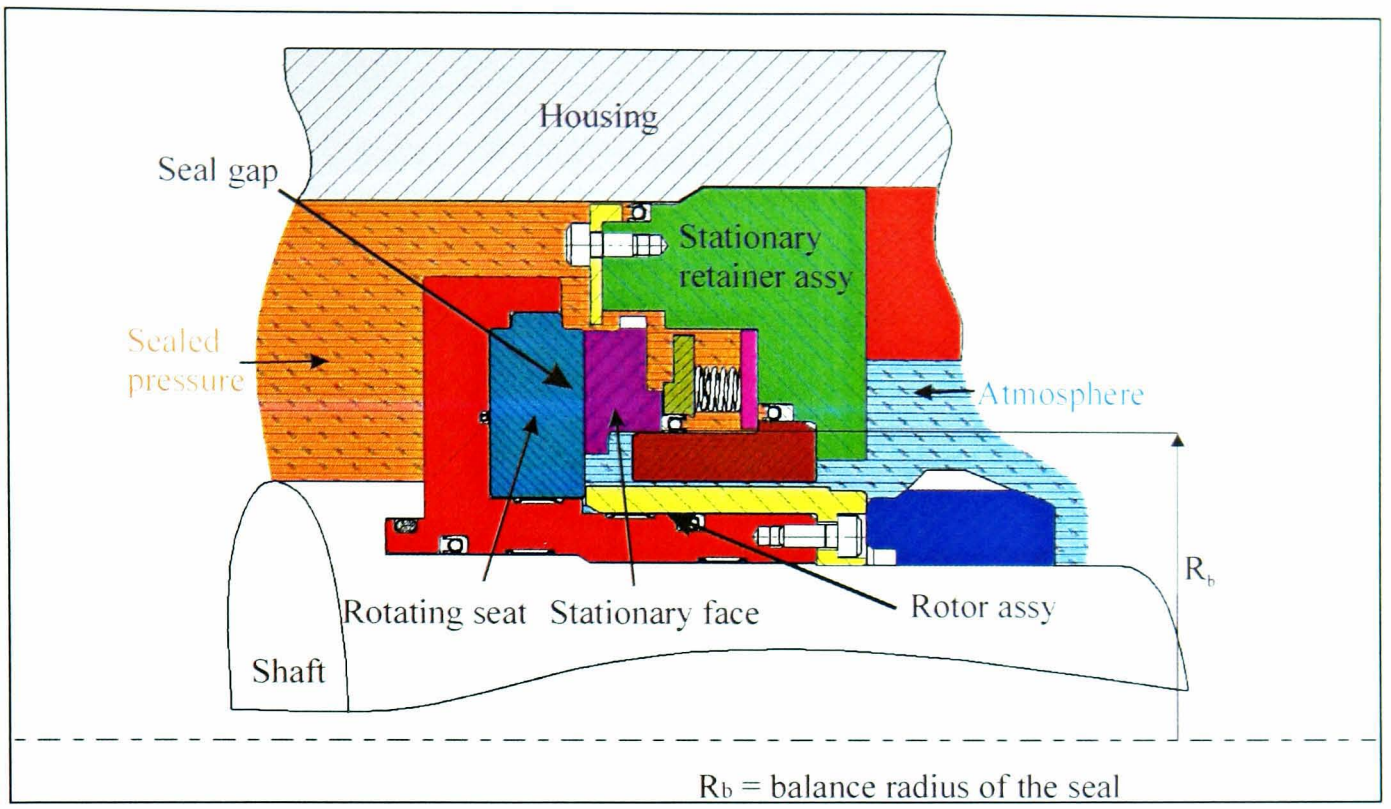

Figure 23: Basic construction of a cartridge gas seal

5.2.2 Balance ratio.

The balance ratio or the balance factor as it is otherwise known is a very important term associated with mechanical seal design. It is important enough to warrant a clear definition. The definition of the balance ratio shall be taken as the ratio between the average load, P_f within the seal interface, expressed as a pressure, imposed on the seal face by the action of the sealed pressure, and the sealed pressure itself P_o. This is also expressed as load acting on the seal faces. Figure 24 shows how it is applied to an outside-pressurised seal, as is the case here. Outside pressured means the sealed pressure P_o is on the outer periphery of the seal and the atmospheric pressure is on the inner periphery of the seal.

Balance ratio (or factor) equations are given by:

$$P_o \pi (R_o^2 - R_b^2) = P_f \pi (R_o^2 - R_i^2)$$

eqn. 5.1

$$BF = \frac{P_f}{P_o}$$

eqn. 5.2

$$BF = \frac{R_o^2 - R_b^2}{R_o^2 - R_i^2}$$

eqn. 5.3

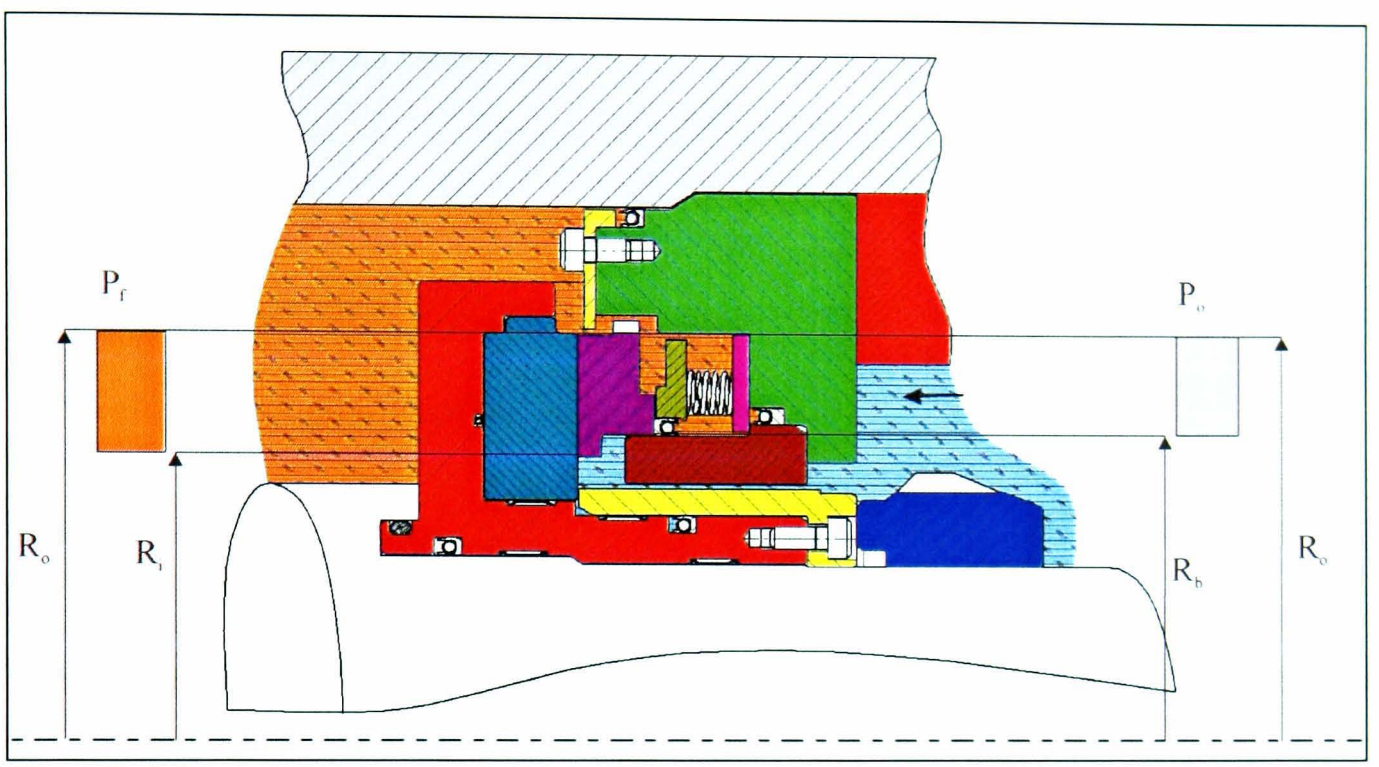

Figure 24: Definition of balance factor for an outside-pressurised seal

5.3 SUMMARY OF THE SLOT FEED MODEL ASSUMPTIONS AND CONSIDERATIONS

1. The flow model is 1-dimensional from the high-pressure source to the low-pressure source.
2. The fluid film pressure and operating gap are modelled in one dimension for the outer to the inner radii.
3. Flow is laminar and not turbulent.
4. The sealed fluid is Newtonian in its nature.
5. The fluid density is constant across the fluid film (axially across).
6. Fluid viscosity is constant across the film.
7. Effect of surface roughness on fluid flow is negligible.
8. Squeeze motions are not included and effects of small amounts of unplanned squeeze are negligible.

9. The film is thin, such that the velocity gradients across the film predominate.

10. There are no shockwaves or other sources of discontinuity.

11. The film is isothermal.

12. Slip flow effects are neglected.

13. Pressure and temperature dependent properties for gas viscosity are utilised.

14. Gas compressibility coefficient is ignored.

15. Effects of sonic flow are ignored.

16. Real viscosity properties for the gas are used

5.4 THEORY

The staring point will be the reduced form of the Navier-Stokes equation for viscous flow. The system under consideration comprises of two annular plates separated by a gap 'h' and neither of the plates rotates (see Figure 25)

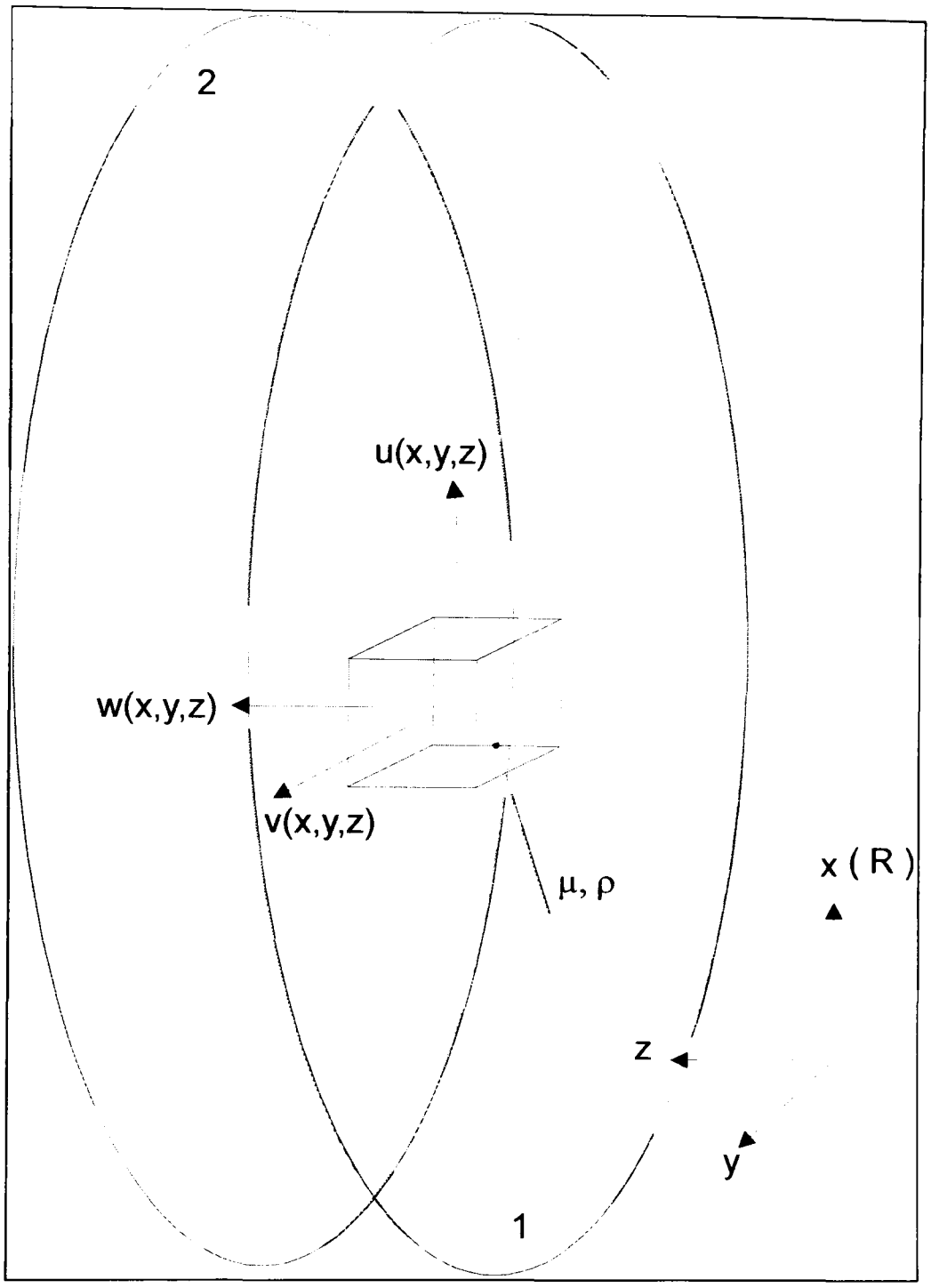

Figure 25: Two annular non-rotating plates (labels 1 and 2)

With reference to Figure 25, consider a thin film that is present between two annular surfaces 1 and 2, both lying in the x-y plane. Within that film is a fluid element depicted by the cube (of a given viscosity and density). Both, the viscosity and the density are taken as constant across and through the film. Component velocities u, v and w may be present in the x, y, z directions. In the case of this simplified analysis, the velocity across the film, w, in direction z is equal to zero. We are also only considering radial flow in direction, x. Thus, the v-component of velocity is also equal to zero. The fluid between the plates flows with a radial velocity `u` that is treated as positive in the radially outward direction.

Pressure gradients $\frac{\partial p}{\partial x}$ and $\frac{\partial p}{\partial y}$ in the x and y directions are independent of direction z (across the film) in a thin film scenario such as this. Thus, $\frac{\partial p}{\partial z} = 0$.

The fundamental relationship between the radial pressure gradient and velocity u is given by:

$$\frac{\partial p}{\partial x} = \mu \frac{\partial^2 u}{\partial z^2}$$

eqn. 5.4

This is a reduced form of the Navier-Stokes equation of motion, in which the higher than the first order values terms have been dropped. No inertia terms have been included, as it has been assumed that flow accelerations are small.

If one then undertakes successive integration with respect to z with the boundary conditions being: u = 0 at z = 0 and z = h, together with the assumption that P is independent of z (across the film). The resulting equation is:

$$u = \frac{1}{2\mu}\frac{dP}{dR}(z^2 - hz)$$

eqn. 5.5

The volume flow is then given by:

$$\dot{V} = 2\pi R \int_0^h u dz$$

eqn. 5.6

Integrating eqn. 5.6, after substituting in for velocity u, the equation becomes:

$$\dot{V} = -\frac{1}{6}\frac{dP}{dR}\pi R h^3$$

eqn. 5.7

If the fluid were incompressible, then one would have continuity of volume flow. However, in the case of a non-contacting gas seal the fluid is compressible and the volume flow will change as the fluid pressure changes. Thus, we must have mass flow continuity. The mass flow, $\dot{m}$, is given by:

$$\dot{m} = \dot{V}\rho$$

eqn. 5.8

At this stage, the flow will be treated as isothermal, and given this assumption, the fluid density can be expressed as:

$$\rho = \varepsilon P$$

eqn. 5.9

Substituting in for the density in the mass flow equation:

$$\dot{m} = \varepsilon P V$$

eqn. 5.10

The gas will be treated as a perfect gas. And for a perfect gas:

$$\rho = \frac{1}{\dot{V}} \frac{P}{RT}$$

eqn. 5.11

and consequently,

$$\varepsilon = \frac{1}{RT}$$

eqn. 5.12

It then follows that eqn. 5.7, becomes:

$$\dot{m} = -\frac{\varepsilon}{6\mu} \frac{PdP}{dR} \pi R h^3$$

eqn. 5.13

If one now takes the two annular plates shown in Figure 25, and modifies them to two rings representing the seal faces, having an arbitrary inner radius R_1 and outer radius R_2. The inner pressure at the plate inner radius R_1, is P_1, and at the outer radius, R_2 it is P_2 (see Figure 26). Those make up the boundary conditions for integration of eqn. 5.13.

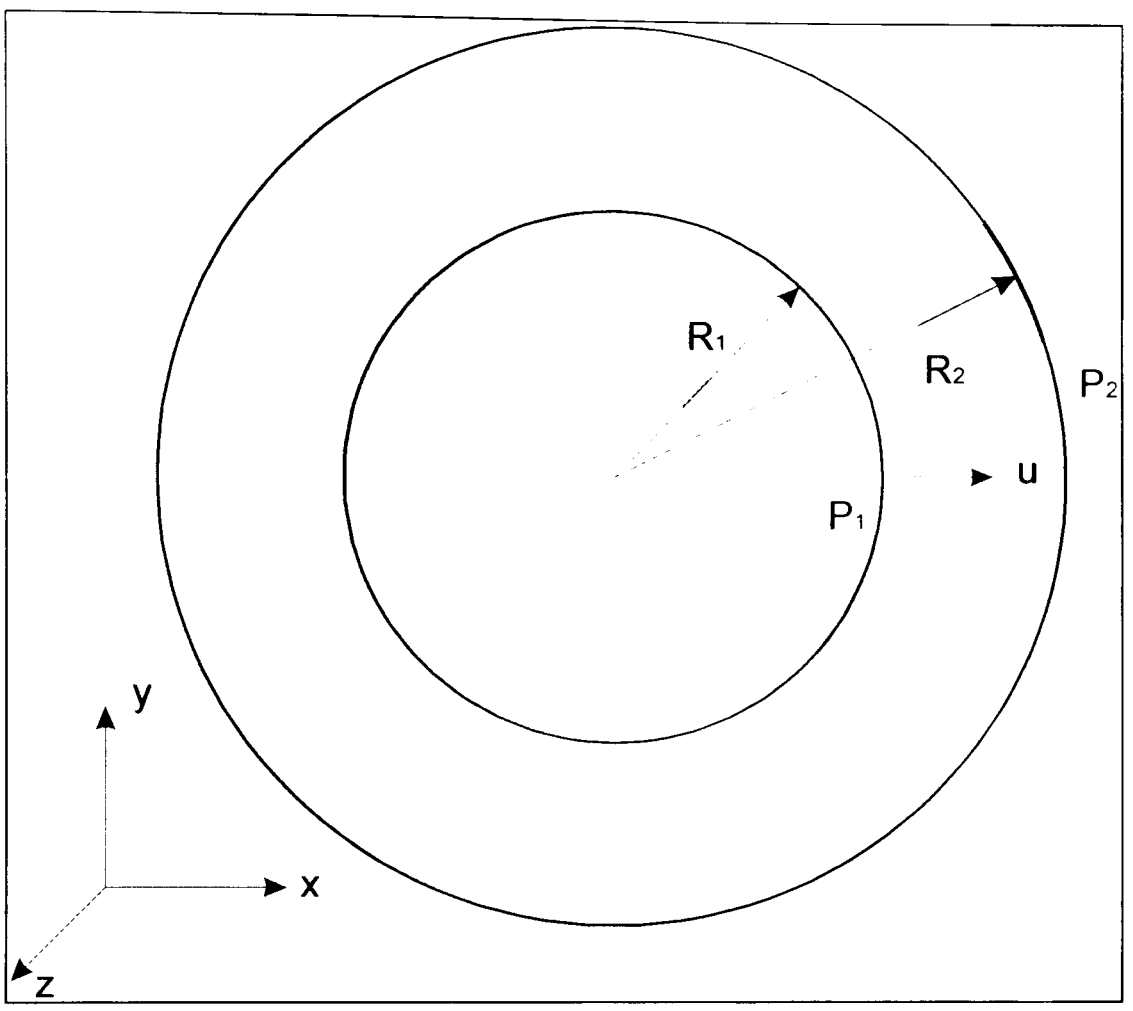

Figure 26: Front view of seal face with arbitrary inner and outer radii and corresponding pressures.

Rearranging **eqn. 5.13** with the aim of integrating with respect to P and R:

$$\int_{P}^{P2} P dP = -\frac{6\mu\dot{m}}{\varepsilon\pi h^3}\int_{R}^{R2}\frac{1}{R}dR$$

eqn. 5.14

Integration of

eqn. 5.14, above produces:

$$P^2 - P_2^2 = \frac{12\mu\dot{m}}{\pi h^3}\ln(R_2 / R)$$

eqn. 5.15

Substitute in the boundary conditions, where $P = P_1$ when $R = R_1$:

$$P_1^2 - P_2^2 = \frac{12\mu\dot{m}}{\pi h^3}\ln(R_2 / R_1)$$

eqn. 5.16

From which the mass flow rate will be given by:

$$\dot{m} = \frac{\varepsilon\pi h^3 (P_1^2 - P_2^2)}{12\mu \ln(R_2 / R_1)}$$

eqn. 5.17

Substituting eqn. 5.17 above in eqn. 5.15 produces:

$$\frac{P^2 - P_2^2}{P_1^2 - P_2^2} = \frac{\ln(R_2 / R)}{\ln(R_2 / R_1)}$$

eqn. 5.18

Rearranging eqn. 5.18 above in terms of unknown pressure p, we get:

$$P = \left[P_2^2 + (P_1^2 - P_2^2 (\frac{\ln(R_2 / R)}{\ln(R_2 / R_1)} \right]^{0.5}$$

eqn. 5.19

It is worth noting from the above equation, that the seal interface pressure as a function of face radius, is independent of the gas properties and is independent of the gap h.

A schematic diagram of the actual slot fed design is shown in Figure 27. The 'bleed' resistance is provided by an annular gap of depth H, formed in the rotating member and connected to the distribution groove, the position of which is defined by radius, R_2. The pressure in that circumferential groove will be denoted as P_2. The seal gap is value h. The inner and outer radii of the seal faces are defined as R_1 and R_3 respectively.

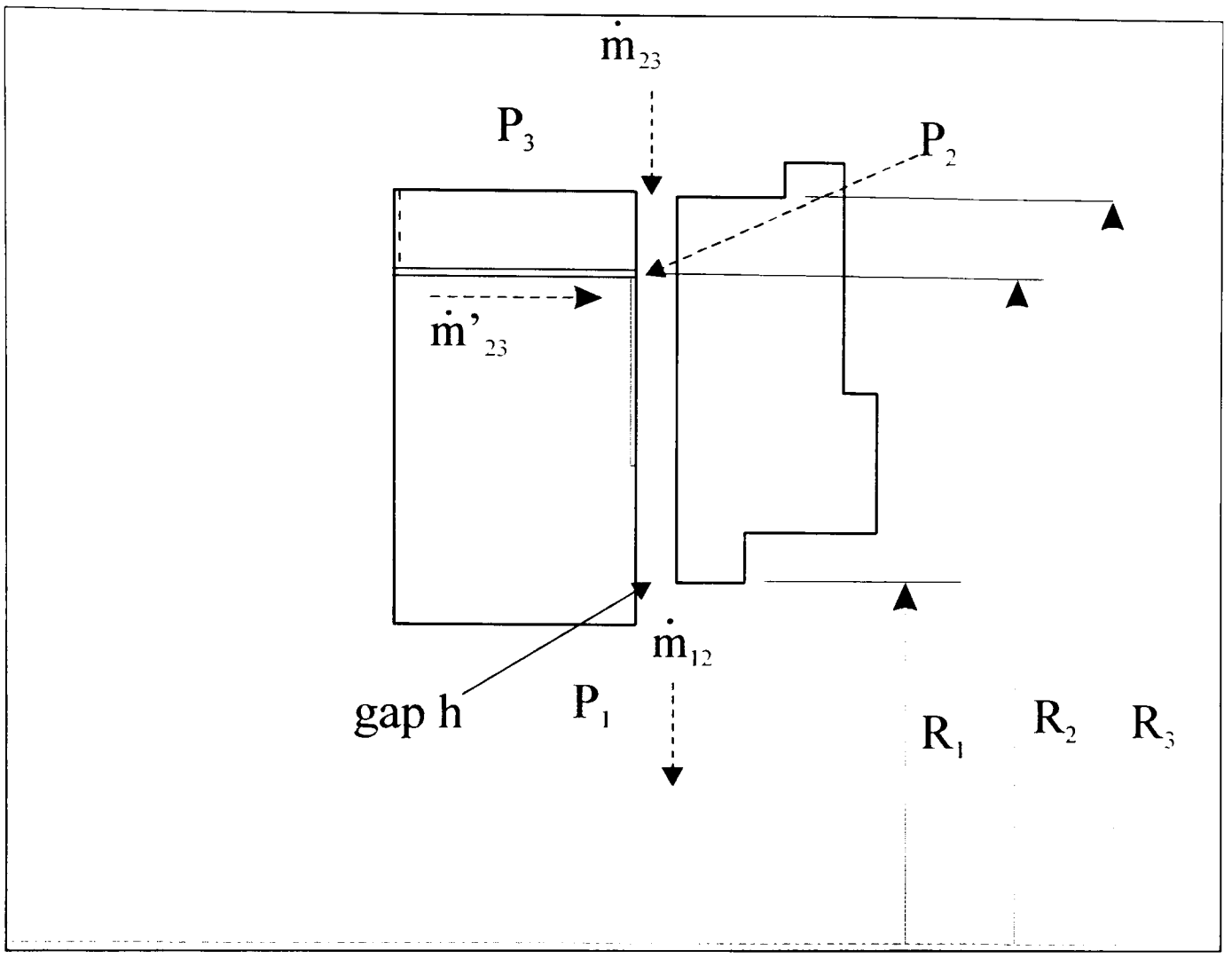

Figure 27: Slot feed gas seal schematic

The respective mass flows, m, are indicated in the same figure. The convention has been adopted in this analysis in that the flows are positive in the positive direction of radius R. As a consequence, the positive mass flows are shown as flowing radially outwards. Thus, for an outside-pressurised seal, where the flow will be radial inwards, the leakage values produced by the analysis will be negative. Defining the mass flow rates in terms of physical radii R_1, R_2 and R_3:

$\dot{m}_{1,2}$ in the gap h from R_1 to R_2,

$\dot{m}_{2,3}$ in the gap h from R_2 to R_3,

$\dot{m}'_{2,3}$ in the rear slot gap H, from R_2 to R_3,

By mass continuity of fluid flow we require that:

$$\dot{m}_{1,2} = \dot{m}_{2,3} + \dot{m}'_{2,3}$$

eqn. 5.20

An expression for the mass flow has already been developed earlier (eqn. 5.17). The expression is for a viscous flow of gas, treated as isothermal and compressible. Substituting eqn. 5.17 into eqn. 5.20, above, results in the following:

$$\frac{\varepsilon\pi h^3(P_1^2 - P_2^2)}{12\mu \ln(R_2/R_1)} = \frac{\varepsilon\pi h^3(P_2^2 - P_3^2)}{12\mu \ln(R_3/R_2)} + \frac{\varepsilon\pi H^3(P_2^2 - P_3^2)}{12\mu \ln(R_3/R_2)}$$

eqn. 5.21

Rearranging the above expression in terms of the unknown groove pressure p_2 results in the following:

$$P_2^2 = \frac{\left[P_1^2 h^3 / \ln(R_2/R_1)\right] + \left[P_3^2(h^3 + H^3)/\ln(R_3/R_2)\right]}{\left[h^3/\ln(R_2/R_1)\right] + \left[(h^3 + H^3)/\ln(R_3/R_2)\right]}$$

eqn. 5.22

In the above expression, all the quantities, except for the gap h and groove pressure P_2, are predetermined from the dimensions of the seal, and from the pressures across it. So the above expression can be used to calculate P_2 as a function of the operating gap h. Once this is done, everything else will follow suit from here, namely the leakage flows, the pressure distribution and the resultant opening force.

The fluid mass flow through the seal is given by:

$$\dot{m}_{1,2} = -\frac{\varepsilon\pi h^3(P_1^2 - P_2^2)}{12\mu \ln(R_2/R_1)}$$

eqn. 5.23

The pressure distributions are found from eqn. 5.19. From radii R_1 to R_2 the distribution is:

$$P = \left[P_2^2 + (P_1^2 - P_2^2)\frac{\ln(R_2/R)}{\ln(R_2/R_1)}\right]^{0.5}$$

eqn. 5.24

And for radii R_2 to R_3 the interface pressure as a function of radius is:

$$P = \left[P_3^2 + (P_2^2 - P_3^2)\frac{\ln(R_3/R)}{\ln(R_3/R_2)}\right]^{0.5}$$

eqn. 5.25

The opening force is then obtained by numerically integrating the pressure distribution over the seal face from R_1 to R_2, and in a similar manner from R_2 to R_3.

5.4.1 Effect of centrifugal forces

Rotation of the plates causes the gas flow to rotate, and subsequently, centrifugal force acts upon it. In this section, expressions are developed which take into consideration the centrifugal forces.

Subsequent calculations demonstrate that the effects of the centrifugal force upon the mass flow and the pressure distribution are small. There are two circumstances of interest, when both annuli rotate together and when one of them is stationary (see Figure 28). In the upper part of the figure, the upper annulus is indicated as rotating with an angular velocity ω_2 and the lower with ω_1. The shearing of the fluid on a cylindrical surface of radius R, is illustrated in the lower part of the figure. In the circumferential direction there can be no pressure gradient, and consequently the fluid velocity profile is linear.

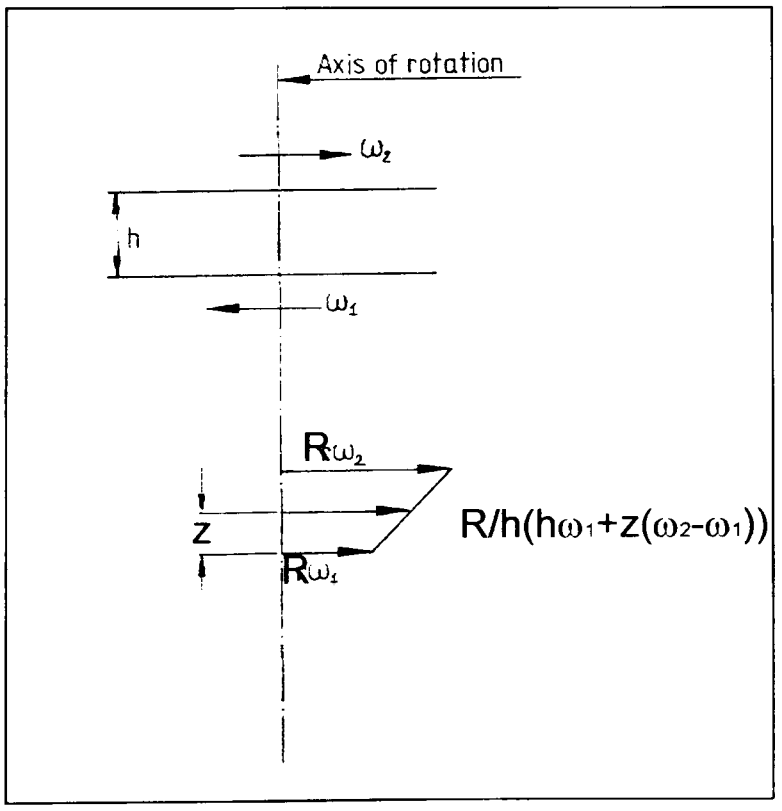

Figure 28: Rotating annuli

The velocity at a gap z, is given by:

$$\frac{R}{h}\left(h\omega_1 + z(\omega_2 - \omega_1)\right)$$

eqn. 5.26

The centrifugal force acting on each unit volume is thus:

$$\rho R\left[\omega_1 + \frac{z}{h}(\omega_2 - \omega_1)\right]^2$$

eqn. 5.27

This force can now be added to the set of forces depicted by the simplified Navier-Stokes equation. The equation becomes:

$$\frac{dP}{dR} = \frac{\mu d^2 u}{dz^2} + \rho R\left[\omega_1 + \frac{z}{h}(\omega_2 - \omega_1)\right]^2$$

eqn. 5.28

Given that we have compressible flow, expressing ρ in terms of P, the following results:

$$\frac{dP}{dR} = \frac{\mu d^2 u}{dz^2} + \varepsilon PR\left[\omega_1 + \frac{z}{h}(\omega_2 - \omega_1)\right]^2$$

eqn. 5.29

It should also be noted that the forces are in the radial direction and that the flow velocity, u, is the fluid flow velocity in the radial-axial planes. The boundary conditions are such that: u = 0 when z = 0 and when z = h. It can be taken that pressure P is independent of gap z. Successive integration of eqn. 5.29 with respect to z, and using the above boundary conditions yields the following:

$$u = \frac{1}{\mu}\left[\frac{1}{2}\frac{dP}{dR}(z^2 - hz) + \frac{\varepsilon PRhz}{12}(3\omega_1^2 + \omega_1\omega_2 + \omega_2^2) - \varepsilon PR\left[\frac{\omega_1^2 z^2}{2} + \frac{z^3}{3h}(\omega_1\omega_2 - \omega_1^2) + \frac{z^4}{12h^2}(\omega_2^2 - 2\omega_1\omega_2 + \omega_1^2)\right]\right]$$

eqn. 5.30

The volume flow is given by:

$$V = 2\pi R\int_0^h u\,dz$$

eqn. 5.31

Substituting for u and integrating produces the following:

$$\dot{V} = -\frac{\pi r h^3}{6\mu}\left[\frac{dP}{dR} - \frac{\varepsilon P R}{10}(3\omega_1^2 + 4\omega_1\omega_2 + 3\omega_2^2)\right]$$

eqn. 5.32

For convenience, one can rewrite the above equation in the form of:

$$\dot{V} = -\frac{\pi r h^3}{6\mu}\left[\frac{dP}{dR} - \varepsilon \,\mathrm{Pr}\,\Omega_2\right]$$

eqn. 5.33

where: $$\Omega^2 = \frac{(3\omega_1^2 + 4\omega_1\omega_2 + 3\omega_2^2)}{10}$$

eqn. 5.34

The mass flow is expressed by:

$$\dot{m} = \rho V = \varepsilon P V$$

eqn. 5.35

Substituting into the volume flow equation (eqn. 5.33) to get the mass flow rate:

$$\dot{m} = -\frac{\varepsilon \pi R h^3}{6\mu}\left[\frac{PdP}{dR} - \varepsilon P^2 R\Omega_2\right]$$

eqn. 5.36

From which it follows that:

$$\dot{m}\int_R^{R2}\frac{dR}{R} - \frac{\varepsilon^2 \pi h^3 \Omega^2}{6\mu}\int_R^{R2} P^2 R dR = -\frac{\varepsilon \pi h^3}{6\mu}\int_P^{P2} P dP$$

eqn. 5.37

To date it has not been possible to find an analytical solution to the differential equation. Thus for simplicity of analysis only the term containing the centrifugal effect will be taken, i.e. the second integral on the left. The assumed pressure would be the pressure that would exist without centrifugal effects. That is, it will be taken that the pressure in the centrifugal term is given by eqn. 5.25

$$P^2 = \left[P_2^2 + (P_1^2 - P_2^2) \frac{\ln(R_2 / R)}{\ln(R_2 / R_1)} \right]$$

eqn. 5.38

Then the integral:

$$\int_2^{r2} P^2 R dR$$

eqn. 5.39

Becomes:

$$I_r^{r2} = \int_r^{r2} \left[P_2^2 r + \frac{(P_1^2 - P_2^2)}{\ln(R_2 / R_1)} (R \ln R_2 - R \ln R) \right] dR$$

eqn. 5.40

Evaluation of the integral produces:

$$I_R^{R2} = \frac{P_2^2}{2}(R_2^2 - R^2) + \left[\frac{(P_1^2 - P_2^2}{\ln(R_2 / R_1)} \left\{ -\frac{R^2}{2} \ln(\frac{R_2}{R}) + \frac{1}{4}(R_2^2 - R^2) \right\} \right]$$

eqn. 5.41

The above can be expressed more conveniently as:

$$I_R^{R2} = P_2^2 \left[\frac{(R_2^2 - R^2)}{2} - \frac{1}{\ln(R_2/R_1)} \left\{ -\frac{r_2}{2} \ln(R_2/R) + \frac{1}{4}(R_2^2 - R^2) \right\} \right] + P_1^2 \left[\frac{1}{\ln(R_2/R_1)} \left\{ -\frac{R^2}{2} \ln(R^2/R) + \frac{1}{4}(R_2^2 - R^2) \right\} \right]$$

eqn. 5.42

It then follows that:

$$I_R^{R2} = P_2^2 \left[\frac{R_2^2}{2} - \frac{1}{4\ln(R_2 / R_1)} (R_2^2 - R_1^2) \right] - P_1^2 \left[\frac{R_1^2}{2} - \frac{1}{4\ln(R_2 / R_1)} (R_2^2 - R_1^2) \right]$$

eqn. 5.43

Now if we return back to equation (eqn. 5.37), the integral becomes:

$$\dot{m} \ln(R_2 / R) - \frac{\varepsilon^2 \pi h^3 \Omega^2}{6\mu} I_R^{R2} = -\frac{\varepsilon \pi h^3}{12\mu} (P_2^2 - P^2)$$

eqn. 5.44

Rearranging the above equation in terms of P:

$$P = \left[P_2^2 + \frac{12\mu\dot{m}}{\varepsilon\pi h^3}\ln(R_2 / R) - 2\varepsilon\Omega I_R^{R2} \right]^{0.5}$$

eqn. 5.45

Between the limits of R_2 and R_1, expression (eqn. 5.44) becomes:

$$\dot{m}\ln(R_2 / R_1) - \frac{\varepsilon^2\pi h^3\Omega^2}{6\mu} I_R^{R2} = -\frac{\varepsilon\pi h^3}{12\mu}(P_2^2 - P_1^2)$$

eqn. 5.46

Substituting for the integral I from equation (eqn. 5.43), the above equation becomes:

$$\dot{m} = \frac{\varepsilon\pi h^3}{12\mu\ln(R_2 / R_1)}\left[P_1^2\left\{1 - \varepsilon\Omega^2(R_1^2 - \frac{1}{2\ln(R_2 / R_1)}(R_2^2 - R_1^2))\right\} - P_2^2\left\{1 - \varepsilon\Omega^2(R_2^2 - \frac{1}{2\ln(R_2 / R_1)}(R_2^2 - R_1^2))\right\}\right]$$

eqn. 5.47

The circumstance of particular interest to us is when one face is stationary and the other is rotating. In that case:

$$\Omega^2 = \frac{3\omega^2}{10}$$

eqn. 5.48

5.4.2 Fully incorporating the speed effects.

Basing the analysis on the fact that one of the faces rotates and the other is stationary, the above value for Ω will be utilised.

Returning back to our mass continuity equation:

$$\dot{m}_{1,2} = \dot{m}_{2,3} + \dot{m}'_{2,3}$$

eqn. 5.49

But this time the expressions for the mass flow rate are now drawn from equation (eqn. 5.47). Thus the individual mass flow rates become:

$$\dot{m}_{1,2} = \frac{\varepsilon\pi h^3}{12\mu\ln(R_2 / R_1)}\left[P_1^2\left\{1 - \frac{3}{10}\varepsilon\omega^2(R_1^2 - \frac{1}{2\ln(R_2 / R_1)}(R_2^2 - R_1^2))\right\} - P_2^2\left\{1 - \frac{3}{10}\varepsilon\omega^2(R_2^2 - \frac{1}{2\ln(R_2 / R_1)}(R_2^2 - R_1^2))\right\}\right]$$

eqn. 5.50

$$\dot{m}_{2,3}=\frac{\varepsilon\pi h^3}{12\mu\ln(R_3/R_2)}\left[P_2^2\left\{1-\frac{3}{10}\varepsilon\omega^2(R_2^2-\frac{1}{2\ln(R_3/R_2)}(R_3^2-R_2^2))\right\}-P_3^2\left\{1-\frac{3}{10}\varepsilon\omega^2(R_3^2-\frac{1}{2\ln(R_3/R_2)}(R_3^2-R_2^2))\right\}\right]$$

eqn. 5.51

$$\dot{m}_{2,3}=\frac{\varepsilon\pi H^3}{12\mu\ln(R_3/R_2)}\left[P_2^2\left\{1-\varepsilon\omega^2(R_2^2-\frac{1}{2\ln(R_3/R_2)}(R_3^2-R_2^2))\right\}-P_3^2\left\{1-\varepsilon\omega^2(R_3^2-\frac{1}{2\ln(R_3/R_2)}(R_3^2-R_2^2))\right\}\right]$$

eqn. 5.52

For simplicity, the coefficients of squares of the individual pressures in the above mass flow rate equations will be written as elements of a 1-D matrix: Z (I). So, for example, the mass flow rate $\dot{m}_{1,2}$ will be:

$$\dot{m}_{1,2}=\frac{\varepsilon\pi h^3}{12\mu\ln(R_2/R_1)}\left[P_1^2Z(1)-P_2^2Z(2)\right]$$

eqn. 5.53

Where Z(1) is the coefficient of squares for the pressure P_2 in above equation (eqn. 5.50), and so on.

Thus the above mass continuity equation can be expressed as the following:

$$\frac{\varepsilon\pi h^3}{12\mu\ln(R_2/R_1)}\left[P_1^2Z(1)-P_2^2Z(2)\right]=\frac{\varepsilon\pi h^3}{12\mu\ln(R_3/R_2)}\left[P_2^2Z(3)-P_3^2Z(4)\right]=\frac{\varepsilon\pi H^3}{12\mu\ln(R_2/R_1)}\left[P_2^2Z(5)-P_3^2Z(6)\right]$$

eqn. 5.54

Rearranging the above equation to be expressed in terms of p_2, we get:

$$P_2^2=\frac{\frac{P_1^2}{\ln(R_2/R_1)}\left(h^3Z(1)\right)+\frac{P_3^2}{\ln(R_3/R_2)}(h_3Z(4)+H^3Z(6)}{\frac{h^3Z(2)}{\ln(R_2/R_1)}+\frac{1}{\ln(R_3/R_2)}(h^3Z(3)+H^3Z(5)}$$

eqn. 5.55

The mass flow rate leakage is established by substituting the above expression. Now that feed groove pressure is known for a given operating pressure, seal geometry and

operating gap 'h', the mass flow rate through the seal can be established, implicitly. This is done by substituting the above equation for P_2 (eqn. 5.55) into (eqn. 5.53).

Having obtained the feed groove pressure P_2, the pressure distribution as a function of radial position R, is obtained from the following two equations derived earlier:

$$I_R^{R2} = P_2^2\left[\frac{R_2^2}{2} - \frac{1}{4\ln(R_2/R_1)}(R_2^2 - R_1^2)\right] - P_1^2\left[\frac{R_1^2}{2} - \frac{1}{4\ln(R_2/R_1)}(R_2^2 - R_1^2)\right]$$

eqn. 5.56

$$P = \left[P_2^2 + \frac{12\mu\dot{m}}{\varepsilon\pi h^3}\ln(R_2/R) - 2\varepsilon\Omega I_R^{R2}\right]^{0.5}$$

eqn. 5.57

Thus, pressure P from R_1 to R_2 is:

$$P = \left[P_2^2 + \frac{12\mu\dot{m}_{1,2}}{\varepsilon\pi h^3}\ln(R_2/R) - \frac{3}{5}\varepsilon\omega I_R^{R2}\right]^{0.5}$$

eqn. 5.58

where

$$I_R^{R2} = \frac{P_2^2}{2}(R_2^2 - R^2) + \frac{(P_2^2 - P_1^2)}{2\ln(R_2/R_1)}(R^2\ln(R_2/R) - \frac{1}{2}(R_2^2 - R^2))$$

eqn. 5.59

And from R_2 to R_3 it is:

$$P = \left[P_3^2 + \frac{12\mu\dot{m}_{2,3}}{\varepsilon\pi h^3}\ln(R_3/R) - \frac{3}{5}\varepsilon\omega I_R^{R3}\right]^{0.5}$$

eqn. 5.60

Where:

$$I_R^{R2} = \frac{P_2^2}{2}(R_2^2 - R^2) + \frac{(P_2^2 - P_1^2)}{2\ln(R_2/R_1)}(R^2\ln(R_2/R) - \frac{1}{2}(R_2^2 - R^2))$$

eqn. 5.61

For the benefit of subsequent computer programming of the above the equations, the equation for pressure distribution 'p' as function of radius R is expressed as:

$$P = \left[P_2^2 + X_3 \dot{m}_{1,2} \ln(R_2 / R) - X_4 I_R^{R2}\right]^{0.5}$$

eqn. 5.62

And equation (eqn. 5.59) is expressed as:

$$I_R^{R2} = P_2^2 X_2 + (P_2^2 - P_1^2) X_1$$

Equations (eqn. 5.60) and eqn. 5.59 would be expressed in a similar way.

In the above expressions, written for the pressure distribution from R_1 to R_2,

$$X_1 = \frac{R^2 \ln(R_2 / R) - 0.5(R_2^2 - R^2)}{2\ln(R_2 / R_1)}$$

eqn. 5.63

$$X_2 = \frac{R_2^2 - R^2}{2}$$

eqn. 5.64

$$X_3 = \frac{12\mu}{\varepsilon \pi h^3}$$

eqn. 5.65

$$X_4 = \frac{3\varepsilon\omega^2}{5}$$

eqn. 5.66

From R_2 to R_3, the subscripts of the radii change accordingly:

$$X_1 = \frac{R^2 \ln(R_3 / R) - 0.5(R_3^2 - R^2)}{2\ln(R_3 / R_2)}$$

eqn. 5.67

$$X_2 = \frac{R_3^2 - R^2}{2}$$

eqn. 5.68

$$X_3 = \frac{12\mu}{\varepsilon \pi h^3}$$

eqn. 5.69

$$X_4 = \frac{3\varepsilon\omega^2}{5}$$

eqn. 5.70

The total opening force is obtained from integrating the radial pressure distribution over the area of the seal faces. The representative formula is expressed as:

$$W_o = \sum_{R1}^{R3} 2\pi PRdR$$

eqn. 5.71

In the above equation, R is the mid-radius position of a face annulus element, of radial width dR, and 'P' is the calculated opening pressure acting at that mid radius of that element.

Acting against the opening force will be the seal closing force W_c, which is a function of the face geometry, the balance ratio, the spring pressure and the sealed pressure. It is represented by the following equation:

$$W_c = \pi\left(R_3^2 - R_1^2\right)\left(P_3 B + P_1(1-B)\right) + P_{spring}$$

eqn. 5.72

The principle of a 'back' depression is to act as a flow restriction. Of course, there is no practical need for the depression to extend the full circumference. In reality, it would be confined to a partial arc of $D<<360^o$. An arrangement for a partial arc is shown in Figure 29. In this case, the total feed groove arc is divided into three sub-arcs of D/3 degrees.

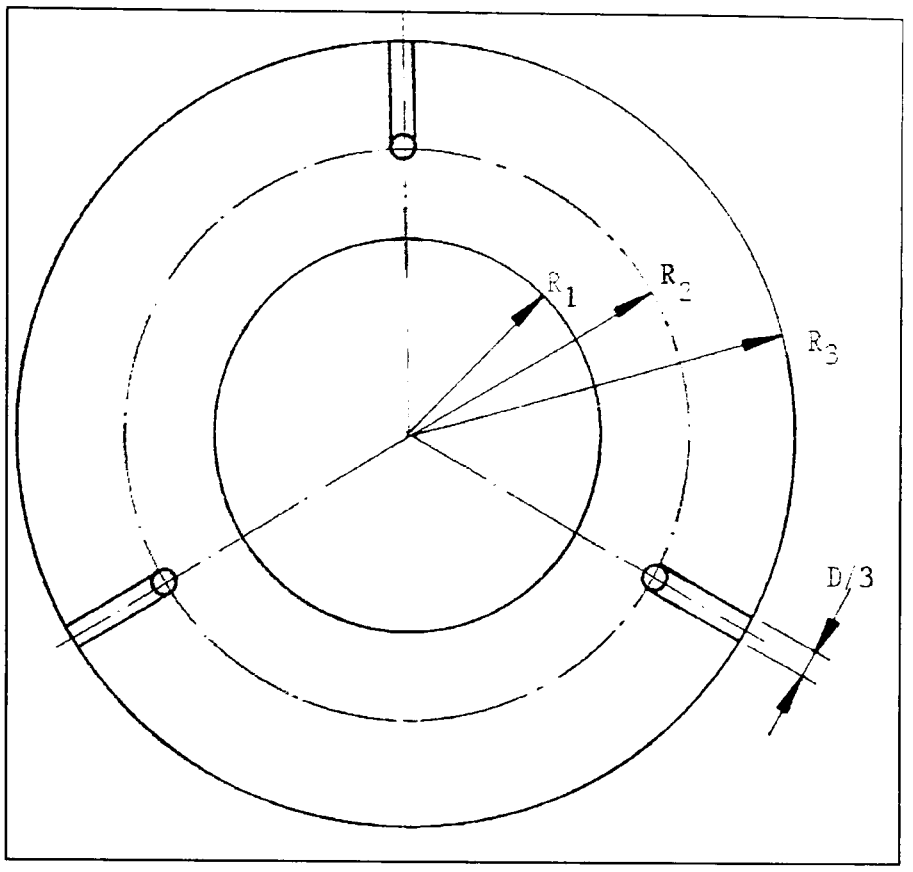

Figure 29: Rear feed groove geometry schematic

The modified mass flow equation through the feed grooves is given by:

$$\dot{m}_{2,3} = \frac{D}{360} \cdot \frac{\varepsilon \pi H^3}{12 \mu \ln(R_3 / R_2)} \left[P_2^2 Z(5) - P_3^2 Z(6) \right]$$

eqn. 5.73

And the modified equation for the feed groove pressure P_2 is:

$$P_2^2 = \frac{\dfrac{P_1^2}{\ln(R_2 / R_1)} \left(h^3 Z(1) \right) + \dfrac{P_3^2}{\ln(R_3 / R_2)} \left(h_3 Z(4) + \dfrac{D}{360} H^3 Z(6) \right)}{\dfrac{h^3 Z(2)}{\ln(R_2 / R_1)} + \dfrac{1}{\ln(R_3 / R_2)} \left(h^3 Z(3) + \dfrac{D}{360} H^3 Z(5) \right)}$$

eqn. 5.74

5.5 SLOT FEED (SF) SEAL COMPUTER MODEL

A computer model has been created based on the theory and the model assumptions described above. The computer program has been written using Visual Fortran. A flowchart in Figure 30, shows the program structure.

Firstly, an input file is created containing the seal geometry and the operating conditions. For a given seal gas, air in this case, real gas property tables are created

for viscosity, thermal conductivity, and gas specific hear capacities. An algorithm is built into the model to select the gas properties that are the closest to the seal operating conditions in terms of pressure and temperature.

The model is iterative in its nature. It first calculates the Z(speed) parameters and the seal closing force. It then calculates the mass flow rates through the seal based on an initial guess of seal gap. The numerical value of the orifice pressure is then calculated and with it the actual pressure profile across the seal face from the outer to the inner radii. That pressure profile would normally be parabolic in form. The model integrates the area under that pressure profile, the result of which is the seal opening force. That opening force is then compared with the closing force already calculated. Using an appropriate error-handling algorithm, the error between the two values is used to select a new value for the film thickness. The whole process is repeated iteratively, with the film thickness being adjusted every iteration, until the seal opening force equals the seal closing force and equilibrium is reached.

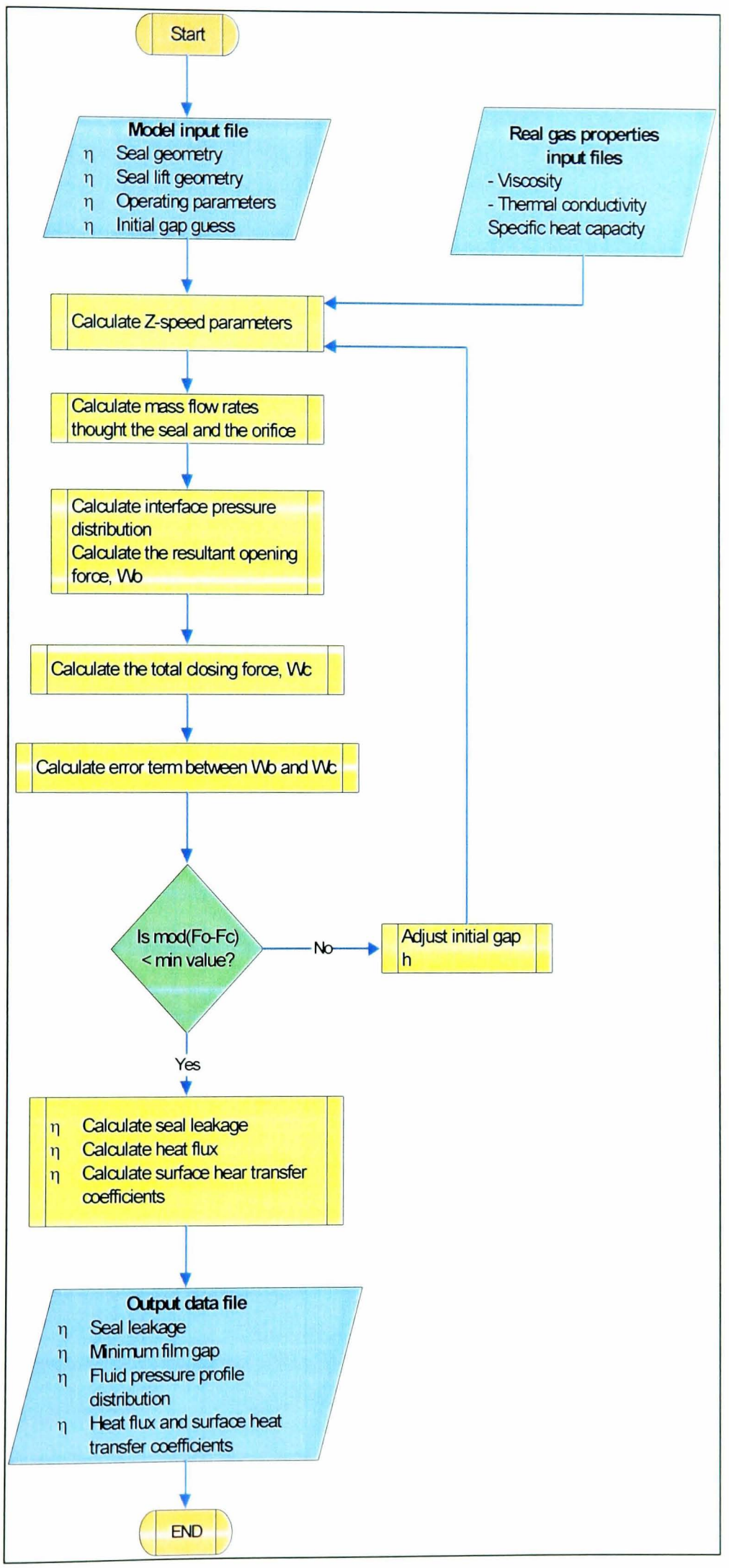

Figure 30: Slot feed gas seal computer model flow chart

5.6 PROPOSED SLOT FEED GAS SEAL DESIGN

5.6.1 General configuration

The test vehicle for evaluating the concept is in the form of a tandem gas seal cartridge (see Figure 31 below). The tandem cartridge is made up of two identical seal modules, or stages. Each one of these is designed to be able to hold the entire sealed pressure. Under normal operation, the inboard seal (IB) holds the full process gas pressure and the outboard seal runs as a back up at a few bar. The OB seal or stage is also designed to take the full process gas pressure. A solid model and part section of the tandem cartridge is shown in Figure 32.

The metal parts for the seal cartridges are made from a combination of: 410 and high strength 17-4 PH stainless steels. The stationary metal parts are constructed from 410-stainless steel. The rotating parts are made from 17-4 PH stainless steel.

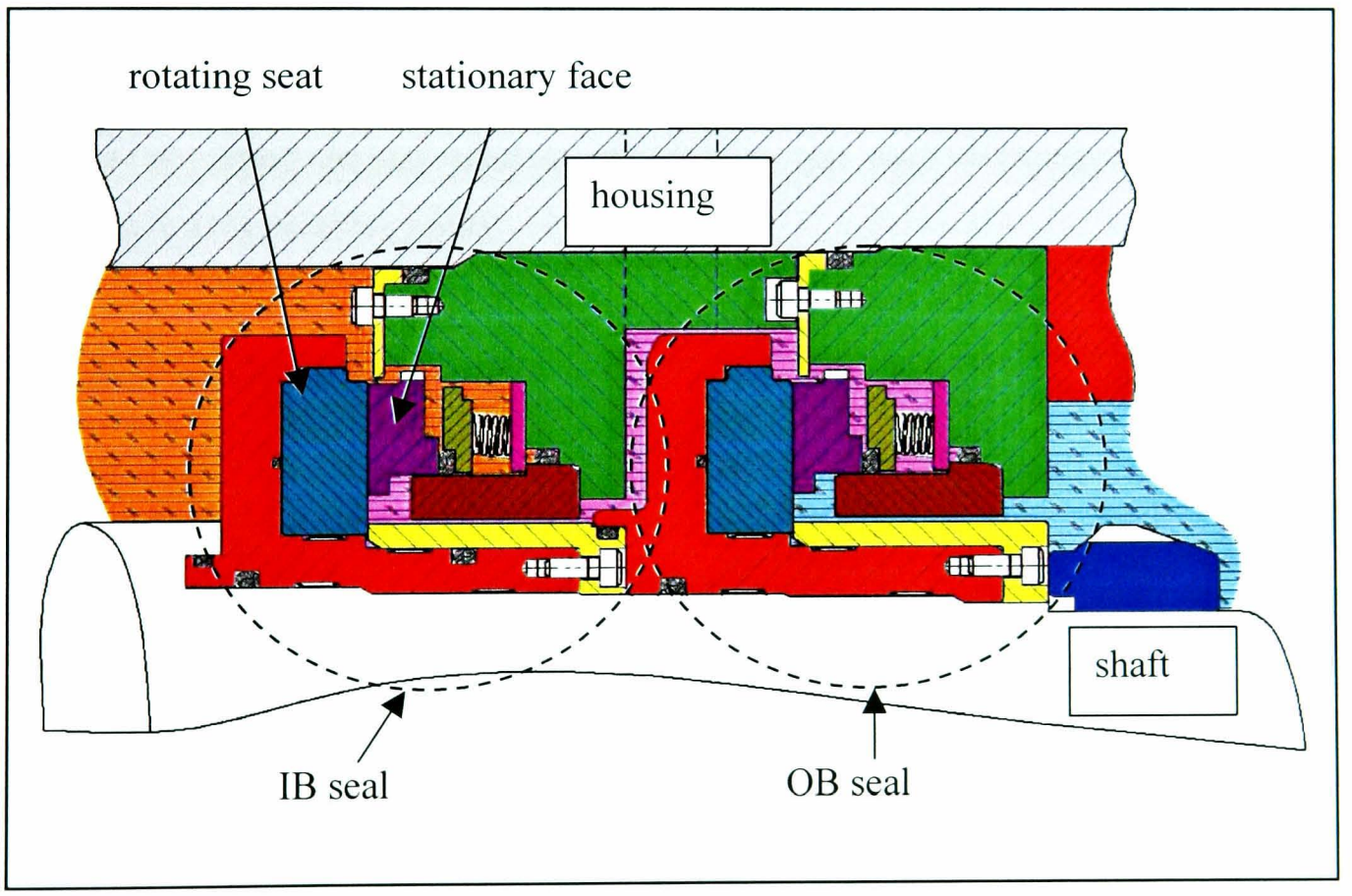

Figure 31: Tandem gas seal configuration showing the inboard and outboard seal stages.

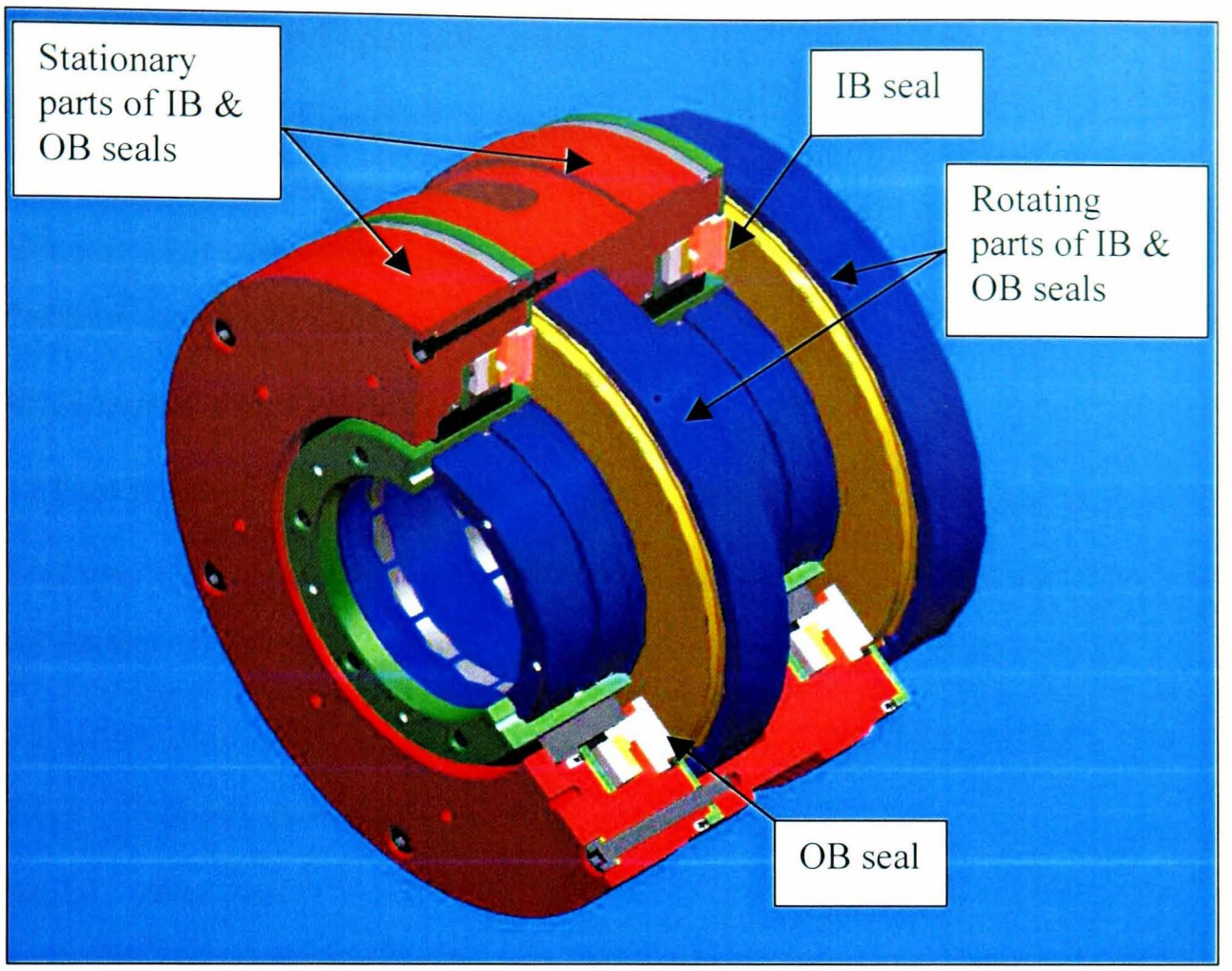

Figure 32: Solid model section of tandem gas seal cartridge, showing the stationary and rotating parts

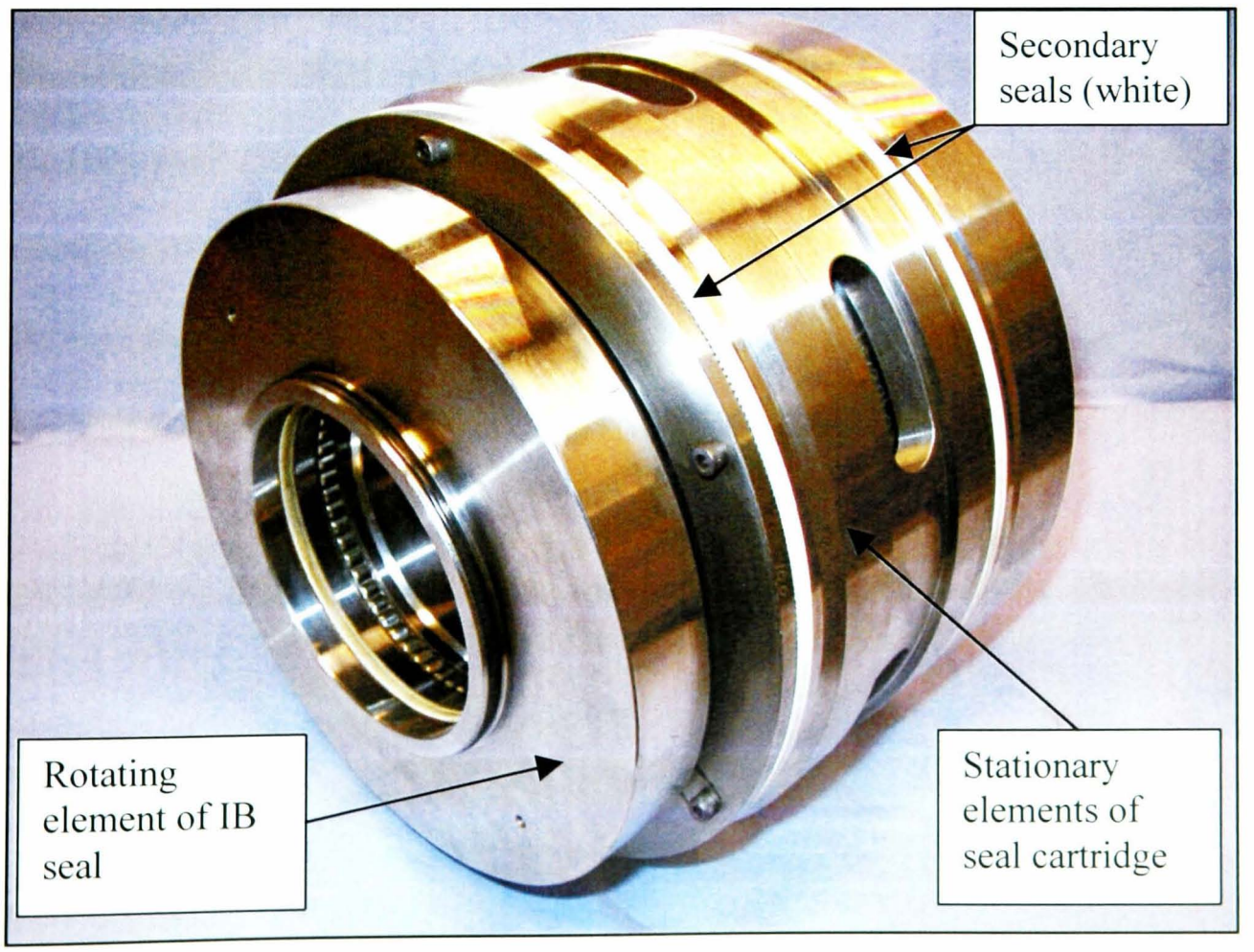

Figure 33: Isometric view of the tandem gas seal cartridge, as made

5.6.2 Seal size and operating range

Seal size (balance diameter): 129 mm

Shaft diameter: =90 mm

Housing diameter: = 260 mm

Pressure range: 20 - 300 bar.

Maximum speed: 12000-14000 rpm

At high pressures of 300 bar and, the maximum operating temperature is 120° C.

Seal gas: Compressed air delivered from a dedicated test compressor (see section 4) for details of the test facility).

5.6.3 Primary seal zone design

5.6.3.1 Seal faces

Both components are made from high strength engineered ceramics. The material family is covalently reaction bonded silicon carbide

5.6.3.2 Rotating seats

Young's modulus = 420 GPa

4-point flexural strength = 550 MPa

Thermal conductivity = 75 $W.m^{-1}.K^{-1}$

Coefficient of thermal expansion = 3.5 x $10^{-6}.K^{-1}$

Weibull modulus = 15

Number of rear feed slots: 3

Number of front circumferential grooves: 3

The solid model figures and engineering drawing extracts of the rotating seat are shown in Figure 34 through to Figure 38.

5.6.3.3 Stationary Faces

Young's modulus = 410 GPa

4-point flexural strength = 400 MPa

Thermal conductivity: = 125 $W.m^{-1}.K^{-1}$

Coefficient of thermal expansion: = 4.1 x $10^{-6}.K^{-1}$

Diamond-like coating (DLC) is applied to the stationary faces to further improve dry running and dry start properties. Solid model figures and engineering drawing extracts of the rotating seat are shown in Figure 39 and Figure 40.

5.6.3.4 Lift groove geometry on rotating seat

Number of rear feed slots: 3

Rear feed slto depth = 14 μm

Feed hole diameter = 1 mm

Number of front circumferential grooves: 3

Front distribution groove depth = 30-50 μm

5.6.3.5 Secondary seals

The stationary metals parts sealing against the housing and the rotating metal parts sealing against the shaft will be sealed by metal spring energised cup polymer seals. Those polymers can be seen as white rings in Figure 33.

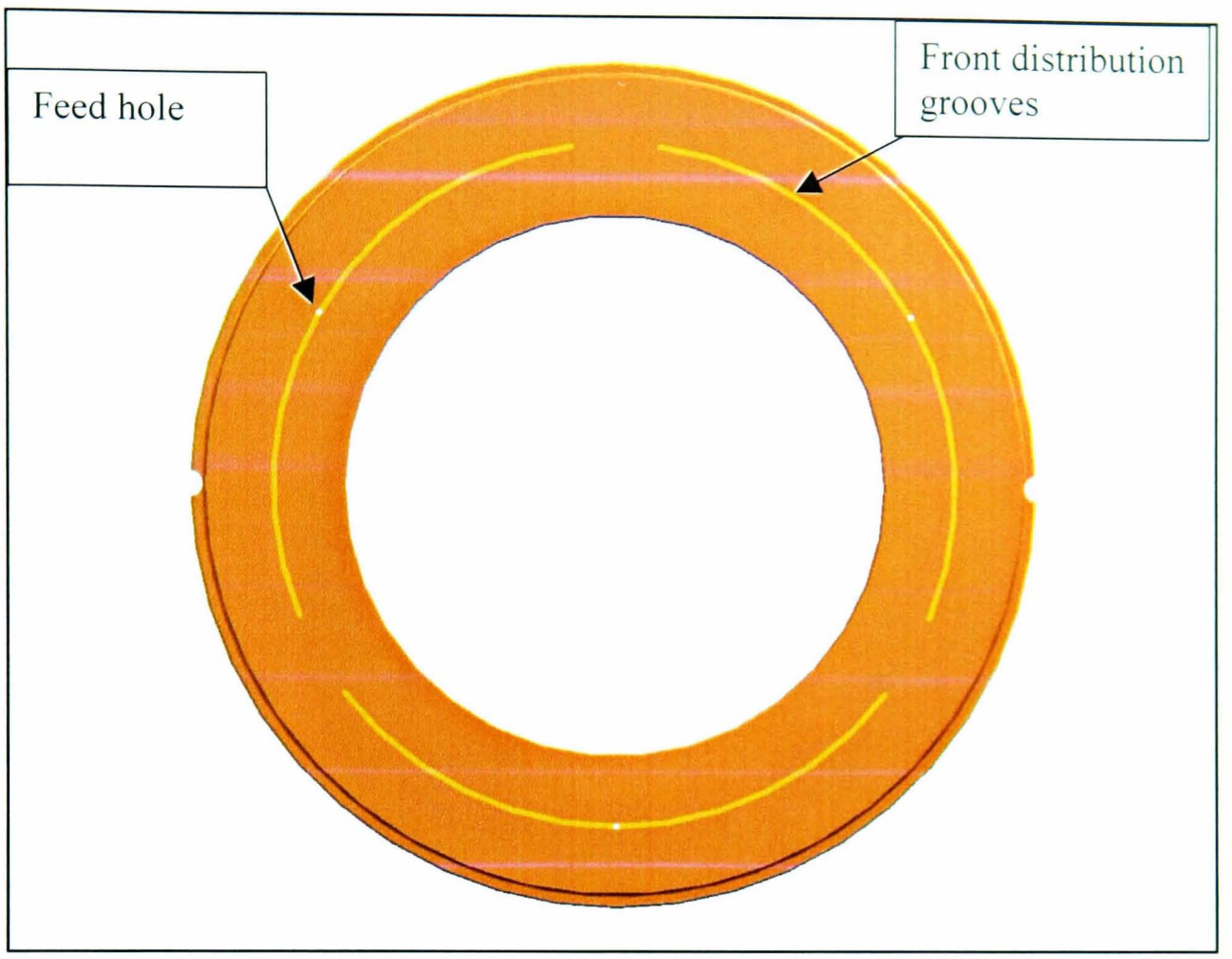

Figure 34: Front of rotating seat the three distribution grooves and feed holes

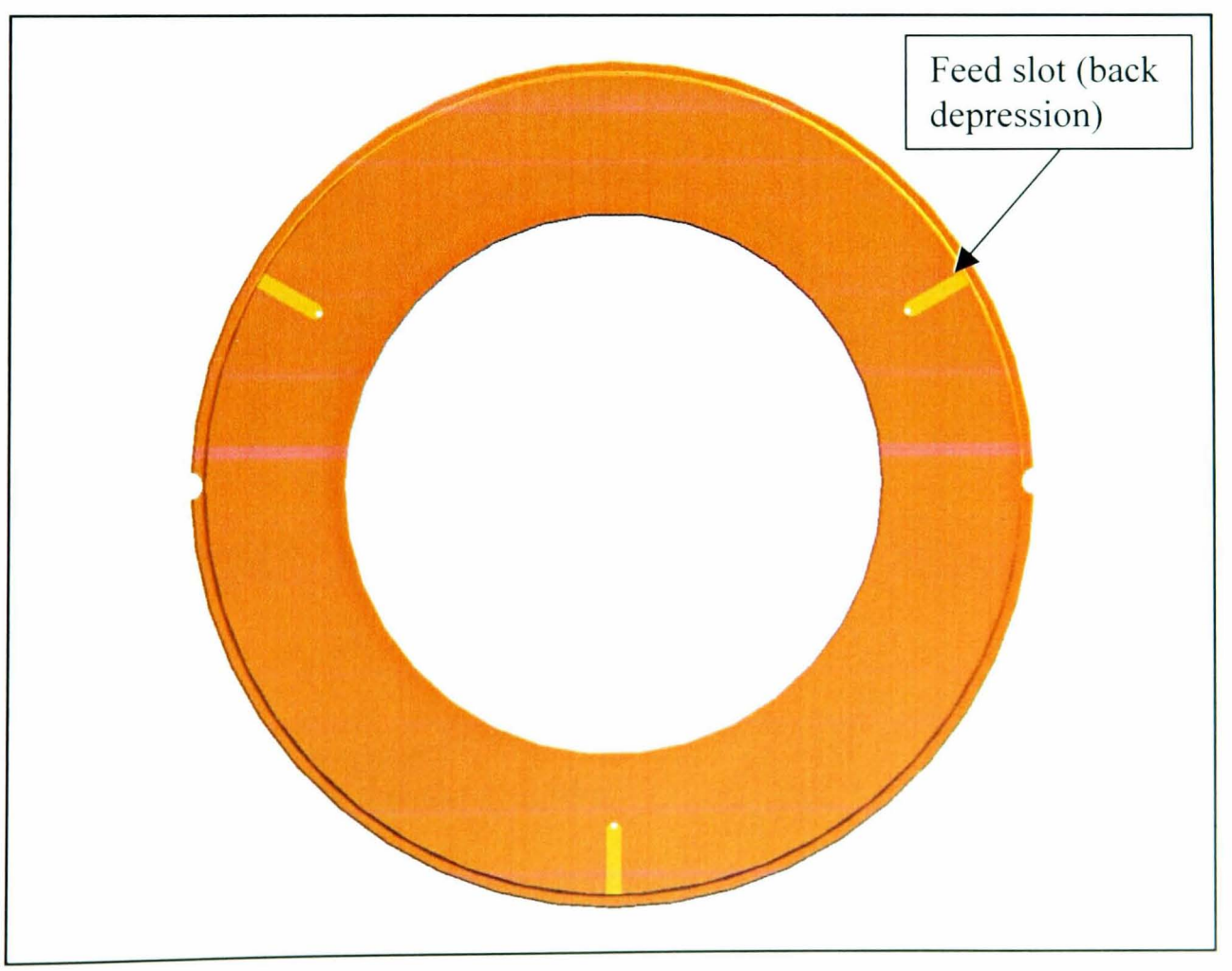

Figure 35: Rear view of rotating seat showing the 3 feed slots and the feed holes

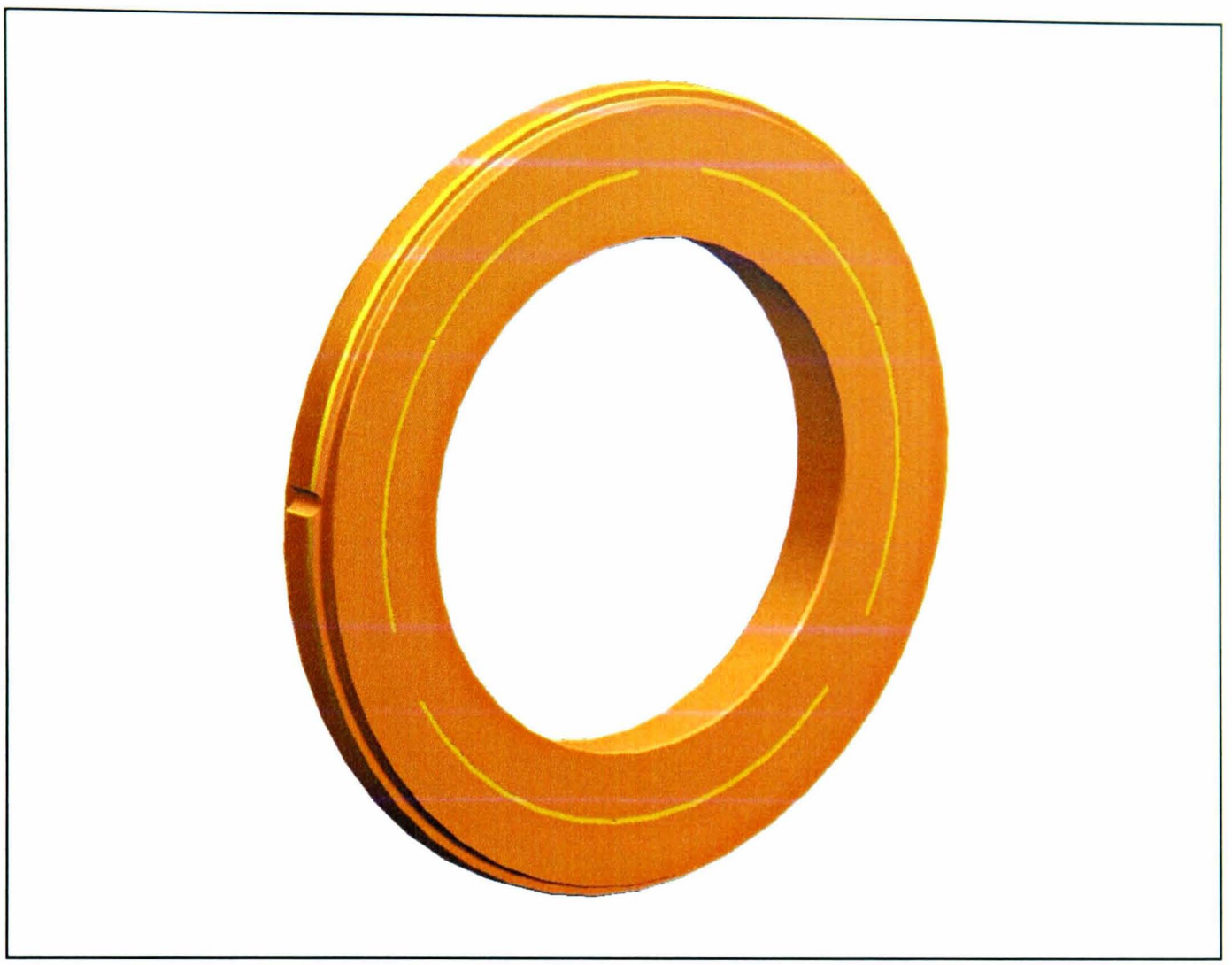

Figure 36: Isometric view of rotating seat showing the front distribution grooves

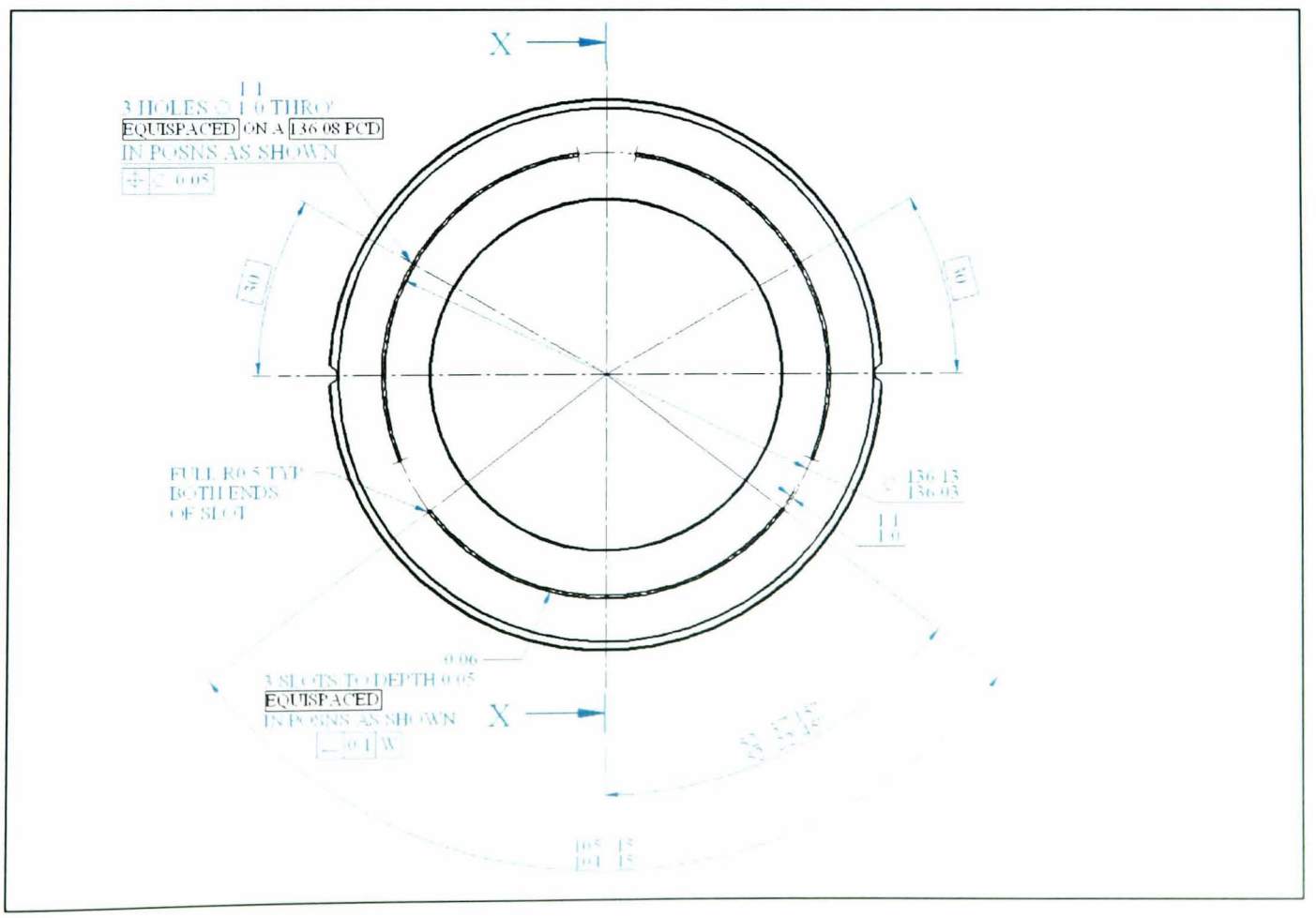

Figure 37: Front view of rotating seat – engineering drawing

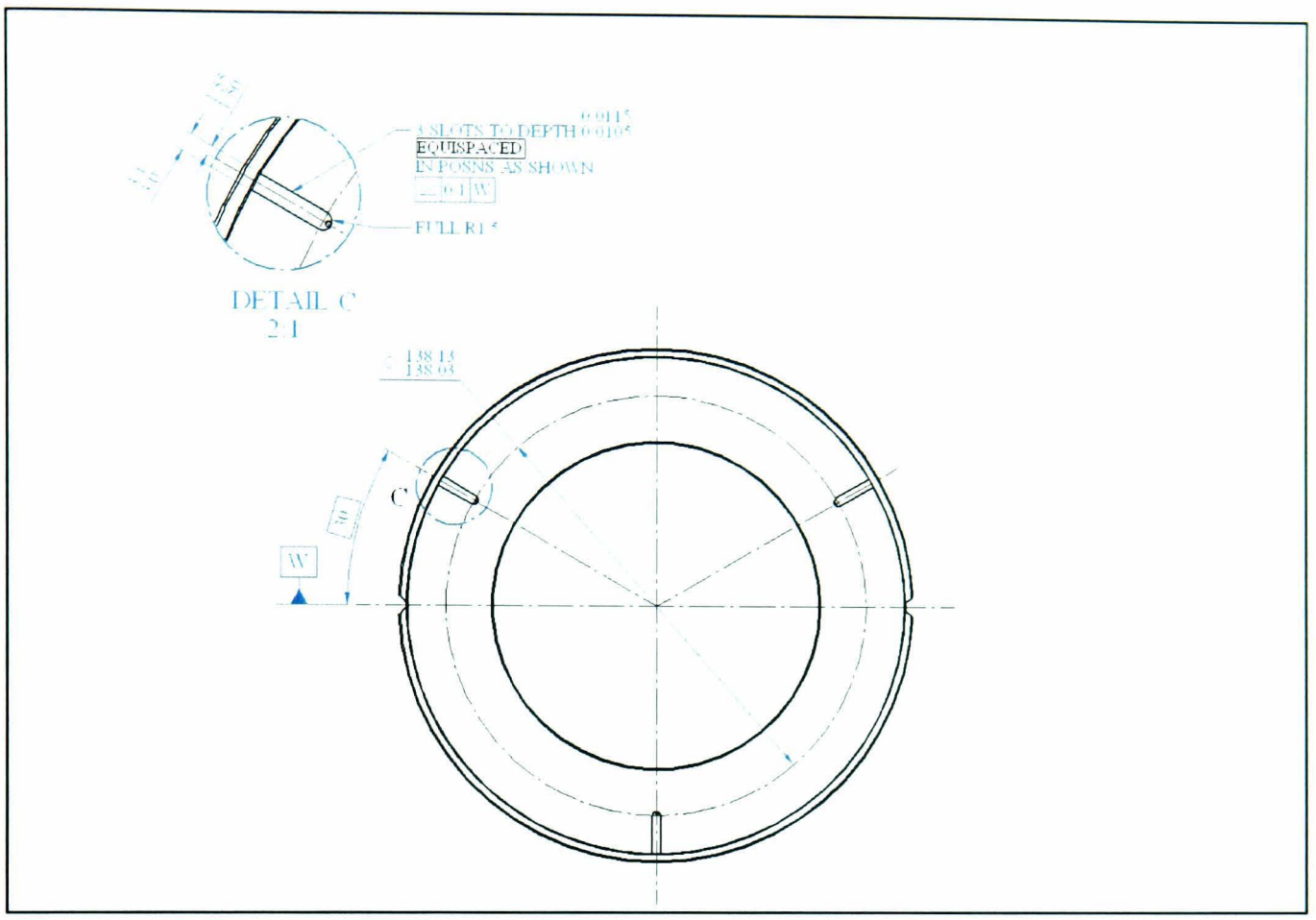

Figure 38: Rear view of rotating seat – engineering drawing

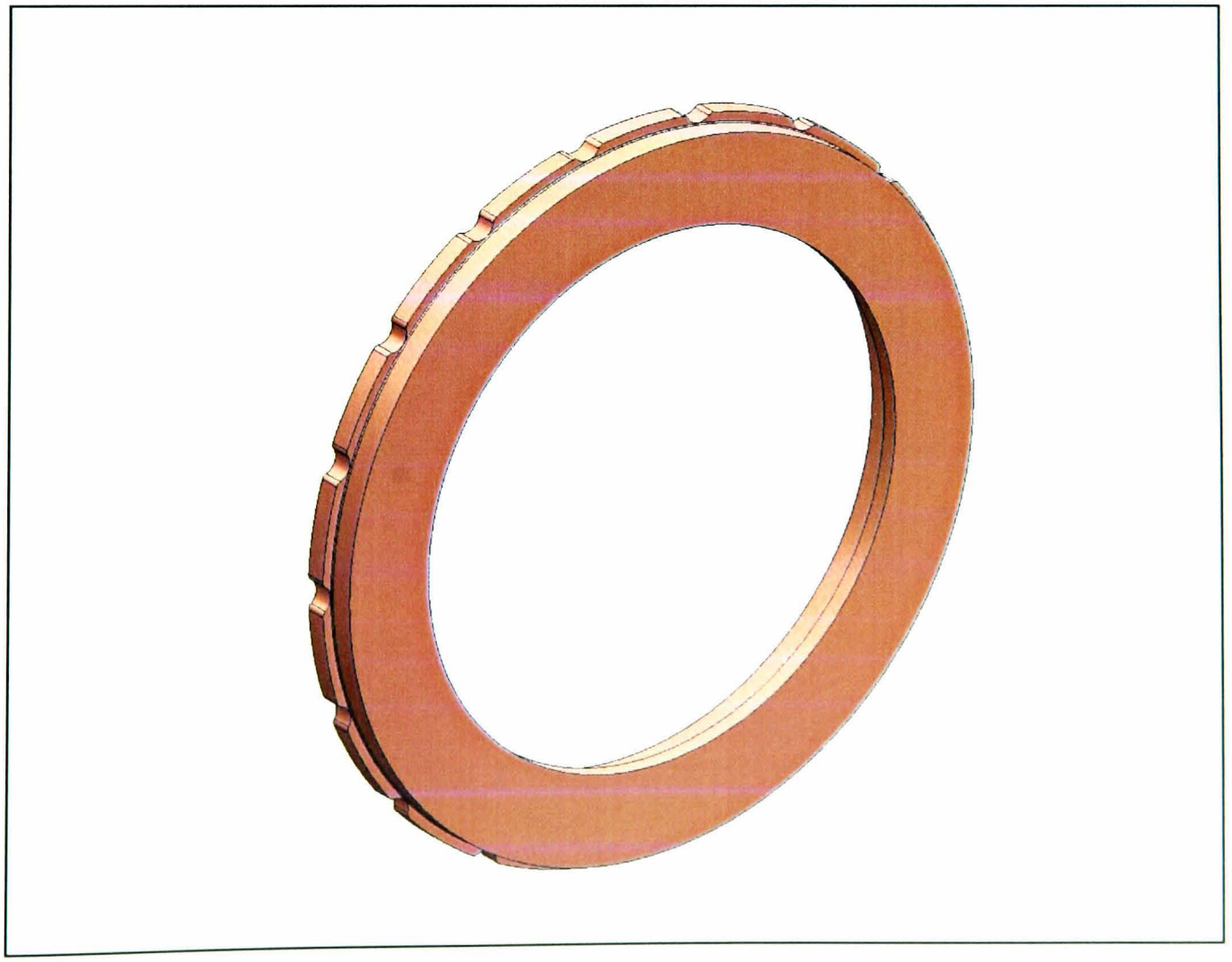

Figure 39: Front isometric view stationary face

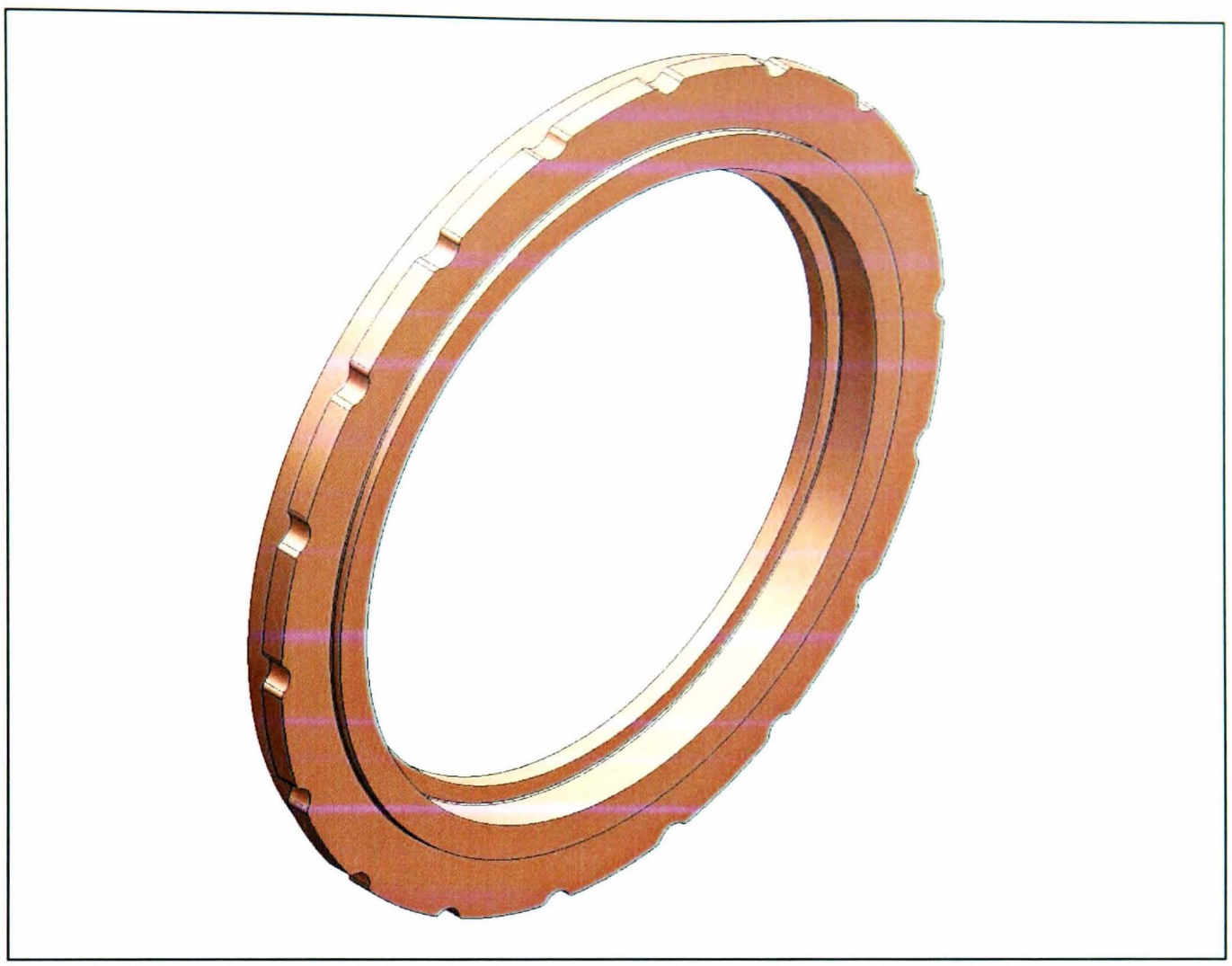

Figure 40: Rear isometric view stationary face

5.7 SLOT FED GAS SEAL DESIGN MODEL PREDICTIONS

5.7.1 Opening pressure profile predictions

One important output from the computer model is that of the pressure profile in the primary seal zone. That pressure profile creates an effective opening force, separating the two seal faces. The predicted pressure profile is shown in Figure 41. It can be seen that the model predicts virtually identical pressure profile for both the ambient static condition (300 bar, 293K) and full dynamic conditions (300 bar, 12000 rpm, 393K)

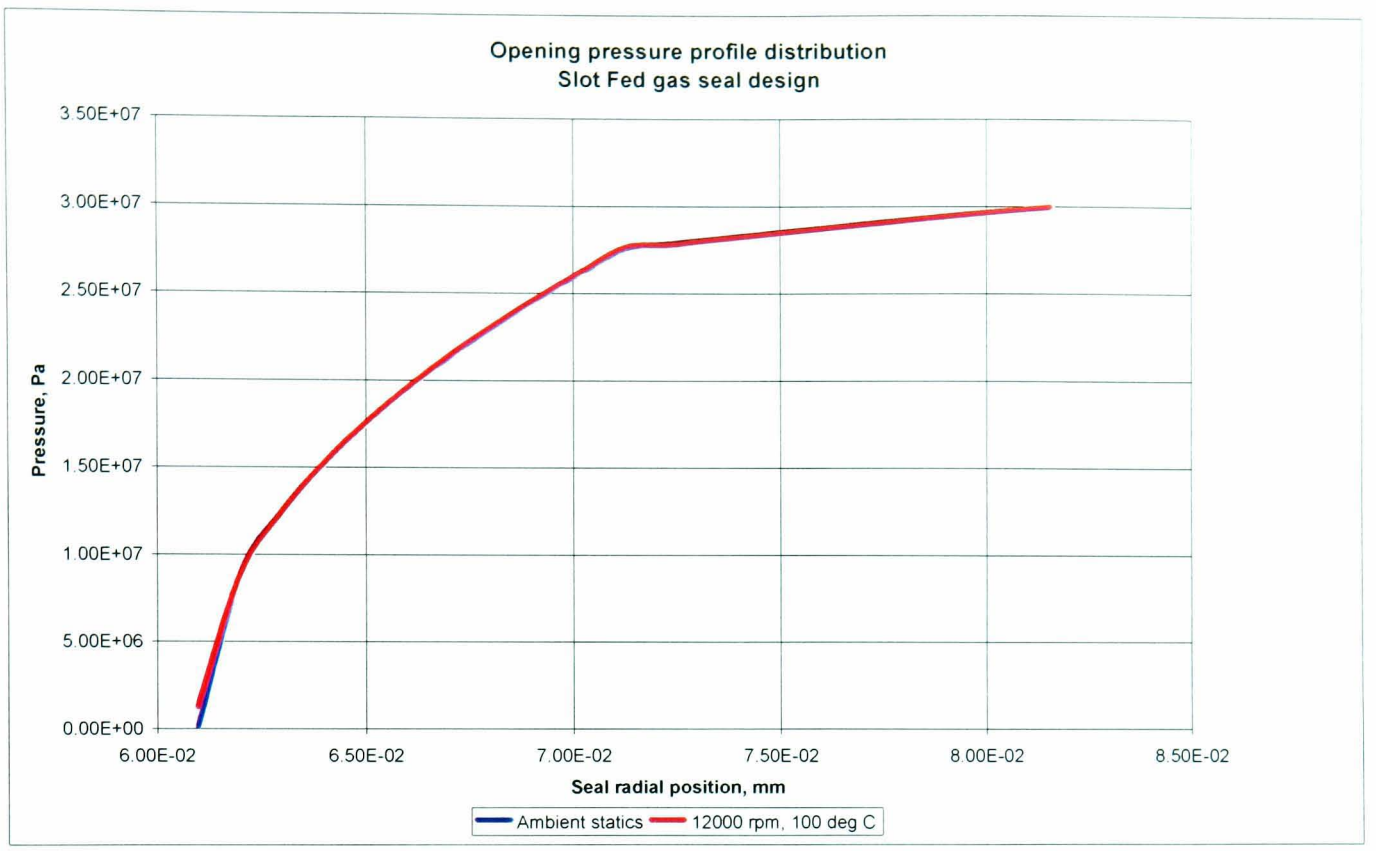

Figure 41: Opening pressure profile distribution for the slot fed design – ambient statics versus full speed dynamics.

5.7.2 Static leakage and lift off pressure predictions

The predictions for seal gap and leakage as a function of pressure under static conditions are shown in Figure 42 and Figure 43. As with the pressure profile, leakage and predicted gaps for a given seal pressure were the direct outputs from the SF gas seal computer model. In Figure 43, the red box shows the zone of predicted seal lift off.

Pressure, bar	Leakage, $l.min^{-1}$	Gap, micron
0	0	0
2	0	0.2
4	0	0.35
5	0.0073	0.643
6	0.036	0.993
7	0.073	1.16
8	0.12	1.26
9	0.17	1.34
10	0.23	1.4
25	2.03	1.69
50	9.3	1.8
100	37.68	1.86
150	80.61	1.87

Figure 42: SF Seal operating gap and leakage predictions

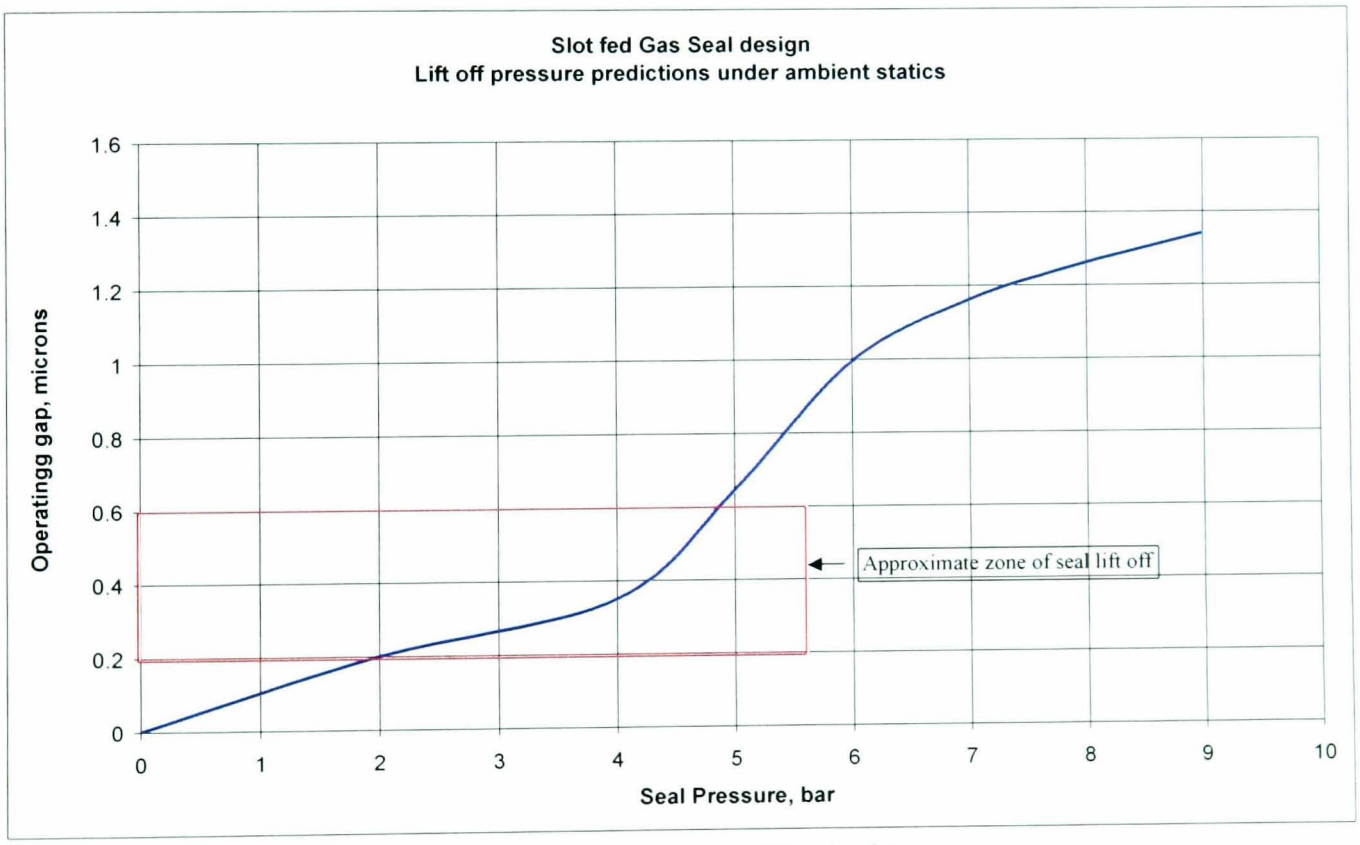

Figure 43: Slot fed gas seal lift off pressure predictions

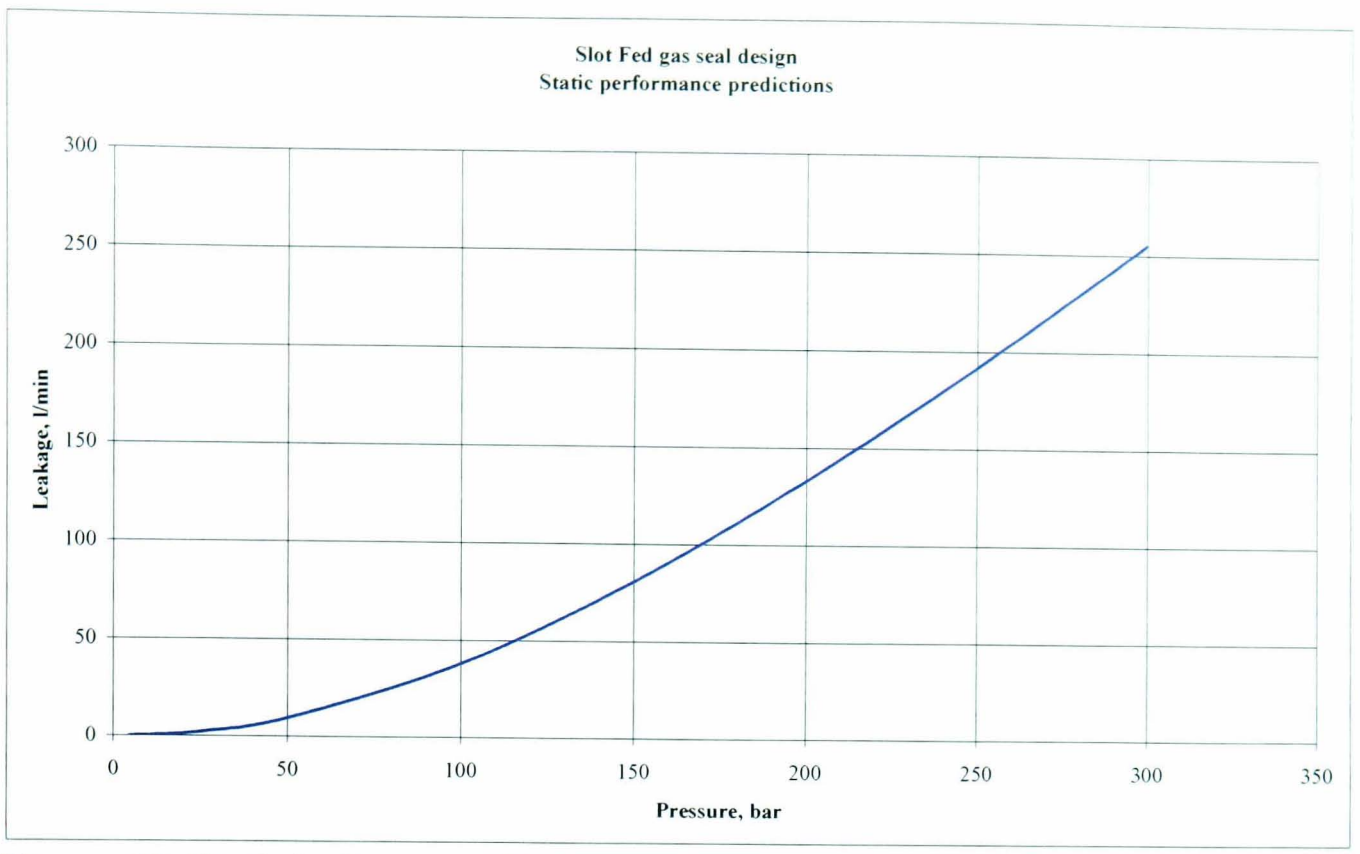

Figure 44: Static leakage predictions

5.7.3 Dynamic performance predictions

Figure 45 gives a tabulated set of leakage and operating gap predictions for a range of dynamic operating conditions, as predicted by the SF computer model. The same dynamic leakages are shown in Figure 46 in graphical form as a function of seal pressure

	6000 rpm, 100° C		8000 rpm, 100° C	
Pressure, bar	Leakage, l.min^{-1}	Gap, micron	Leakage, l.min^{-1}	Gap, micron
50	6.1	1.79	6.1	1.79
100	25.6	1.85	25.4	1.85
150	56.7	1.87	56.4	1.86
200	97.4	1.88	96.9	1.88
250	146.1	1.88	145.3	1.88
300	201.1	1.89	200	1.88

	10000 rpm, 100° C		12000 rpm, 100° C	
Pressure, bar	Leakage, l.min^{-1}	Gap, micron	Leakage, l.min^{-1}	Gap, micron
50	6	1.78	5.96	1.78
100	25.26	1.83	24.99	1.83
150	55.98	1.86	55.4	1.85
200	96.14	1.87	95.16	1.86
250	144.15	1.87	142.68	1.87
300	198.4	1.88	196.4	1.86

Figure 45: SF gas seal dynamic performance predictions

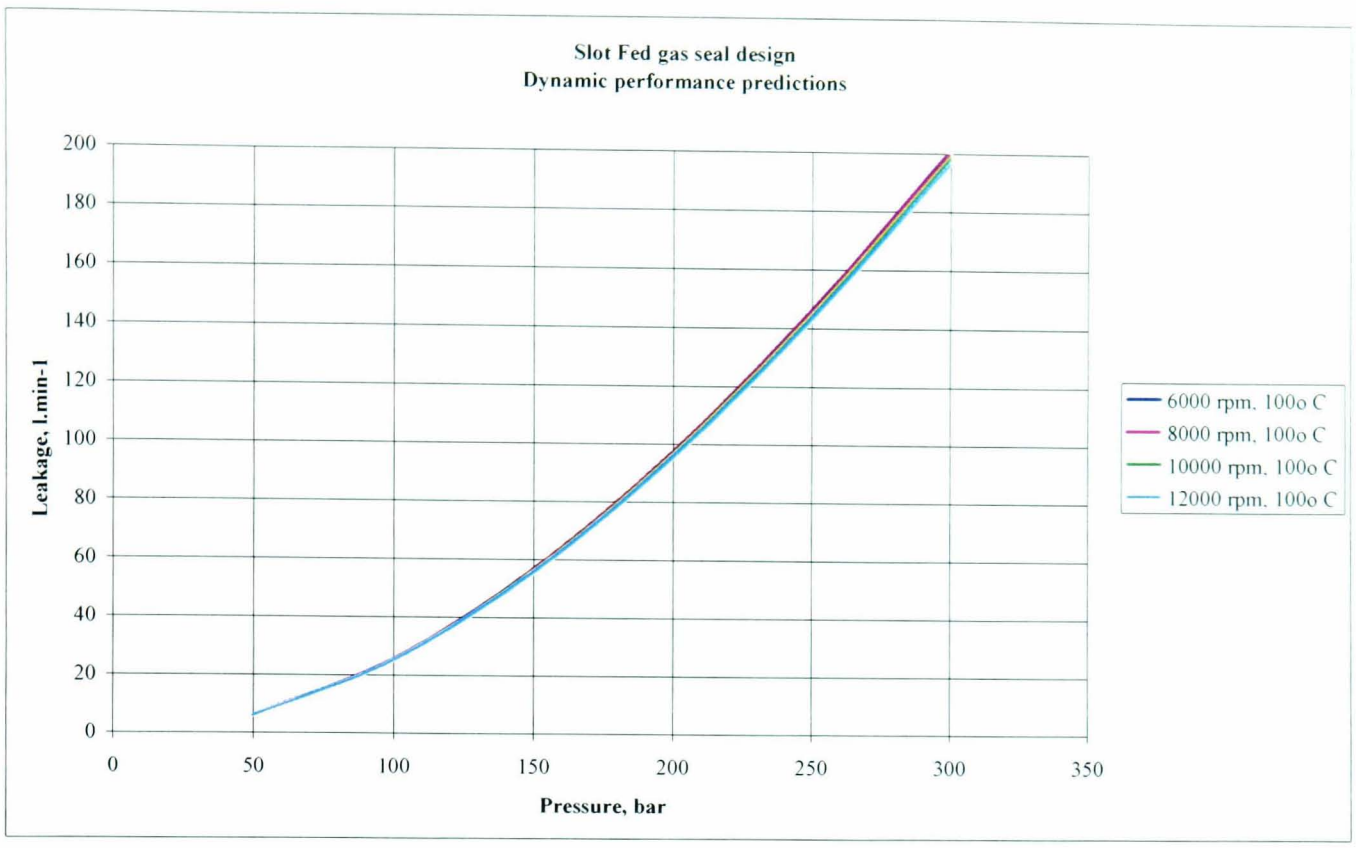

Figure 46: SF gas seal dynamic leakage predictions

5.7.4 Modelling the seal face deformations

In order to gain an understanding of the structural deformations of the seal faces, a 2-D finite element model was constructed using ANSYS [1]. The main objective of this part of the modelling process was to predict the relative deformations of the two seal faces under full pressure conditions. The aim was to ensure that faces still maintained either a parallel or a slightly divergent gap relative to each other, when sealing the full pressure of 300 bar. This was a necessary requirement in order to achieve positive film stiffness and reliable operation. This was undertaken in the knowledge that under full dynamic conditions, the thermal effects would impose even greater positive thermal rotations on the seal faces thus causing them be even more convergent. Hence, the key starting design point from the point of view of seal face convergence angle was the ambient static condition.

As shown in Figure 47, the following boundary constraints were applied. Both the rotating seal and the stationary face were constrained in the axial translation degree of freedom about their respective pivot points. Full operating pressure was applied to both seal faces up their respective sealing off points – locations where the secondary seals (MSE polymers) provided the sealing. Spring pressure would be

applied to the stationary face. Finally the interface pressure, calculated by the SF fluid film model and shown in Figure 41, is applied to the two seal faces.

If the results of the FE analysis predicts a divergent seal face gap at full pressure ambient static conditions, then the cross section of the stationary face has to be adjusted by a few decimal points of a millimetre. By adjusting the shoulder on the rear surface of the stationary face, its centroid position is altered thus encouraging a more convergent rotation of the stationary seal face. In essence this is an established part of the optimisation process.

The resultant deformations were extracted directly from the ANSYS post processor and converted to angular rotations in radians. The chosen stationary face cross section was found to have a combined face angle of 15μrad at 300 bar ambient statics. This satisfied the design criterion of near parallel film gap and the face design was accepted for manufacture.

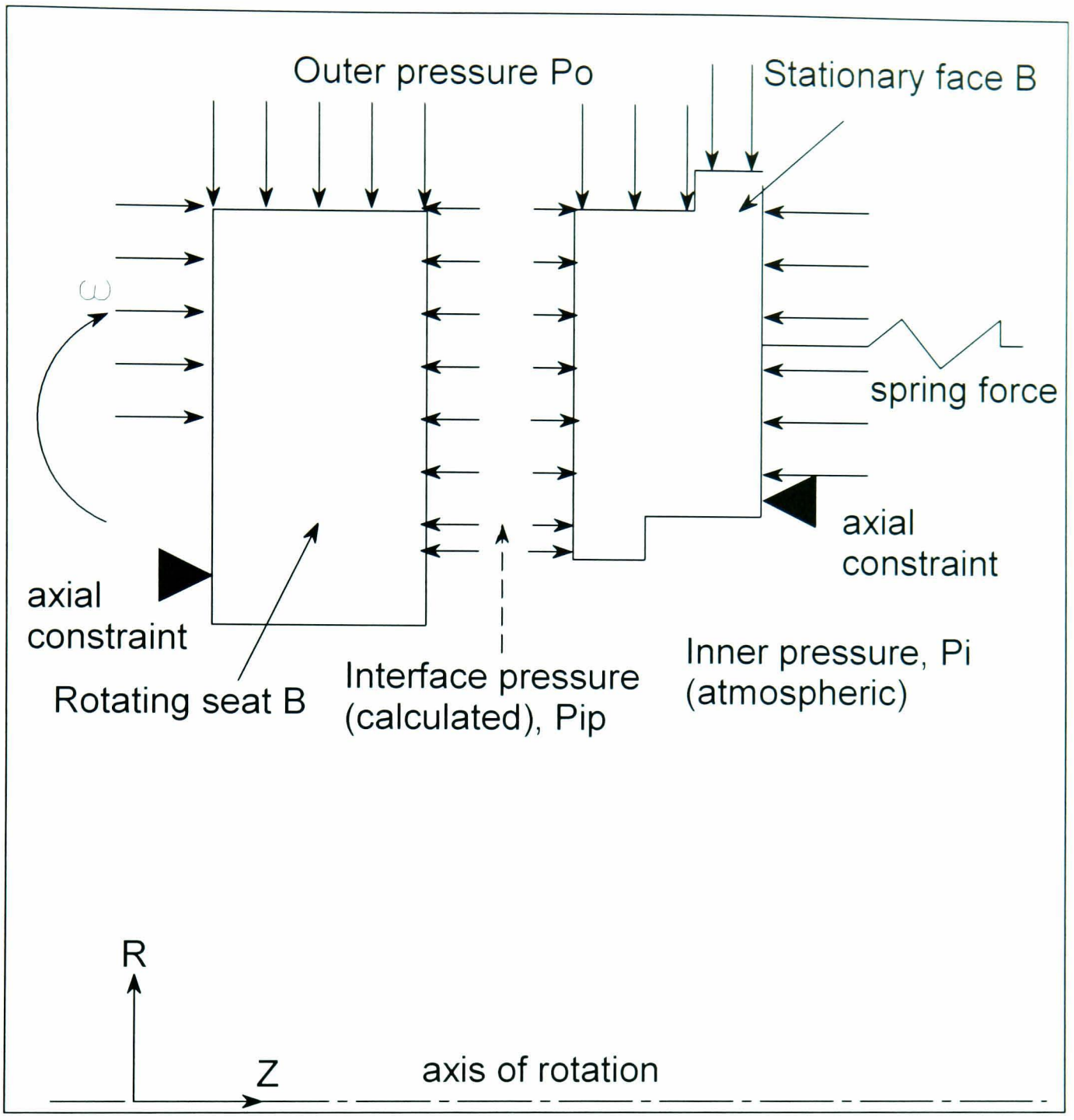

Figure 47: 2-D model of the seal faces showing the boundary conditions

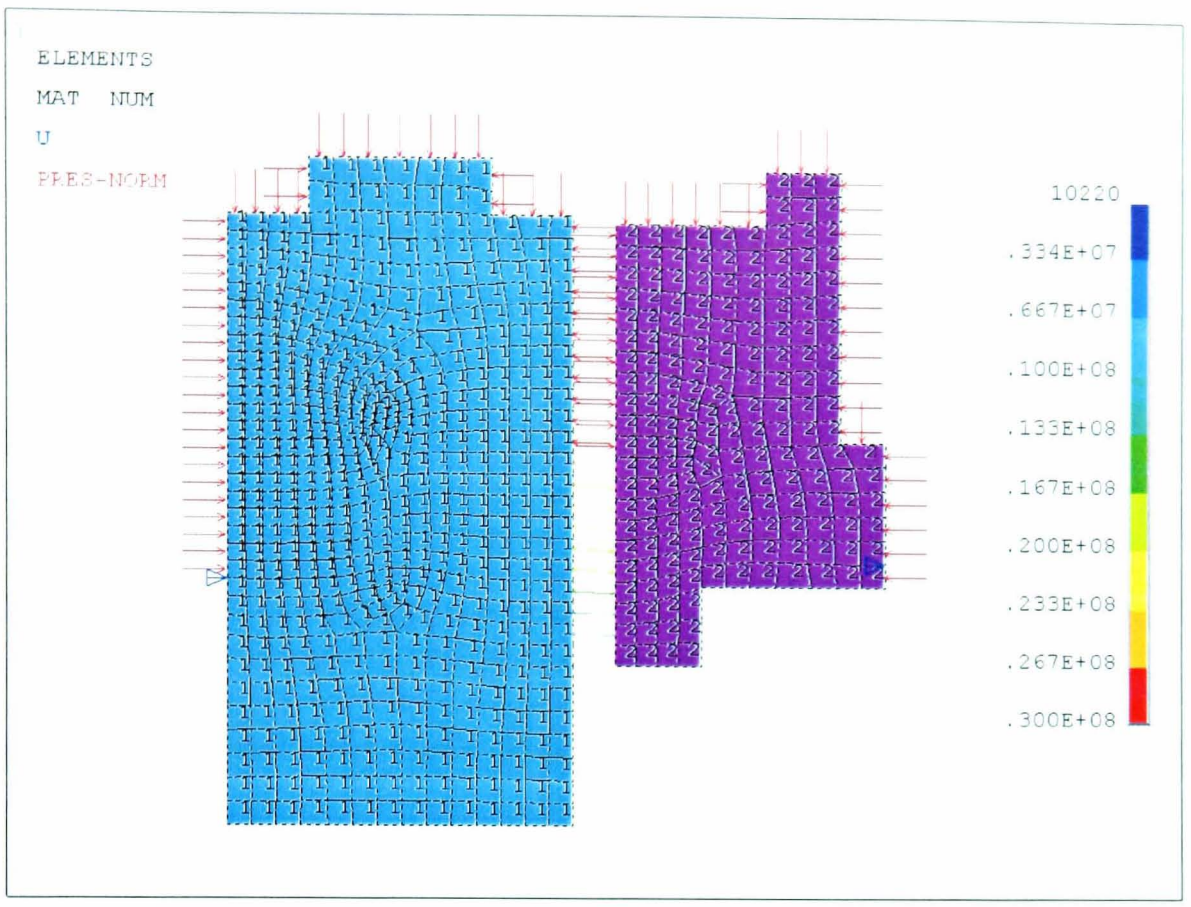

Figure 48: 2-D FE model of the seal faces showing the modelled pressure distribution

A simple 2-D linear static model of the seat and the face was constructed to model the pressure distribution. This was used to predict the component deformations and thus fine tune the cross section of the parts, to give near parallel gap at full pressure conditions (Figure 48).

5.8 SF GAS SEAL DESIGN ACTUAL TEST RESULTS

The following graphs show key results as recorded during experimental testing of the gas seals using the facility and the test equipment described in section 4.

The first two graphs in Figure 49 and Figure 50 show the measured break out torque of the seals as a function of pressure. Breakout torque is by far the most effective means of measuring the point at which the seal faces have lifted off. From Figure 50 in particular it can be seen that the breakout torque reaches a minimum asymptote value of just over 1 N.m just beyond 1 bar of pressure. This confirms the point at which the seal faces have attained complete separation.

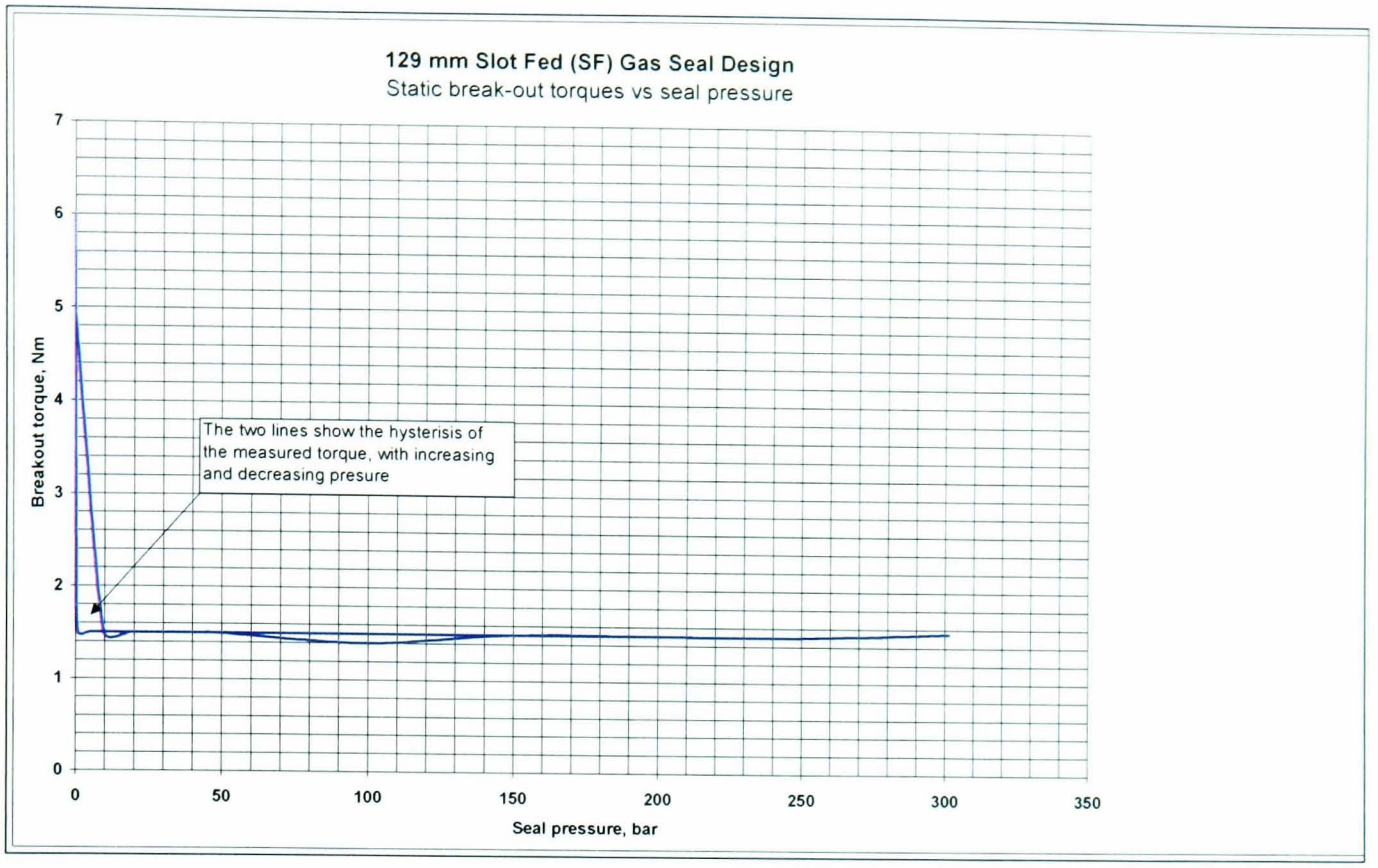

Figure 49: Seal static break out torque as a function of pressure

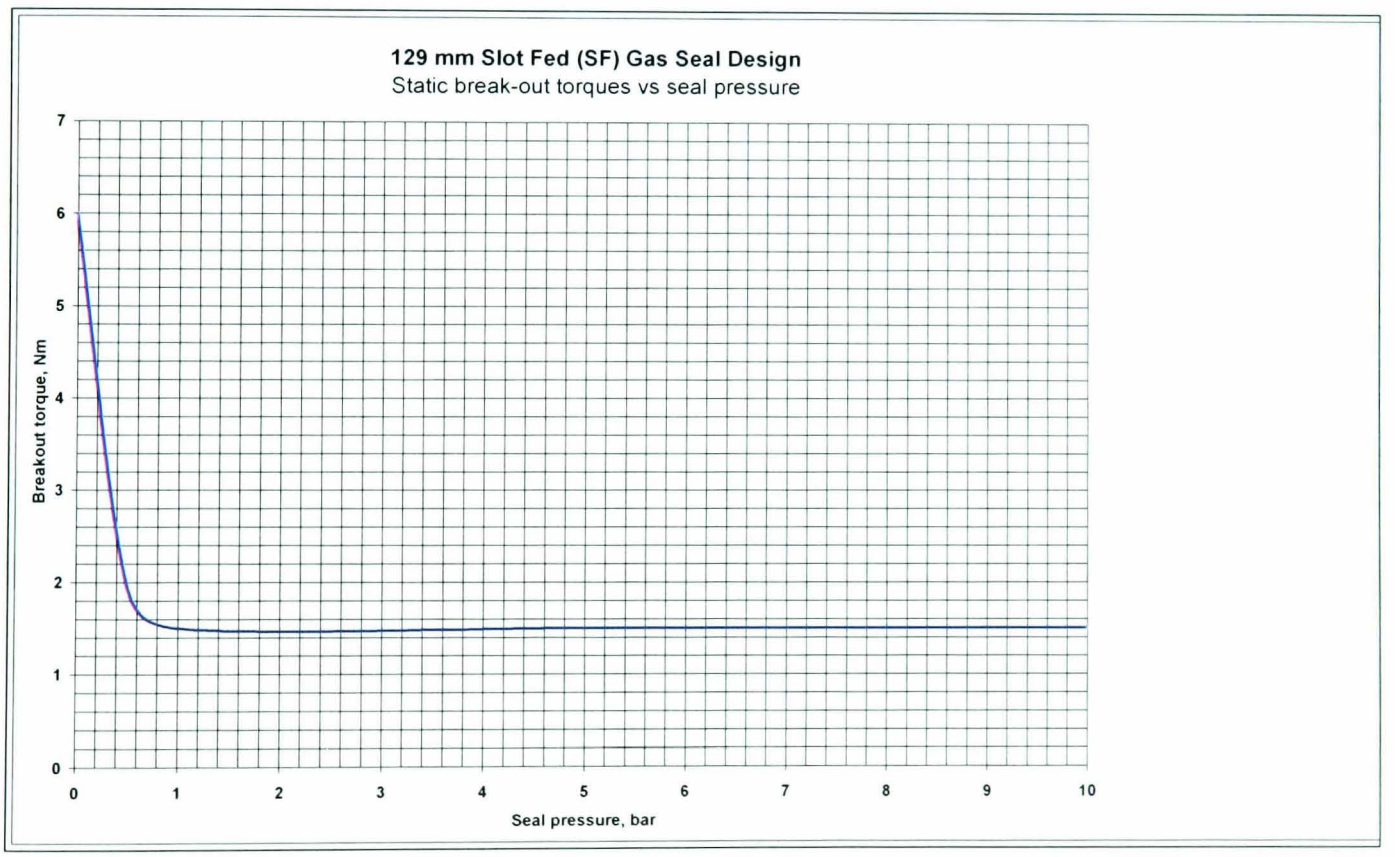

Figure 50: Seal static break out torque as a function of pressure – zoomed in

Key to graphical legends

Reference	Description
DE IB	Drive End inboard position
NDE IB	Non-drive end inboard position (not used)
DE OB	Drive End outboard position
NDE OB	Non-drive end outboard position (not used)

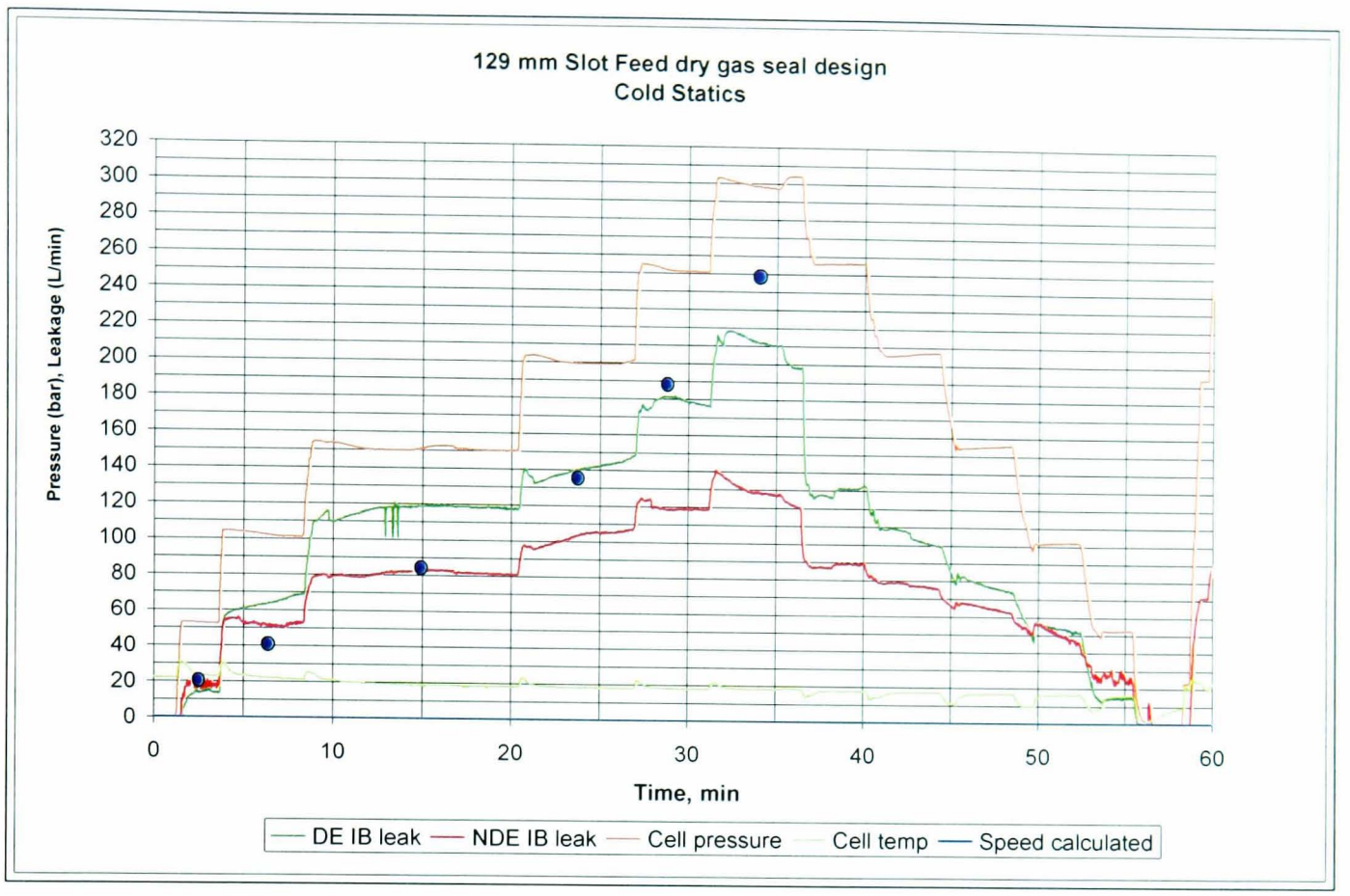

Figure 51: Static seal leakage performance. Model predictions are shown as blue dots

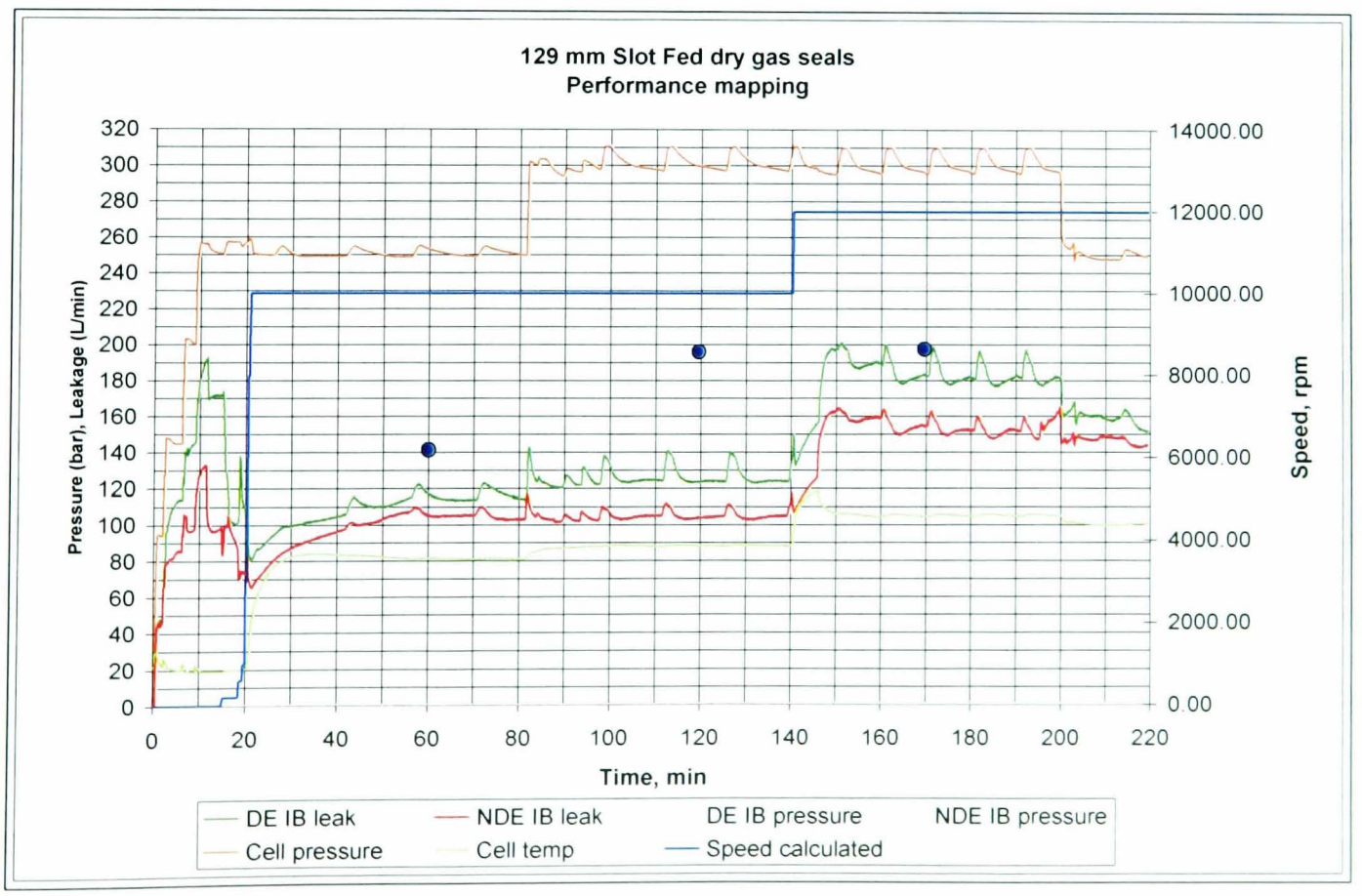

Figure 52: Dynamic seal leakage performance. Model predictions shown as blue dots

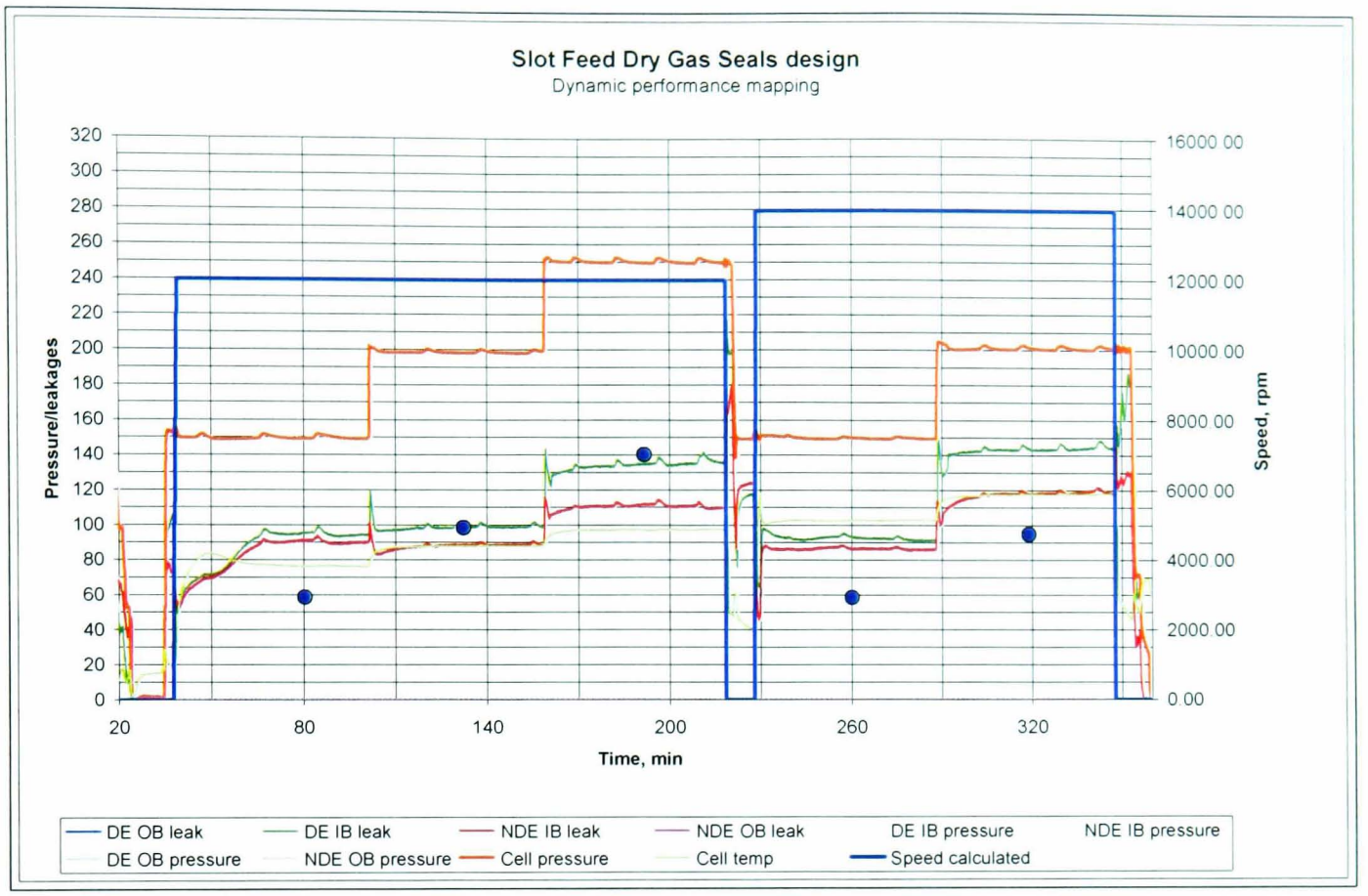

Figure 53: Dynamic seal leakage performance – further performance mapping. Model predictions shown as blue dots

Figure 51 through to Figure 53 show the measured seal performance in terms of static as well dynamic leakage at various operating points within the performance envelope. On each of the graphs, the ordinate axis carries the seal pressure (in bar) and the seal leakage in $l.min^{-1}$ and the operating temperature in deg C. The second ordinate axis on the right hand side carries the seal operating speed in rpm. The abscissa axis carries the time history of the test in minutes.

For comparative evaluation, superimposed on these results graphs is the predicted seal performance from the SF computer model. Those prediction points are shown as blue dots on the graphs. The results are discussed in detail in section 5.9

5.9 MODEL VALIDATION – RESULTS DISCUSSION

5.9.1 Static leakage

The SF computer model predicts a non-linear increase in predicted leakage with pressure. The relationship is almost a square law. Superimposing the modelling predictions onto actual test date yields some interesting observations (see Figure 51).

The following observations can be made. Firstly, at lower pressures, sub-100 bar, the model predictions replicate the test data very accurately. However, as the pressures increase beyond 100 bar, the predictions deviate more and more away from the actual data, increasingly over predicting with greater pressures. At 300 bar, the discrepancy between predicted and actual is: 250 $l.min^{-1}$ (predicted) and 170 $l.min^{-1}$ actual (the average leakage between the two stages). So at higher pressures, the modelling tends to overestimate the predicted leakage. It is worth noting at this stage that static leakages in practice tend to give substantial variations, both build-to-build and often stage-to-stage. Much of this variation is attributed to leakage through the secondary seals. Those seals, typically, cup shaped polymers, often require bedding down after reassembly, before sealing off. Overall, the whole system is stabilised by elevated temperature. This, and individual assembly variations, mean that ambient static leakages can have substantial variability, both from seal to seal as well as build to build. By far the more accurate representation is when the seals are operating dynamically and at elevated temperatures. Never the less, and taken as a whole, there is good correlation between static and dynamic leakages.

One key feature of the model that would lead to over prediction of leakage at higher pressures is that it does not take account of choked flow. In practice, this would restrict the leakage flow rate. If the model were to include this, the predicted leakages, particularly at higher temperatures would drop substantially.

5.9.2 Lift-off pressure

Test results of break out torque against seal pressure give a direct indication of the pressure at which the seals effectively lift off. From Figure 49and Figure 50 it can be seen that the torque plummets to a minimum value of 1 Nm between 1 and 2 bar. From then on the torque remains at that value all the way up to the maximum pressure of 300 bar. It is fair to state that the seals do indeed lift off at that pressure.

Comparing this to the model predictions shown in Figure 43, 1-2 bar corresponds to predicted gap of 0.2 microns. The surface finish of the two parts is very highly polished, measuring: R_a=0.02 microns. After measurement, it was established that these components were in fact perfectly flat. This would not be the case every time. The flatness tolerance on both parts is 1 light band. This translates to 0.3 mm waviness. Doubling that to 0.6 micron, we have the worst-case value for seal operating gap at which the seal will lift off completely, that is 0.6 microns. The fact that the seals lifted off at a lower pressure in this case would simply suggest that the components' individual flatness was significantly better than 1 light band each. So allowing for the worst and the best-case scenario, one would expect the seals to lift off between 0.2 (perfectly flat) and 0.6 microns (allowing for waviness tolerance of 0.3 microns on each sealing face). Analysis predicts the corresponding seal pressures to be between 2 and 5.6 bar. Results put the lift-off pressure at 2 bar. Thus the correlation between theory and experiment is very close.

5.9.3 Dynamic leakage

From Figure 45 and Figure 46, it can be seen that the dynamic leakage prediction against seal pressure for a given temperature, has a similar trend to the static leakage prediction. The only difference is that the numerical value of the leakage is less, attributed to the higher viscosity gas limiting the leakage flow at elevated temperatures. Interestingly to note, the predicted speed effects are very minimal. The variation in predicted leakage between the 6000 and 12000 rpm speed curves is at most 2.3%. This would indicate the seal to be almost 100% hydrostatic. Evaluation of experimental results with the superimposed theoretical predictions (shown in Figure 52 and Figure 53) indicates some degree of variation. Firstly, examining the leakage trend as a function of temperature. It is clear from results that for a constant supply pressure, the leakage does in fact undergo a noticeable increase, when the speed is increased from 10000 to 12000 rpm, the leakage jumps from 120 to 170 $l.min^{-1}$, average for the two seals. One possible explanation for this is that the grooves do indeed have some hydrodynamic lift competence associated with their geometry. The other possible explanation is that one of the secondary seal polymers was leaking progressively more at higher speeds. The experiments were repeated after a rebuild of the seal parts. The results are shown in Figure 53. As can be seen,

the leakage difference between 14000 and 12000 rpm is in the order of 10l.min^{-1}. Allowing for the difference in temperature, that leakage change in speed is in the region of 15-20 l.min^{-1} for an average value of 130 l.min^{-1} at 14000 rpm. Thus, one can conclude that the seals do exhibit a modest component of hydrodynamic lift. Further more, the 1-D SF model is unable to predict any hydrodynamic lift. Instead, it predicts a small reduction in leakage with speed by deducing that the rear slots loose some of their ability to draw in the gas at higher speeds. The predictions for dynamic leakage vary from 100% correlation with specific test points to over predicting by 80% on one specific test point. However, on the vast majority of other test points the model predictions fall within 30% of the actual test data.

5.9.4 Seal contact at the artificial inter space condition

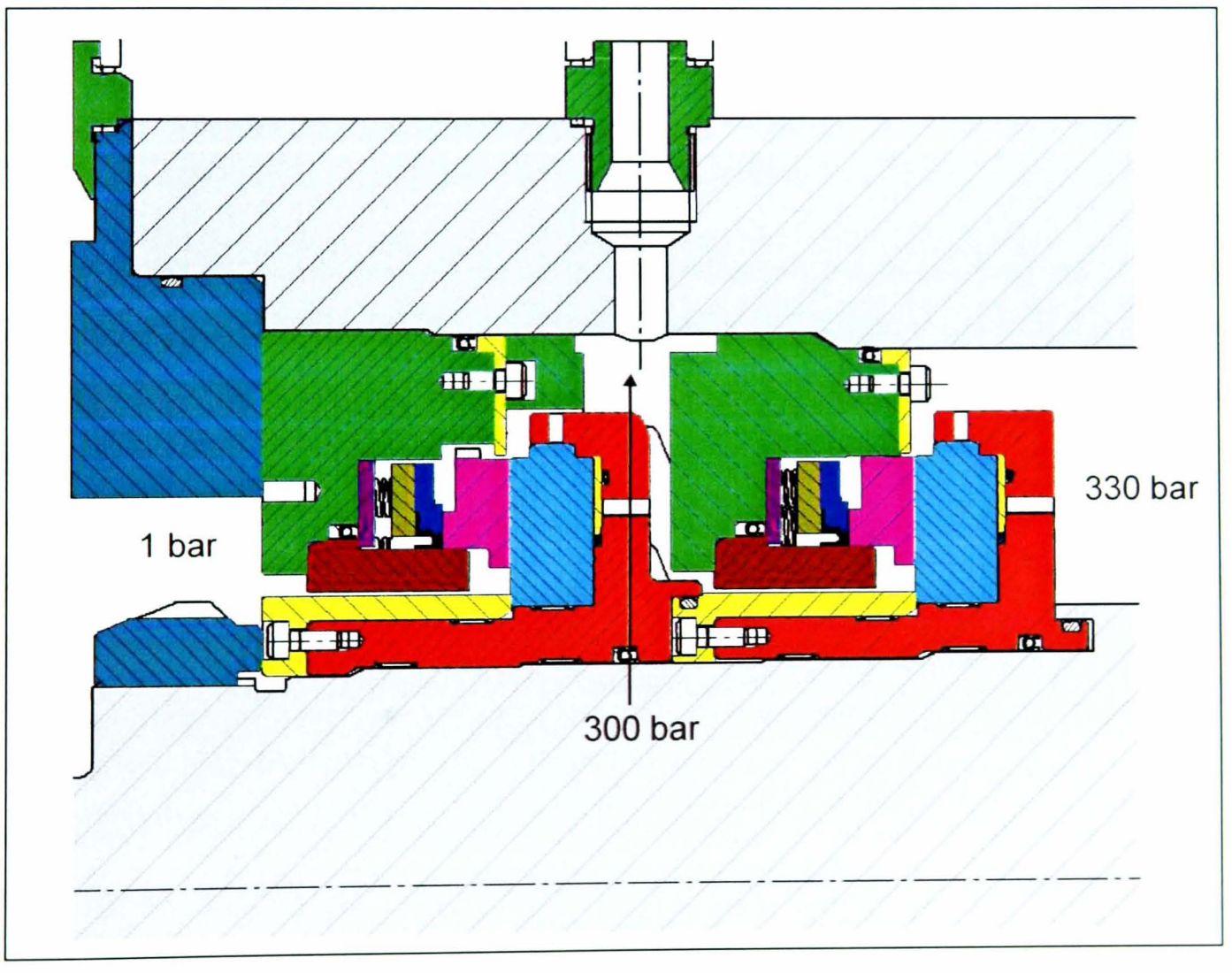

Figure 54: Inter-space test condition shown on the test seals

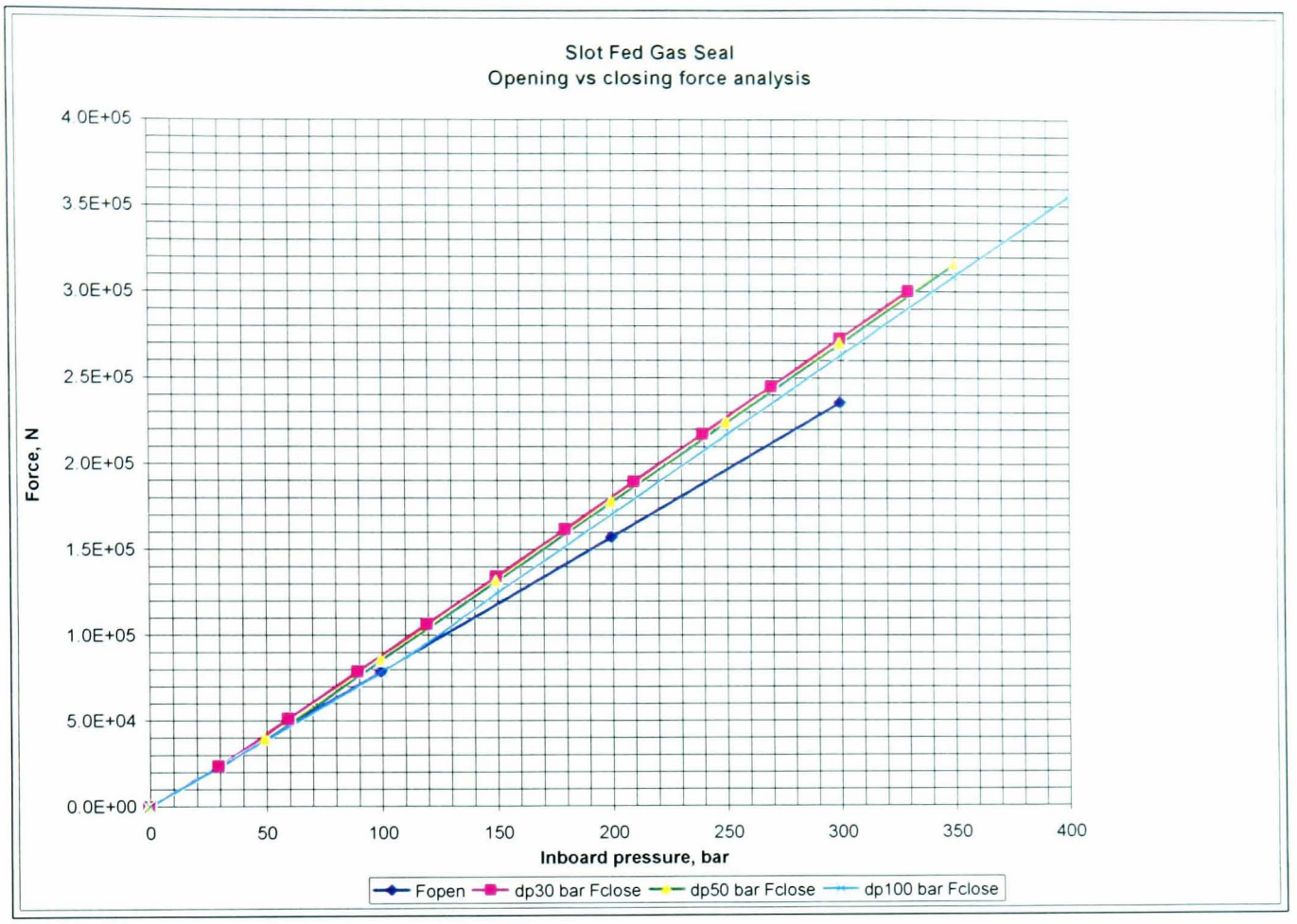

Figure 55: Closing force, versus, opening force analysis

Figure 54 depicts the following test condition that was carried out in the latter stages of performance evaluation. The outboard (OB) stage seal has to be tested as a fully operational seal to simulate the failure of the inboard stage seal (IB). This would normally be done with both stages in situ. To test the full operating capability of the OB seal, it has to be tested to its full operating pressure condition. While testing the OB stage, a certain pressure differential must be present on the IB stage, to avoid reverse pressurisation. The OB seal is being tested at a full operating pressure of 300 bar. To avoid reverse pressurisation, a certain pressure differential is kept on the IB seal. This could be anything from 10 bar to 50 bar. For the example, assume that the IB dP is 30 bar. So the upstream pressure from the IB seal is 330 bar.

Experiments showed that at this condition, when the OB seal was being tested, the IB seal underwent face contact. Further analysis of the design showed that at these conditions, the closing force on the IB seal, the one not under test and under a very artificial condition, was greater than the opening force generated at the seal gap. Referring to the graph in Figure 55, the blue line is the opening force being generated at the seal faces for a given sealing pressure. The other lines referred to by the dP legends represent the closing forces at various pressure ratios. As can be seen,

whenever this condition is imposed, the resultant closing force on the IB seal is greater than the opening force that it can generate. Given that the seal is of a balanced design, under such a condition, the seal would tend to close the operating gap, thus increasing the opening force, until equilibrium between the opening and the closing forces was again re-established. Seal face contact evident from the test clearly indicated that equilibrium between the closing and opening forces was not being established before the operating seal gap was reduced to near zero and contact occurred. What it indicates is that at a certain gap, the film stiffness falls off to near zero. The question was whether that value of film gap was greater or less than the film thickness at which contact was to be expected. To verify this scenario the SF model was modified and reanalysed under varying values of seal face load. For each load value, the predicted equilibrium film gap was calculated. These values were plotted on a graph in Figure 56. As can be seen from a graph, as the seal face load, which can also be seen as the net closing force on the seal, increases, the seal face gap first reduces, but then starts approaching a load asymptote. Looking at this another way, the seal stiffness, which is effectively the gradient of the curve, approaches zero. Hence at a certain load and gap, any further small increase in closing force, will lead to a collapse in seal gap, as can be seen from the graph.

So one can conclude that the loading regime on the OB stage as shown in Figure 55, highlights the characteristic of the seal as shown in Figure 56, which predicts a collapsing film at a an increased seal closing force. The test evidence of face contact at this interspace condition confirms this with little room for doubt.

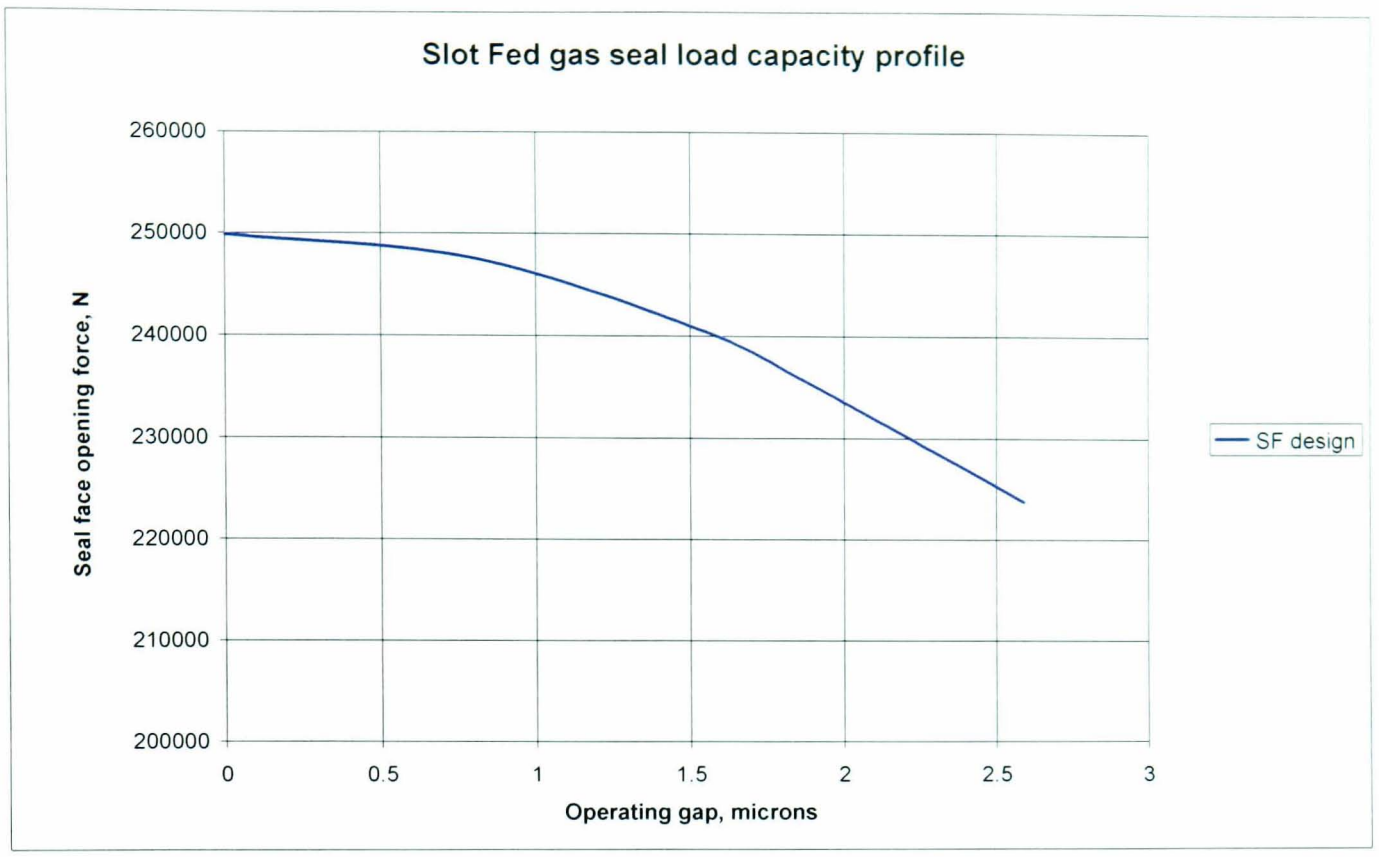

Figure 56:Prediction of operating gap versus seal face load capacity

6 NOVEL HYBRID GAS SEAL CONCEPT

6.1 SLOT FEED LOGARITHMIC SPIRAL GAS SEAL DESIGN CONCEPT

Experimental results at elevated operating pressures and subsequent theoretical verification showed that the SF gas seal design did not give adequate load carrying capacity at artificial interspace test condition described in the previous section. This situation only occurred under dynamic conditions, simulating a failed IB seal. Nevertheless it became clear that a design having greater load carrying capacity under dynamic conditions was necessary. One of the most promising ways to achieve this was to incorporate a greater hydrodynamic lift component to the seals through the use of suitable grooves in one of the seal faces. At the same time it was highly desirable to retain the benefits of the SF design, namely the extremely low lift off pressure and low breakout torques across the entire pressure envelope. A number of hydrodynamic lift options were available, ranging from the well established Rayleigh step, radial slot right to spiral grooves. The latter groove design has received a number of claims to its superior load carrying capacity, as reported by Muijderman [22].

A number of concepts were brainstormed. Given all of the known art, it was decided to combine with the best hydrostatic concept produced thus far, with the best-perceived hydrodynamic design, namely the spiral groove. In order the produce an effective and practical hybrid design, some modifications to the spiral groove geometry had to be made. The design concept was in effect a totally novel and unique hybrid design of gas seal, previously unreported.

Only two components were changed from the SF design. Starting with the minor first, the face cross section had to be altered slightly because the calculated interface pressure profile was predicting a different face convergence.

By far the biggest change occurred on the rotating seat, the seal component containing all of the lift groove geometry. In terms of retained features, the actual SF concept has been retained in its complete entirety, consisting of 3 radial feed slots on the rear surface of the seat. Each of these slots feeding gas to the front of the seat via 3 drilled feed holes. The solid model and a geometry engineering drawing extract are shown in Figure 57 and Figure 58. As can be seen, the only element of this feature that has changed is the pitch circle radius (PCR) of the termination of the feed

slots and the coincident location of the axial feed grooves. In the SFLS design this PCR has been raised. This has been done in order to reduce the hydrostatic component of the seal and make greater space provision for the partial logarithmic spiral grooves located on the front running surface of the seat. The depth of the feed slots has not changed wither.

The front groove geometry is shown in Figure 59 and Figure 60. As can be seen, the first change from the SF design is the continuous nature of the front distribution groove (before it was arched). It was decided to adopt this design to provide an unrestricted gas supply to the entire periphery of the spiral grooves.

Finally, there are the partial spiral grooves themselves. As can be seen from Figure 59, the grooves are partial in their geometry, that is, they don't run the continuously length of the seat face. Their outer radius coincides with the pitch circle radius (PCR) of the front distribution groove. Their inner radius terminates at a predetermined radius. The ungrooved area below the spiral grooves is known as the seal dam and it acts as a restriction to the gas being pumped by the spiral grooves. As is the convention with spiral grooves, they are designed to pump the gas into the seal zone, against the dam thus helping to build up the pressure in the seal interface, as explained by Muijderman [22] and Sedy [29].

6.1.1 Primary seal zone design

In a nutshell, the material specification and surface treatments are identical for the SF and the SFLS design concept. The difference lies with the actual lift groove features. The actual geometry and dimensions of face grooves have been set through a series of basic computer simulations and preliminary experimental testing.

6.1.1.1 Seal faces

Both components are made from high strength engineered ceramics. The material family is covalently reaction bonded silicon carbide

6.1.1.2 Rotating seat

Young's modulus = 420 GPa

4-point flexural strength = 550 MPa

Thermal conductivity = 75 $W.m^{-1}.K^{-1}$

Coefficient of thermal expansion = 3.5 x $10^{-6}.K^{-1}$

Weibull modulus = 15

Number of rear feed slots: 3

Rear slot depth = 14 μm

Number of logarithmic spirals = 18

Dam to groove width ratio = 1

Spiral groove depth = 14 μm

Number of front circumferential grooves: 1 (continuous)

Front circumferential groove depth = 30-50 μm

The solid model figures and engineering drawing extracts of the rotating seat are shown in Figure 57 through to Figure 60.

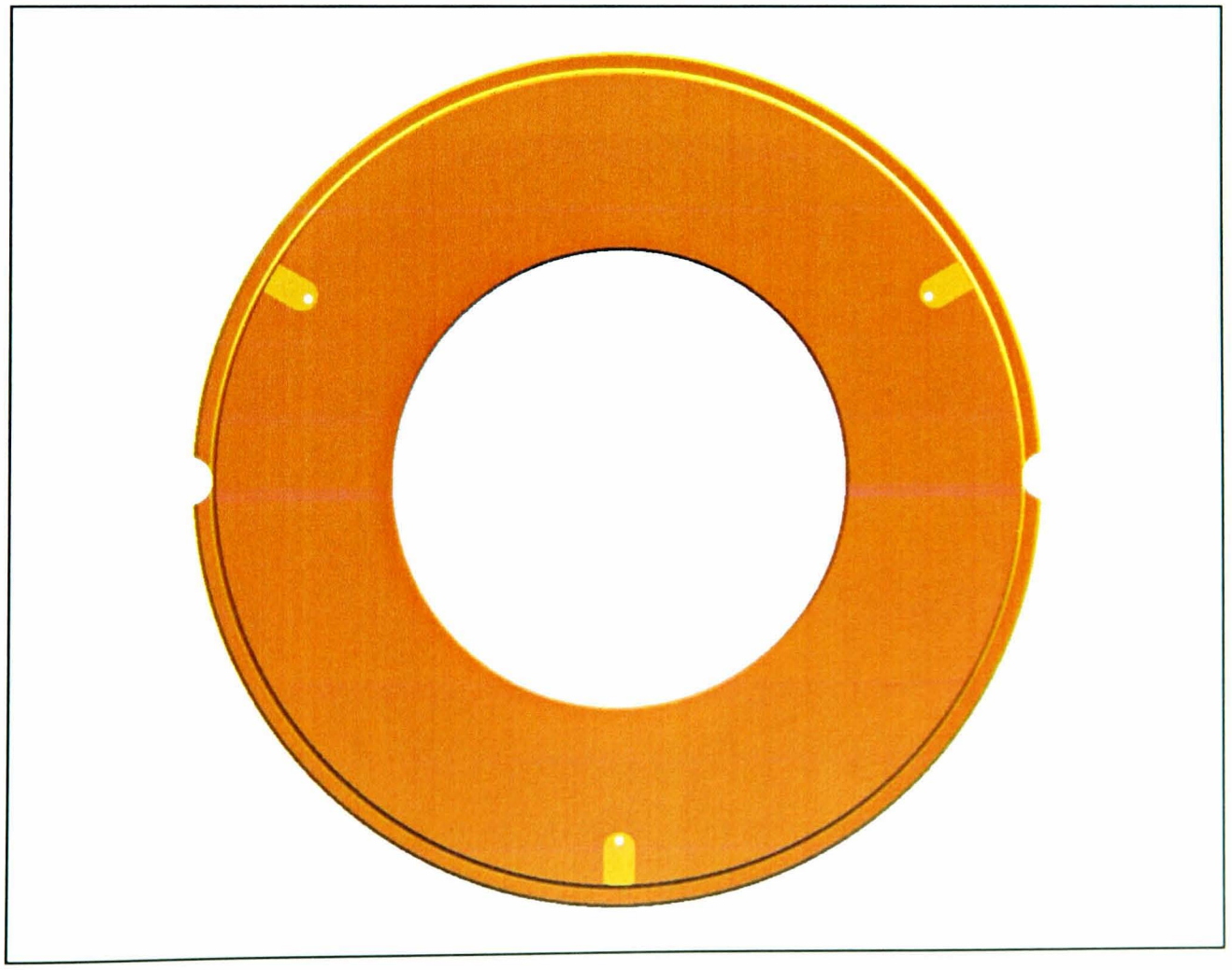

Figure 57: Rear view of SFLS rotating seat showing 3 feed slots and feed holes

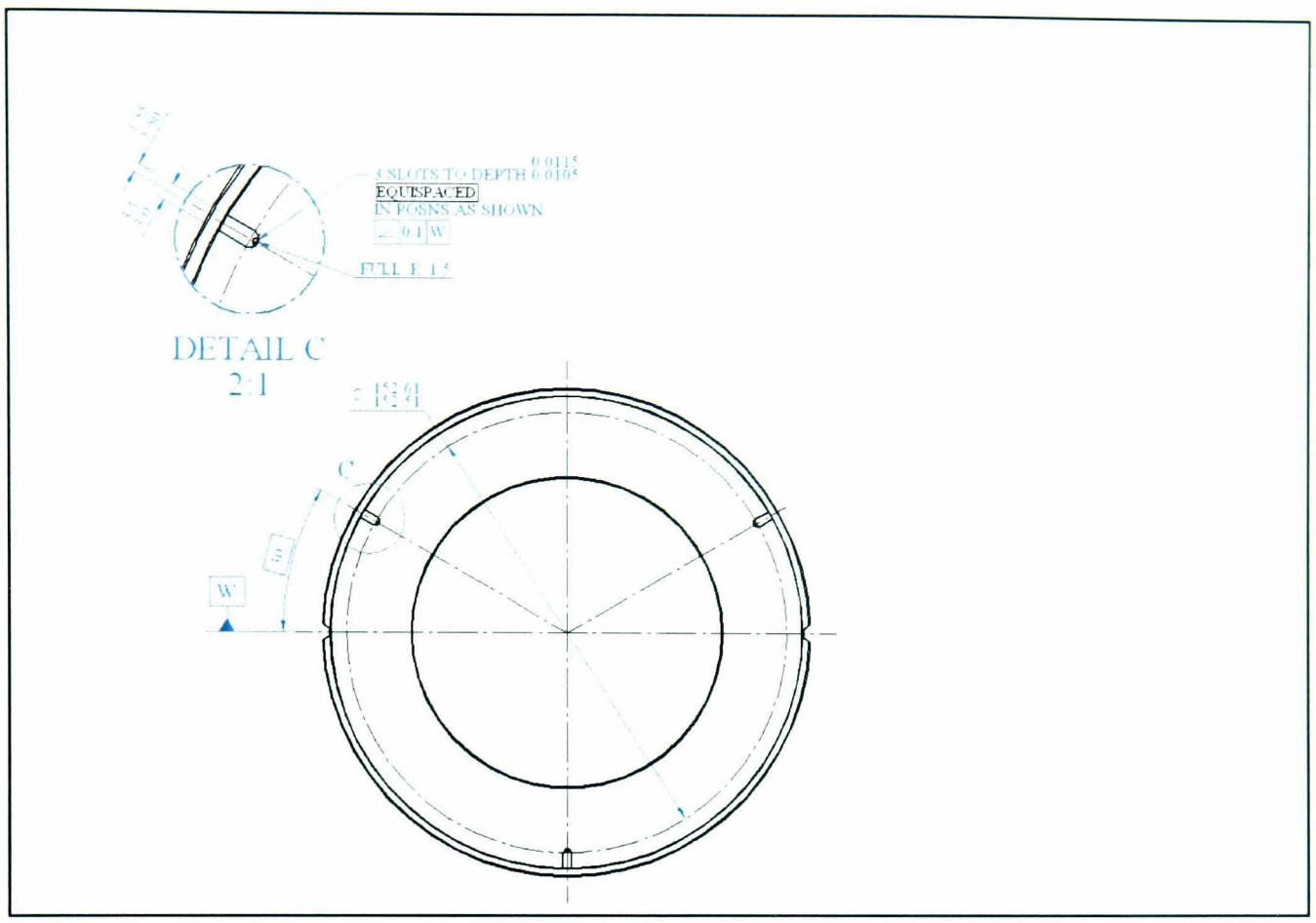

Figure 58: Rear view of SFLS rotating seat – engineering drawing

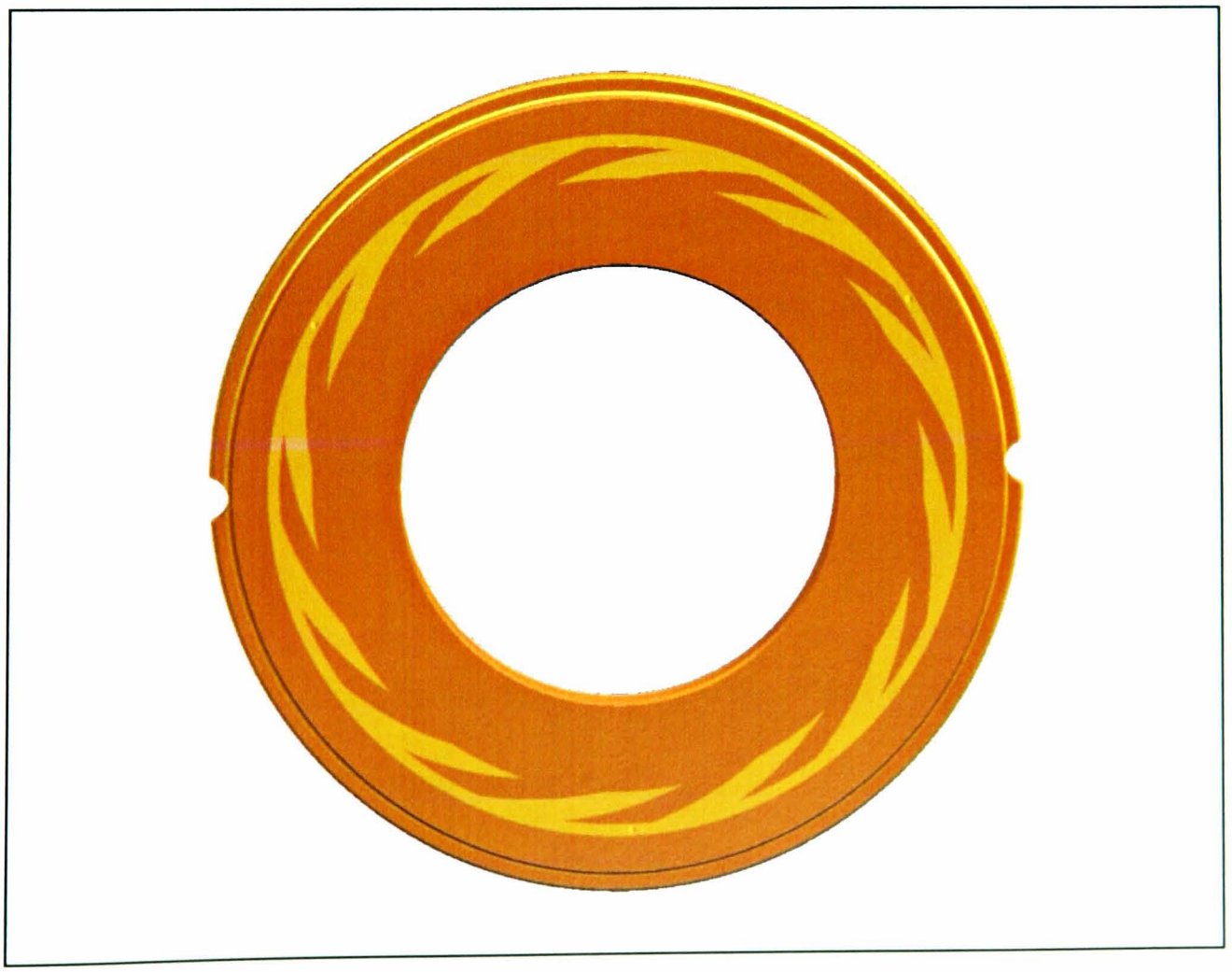

Figure 59: Front view of the seat, showing the periodic logarithmic spirals.

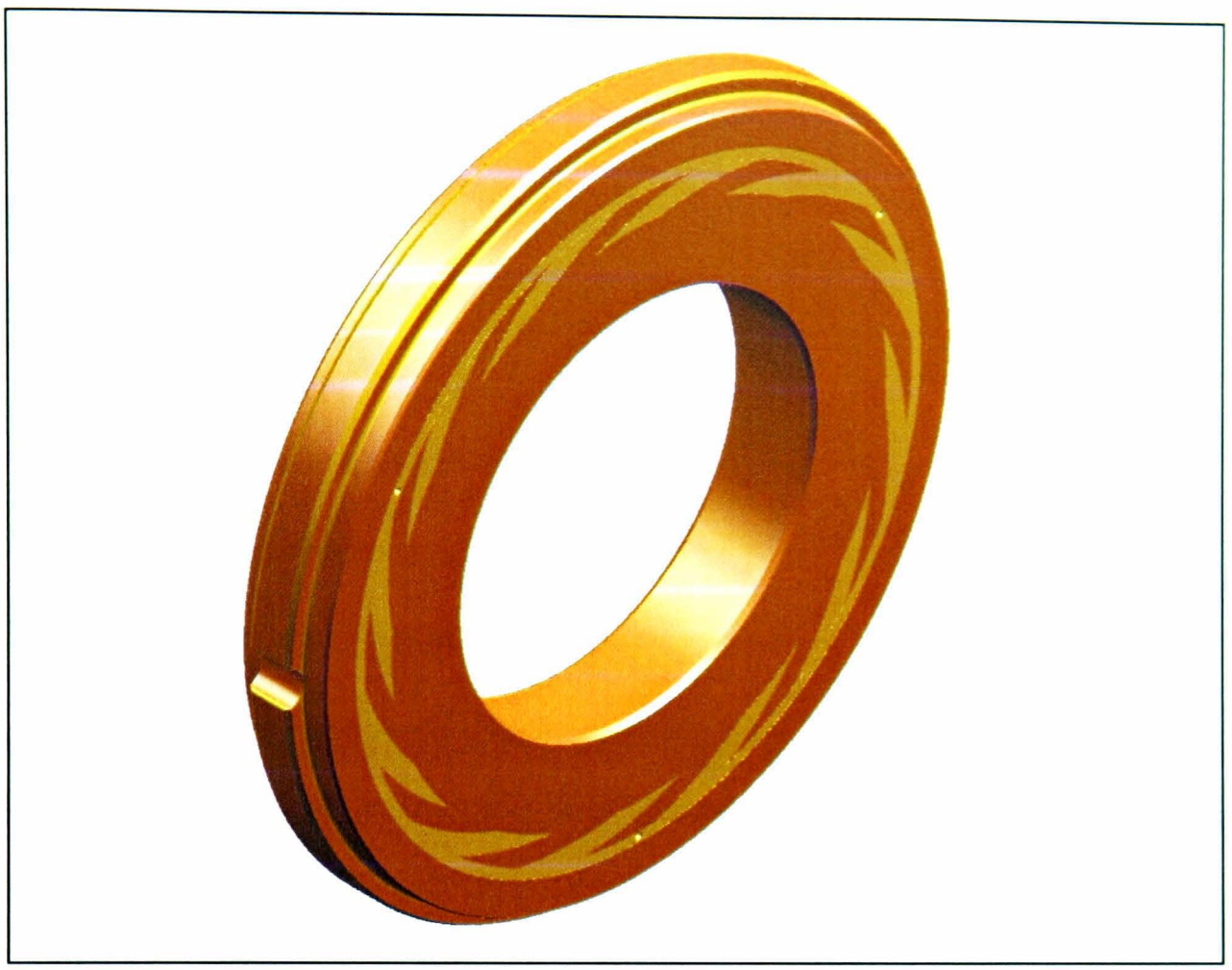

Figure 60: Slot Fed Logarithmic Spiral gas seal design – isometric view of rotating seat

6.2 SUMMARY OF SFLS FLUID FILM MODEL ASSUMPTIONS AND CONSIDERATIONS

- The flow is from the high-pressure source to the low-pressure source.
- The fluid film pressure and operating gap are modelled across the 2-d sector of the seal geometry.
- Flow is laminar, given the nature of the gap and the operating conditions. Justification for this is made in Section 6.7.9.
- The sealed fluid is Newtonian in its nature
- The fluid density is constant across the fluid film (axially across)
- Fluid inertia effects are considered
- Fluid viscosity is constant across the film
- Effect of surface roughness on fluid flow is negligible

- Squeeze motions are not included and effects of small amounts of unplanned squeeze are negligible.
- The film is thin, such that the velocity gradients across the film predominate.
- There are no shockwaves or other sources of discontinuity.
- The film is isothermal.
- Slip flow effects are neglected.
- Real gas properties, appropriate to any condition are utilised.
- Real gas compressibility is accounted for.
- Full effects of sonic flow are accounted for.
- Spiral groove end effect corrections are made for any geometry and duty condition
- Full gas seal geometry effects including the specified gas lift geometry.
- Full operating conditions of the gas seal.
- Real gas properties relevant to the fluid film analysis.
- Pressure, speed and temperature effects.
- Thermal effects in the structural model.
- Heat fluxes at the seal interface
- Surface heat transfer coefficients.

6.3 DERIVATION OF THE GOVERNING EQUATIONS FOR SFLS MODEL:

The design was significantly more complex than its SF predecessor. More so, given periodic nature of the SFLS lift geometry, it was felt, that the geometry could no longer be modelled in simple 1-D. In order to correctly represent the new and novel geometry, a suitable 2-D model had to be developed. This model had to incorporate the features and the interaction of both, the slot feed design and the partial spiral grooves. One of the goals from the outset was to develop a model that could be used

to predict seal performance not just for the hybrid slot feed logarithmic spiral seal, but also variants of it. Thus the model had to be flexible enough to model the geometry of an arbitrary groove. This in turn would give the model its greatest flexibility.

6.3.1 Solution of the Reynolds equation

The general Reynolds equation is a non-linear partial differential equation. The usual method of solving the Reynolds equation is numerically, by programming an iterative solution algorithm of a finite difference approximation to the differential equation. The use of a computer program is the most efficient means to achieve a solution. The computational effort involved in such a solution is usually very high because a large system of non-linear algebraic equations needs to be solved iteratively.

The solution itself has been the subject of many publications and research papers. In this case the Reynolds equation was taken as the starting point for developing the model. Previous work reported by Szeri [38] and later Lebeck [21], described how Newton's method could be used to solve the compressible flow Reynolds equation using the finite difference technique. This method was applied here in the development of the 2-D performance model. The method of solving the compressible flow Reynolds equation needed to be developed so that it could then be used to solve for a particular complex geometry of the seal, as is the case here with the novel SFLS concept.

In this chapter a full analytical model is developed to accurately predict the performance of such a design by solving the 2-D Reynolds equation, using Newton's method. To date the author has found no reference to using the Reynolds equation to build a model to predict the performance of such a novel design.

For the steady state condition, laminar flow and compressible fluid, the generalised form of the Reynolds equation in 2-dimensions is written as follows (in Cartesian terms): We start from here, no other derivation is necessary.

$$-\frac{\partial}{\partial x}\left(\frac{h^3}{12\mu}\frac{\partial P}{\partial x}\right)+\frac{\partial}{\partial y}\left(\frac{h^3}{12\mu}\frac{\partial P}{\partial y}\right)=\frac{U}{2}\frac{\partial h}{\partial x}$$

eqn. 6.1

Approximate equations for velocity take on the form of the following:

$$u=\frac{1}{2\mu}\frac{\partial P}{\partial x}(z^2-zh)+u\frac{z}{h}$$

eqn. 6.2

$$v=\frac{1}{2\mu}\frac{\partial P}{\partial y}(z^2-zh)$$

eqn. 6.3

Integrating the above to get the mass flow rate per unit width. Note that the density terms is used to convert the volume flow rate to a mass flow rate

$$\dot{m}_x=\rho\int_0^h u dz$$

eqn. 6.4

Substitute in for u:

$$\dot{m}_x=\rho\int_0^h\left(\frac{1}{2\mu}\frac{\partial P}{\partial x}(z^2-zh)+u\frac{z}{h}\right)dz$$

eqn. 6.5

$$\dot{m}_x=\rho\int_0^h\left[\frac{1}{2\mu}\frac{\partial P}{\partial x}z^3-\frac{1}{2\mu}\frac{\partial P}{\partial x}zh+uz/h\right]dz$$

eqn. 6.6

$$\dot{m}_x=\rho\left[\frac{1}{2\mu}\frac{\partial P}{\partial x}\frac{z^3}{3}-\frac{1}{2\mu}\frac{\partial P}{\partial x}\frac{z^2}{2}h+\frac{uz^2}{2h}\right]_0^h$$

eqn. 6.7

$$\dot{m}_x=\rho\left(-\frac{1}{12\mu}\frac{\partial P}{\partial x}h^3+\frac{uh}{2}\right)$$

eqn. 6.8

Similarly for $\dot{m}_y$:

$$\dot{m}_y = \rho \int_0^h v dz$$

eqn. 6.9

$$\dot{m}_y = \rho \int_0^h \frac{1}{2\mu} \frac{\partial P}{\partial y} (z^2 - zh) dz$$

eqn. 6.10

$$\dot{m}_y = \rho \left[\frac{1}{2\mu} \frac{\partial P}{\partial y} \frac{z^3}{3} - \frac{1}{2\mu} \frac{\partial P}{\partial y} \frac{z^2}{2} h \right]_0^h$$

eqn. 6.11

$$\dot{m}_y = \rho \left(\frac{1}{2\mu} \frac{\partial P}{\partial y} \left(\frac{h^3}{3} - \frac{h^3}{2} \right) \right)$$

eqn. 6.12

$$\dot{m}_y = \rho \left(-\frac{h^3}{12\mu} \frac{\partial P}{\partial y} \right)$$

eqn. 6.13

Note that to get the volume flow rate per unit length, one simply has to divide by the density. However, as we are dealing with a compressible fluid in the case of gas seals, the density will eventually be a variable. Thus it makes sense to work with mass flow rates rather than volume flows, from the outset.

For mechanical seals it is more convenient to represent the Reynolds equation in its polar coordinate form. Using the polar coordinate system shown in Figure 61 the radial and tangential mass flow equations may be rewritten as follows:

$$\dot{m}_\theta = \rho \left(-\frac{1}{12\mu} \frac{\partial P}{r \partial \theta} h^3 + r\omega \frac{h}{2} \right)$$

eqn. 6.14

$$\dot{m}_r = \rho \left(-\frac{h^3}{12\mu} \frac{\partial P}{\partial r} \right)$$

eqn. 6.15

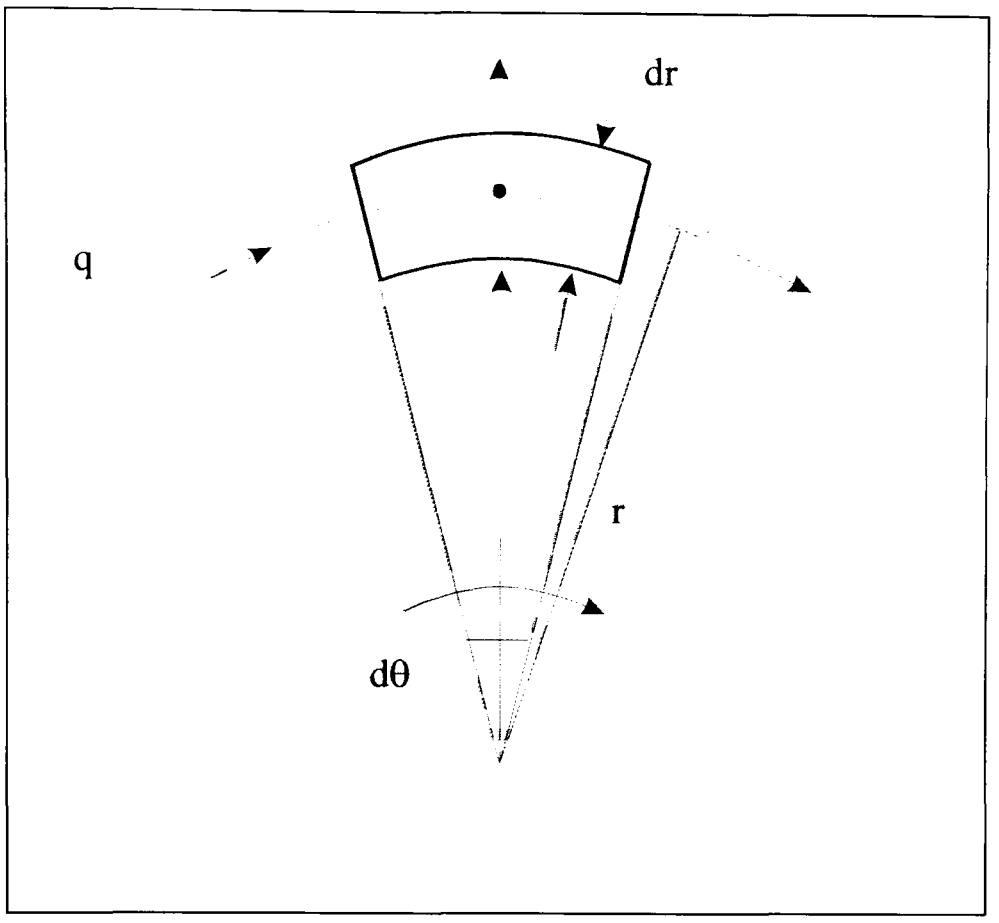

Figure 61: Control volume in polar coordinates.

With reference to Figure 61 above depicting the control volume in polar coordinates, the net sum mass flow rate into the control volume can be established by summing the mass flows as shown. Neglecting the squeeze film effects, mass continuity results in the following equation:

$$\frac{\partial m_\theta}{\partial \theta} + \frac{\partial}{\partial r}(r\dot{m}_r) = 0$$

eqn. 6.16

Substituting the above equations for mass flow rates in the radial and circumferential directions, the Reynolds equation in polar co-ordinates is given by:

$$\frac{1}{r}\left(\frac{\rho h^3}{12\mu}\frac{\partial P}{\partial \theta}\right) + \frac{\partial}{\partial r}\left(\frac{\rho h^3}{12\mu}\frac{\partial P}{\partial r}\right) = \frac{r\omega}{2}\frac{\partial h}{\partial \theta}$$

eqn. 6.17

6.3.1.1 Deriving compressible flow finite difference equations.

First consider the flow balance on a control volume shown above.

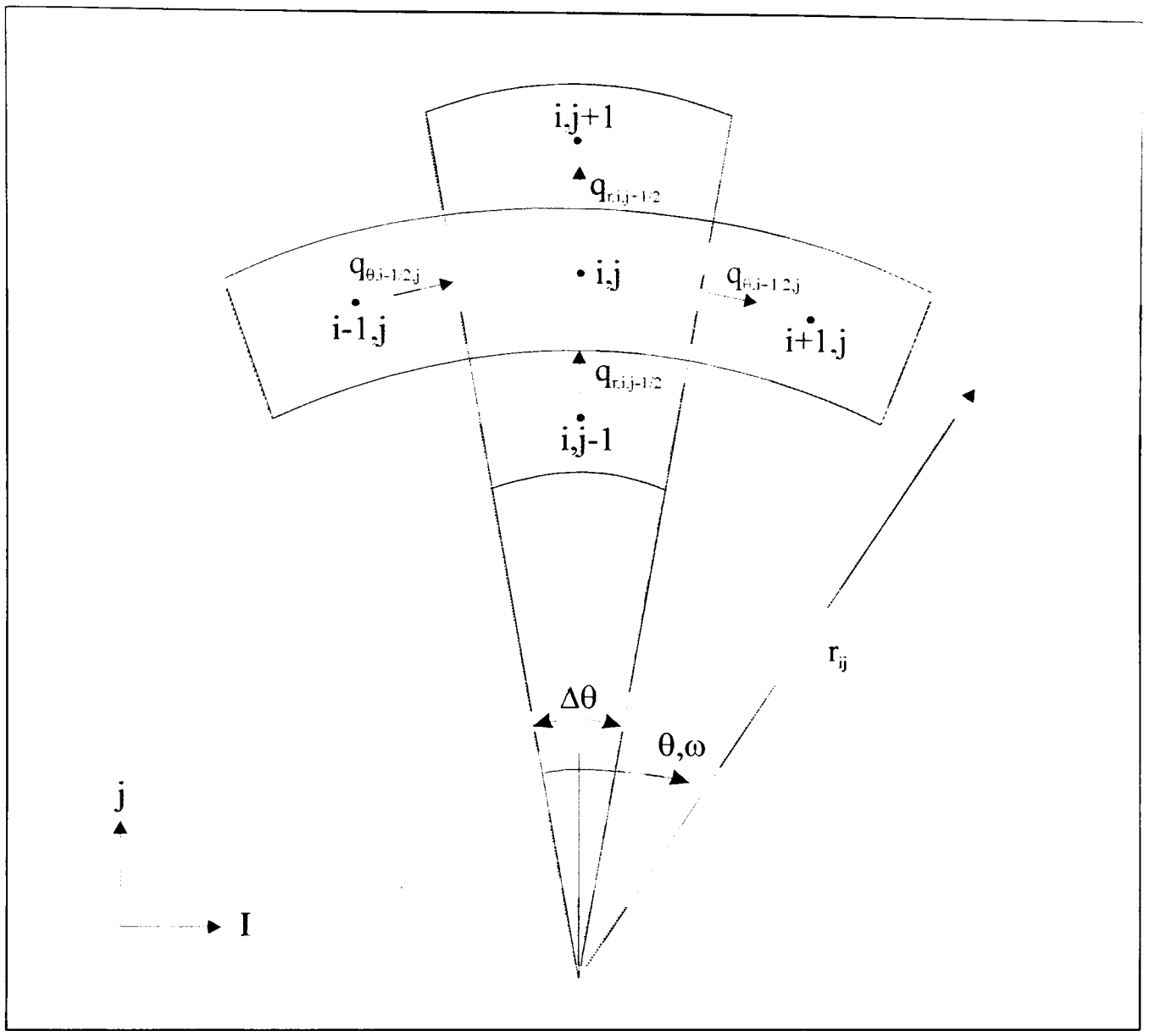

Figure 62: Finite difference control volume for the primary sealing zone

Using the equation for the circumferential and radial mass flow rates derived earlier become

$$\dot{m}_{\theta,i-1/2,j} = \left(-\frac{\rho h^3}{12\mu r}\frac{\partial P}{\partial \theta} + \frac{\rho r \omega h}{2} \right)_{i-1/2,j} \partial r$$

eqn. 6.18

$$\dot{m}_{\theta,i+1/2,j} = \left(-\frac{\rho h^3}{12\mu r}\frac{\partial P}{\partial \theta} + \frac{\rho r \omega h}{2} \right)_{i+1/2,j} \partial r$$

eqn. 6.19

$$\dot{m}_{r,i,j-1/2} = \left(-\frac{\rho h^3}{12\mu r}\frac{\partial P}{\partial r} r \partial \theta \right)_{i,j-1/2}$$

eqn. 6.20

$$\dot{m}_{r,i,j+1/2} = \left(-\frac{\rho h^3}{12\mu r}\frac{\partial P}{\partial r} r\partial\theta \right)_{i,j+1/2}$$

eqn. 6.21

For the Newton method it is more convenient to rewrite the above equation (eqn. 6.18) as follows:

$$\dot{m}_{\theta,i-1/2,j} = \rho_{i-1/2,j}\left[\frac{-h^3{}_{i-1/2,j}}{12\mu r_{i,j}}\frac{\partial P}{\partial\theta}\bigg|_{i-1/2,j} + \frac{r_{i,j}\omega h_{i-1/2,j}}{2} \right]\partial r$$

eqn. 6.22

The pressure gradient at the control volume edge is expressed as follows:

$$\frac{\partial P}{\partial\theta}\bigg|_{i-1/2,j} = \frac{P_{i,j} - P_{i-1,j}}{\partial\theta}$$

eqn. 6.23

For the time being, assume that the fluid is a perfect gas, so defining the compressibility term:

$$\rho = \frac{P}{R_{gas}T}$$

eqn. 6.24

It should be noted at this stage that in the final model, the actual density is used in the analysis. This density is derived from a real gas properties database, which in itself has been derived from a proprietary real gas properties software database called PPDS2, developed and supplied by the National Engineering Laboratory [26].

Density at the control volume edge will be taken as the average density. Thus:

$$\rho_{i-1/2,j} = \frac{\rho_{i,j} + \rho_{i-1,j}}{2} = \frac{p_{i,j} + p_{i-1,j}}{2R_{gas}T}$$

eqn. 6.25

Substitute eqn. 6.23 and eqn. 6.24 into the mass flow rate equation eqn. 6.22, written above to give the following:

$$\dot{m}_{\theta,i-1/2,j} = \frac{P_{i,j} + P_{i-1,j}}{2R_{gas}T}\left[\frac{-h^3{}_{i-1/2,j}}{12\mu r_{i,j}}\left(\frac{p_{i,j} - p_{i-1,j}}{\partial\theta}\right) + \frac{r_{i,j}\omega h_{i-1/2,j}}{2}\right]\partial r$$

eqn. 6.26

Repeating for the other 3 sides of the control volume:

Pressure gradient will be: $\left.\frac{\partial P}{\partial\theta}\right|_{i+1/2,j} = \frac{P_{i,j} - P_{i+1,j}}{\partial\theta}$

eqn. 6.27

Density will be: $\rho_{i+1/2,j} = \frac{P_{i,j} + P_{i+1,j}}{2R_{gas}T}$

eqn. 6.28

Resultant mass flow rate through that side of the control volume will be:

$$\dot{m}_{\theta,i+1/2,j} = \rho_{i+1/2,j}\left[\frac{-h^3{}_{i+1/2,j}}{12\mu r_{i,j}}\left.\frac{\partial P}{\partial\theta}\right|_{i+1/2,j} + \frac{r_{i,j}\omega h_{i+1/2,j}}{2}\right]\partial r$$

eqn. 6.29

Substitute equations eqn. 6.27 and eqn. 6.28 into eqn. 6.29 to give the following:

$$\dot{m}_{\theta,i+1/2,j} = \frac{P_{i,j} + P_{i+1,j}}{2R_{gas}T}\left[\frac{-h^3{}_{i+1/2,j}}{12\mu r_{i,j}}\left(\frac{P_{i,j} - P_{i+1,j}}{\partial\theta}\right) + \frac{r_{i,j}\omega h_{i+1/2,j}}{2}\right]\partial r$$

eqn. 6.30

Now for the third side of the control volume (label 3):

Pressure gradient across the 3rd side of the control volume:

$$\left.\frac{\partial p}{\partial r}\right|_{i,j-1/2} = \frac{P_{i,j-1} - P_{i,j}}{\partial r}$$

eqn. 6.31

Density at the control volume edge will be:

$$\rho_{i,j-1/2} = \frac{P_{i,j-1} + P_{i,j}}{2R_{gas}T}$$

eqn. 6.32

Mass flow rate across the 3rd side of the control volume will be:

$$\dot{m}_{\theta,i+1/2,j} = \left(\frac{P_{i,j-1} + P_{i,j}}{2R_{gas}T}\right)\left[\frac{h^3{}_{i,j-1/2}}{12\mu}\left(\frac{P_{i,j-1} - P_{i,j}}{\partial r}\right)\right]\partial\theta$$

eqn. 6.33

In a similar manner for the 4th side of the control volume the mass flow rate will be:

$$\dot{m}_{\theta,i+1/2,j} = \left(\frac{P_{i,j+1} + P_{i,j}}{2R_{gas}T}\right)\left[\frac{h^3{}_{i,j+1/2}}{12\mu}\left(\frac{P_{i,j+1} - P_{i,j}}{\partial r}\right)\right]\partial\theta$$

eqn. 6.34

The problem is considered to be steady state , with no squeeze film effects, thus:

$$\frac{\partial h}{\partial t} = 0 \text{ and } \frac{\partial P}{\partial t} = 0$$

The mass flow for each control volume in the model mesh should sum up to zero as given by:

$$\dot{m}_{\theta,i-1/2,j} - \dot{m}_{\theta,i+1/2,j} + \dot{m}_{r,i,j-1/2} - \dot{m}_{r,i,j+1} = 0$$

eqn. 6.35

Substituting in for the four mass flow rates into the above equation gives the following:

$$F[p] = F_{i,j} = 0$$

$$= \left(P_{i-1,j} + P_{i,j}\right)\left[a_{i-1/2,j}\left(P_{i,j} - P_{i-1,j}\right)h^3_{i-1/2,j} + b_{i-1.2,j}h_{i-1/2,j}\right] -$$

$$-\left(P_{i,j} + P_{i+1,j}\right)\left[a_{i+1/2,j}\left(P_{i+1,j} - P_{i,j}\right)h^3_{i+1/2,j} + b_{i+1.2,j}h_{i+1/2,j}\right] +$$

$$+\left(P_{i,j-1} + P_{i,j}\right)\left[a_{i,j-1/2}\left(P_{i,j} - P_{i,j-1}\right)h^3_{i,j-1/2}\right] -$$

$$+\left(P_{i,j} + P_{i,j+1}\right)\left[a_{i,j+1/2}\left(P_{i,j+1} - P_{i,j}\right)h^3_{i,j+1/2}\right]$$

eqn. 6.36

where:

$$a_{i-1/2,j} = a_{i+1/2,j} = -\frac{1}{2R_{gas}T}\frac{1}{12\mu r_{i,j}}\frac{\Delta r}{\Delta\theta}$$

eqn. 6.37

$$b_{i-1/2,j} = b_{i+1/2,j} = -\frac{1}{2R_{gas}T}\frac{r_{i,j}\omega}{2}\Delta r$$

eqn. 6.38

$$a_{i,j-1/2} = -\frac{1}{2R_{gas}T}\frac{1}{12\mu}\left(r_{i,j} - \frac{\Delta r}{2}\right)\frac{\Delta\theta}{\Delta r}$$

eqn. 6.39

$$a_{i,j+1/2} = -\frac{1}{2R_{gas}T}\frac{1}{12\mu}\left(r_{i,j} + \frac{\Delta r}{2}\right)\frac{\Delta\theta}{\Delta r}$$

eqn. 6.40

Equation eqn. 6.36 represents the entire set of equations, one for each unknown pressure point in the grid that discretizes the seal face sector. The unknown is the pressure point in the grid. Solution to the problem will be when a set of pressure values of P result in the equation having a zero residual value, that is:

$$F[P] = [0]$$

eqn. 6.41

To find a solution to those non-linear equations, one could employ the Newton's method. First assume that there will be a set of values P^n that represent an estimate to the solution, such that:

$$F\left[P^n\right] \neq [0]$$

eqn. 6.42

Using Newton's method, one can calculate a set of corrections ΔP to the proceeding calculation estimate, using the following matrix equation:

$$F'\left[P^n\right][\Delta P] = -F\left[P^n\right]$$

eqn. 6.43

The above equation represents a set of simultaneous linear equations that can be solved for the pressure correction terms ΔP. Then a new estimate of the solution will be given by:

$$\left[P^{n+1}\right]=\left[P^{n}\right]+\Delta P$$

eqn. 6.44

The process of creating F' and solving the equation containing F' is repeated until the condition of eqn. 6.42 is approximated to the desired level of accuracy.

For a seal, the region of unknown can be represented by a sector of seal face geometry representing one period only. The period would include at least one spiral groove and one land. The nodes on the outside radius R_o of the sector would have a known pressure Po, the gas pressure being sealed. The nodes on the inner radii R_i will also have a known pressure in the form of the atmospheric pressure P_i. The nodes at i=1 and i=max are the same nodes, bearing in mind that we are modelling one period. This periodic condition is required for a solution around the entire seal, or for modelling just one period of the same seal.

The matrix F' is made up of partial derivatives of $F_{i,j}$, with respect to each of the pressures $P_{i,j}$.

$$\left[F'_{i,j}\right]=\begin{bmatrix}\frac{\partial F_1}{\partial P_1} & \frac{\partial F_1}{\partial P_2} & \frac{\partial F_1}{\partial P_3} & \frac{\partial F_1}{\partial P_n}\\ \frac{\partial F_2}{\partial P_1}\\ \frac{\partial F_3}{\partial P_1}\\ \frac{\partial F_n}{\partial P_1}\end{bmatrix}=\begin{bmatrix}\frac{\partial F_{i,j}}{\partial P_{i,j}} & 0\\ 0 & \end{bmatrix}$$

eqn. 6.45

Referring back to the equation (eqn. 6.36), one can see that there are five factors in the equation. Thus, only five partial derivatives would exist. Each row in the F' matrix will consist of:

$$F'_{i,j,row}=\frac{\partial F_{i,j}}{\partial P_{i-1,j}}\cdots\frac{\partial F_{i,j}}{\partial P_{i,j-1}}\cdots\frac{\partial F_{i,j}}{\partial P_{i,j}}\cdots\frac{\partial F_{i,j}}{\partial P_{i,j+1}}\cdots\frac{\partial F_{i,j}}{\partial P_{i+1,j}}$$

eqn. 6.46

All the derivatives of equation (eqn. 6.36) can be evaluated using the current estimate of the pressure. Errors will be shown on the RHS of the equation (eqn. 6.43). In the final form, equation (eqn. 6.43) will take the following matrix form:

$$\begin{bmatrix} - & - & - & - & 0 \\ - & - & - & - & - \\ - & - & \dfrac{\partial F_{i,j}}{\partial P_{i,j}} & - & - \\ - & - & - & - & - \\ 0 & - & - & - & - \end{bmatrix} \begin{bmatrix} - \\ - \\ \Delta P_{i,j} \\ - \\ - \end{bmatrix} = \begin{bmatrix} - \\ - \\ -F_{i,j} \\ - \\ - \end{bmatrix}$$

eqn. 6.47

6.3.1.2 Simultaneous solution of load equilibrium and film thickness function

The above technique was employed to solve for equilibrium load support at the seal interface, simultaneously with the interface pressure solution described above. The problem is defined by the following equations:

$$F([P], h_i) = 0$$

eqn. 6.48

$$W([P], h_i) = 0$$

eqn. 6.49

Equation (eqn. 6.48) represents non-linear pressure distributions as defined by equation (eqn. 6.36). The only key difference is the recognition that the minimum film thickness h is also a variable. Equation (eqn. 6.49) states that the load support W is a function of pressures and the minimum film thickness. The load function is given by:

$$W = W_o - W_c$$

eqn. 6.50

W_o is the force due to the fluid pressure at the interface – the seal face opening force. W_c is the closing force due to the seal pressure itself. The above equation states that for equilibrium solution, the load support function W, which is to be zeroed.

Next, one must consider the film function, and its definition of the lift groove geometry on the seal face. The algorithm has been deliberately chosen because one can use just about any film function, as long as it can be defined mathematically. This is an important point when dealing with complex lift groove geometry as encountered in the case of the slot fed logarithmic spiral seal. The film thickness distribution function can be expressed as follows:

$$h = h_i + f(r,\theta)$$

eqn. 6.51

The film thickness is allowed to vary as a function of r and θ. In the case of SFLS design, the film thickness distribution function is the mathematical definition for the spiral groove geometry (defined by eqn. 6.90).

The problem requiring a solution is fundamentally made up of equations developed earlier for pressures, plus just one more equation for the load support. That is, only one more non-linear equation has been added to the system of equations.

A trapezoidal integration technique can be used to calculate the opening force W_o, over the entire seal surface. Summing the pressures over the region does this. The following formula is employed:

$$W_o = \int_A P dA = \sum_{i=1}^{i\max-1} \left(\frac{P_{i,1} r_{i,1}}{2} + \frac{P_{i,j\max} ri, j_{\max}}{2} + \sum_{j=2}^{j\max-1} P_{i,j} r_{i,j} \right) \Delta r \Delta\theta$$

eqn. 6.52

For the equilibrium condition, the above opening force is equated to the seal closing force W_c.

Additional derivatives required are:

$$\frac{\partial F_{i,j}}{\partial h_i} = \left(P_{i-1,j} + P_{i,j}\right) \left[a_{i-1/2,j} (P_{i,j} - P_{i-1,j}) 3 h_{i-1/2,j}^2 \frac{\partial h_{i-1/2,j}}{\partial h_i} + b_{i-1/2,j} \frac{\partial h_{i-1/2,j}}{\partial h_i} \right]$$

eqn. 6.53

We also need: $\frac{\partial W}{\partial P_{i,j}} = \frac{\partial W_o}{\partial P_{i,j}}$

eqn. 6.54

From (eqn. 6.52): $\frac{\partial W_o}{\partial P_{i,j}} = r_{i,j}\Delta r\Delta\theta$

eqn. 6.55

Then to finish: $\frac{\partial W}{\partial h_i} = \frac{\partial W_o}{\partial h_i}$

eqn. 6.56

From equation (eqn. 6.52): $\left|\frac{\partial W_o}{\partial h_i}\right| P_{i,j=cons\tan t} = 0$

eqn. 6.57

The final matrix form, when applying the Newton method to equations (eqn. 6.48) and (eqn. 6.49) is as follows:

$$\begin{bmatrix} & 0 & \\ \frac{\partial F_{i,j}}{\partial P_{i,j}} & & [\frac{\partial F_{i,j}}{\partial h_i}] \\ 0 & & \\ [\frac{\partial W}{\partial P_{i,j}} & & \frac{\partial W}{\partial h_i}] \end{bmatrix} \begin{bmatrix} \Delta P_{i,j} \\ \Delta h_i \end{bmatrix} = \begin{bmatrix} F_{i,j} \\ W \end{bmatrix}$$

eqn. 6.58

A Gaussian elimination technique can be applied to the matrix to obtain a solution.

6.3.2 Modelling the slot feed gas supply to the seal interface.

The Newton's method described above formed a good foundation for the analytical model of the seal. However, further original development was necessary in order to produce an effective and comprehensive model for the novel design in question.

The feed slots at the back of the seat and the feed hole supply had to be modelled effectively. After detailed consideration, it was decided that the most effective means of doing this would be to model them in the form of an additional mass flow source within the model grid. The SFLS model incorporates this mass flow source by positioning it at the nearest node in the grid of the modelled sector. For fixing the radial position of the feed orifice, the computer model has a built-in routine that automatically assigns the orifice to the nearest grid node. The radial mesh density

from R_i to R_o is 40. It has been established that in practical terms, this mesh density is adequate enough to place the node in a position that would be within the best manufacturing tolerance achievable. Circumferentially, the feed orifice is positioned in the middle of the modelled sector. Figure 63 shows the modelling of the additional mass flow source.

The mass flow rate through the orifice is governed by the geometry of the feed slots and their radial position relative to the seal faces. The relationship for the mass flow rate through the orifice has already been derived in Chapter 5.4, dealing with the slot feed design. These were incorporated into the new seal model and are simply repeated here for clarity:

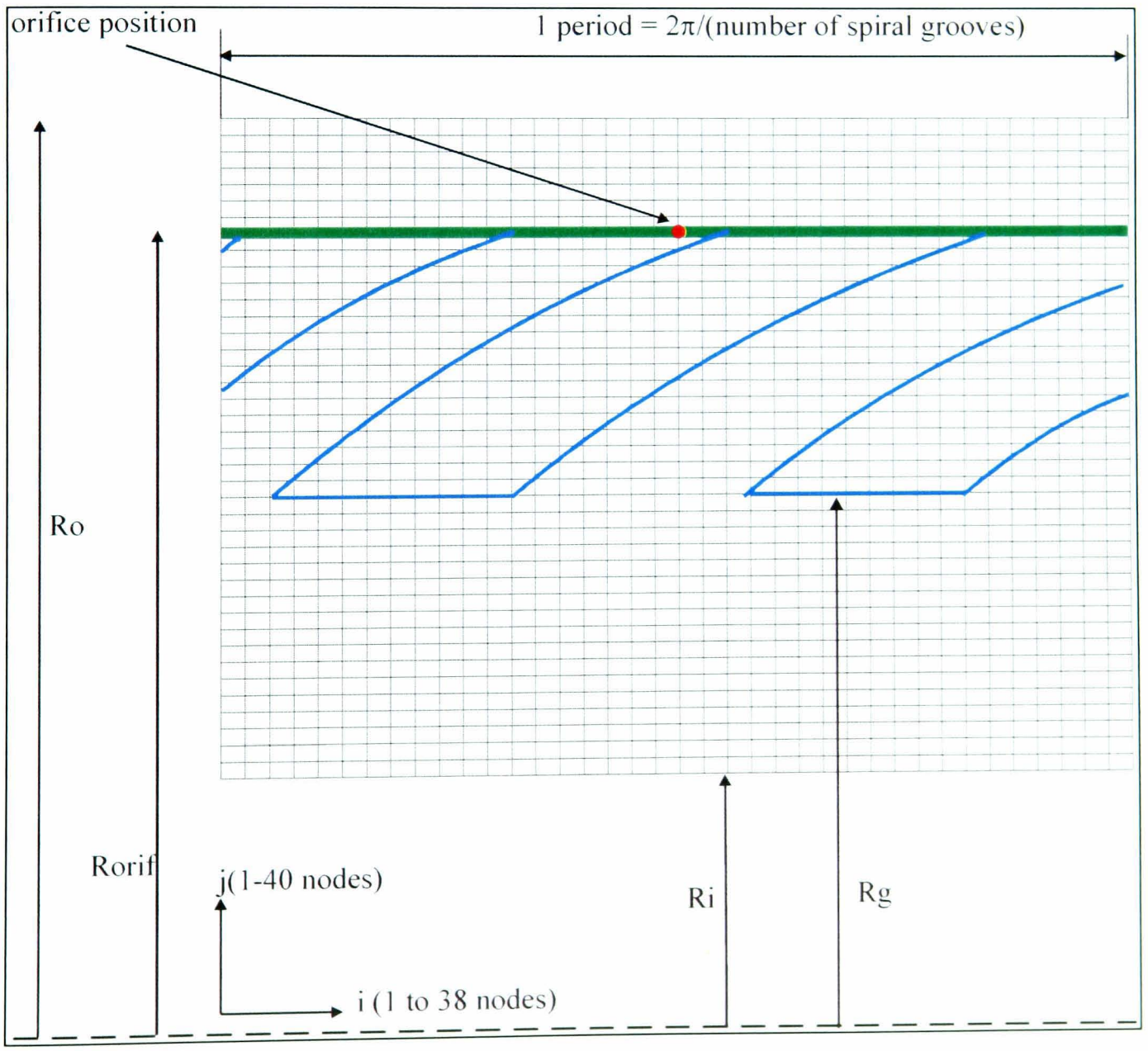

Figure 63: Modelling the slot feed gas supply as an additional mass flow term

Mass flow through the feed orifice, derived earlier and is given by eqn. 5.73. It has been rewritten in terms of the R_o, P_o, R_{orif} and P_{orif} notations for the SFLS seal:

$$\dot{m}_{orif} = \frac{SD}{360} \cdot \frac{\pi H^3}{12\mu R_{gas} T \ln(R_o / R_{orif})} \left[P_{orif}^2 Z(5) - P_o^2 Z(6) \right]$$

eqn. 6.59

The total arc subtended by the N number of feed slots is given by:

$$SD = 2\tan^{-1}\left(\frac{W_{slot}}{2R_{orif}}\right)\frac{N_{slots}}{2\pi}$$

eqn. 6.60

Note that P_{orif} is the calculated pressure at the interface of the two seal faces in the vicinity of the feed orifice. It is assumed that the orifice pressure P_{orif} is uniformly distributed along the whole of the front circumferential distribution groove.

The computer model fixes the location of the feed orifice in the grid. For the control volume containing the feed orifice, the additional mass flow represented by **eqn. 6.59** rate entering is added to the net mass flow eqn. 6.36, producing the following equation:

$$F[p] = F_{i,j} = F_{i,j} + \dot{m}_{orif}$$

eqn. 6.61

The calculation then takes its normal form. At every iteration step, the orifice mass flow is recalculated based on the current value of $P_{i,j}$. and added to the overall mass flow rate leaving the gas seal.

6.4 BASIC DESCRIPTION OF THE SLOT FED LOGARITHMIC SPIRAL SEAL (SFLS) PERFORMANCE ANALYSIS.

The suite of software and the architecture covered by the specification was developed for performance analysis, design and optimisation of the SFLS dry gas seal concept. The package, or 'suite' is made up of the following modules driven by one 'engine'.

- External input and output data files (for user manipulation/interrogation).

- Internal data transfer files between respective solver modules.
- Real gas properties database (user activated and generated by an external program).
- SFLS fluid film model to compute compressible gas flow, gap and pressure profiles,
- Integral modules to calculate seal interface power generation and the surface heat transfer coefficients.
- Structural finite element model utilising a propriety FE analysis solver (ANSYS [1]).
- Customised macro 'engine' running the whole suite of modules.

The SFLS model is fully coupled between the fluid film model element and the structural analysis of the seal parts. The model iterates to an equilibrium solution of seal face angle for a given seal geometry and operating conditions.

6.4.1 Model operation

The SFLS model consists of a rotating mating ring and a stationary primary ring, modelled across a predetermined 2-D symmetrical sector, as depicted in Figure 64.

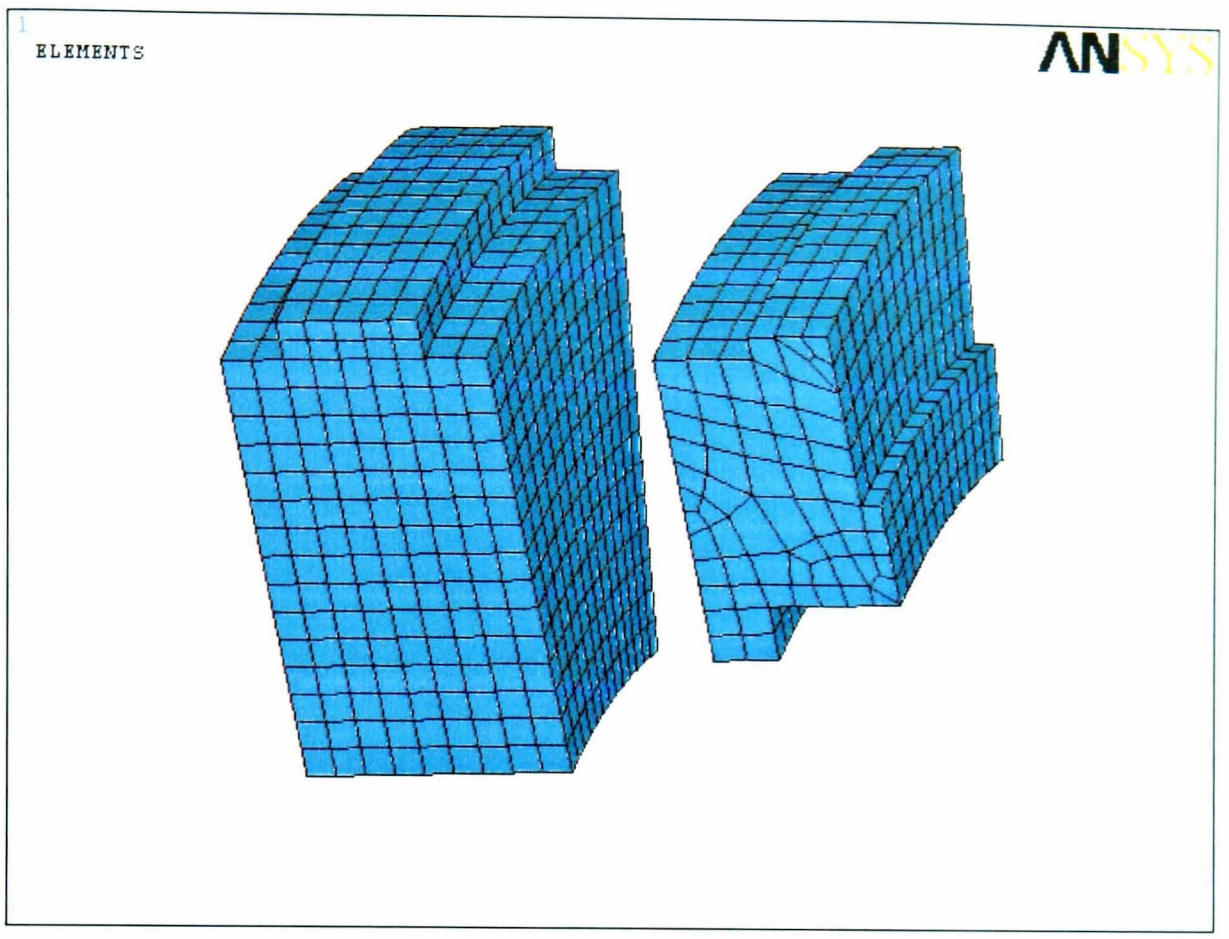

Figure 64: Modelling the seal parts

In the first instance, the seal model is defined using data contained in the input file. The fluid film solver makes a first pass at a solution of the fluid film parameters: the fluid pressure distribution, the operating gap, leakage and the angle between the two faces. It also calculates the heat fluxes and the heat transfer coefficients. The structural model then fully uses relevant data from the input files and the above-mentioned calculated values, added to it. The structural part of the solution is then obtained from the Ansys FE solver, the results of which are then fed back into the fluid film model.

The modelling process is designed to iterate between the fluid and the structural models and their respective solvers, until a predetermined convergence level is achieved for the seal gap angle between two consequent solutions runs. Once this point is reached, the model is considered to have converged and the analysis ends. A flow chart for the model solution describing all of the above is shown in Figure 65.

6.4.2 Model inputs

- External seal geometry (user defined).

- Lift geometry (user defined).
- Operating pressure (user defined).
- Rotational speed (user defined).
- Bulk gas temperature (user defined).
- Real gas properties (user defined and calculated).
- Surface heat transfer coefficients and their distributions across the geometry.
- Heat fluxes and their distributions across the geometry.
- Primary and mating ring material properties (user defined).
- Axial constraints and positions (user defined)
- Any other required external forces (user defined).

All of the above reside within user defined input files

6.4.3 Model outputs

- Pressure profile distribution.
- Operating gap distribution.
- Gas leakage
- Other gas film properties
- Constraint reaction loads
- Temperature distribution
- Principal and equivalent stresses
- Principal and equivalent strains, and strain energy
- Component displacements
- Scope to interrogate specific model locations
- The program has a built in algorithm that automatically assigns the orifice position to the nearest node in the grid. The assignment is carried out as per Figure 63.

6.4.4 Slot Feed Logarithmic Spiral SFLS computer model flow chart

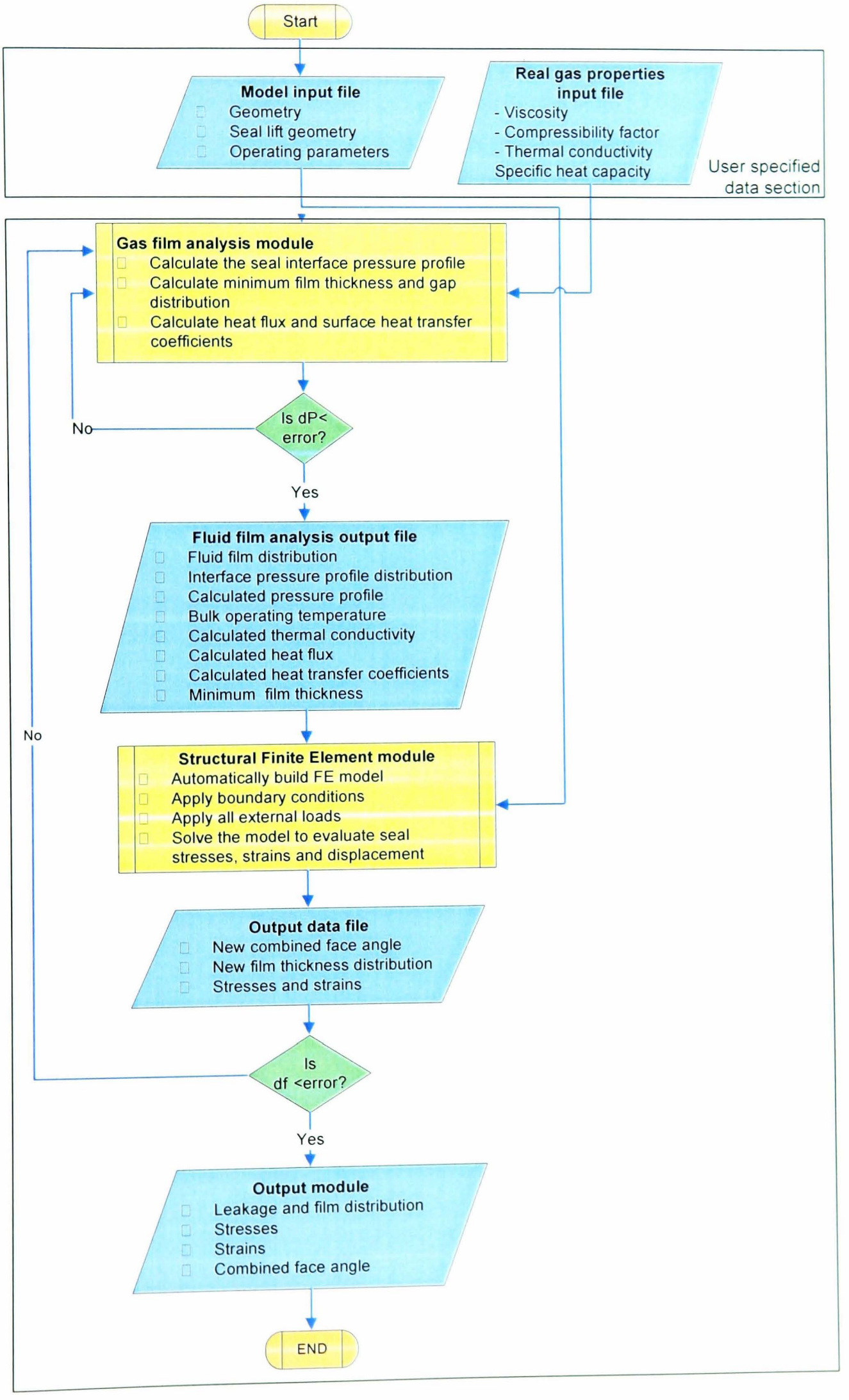

Figure 65: Slot Feed Logarithmic Spiral (SFLS) computer model flow chart

6.4.5 Modelling the surface heat transfer coefficients

After the heat has been conducted away from the running surfaces of the seal through the faces, convection heat transfer to fluid surrounding the seal parts removes most of that heat. The basic heat transfer takes place irrespective of how the surrounding fluid is cooled. The value of the convective coefficient is just as equal as the thermal conductivity of the seal parts themselves. Fortunately, the latter values are easily available. For most seal components the flow created by rotation is turbulent, although the flow along the actual primary seal zone may indeed be laminar if the gap is small, the pressure ratio is high. The convection due to rotation predominates over that due to axial fluid velocity within the seal cavity. The most comparable scenario for a radial contacting seal would be the case of a cylinder rotating in either an annulus or an unbounded fluid body. The corresponding convection coefficient is the most appropriate to represent the seal geometry in question. One of the most useful and relevant studies undertaken in this area has been by Becker [4]. Becker performed a number of experiments on small diameter cylinders in water. The resultant formula for the Nusselt number that best fits the Becker derived data is:

$$Nu_D = 0.133 \mathrm{Re}^{0.667} \mathrm{Pr}^{0.333}$$

eqn. 6.62

The Prandtl number, defined as the ratio of fluid properties controlling the velocity and temperature distributions is given by:

$$\mathrm{Pr} = \frac{\mu Cp}{K}$$

eqn. 6.63

the Reynolds number is given by:

$$\mathrm{Re}_D = \frac{\rho UD}{\mu}$$

eqn. 6.64

In the above equation, U is the tangential velocity of the rotating disk/ring and D is the ring diameter. Becker [4] found that his results agreed with a number of other

investigators. The most important of these was the work undertaken by Kays and Bjorkland [15], who actually carried out their experiments on air. The Nusselt Number formula that fits their data most closely is given by:

$$Nu_D = 0.107\,\mathrm{Re}^{0.667}\,\mathrm{Pr}^{0.333}$$

eqn. 6.65

It can be seen that it closely matches Becker's formula. More recently, validation exercises carried out by Lebeck [21], gives further support for using the above Nusselt number formulations in seal work. However, the formulation is not without its limitations. But as far as the current state of knowledge, they are the most appropriate at this moment in time.

So taking the Nusselt number relationship and from it calculating the surface heat transfer coefficient:

$$\alpha_{all} = \frac{Nu_D K}{2R_o}$$

eqn. 6.66

The maximum convection coefficient will be applied to the regions of the seal containing high velocity gas flow. In stagnant regions of the seal, as highlighted by the blue boundaries in Figure 66, the surface heat transfer coefficient is taken to be 10% of the calculated overall surface heat transfer coefficient.

Thus:

$$\alpha_{high} = \frac{Nu_D K}{2R_o}$$

eqn. 6.67

$$\alpha_{low} = 0.1\frac{Nu_D K}{2R_o}$$

eqn. 6.68

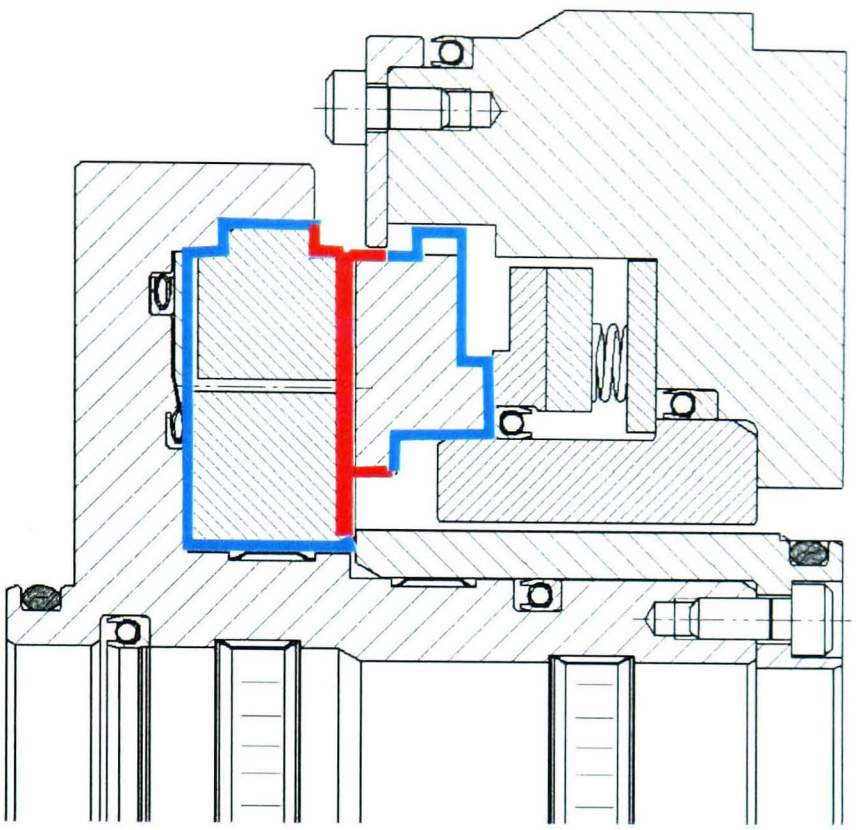

Figure 66: Cross section of a gas seal showing zones of maximum and minimum surface heat transfer coefficients

6.4.6 Modelling power generation at the interface.

The power generated at the interface of the primary seal zone will be modelled as a heat flux applied to the seal interface.

It is assumed all of this power will be converted to heat and will be imparted and absorbed by the adjacent seal parts, taking into account the overall heat transfer coefficient calculated earlier. Newton (1642 – 1727) postulated that for straight parallel motion of a given fluid, the tangential stress between the two adjacent surfaces is proportional to the velocity gradient in a direction perpendicular to the layers. That is:

$$\tau = \mu \frac{\partial u}{\partial y}$$

eqn. 6.69

Stress at a radius R is:

$$\tau = \mu \frac{\omega R}{h}$$

eqn. 6.70

Torque on annulus is given by:

$$T_r = \mu \frac{\omega r}{h} (2\pi R dR) R$$

eqn. 6.71

Power is given by: $P_{\text{int}\,erface} = T_r \omega$

eqn. 6.72

Substituting for torque and integrating with respect to r gives:

$$P_{\text{int}\,erface} = \frac{2\pi\mu\omega^2}{h} \int_{Ri}^{Ro} R^3 dR$$

eqn. 6.73

$$P_{\text{int}\,erface} = \frac{\pi\mu\omega^2 (R_o^4 - R_i^4)}{2h}$$

eqn. 6.74

The resultant heat flux will be given by:

$$H_{flux} = \frac{P_{\text{int}\,erface}}{\pi (R_o^2 - R_i^2)}$$

eqn. 6.75

In the SFLS coupled field model, the heat flux is calculated in the fluid film module and applied uniformly to the two seal faces in the ANSYS structural model as shown in Figure 67.

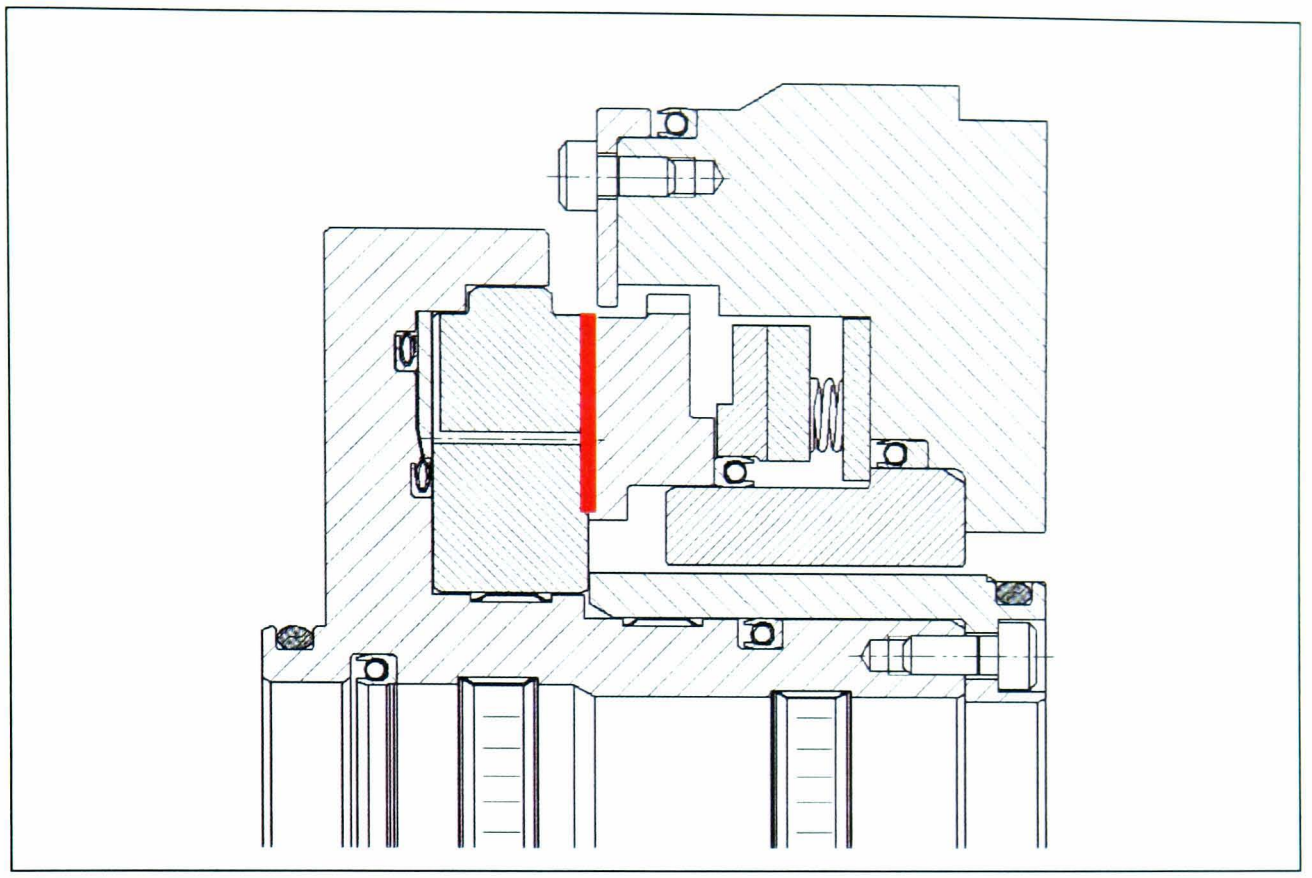

Figure 67:Heat flux boundary condition applied to the finite element seal model

6.4.7 Modelling the real gas properties

For ideal gases it is known that the P-v-T behaviour at low pressures and hence densities is closely given by the following equation of state:

$$P\bar{v} = \bar{R}_{gas}T$$

eqn. 6.76

Where R is the universal gas constant.

Gases operating at low densities closely follow well-known Boyle's and Charles Laws, or rather not laws but observations. The equation of state given above represents the ideal equation of state. However, at higher densities, the behaviour will deviate considerably from the ideal equation of state. The use of the actual density associated with the duty conditions of the gas takers account of the actual density.

Due to its simplicity, the ideal gas equation of state is very convenient to use in thermodynamic calculations. However, in the case of the gas seals, the gas pressures and hence their individual values vary significantly, particularly when operating at

higher pressures as is the case here, where the sealing pressure is up to and including 300 bar.

In these pressure ranges, it is expected that the gas will deviate considerably from the ideal gas behaviour. To take account of this in the model, one has to introduce and utilise the concept of compressibility factor Z_{gas}. The concept of gas compressibility is defined as:

$$Z_{gas} = \frac{P\bar{v}}{\bar{R}_{gas}T}$$

eqn. 6.77

Or $$P\bar{v} = Z_{gas}\bar{R}_{gass}T$$

eqn. 6.78

For an ideal gas, Z_{gas}=1 and the deviation from this value is a measure of deviation of the actual relation from the ideal gas equation of state. Thus, the previously mentioned equations for mass flow and gas densities across the control volume now becomes as follows:

The equation for gas density (eqn. 6.24) now modified for real gas compressibility factor will be:

$$\rho = \frac{P}{Z_{gas}R_{gas}T}$$

eqn. 6.79

The resultant revised density equation at the control volume edge (originally defined by eqn. 6.25) and now taking into account the gas compressibility factor will be:

$$\rho_{i-1/2,j} = \frac{\rho_{i,j} + \rho_{i-1,j}}{2} = \frac{P_{i,j} + P_{i-1,j}}{2Z_{gas}R_{gas}T}$$

eqn. 6.80

Substituting eqn. 6.79, eqn. 6.80 and eqn. 6.23 into the mass flow rate equation originally defined by eqn. 6.22, will produce the modified mass flow rate equation, which takes account of the compressibility factor Z_{gas}, it will be defined as follows:

$$\dot{m}_{\theta,i-1/2,j} = \frac{P_{i,j} + P_{i-1,j}}{2Z_{gas}R_{gas}T}\left[\frac{-h^3{}_{i-1/2,j}}{12\mu r_{i,j}}\left(\frac{P_{i,j} - P_{i-1,j}}{\partial\theta}\right) + \frac{r_{i,j}\omega h_{i-1/2,j}}{2}\right]\partial r$$

eqn. 6.81

Similarly for the other 3 sides of the control volume: Resultant mass flow rate through the second side of the control volume will be:

$$\dot{m}_{\theta,i+1/2,j} = \frac{P_{i,j} + P_{i+1,j}}{2Z_{gas}R_{gas}T}\left[\frac{-h^3{}_{i+1/2,j}}{12\mu r_{i,j}}\left(\frac{P_{i,j} - P_{i+1,j}}{\partial\theta}\right) + \frac{r_{i,j}\omega h_{i+1/2,j}}{2}\right]\partial r$$

eqn. 6.82

Mass flow rate across the 3rd side of the control volume will be:

$$\dot{m}_{\theta,i+1/2,j} = \left(\frac{P_{i,j-1} + P_{i,j}}{2Z_{gas}R_{gas}T}\right)\left[\frac{h^3{}_{i,j-1/2}}{12\mu}\left(\frac{P_{i,j-1} - P_{i,j}}{\partial r}\right)\right]\partial\theta$$

eqn. 6.83

Finally, for the 4th side of the control volume the mass flow rate will be:

$$\dot{m}_{\theta,i+1/2,j} = \left(\frac{P_{i,j+1} + P_{i,j}}{2Z_{gas}R_{gas}T}\right)\left[\frac{h^3{}_{i,j+1/2}}{12\mu}\left(\frac{P_{i,j+1} - P_{i,j}}{\partial r}\right)\right]\partial\theta$$

eqn. 6.84

Finally, modifying equations for coefficient 'a' and 'b' to include the compressibility factor Z:

$$a_{i-1/2,j} = a_{i+1/2,j} = -\frac{1}{2Z_{gas}R_{gas}T}\frac{1}{12\mu r_{i,j}}\frac{\Delta r}{\Delta\theta}$$

eqn. 6.85

$$b_{i-1/2,j} = b_{i+1/2,j} = -\frac{1}{2Z_{gas}R_{gas}T}\frac{r_{i,j}\omega}{2}\Delta r$$

eqn. 6.86

$$a_{i,j-1/2} = -\frac{1}{2Z_{gas}R_{gas}T}\frac{1}{12\mu}\left(r_{i,j} - \frac{\Delta r}{2}\right)\frac{\Delta\theta}{\Delta r}$$

eqn. 6.87

$$a_{i,j+1/2} = -\frac{1}{2Z_{gas}R_{gas}T}\frac{1}{12\mu}\left(r_{i,j}+\frac{\Delta r}{2}\right)\frac{\Delta\theta}{\Delta r}$$

eqn. 6.88

The compressibility factor Z_{gas} will be read in from an external file. The external file is created for a given gas using proprietary real gas properties generation software, such as PPDS from the National Engineering Laboratory. The SFLS fluid film model then interrogates the array and extracts the relevant compressibility factor appropriate to the modelled operating conditions.

The mass flow equation through the feed slots and the orifice, as defined by **eqn. 6.59** will be modified in a similar way, a shown below:

$$\dot{m}_{orif} = \frac{SD}{360}\cdot\frac{\pi H^3}{12\mu R_{gas}TZ_{gas}\ln(R_o/R_{orif})}\left[P_{i,j}^2Z(5)-P_3^2Z(6)\right]$$

eqn. 6.89

The other real gas properties used in the analysis include: the gas viscosity μ, thermal conductivity K, specific heat capacity at constant pressure, C_p, specific heat capacity and constant volume C_v. Unlike in the case of compressibility factor Z_{gas} property, the equations defining the flow field do not need further modification, and the extracted real gas properties can be used directly.

For each one of these properties, a table array is created using the PPDS2 gas gas properties database. The SFLS model then interrogates that array and extracts the correct values appropriate to the modelled operating conditions of the seals.

6.4.8 Modelling the logarithmic spiral

One of the benefits of the spiral groove is its ability to pump either with or against an established pressure gradient across the seal. The proposed geometry of the modified spiral groove for the SFLS concept is shown in Figure 68. The groove geometry consists of a series of periodic recesses (grooves) cut into the seal face. Their profile is logarithmic. Each groove is periodic with an adjacent land – the ungrooved part of the seal face. Thus the total geometry consists of a series of alternating grooves and lands around the circumference of the seal face. The angles of the grooves and lands relative to the seal face tangent produce a pumping flow into the grooves, when the

seal face rotates in the direction of the opening grooves. This flow is used to produce pressure between the seal faces, which in turn can support load. The grooves pump the gas against a dam, a completely ungrooved region of the seal below the spiral grooves. The dam acts as a restriction to leakage flow from the outer to the inner radius, despite the pumping effect of the grooves. A seal fitted with spiral grooves can be used in two ways. Only the one way will be considered here, one that is deemed to be most effective for a seal having a positive pressure gradient from the outer to theinner radii of the seal. This is shown in Figure 68, where $P_o > P_i$ from R_o to R_i. The grooves are positioned at angles to assist the leakage, thus making the seal inward pumping. The grooves pump the fluid from a higher to a lower pressure side of the seal until that fluid flow comes against the dam at the inner periphery of the seal. This has the effect of increasing the pressure in the seal. This pressure should be greater than would be due to the hydrostatic pressure drop alone. Thus should increase the load carrying capacity of the seal, resulting in better fluid film stiffness.

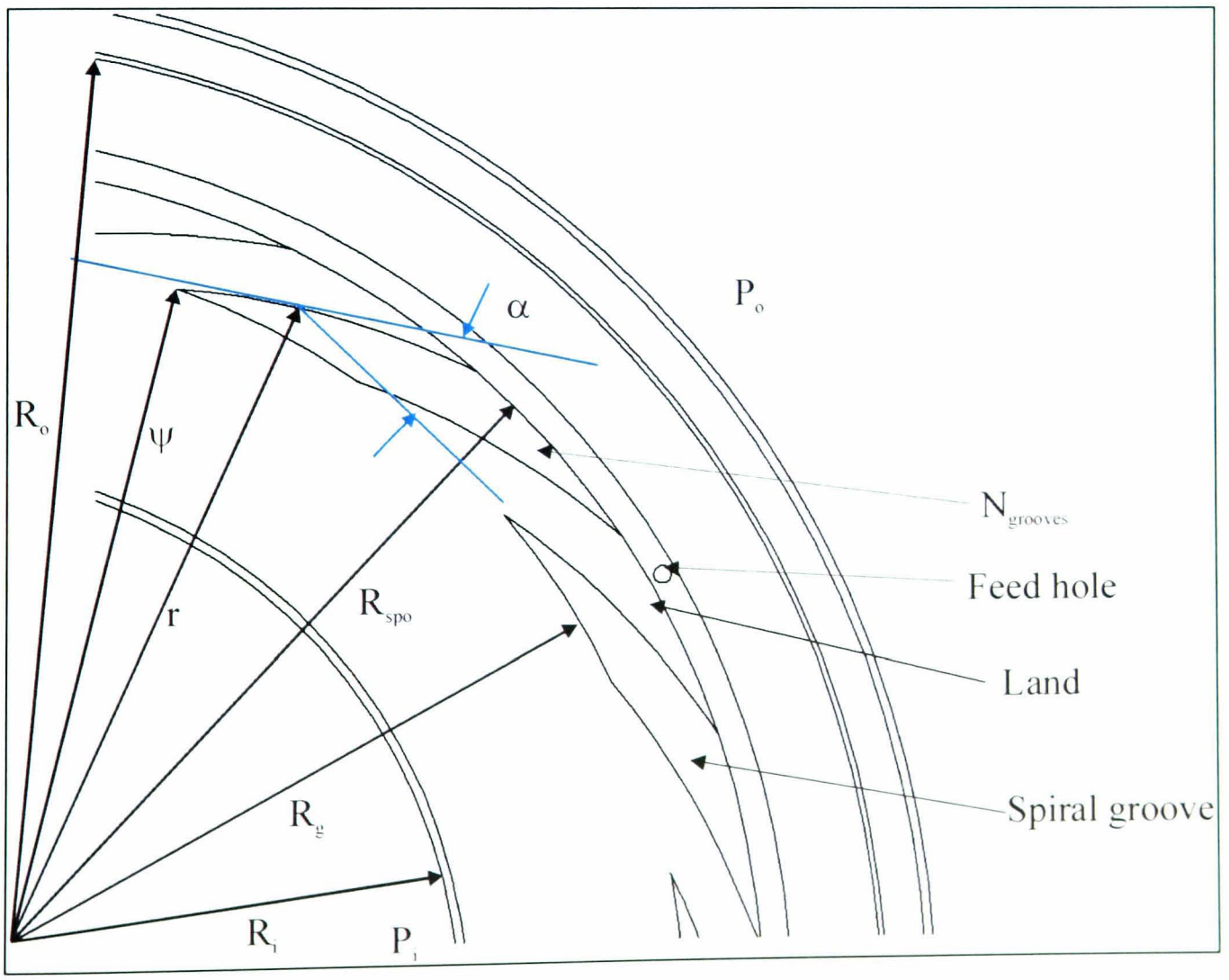

Figure 68: Modified logarithmic spiral groove geometry used in the SFLS concept

As shown in Figure 68, the defining parameters are radii are R_o, R_i and R_g, the outer, the inner and the dam radii of the seal respectively and R_g defines the start of the dam. It is taken that $P_o > P_i$ and the seal rotates in such a way as to draw the gas into the grooves and hence create an inward pumping effect. The grooves have a uniform depth h_g,

Muijderman [22] proposed that a spiral groove, which gives a constant tangent angle, is in effect a logarithmic spiral. With reference to the same figure, a formula defining the spiral groove geometry is given by:

$$r = r_g e^{\psi \tan \alpha}$$

eqn. 6.90

In the above equation Ψ is the angular co-ordinate and r is the radial co-ordinate of the groove boundary and r_g is the inner radius of the spiral grooves. Finally, α defines the spiral groove angle.

The ratio of the spiral groove to land width has a significant effect on performance and is defined by:

$$\gamma = \frac{w_{land}}{w_{grove}}$$

eqn. 6.91

6.4.9 Further improvements to model accuracy

Analysis thus far only takes account of laminar flow. One should bear in mind three other factors, which will affect the model accuracy. They are as follows:

- Firstly one should consider the effect of entrance (contraction losses) at the inlet to the seal. For this, the loss coefficients theory as developed by Zuk [42] was deemed to be most relevant.
- Secondly, it was felt important to consider the effect choked flow at the seal discharge, as discussed by Lebeck [21]. This consideration deemed to be particularly important in this model, given the very high sealing pressures under evaluation.

- Thirdly, a consideration had to be made for the spiral groove pattern end effects. This work was originally developed for spiral groove bearings by Muijderman [22].

- Fourthly one had to consider the possibility of a turbulent regime in the seal interface, as discussed by Shapiro et al.[33]. In the first instance, the SFLS model was used to establish whether the seals indeed experienced turbulent flow.

On this subject, Lebeck [21] also postulated that if the flow in the seal did become turbulent, the leakage flow rate predicted by the laminar theory, would become more erroneous. The laminar theory would tend to over predict the seal leakage. Further more, it has been hypothesised by the same reference that the effects of choked flow and the entrance loss would significantly alter the shape of the opening pressure profile. This would alter the effect of the load support, by as much as 5-10%, but it would also alter the moment produced by the pressure distribution. This in turn would affect the amount by which the seal faces would rotate under the effect of that altered pressure distribution.

6.4.10 Modelling the effects of the entrance losses

Modelling the entrance losses is important because in the case of a high-pressure gas seal, they will be quite significant. They are hence deemed to be important to the ability of the model to predict a more accurate result. The entrance flow region can be assumed to be isentropic and adiabatic. Since real entrance losses are not isentropic because of viscous friction, turning losses and so forth, the entrance loss is accounted for by introducing an empirically determined entrance velocity loss coefficient CL into the isentropic flow equations. The resulting equations for entrance pressure and temperature are:

Revised pressure given the calculated entrance loss:

$$P_{oeff} = \frac{P_o}{\left[1 + \frac{(\gamma_{gas} - 1)M^2}{2C_L^2}\right]^{\frac{\gamma_{gas}}{\gamma_{gas}-1}}}$$

eqn. 6.92

And the revised temperature given the loss coefficient:

$$T_{oeff} = \frac{T_o}{\left[1 + \frac{(\gamma_{gas} - 1)M^2}{2C_L^2}\right]}$$

eqn. 6.93

Zuk [43] claimed excellent agreement with experiment for compressible flow when the entrance loss coefficient C_L of 0.6 was used. Lebeck [21], utilised the same figures, also citing good correlation with experimental data at similar duties to Zuk.

6.4.11 Modelling the effects of sonic discharge at the seal exit – choked flow.

One can expect three types of flow in a gas seal

- Firstly, one can have sub-critical flow. In this case, the velocity through the seal will be subsonic along the entire seal zone.
- The second case is that of critical flow. Here, the velocity at the seal exit is sonic and the pressure at the throat of the seal zone discharge is just equal to the downstream seal pressure (normally atmospheric).
- The third case is that of supercritical flow. Here the exit velocity is also sonic as in the second case. But the pressure at the throat of the seal zone discharge is greater than the downstream pressure, which is normally atmospheric.

While modelling choked flow, one has assumed that the flow is adiabatic. Given the high velocity flow rates associated with choked flow and turbulence, there would be little opportunity for heat to flow into the gas.

In the SFLS computer model, a dedicated subroutine carries out a check to establish if the exit velocity is choked (Mach number =1) during the first iteration pass. If the flow is choked, it then makes the necessary adjustment to the discharge pressure P* which will then be greater than the atmospheric pressure Pi. The methodology is described in detail below:

After the first pass at calculating the pressure profile a check is be made to establish whether the flow at seal exit is sonic. This is achieved as follows:

Sonic flow is given by: $v_{sonic} = \sqrt{\gamma_{gas} R_{gas} T_{gas}}$

eqn. 6.94

First estimate of velocity at the seal exit is taken from the calculated seal exit mass flow rate:

$$\dot{m}_i = \rho_i u_i A_i$$

eqn. 6.95

Where the cross sectional area of the seal exit is defined by:

$$A_i = 2\pi R_i h_i$$

eqn. 6.96

Substituting for A_i into eqn. 6.95 and rearranging in terms of u_i:

$$u_i = \frac{\dot{m}_i}{\rho_i 2\pi R_i h_i}$$

eqn. 6.97

If $u_i > v_{sonic}$, then the flow is choked. If this is the case, a new corresponding gas density is found from the conservation of mass equation:

$$\rho_* u_* = \rho_i u_i$$

eqn. 6.98

Thus: $\rho^* = \frac{\rho_i u_i}{u^*}$

eqn. 6.99

The estimate of revised discharge pressure based on choked flow can be established from the ideal gas equation. It should be noted that the rest of the model assumes real gas behaviour.

$$P^* = \rho^* R_{gas} T_{gas} Z_{gas}$$

eqn. 6.100

The above pressure will be the initial guess value. From the point of view of the SFLS computer model, newly calculated seal exit pressure P^* will become the new boundary condition. The model will be solved again with this revised boundary condition, for equilibrium in the fluid film. Figure 69 shows the effect of choked flow on the pressure profile in the seal interface. It will have a significant effect on both the predicted seal leakage as well as the equilibrium face angle.

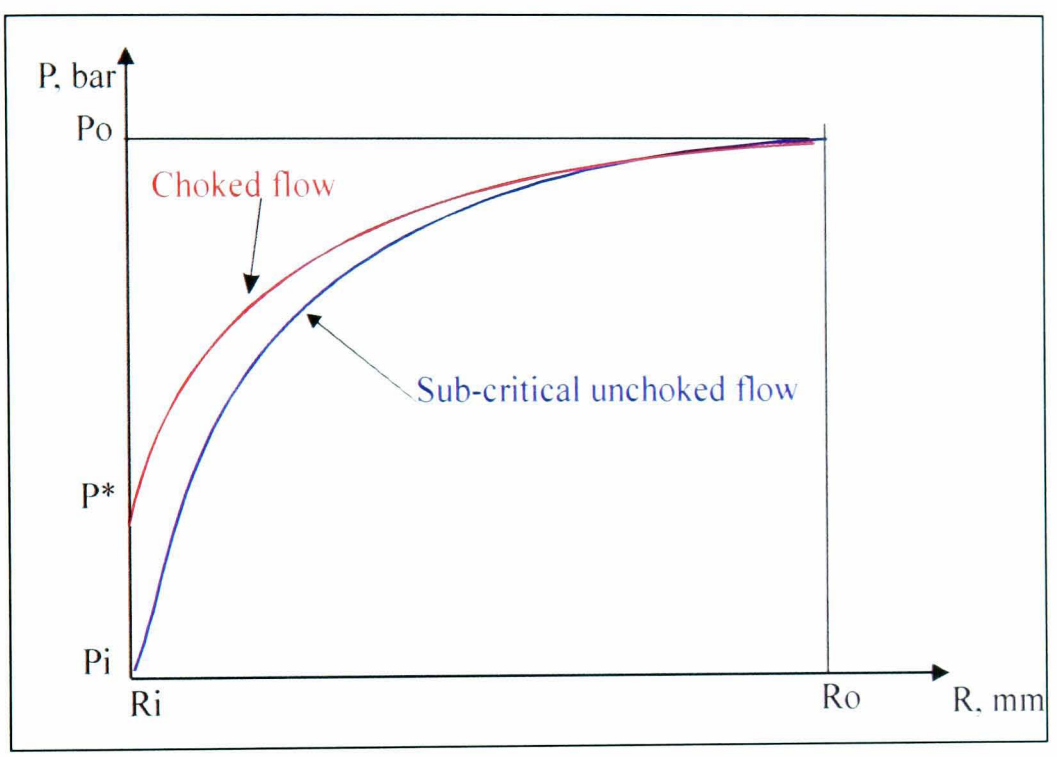

Figure 69: Effect of choked flow on opening pressure profile

6.4.12 Modelling the spiral groove pattern end effect

Muijderman [22], first developed the theory for the definition of end effects associated with the spiral groove pattern geometry in spiral groove bearings. Given the nature of the SFLS lift geometry, spiral groove end effect theory has been built into the SFLS computer model.

Spiral groove end effects can be applied to both the start and the finish of the spiral groove. In essence, the theory states that the start and end points of the spiral groove in terms of when the pressure starts to be generated and when the effect of the groove stops, do not coincide with the actual geometric start and finish points of the groove. Instead, there would be an effective outer radius of the groove and an effective inner radius of the groove. Firstly, both of the end effects will be defined here. Later on an explanation will be given for which one was actually applied in the model and why. The ratio between the 'effective' outer radius $R_{o,eff}$ and the actual radius R_o is given by the following relationship.

$$R_{o,eff} = R_o \exp\left[-\frac{\pi}{2N_{grooves}}\left(1-\frac{\alpha}{90}\right)\tan\alpha\,\frac{2}{1+\gamma}\,\frac{1-H_{3r}^3}{1+H_r^3}\,Fr\right]$$

eqn. 6.101

and

$$R_{g,eff} = R_g \exp\left[-\frac{\pi}{2N_{grooves}}\left(1-\frac{\alpha}{90}\right)\tan\alpha\,\frac{2}{1+\gamma}\,\frac{1-H_r^3}{1+H_r^3}\,Fr\right]$$

eqn. 6.102

Correction for the outer end effect basically states that the pressure build-up in the groove begins at the R_{oeff} and not R_o. Similarly correction for the inner end effect states that the pressure build-up stops at an effective inner radius $R_{g,eff}$ and not R_g, as given by eqn. 6.102.

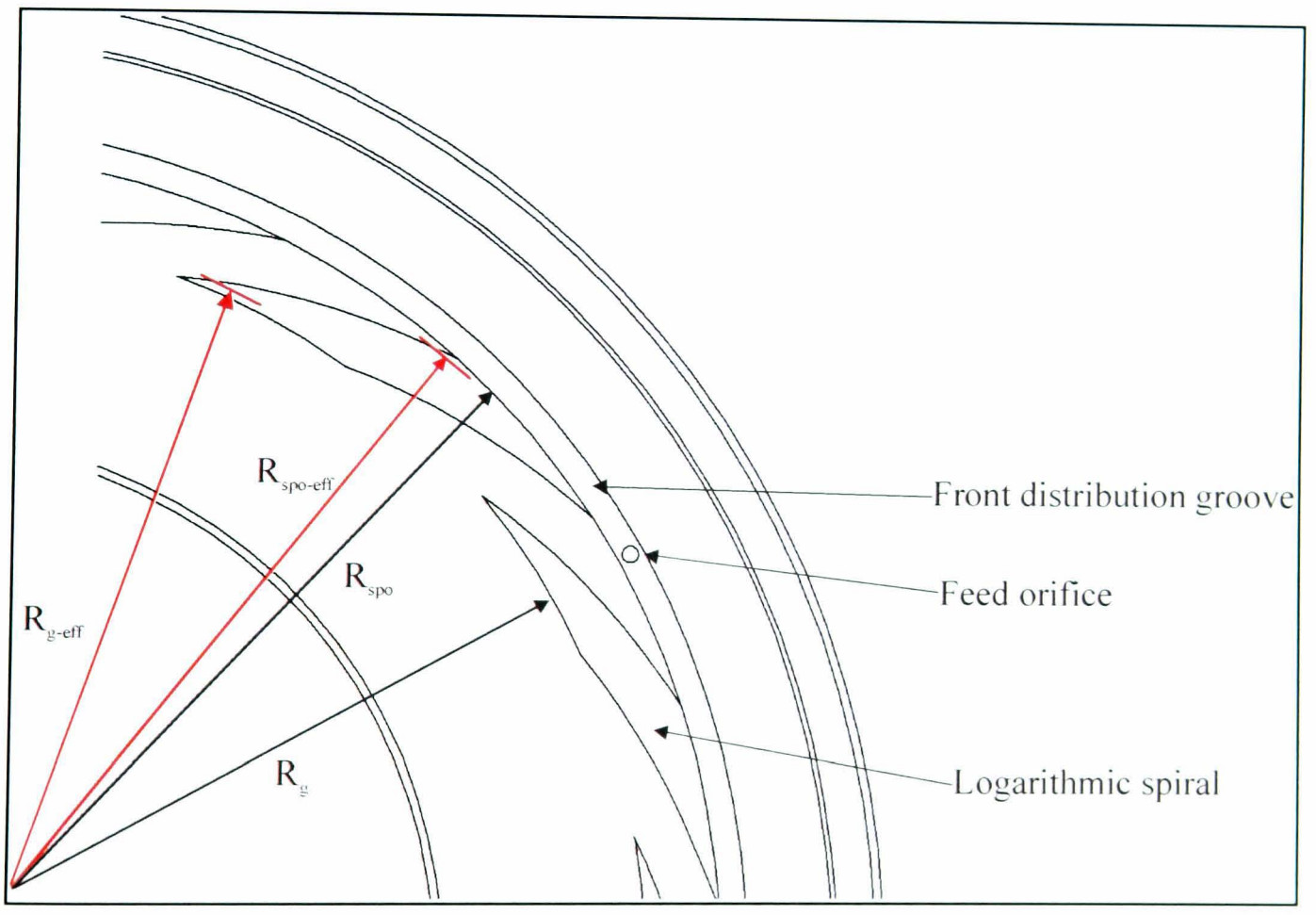

Figure 70: Spiral groove end effect corrections.

Also where:

$$Fr = \frac{A_1 \cot\alpha}{A_1 \cot\alpha + C_1}$$

eqn. 6.103

Where geometry factors A_1 and C_1 are defined as:

$$A_1 = -\gamma(1 - H_r)(1 + \gamma H_r^{\,3}) + S\gamma\cot\alpha(1 - H_r^{\,3})$$

eqn. 6.104

$$C_1 = \gamma H_r^{\,3}\cot\alpha(1+\gamma)(1 - H_r) + S(\gamma + H_r^{\,3} + H_r^{\,3}\cot^2\alpha(1+\gamma))$$

eqn. 6.105

Finally, the S-factor is given by:

$$S = \frac{-2\dot{m}_i(1+\gamma)}{R_o\omega h_1 \rho 2\pi R_o} = \frac{-\dot{m}_i(1+\gamma)}{\pi R_o^2 \omega h_1 \rho(R_o)}$$

eqn. 6.106

Where $\rho(R_o)$ is the gas density at the outer seal radius R_o.

Groove depth relationship in the above formula is defined by:

$$H_r = \frac{h_2}{h_1}$$

eqn. 6.107

where:

$$h_1 = h_2 + h_g$$

eqn. 6.108

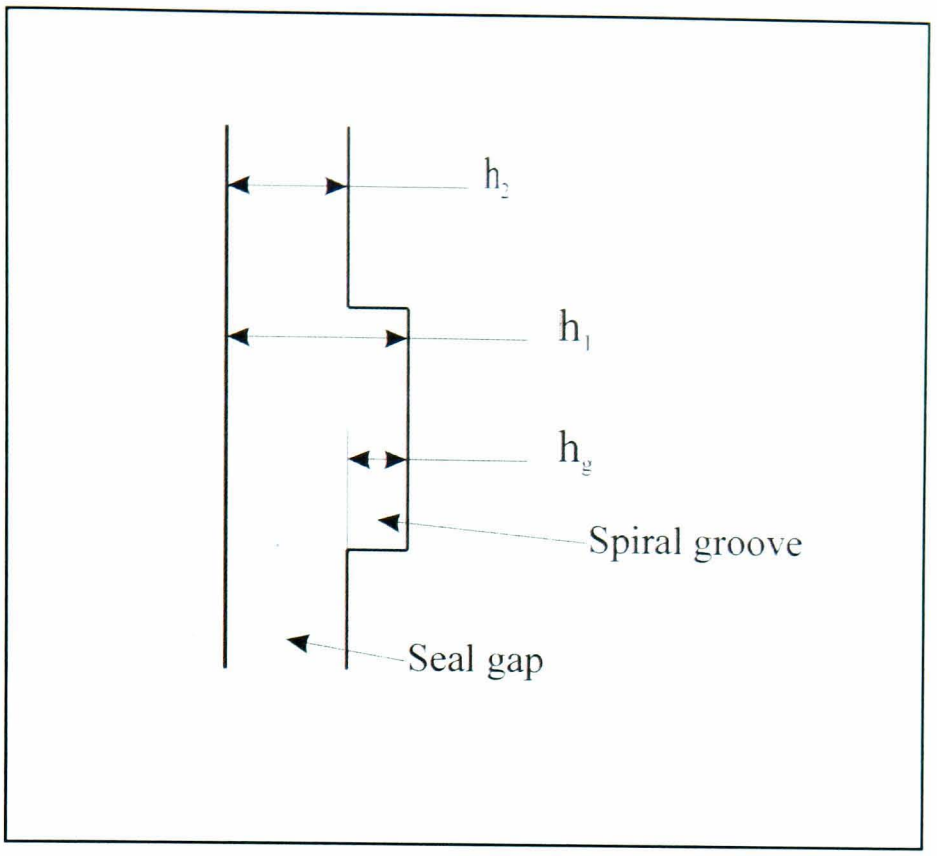

Figure 71: Schematic of relationship between spiral groove depth and the seal gap

In hypothesising about the end effects, Muijderman [22] also pointed out a further important observation from his research. That if the grooves merge into a central chamber then one would expect a uniform pressure distribution at the start and the need to apply end effect correction in that region is not necessary. This is in fact precisely the case with the SFLS seal, where there is a continuous distribution groove feeding the outer periphery of the spiral grooves. Thus it is not necessary to apply end effect correction to the outer radius of the spiral grooves.

However, the same does not apply to the inner radius of the spiral grooves. As the grooves end in a non-grooved portion, the inner radius end effect will be present here and should thus be accounted for. The outcome of the calculation produces an effective inner radius for the spiral grooves, R_{geff}, which is slightly larger that the actual groove inner radius R_g, as shown in Figure 71.

The effective radius may only deviate by a few percent from the actual value; however, this difference between the two values will have significant effect on the seal performance. This correction term has been utilised in the computer model for the SFLS design.

6.5 SLOT FED LOGARITHMIC SPIRAL (SFLS) GAS SEAL PERFORMANCE PREDICTIONS

6.5.1 FE model boundary conditions

Overall, the schematic of the boundary conditions shown in Figure 47 for the SF model applies to the SFLS model. The only difference is that the structural model is now a 3-D axis-symmetric sector of the two seal faces. Figure 72 shows the modelled sectors of the seal faces. The axial translational DOF constraints for both the seat and the face are shown as navy blue arrows. The red arrows on the two seal faces represent the heat flux applied to model. This was calculated within the SFLS fluid film module for the given seal geometry and the operating conditions, before being applied to the seal faces.

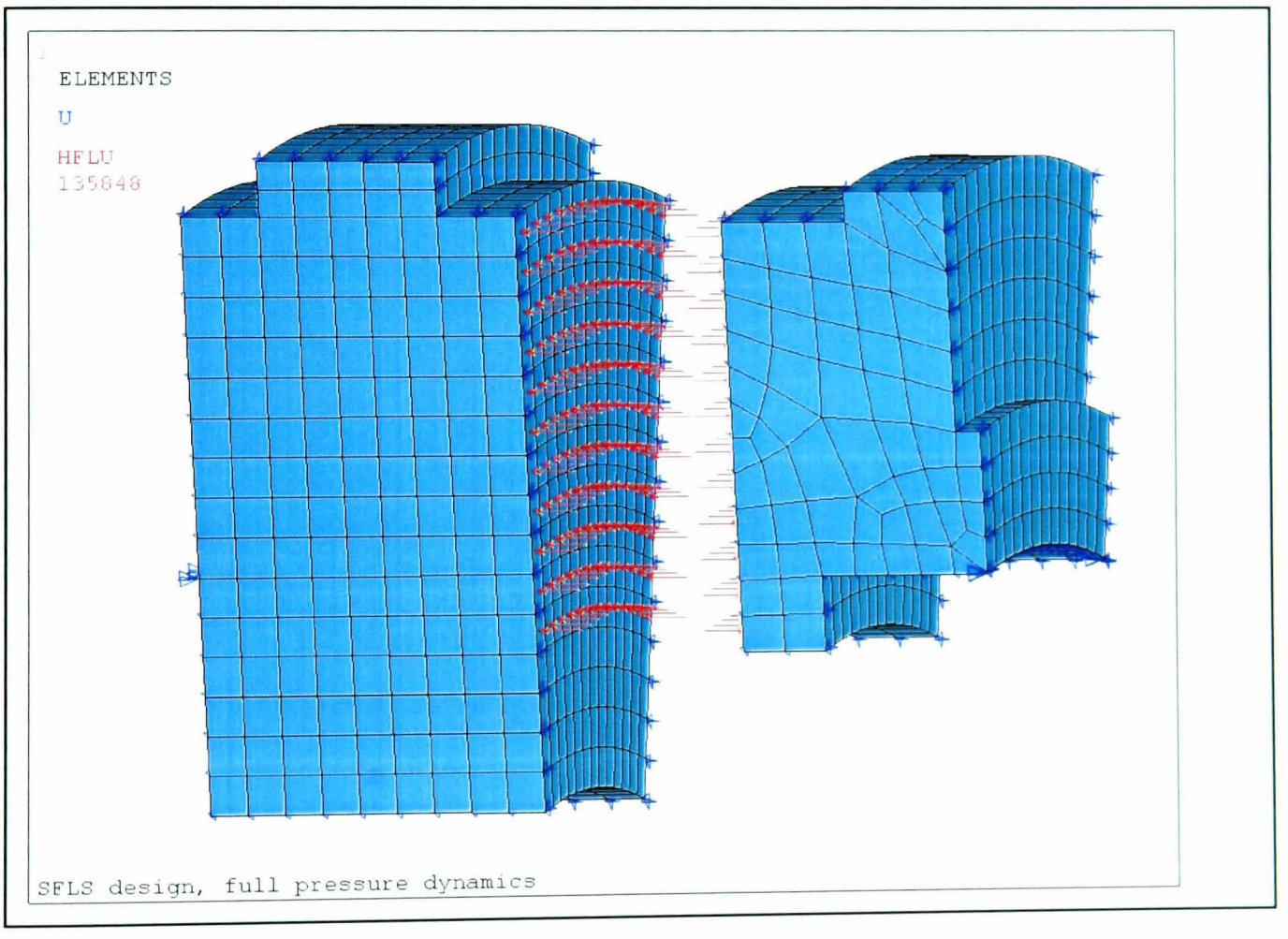

Figure 72: SFLS structural model axial constraint and heat flux boundary conditions

Images, Figure 73 and Figure 74 show the applied pressures to the seal faces. The red contours represent the maximum pressure being sealed, in this case, 300 bar. The pressure profile at the two seal faces decreases in value from the outer to the inner

radius, as indicated by the legend. This is in fact the opening pressure profile as calculated in the fluid film module and as shown in Figure 76 and Figure 77.

Finally, Figure 75 shows the surface heat transfer coefficient distribution around the seal faces. As with the heat flux values, the surface heat transfer coefficients were calculated within the SFLS fluid film module for the given seal geometry and operating conditions, before being applied to the seal faces in the structural module of the model.

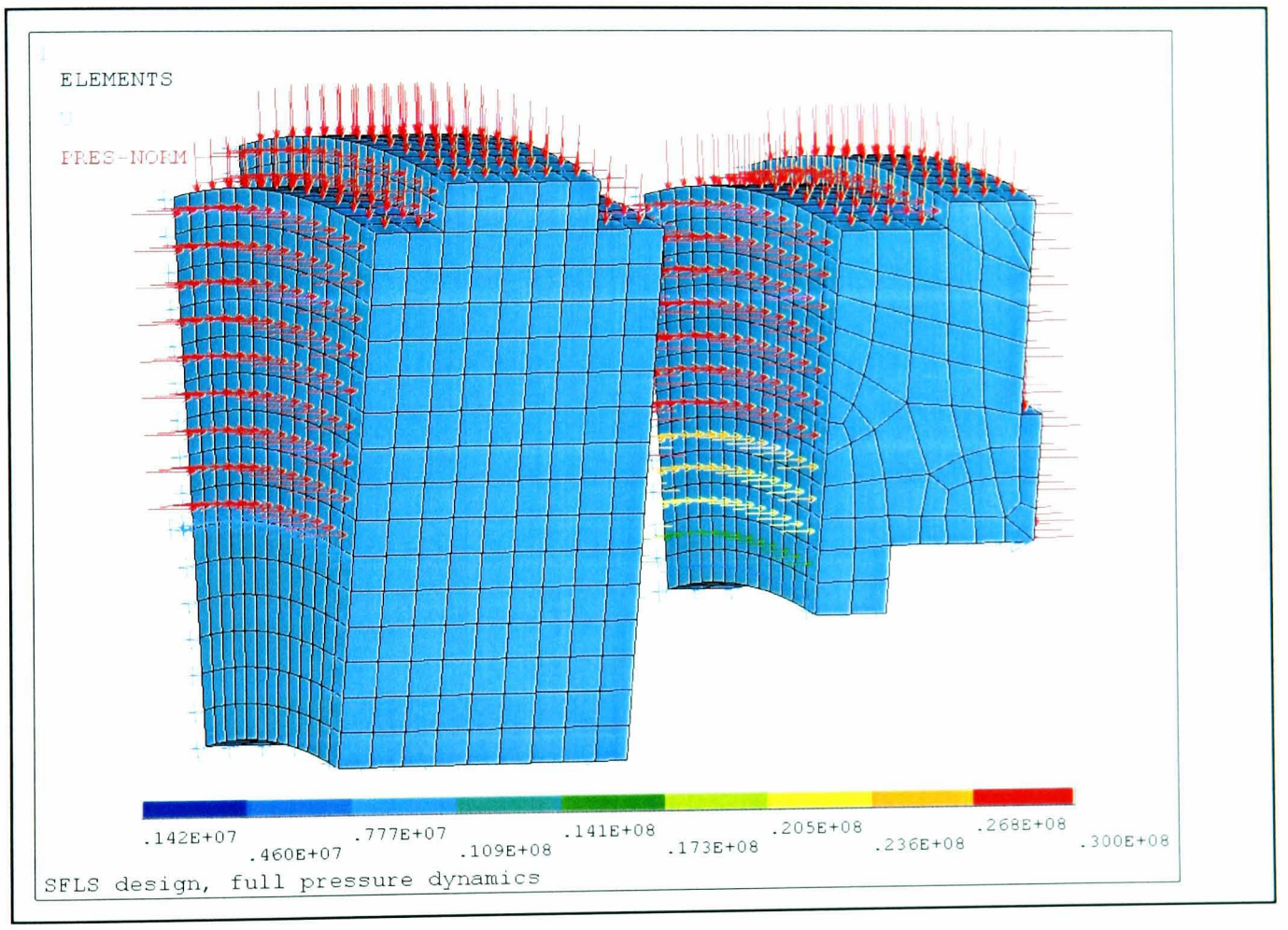

Figure 73: SFLS structural model – pressure boundary conditions

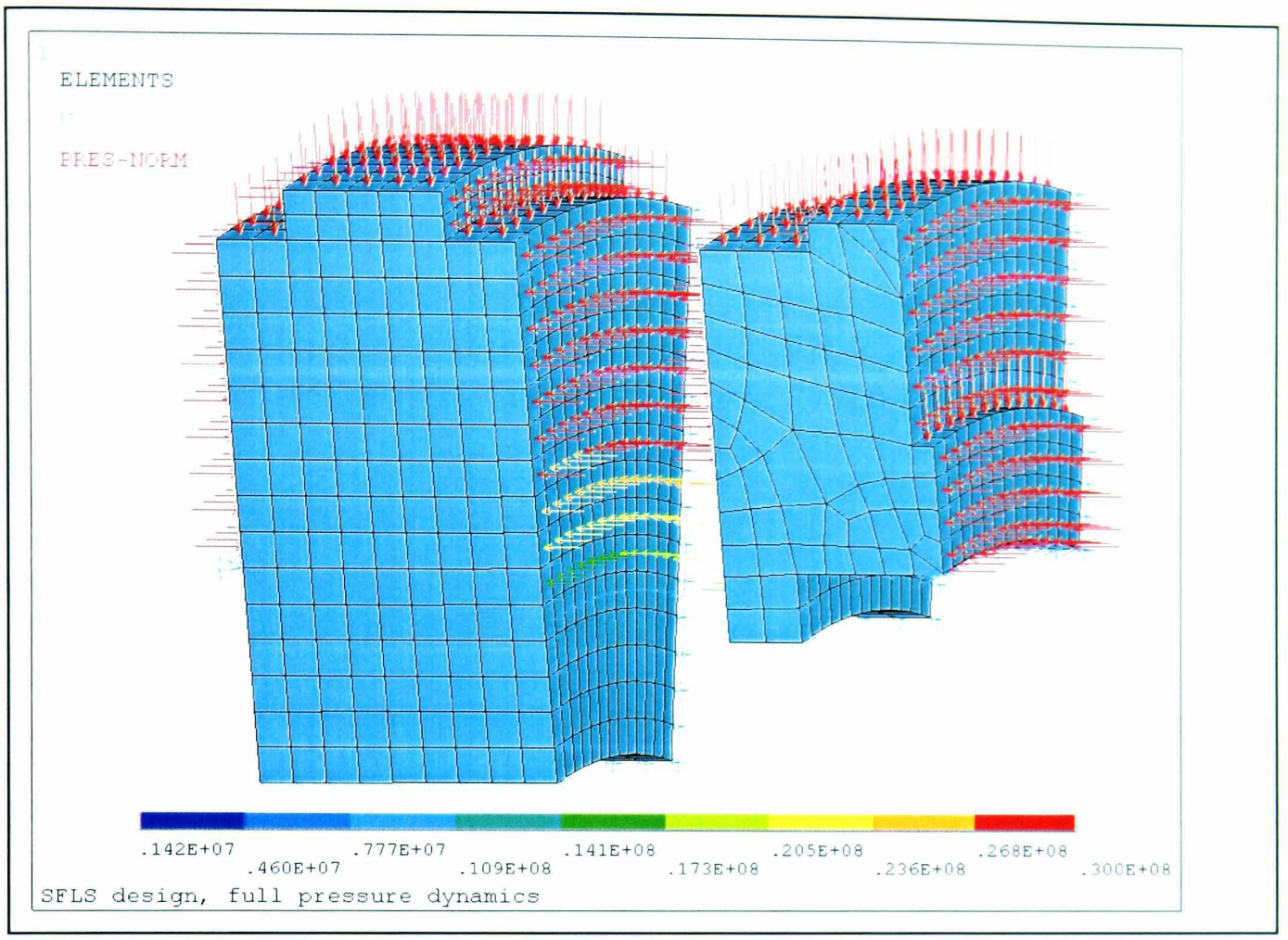

Figure 74: SFLS structural model – pressure boundary conditions

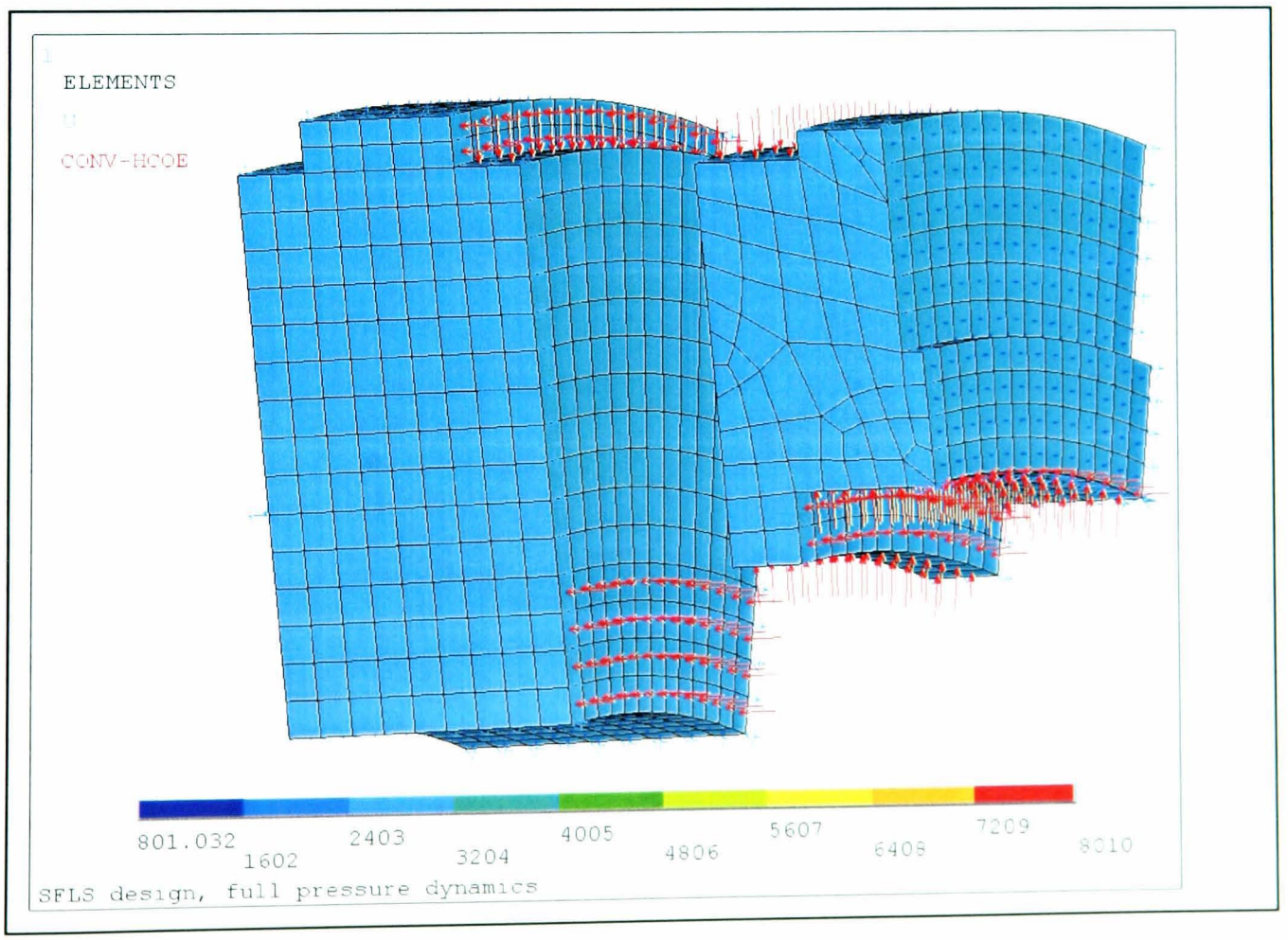

Figure 75: SFLS structural model - convection coefficient boundary conditions

6.5.2 Pressure profile predictions

The first important output from the SFLS computer model is that of the pressure profile in the primary seal zone. That pressure profile creates an effective opening force that counteracts the sealing pressure closing force, thus separating the two seal faces at a given equilibrium position.

The predicted pressure profiles across the modelled sector of the seal faces are shown in Figure 76 and Figure 77. The prediction for full pressure, full speed condition in Figure 77, gives quite a different result to prediction for full pressure ambient statics in Figure 76. The pressure generating effect of the spiral grooves under dynamic conditions is quite pronounced and clearly seen.

The 2-dimensional seal gap prediction at the seal interface as a function of radial and circumferential position is shown in Figure 78. The two horizontal axes correspond to the radial and circumferential co-ordinates in the grid. The grid size is 40x38 nodes. The y-axis gives the actual film depth at that point in the grid. The logarithmic spirals, the adjacent lands are clearly and accurately represented. The front distribution groove being the deepest is also clearly seen.

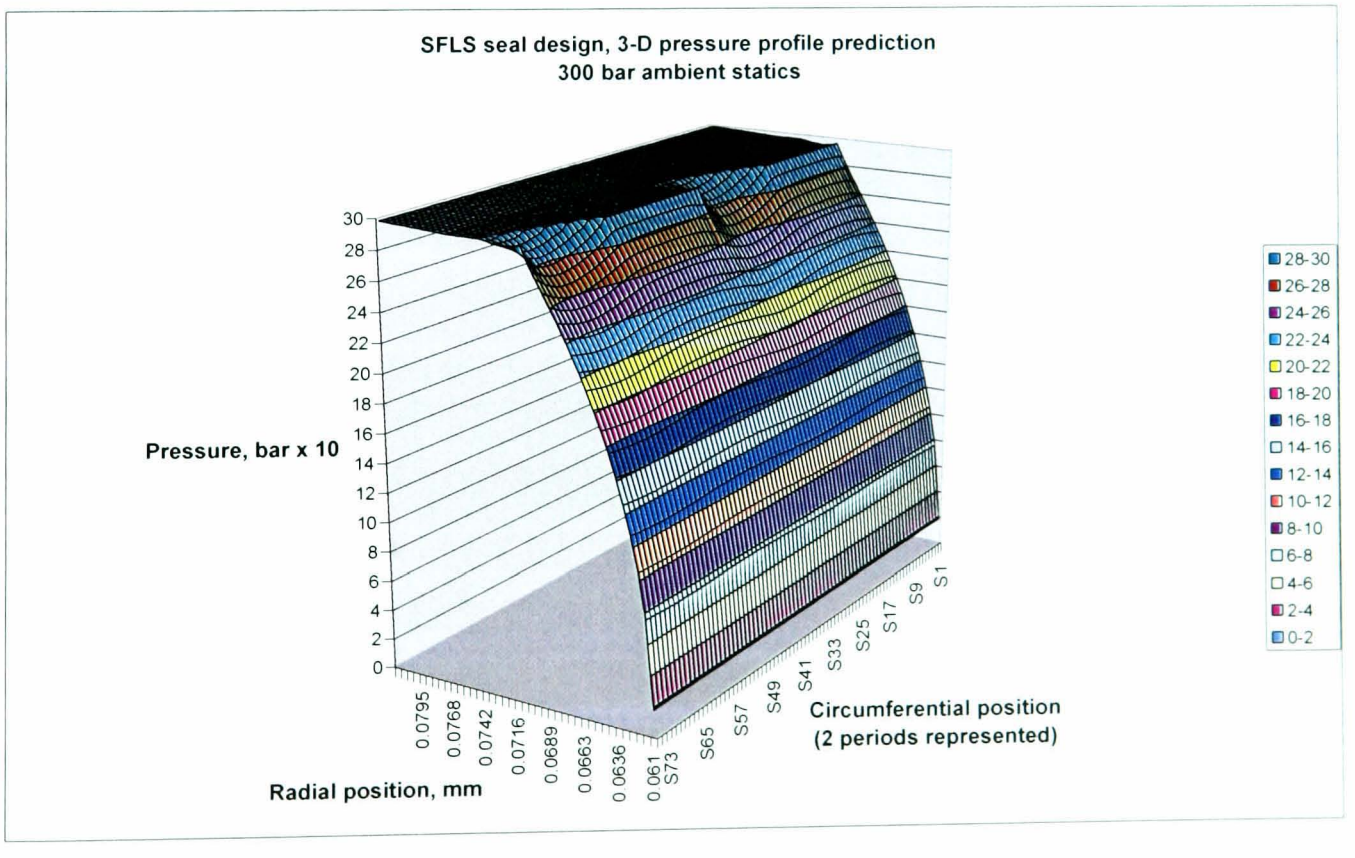

Figure 76: Seal face pressure profile distribution at full pressure ambient statics

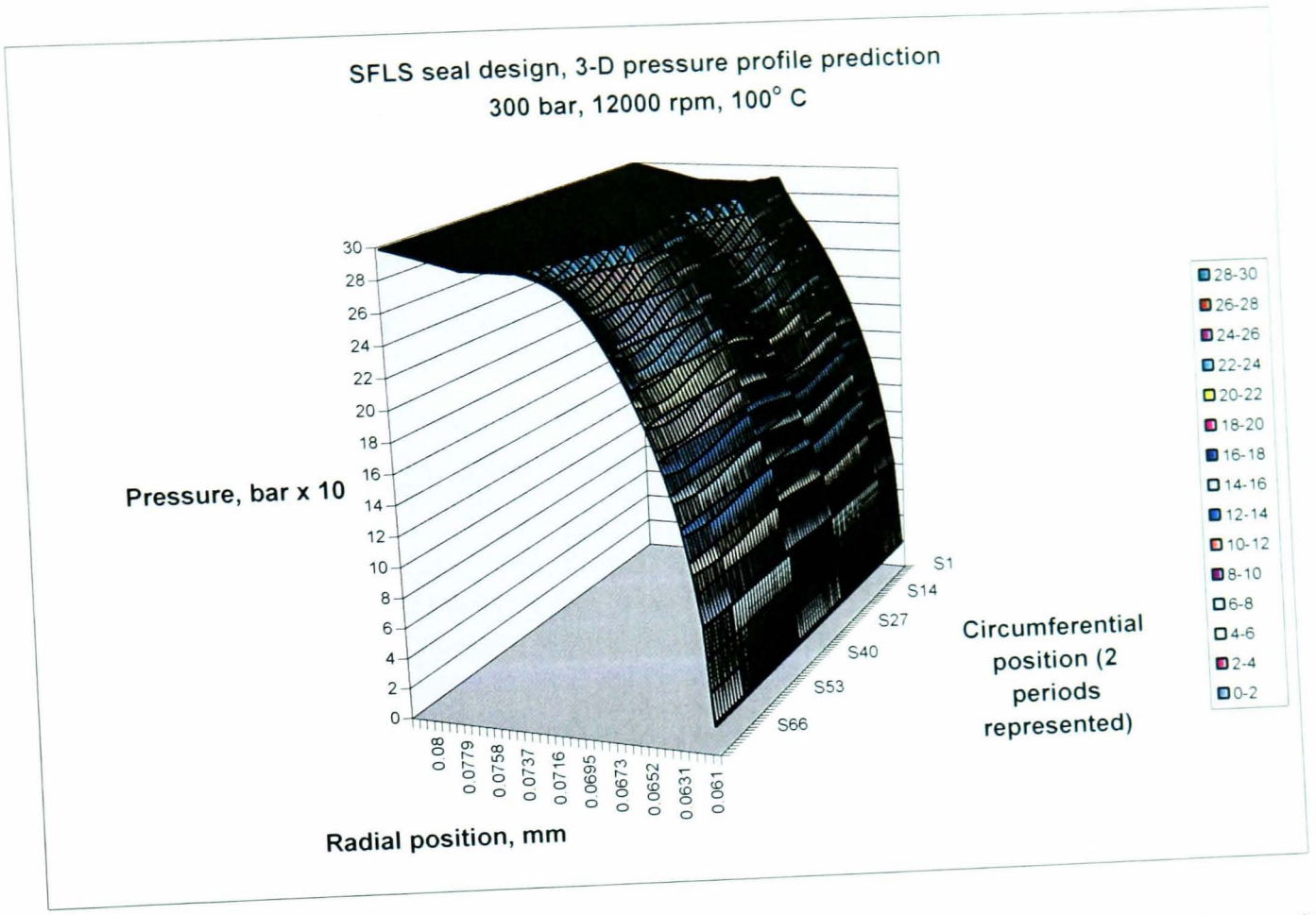

Figure 77: Seal face pressure profile distribution at full pressure dynamic conditions

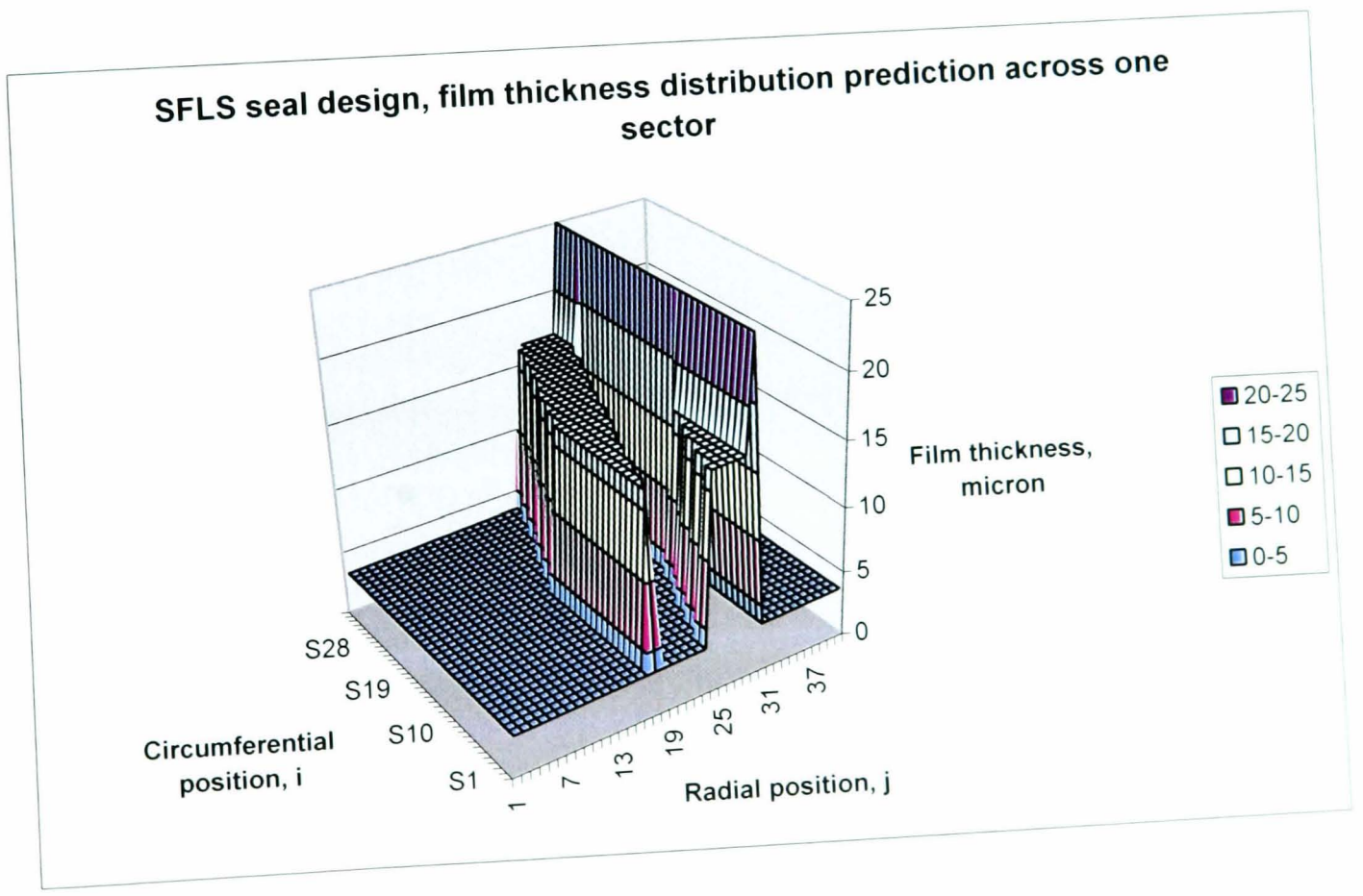

Figure 78: Seal gap distribution as a function of radial face width.

6.5.3 Static leakage and lift off pressure predictions

The predictions for seal gap and leakage as a function of pressure under static conditions are shown in Figure 79 and Figure 80. As with the pressure profile, leakage and predicted gaps for a given seal pressure were the direct outputs from the SFLS gas seal computer model. In Figure 80, the red box shows the zone of predicted seal lift off.

The static leakage plot predicts a near linear increase of leakage with pressure, as shown in Figure 81.

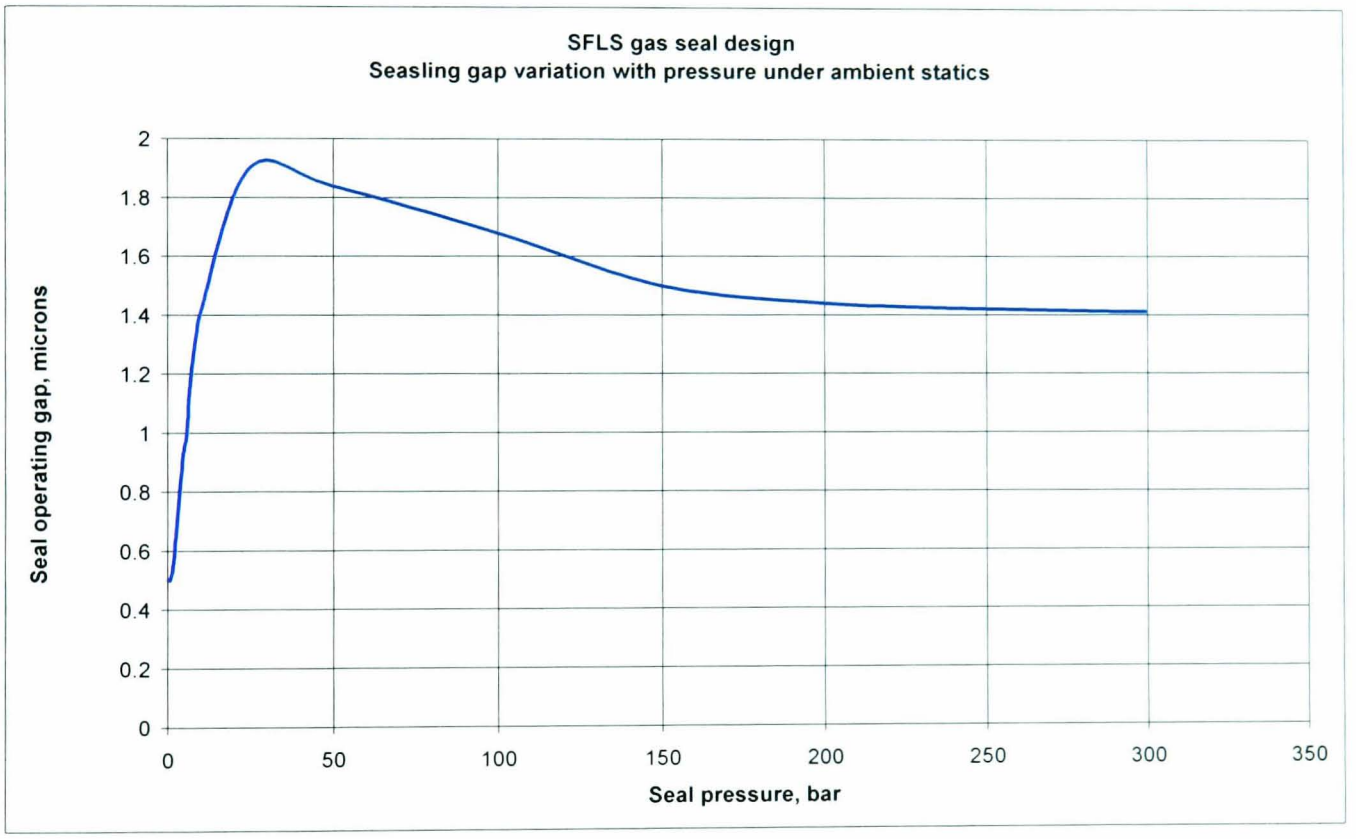

Figure 79: SFLS predicted seal gap variation with ambient pressure

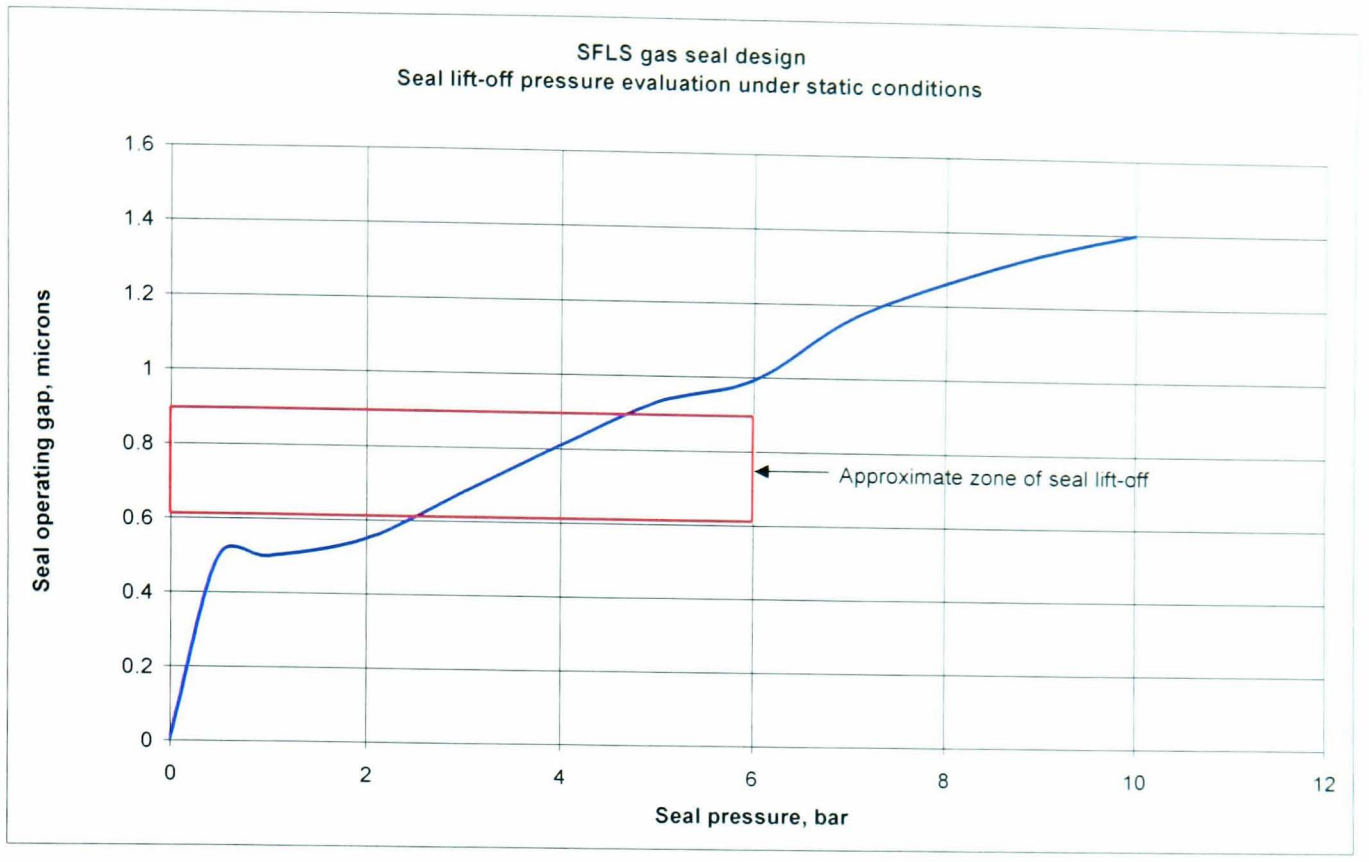

Figure 80: SFLS design predicted seal gap variation with ambient pressure

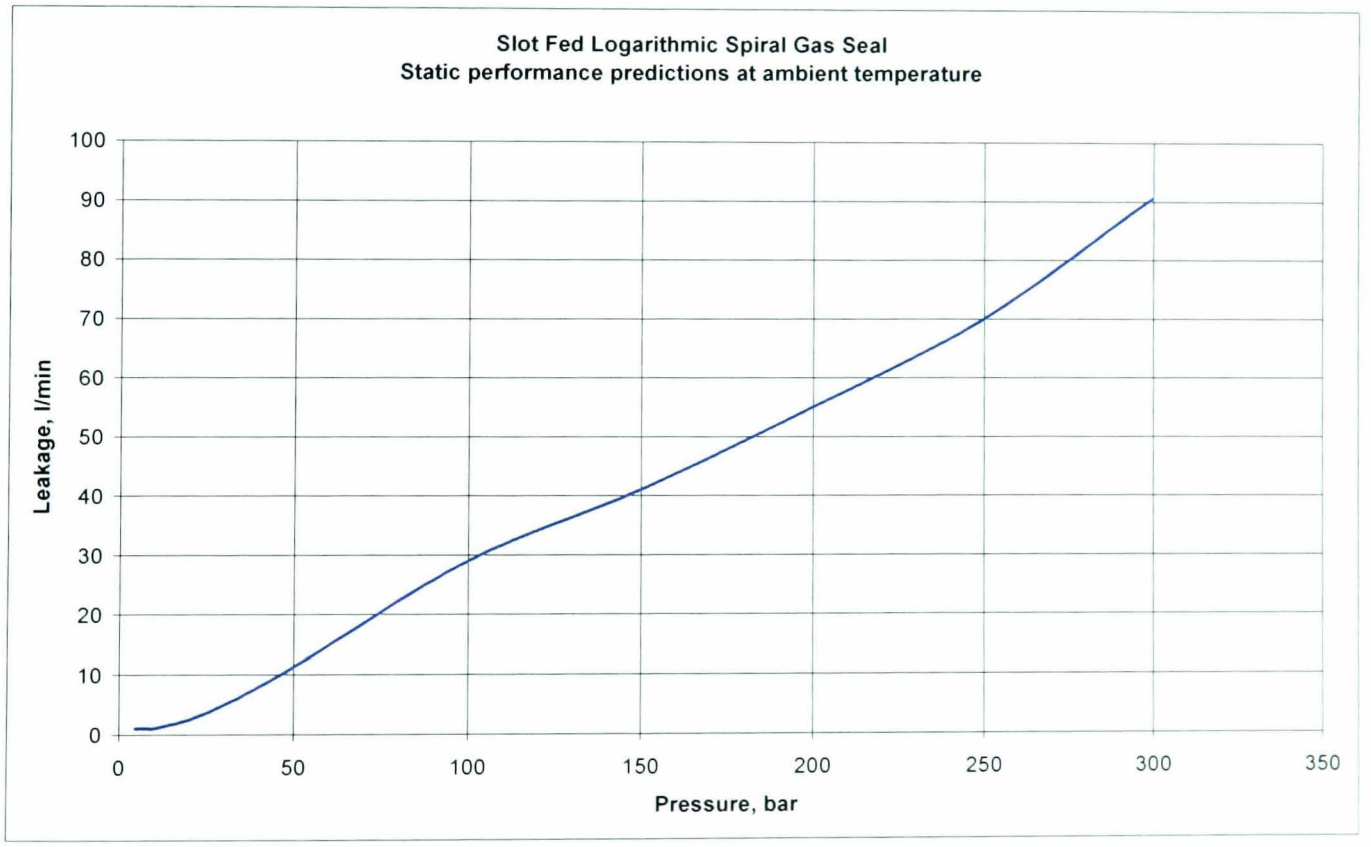

Figure 81: SFLS design static leakage predictions

6.5.4 Dynamic leakage predictions

Figure 82 and Figure 83 give the dynamic leakage predictions as a function of pressure at various speed points from 6000 to 12000 rpm at 2000 rpm increments. Figure 82 is for an operating temperature of 323K and Figure 83 is for an operating temperature of 393 K. In essence, it is a performance map. As expected, with everything else being equal the higher the temperature, the lower is the predicted leakage, due to increased gas viscosity restricting the flow of gas through the seal. The predicted gap variation as a function of pressure at various speed points is shown in Figure 84. As expected, there is significant variation in gap and leakage with varying speed, indicating a strong presence of a hydrodynamic component.

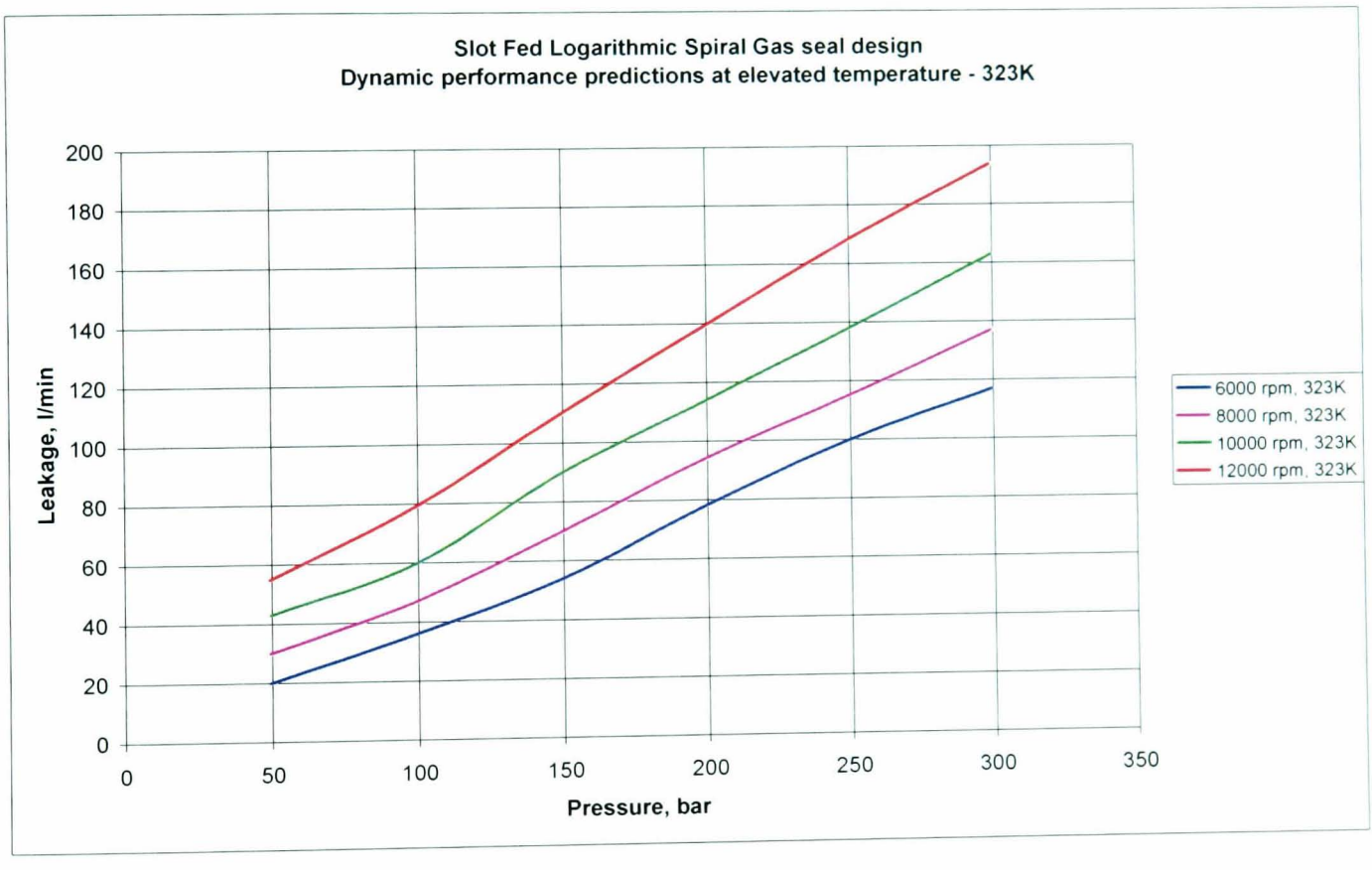

Figure 82: SFLS dynamic leakage performance predictions – 323 K

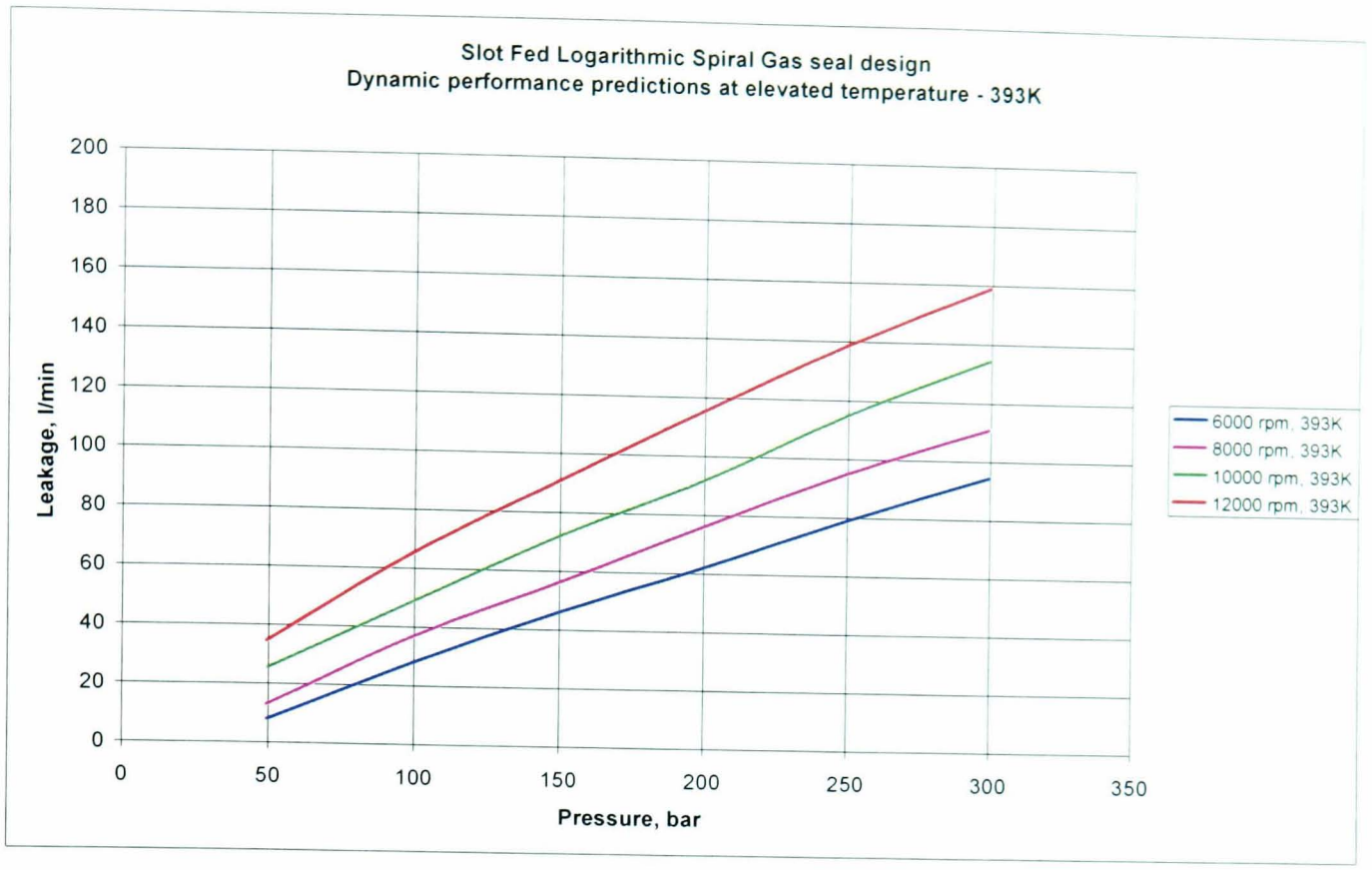

Figure 83: SFLS dynamic leakage performance predictions – 393 K

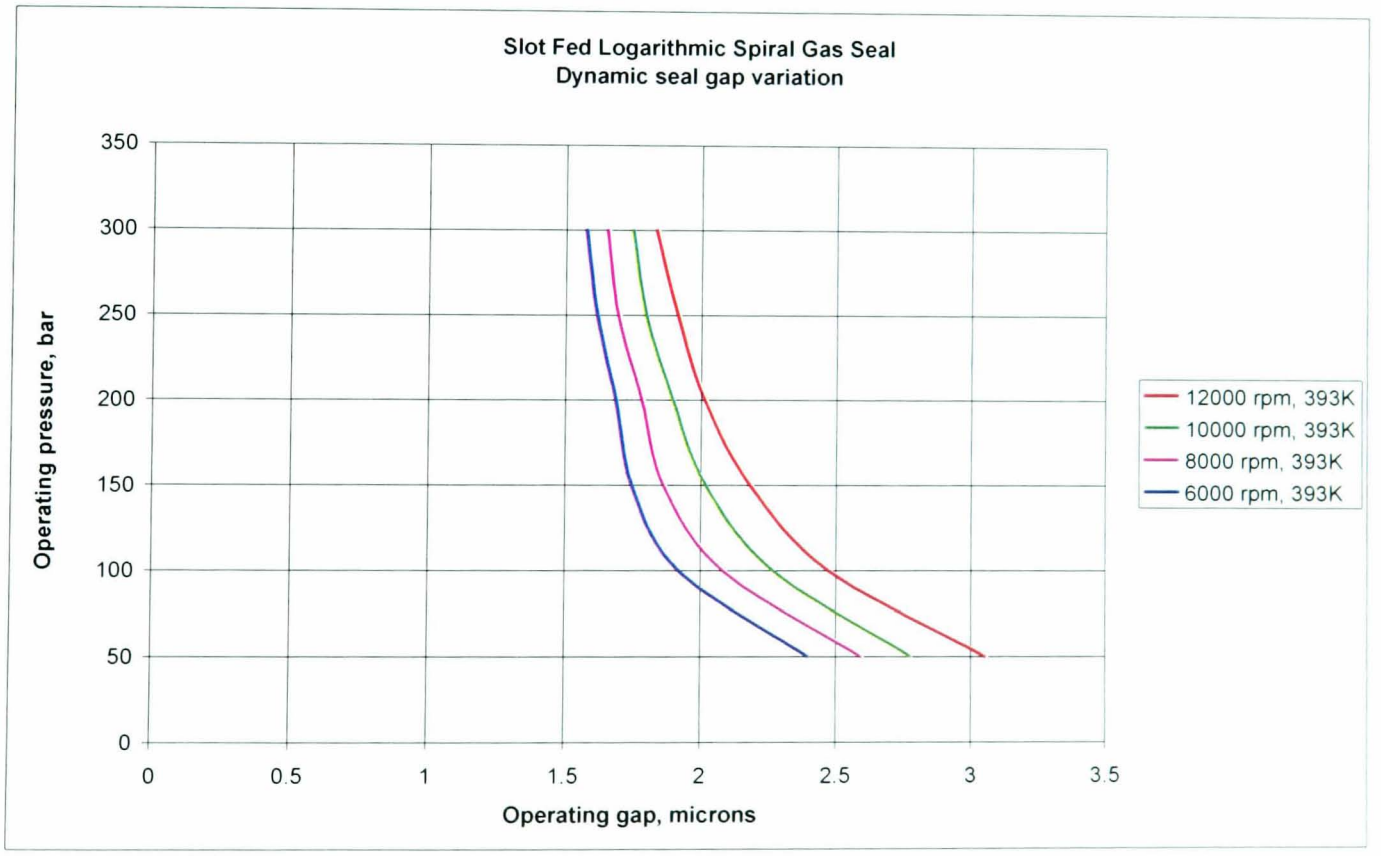

Figure 84: SFLS dynamic operating gap prediction at 393 K

6.5.5 Seal face structural performance predictions

This section contains the SFLS model prediction for structural behaviour of the seal faces under the full operating conditions. The worst case scenario in this case is that of full pressure full speed and full temperature operation – namely 300 bar, 12000 rpm and 298K.

Figure 85 shows a plot of total seal deformation under the full operating condition. Overall, it the seal parts have expanded due to the temperature induced and speed effects. The maximum displacement is on the rotating seat, which has grown by 0.028 m.

Figure 86 shows a plot of principal equivalent stress distribution at the full operating condition. The maximum equivalent stress is to be found at the inner radius of the face with a numerical value of 156 MPa. If one was to look at the principal stresses, one would find the maximum principal stress to the radial component in the compressive direction,

Figure 87 shows a plot of temperature distribution at the full operating condition. The maximum thermal gradient is across the seat, having the lower thermal conductivity of the two parts. The maximum temperature at the seal face is 427.6 K for a bulk seal gas temperature of 393K, thus indicating a local temperature rise of 34.6K.

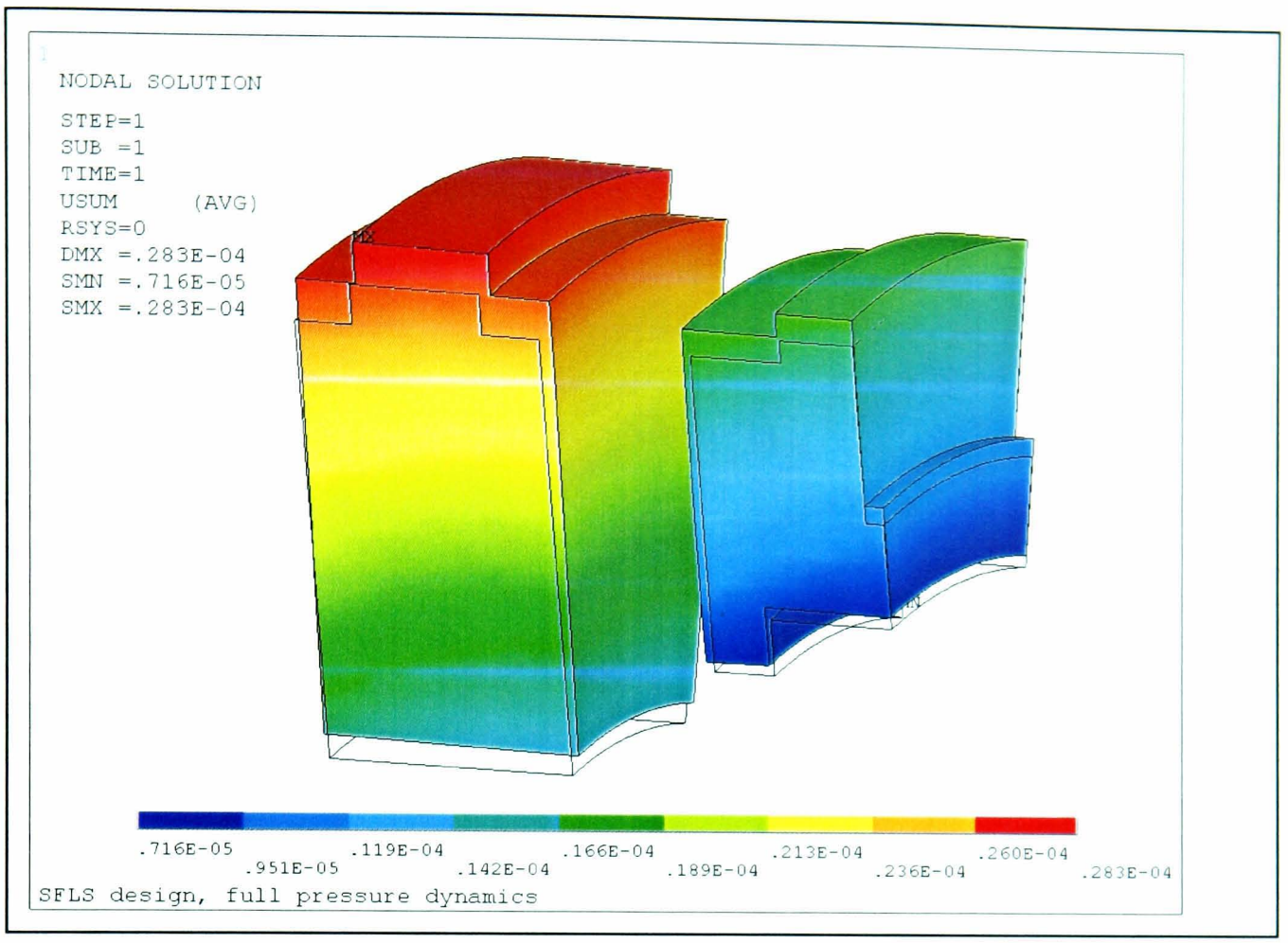

Figure 85: SFLS seal deformation predictions

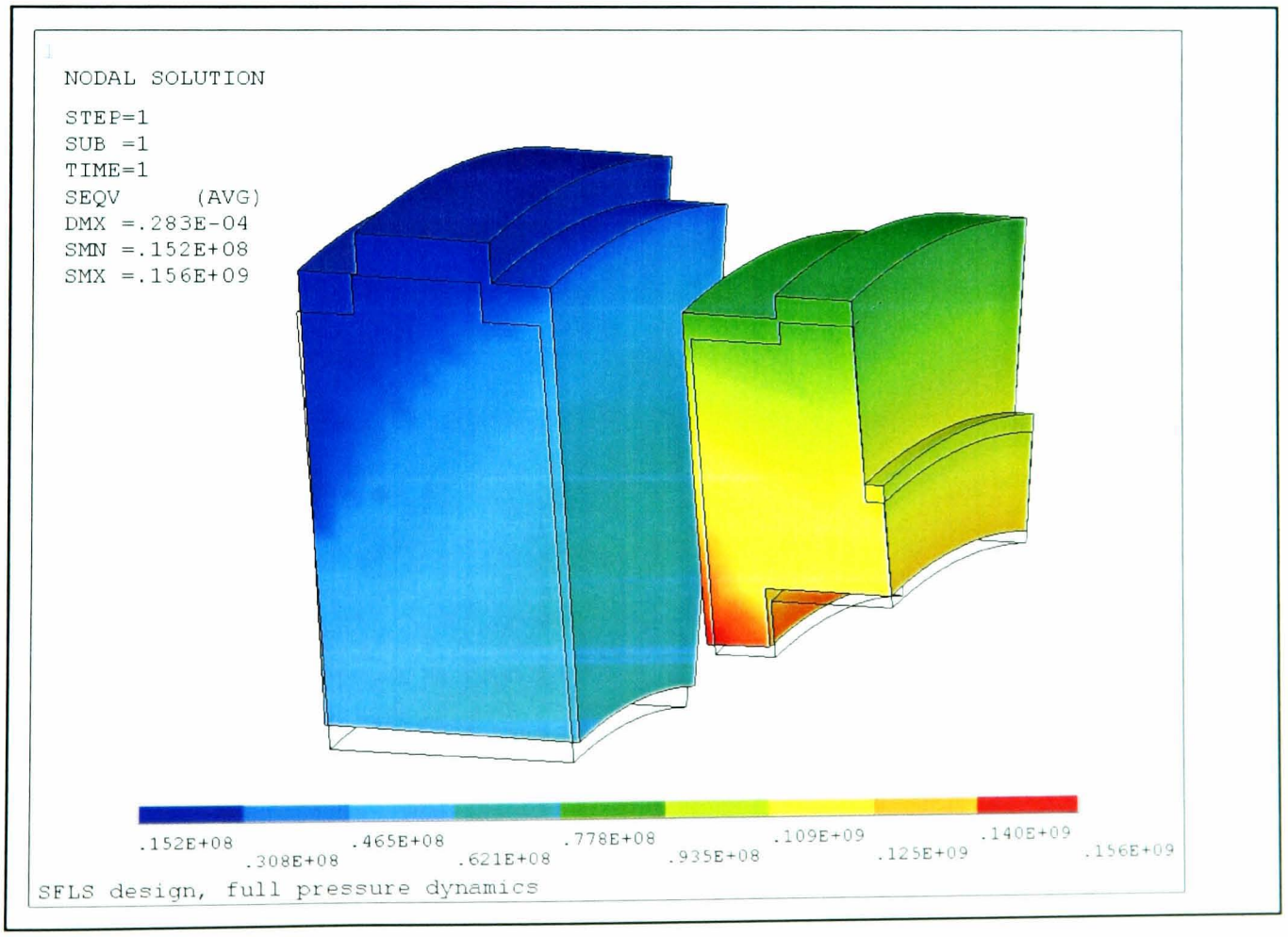

Figure 86: SFLS seal pressure principal stress predictions

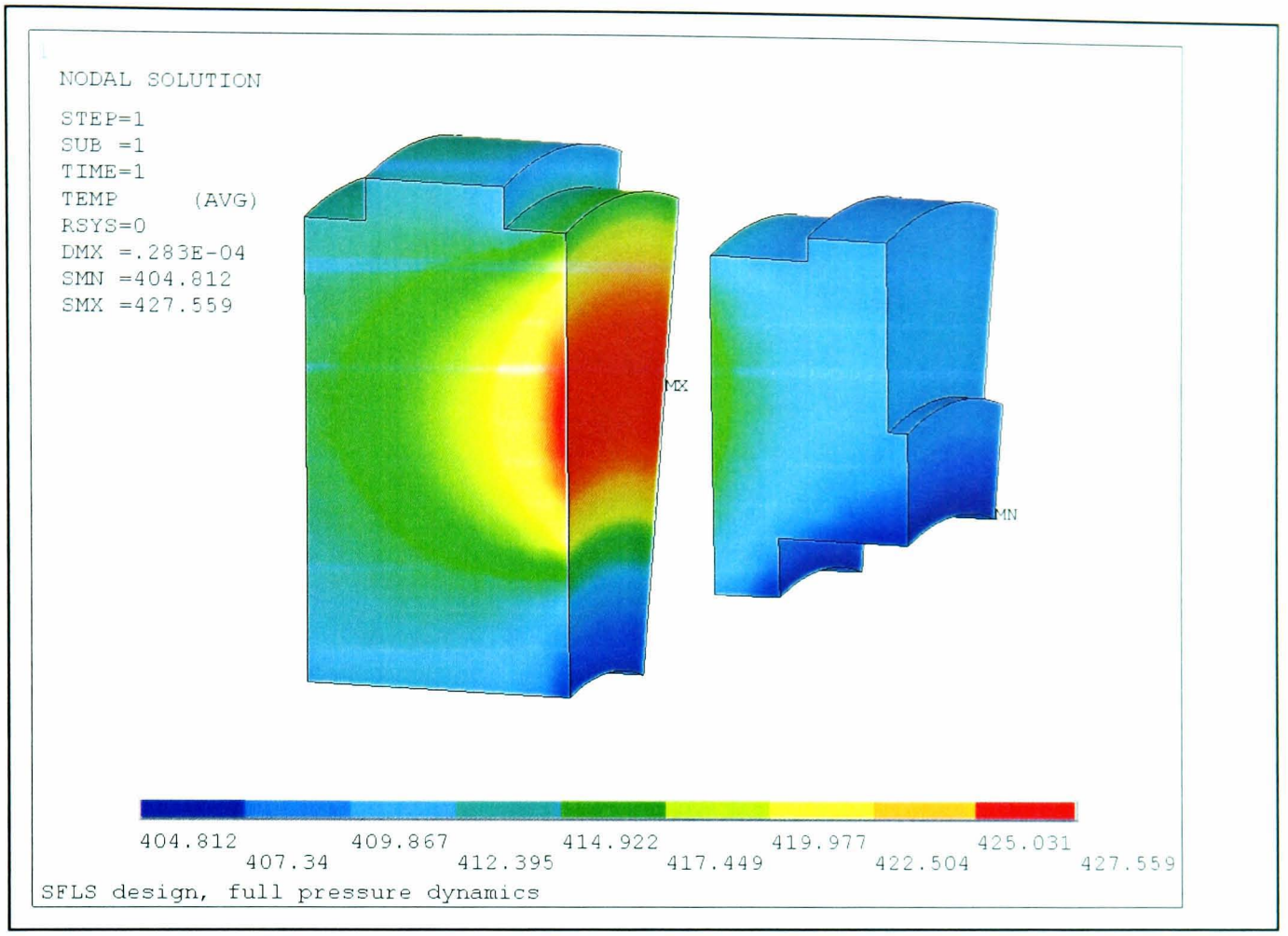

Figure 87: SFLS seal temperature distribution predictions

6.5.6 Modelling the seal load support

As was done with the SF design and shown in Figure 56, the load support capability of the SFLS design was also evaluated. To predict this scenario the SFLS fluid film model was modified and reanalysed under varying values of seal face closing force. For each load value, the predicted equilibrium film gap was calculated. These values were plotted on a graph in Figure 88. As can be seen from the graph, as the equilibrium operating gap is forced to reduce by the increasing seal face load, that load climbs rapidly, almost reaching a vertical asymptote, Looking at this another way, the seal film stiffness, which is effectively the gradient of the curve, progressively increases with reducing gap and the stiffness almost approaches infinity. This is in stark contrast with the experimental results for the SF concept. In practice, this should make the SFLS concept resistant to upset conditions and ensure its full survival under the artificial interspace condition, where the SF concept suffered face contact.

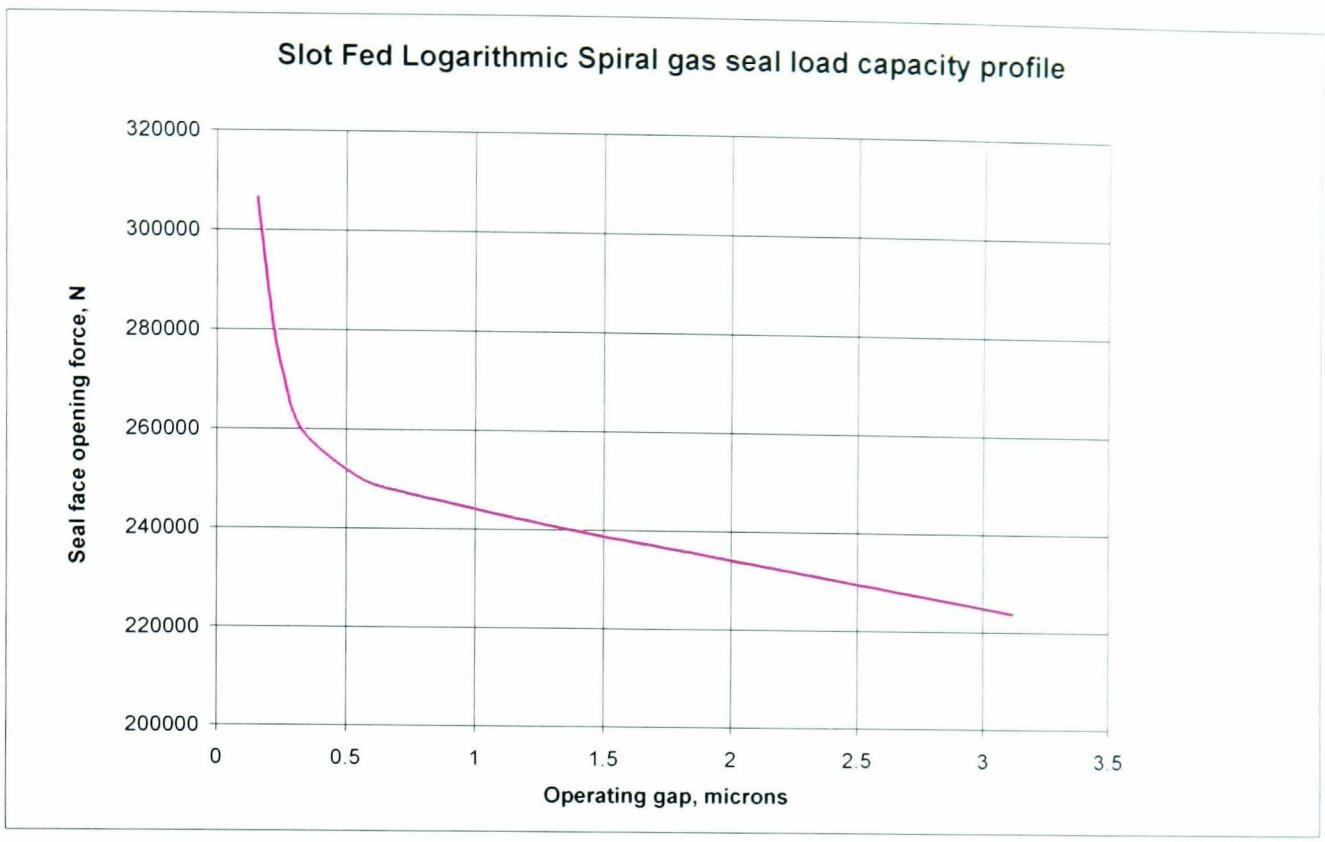

Figure 88: Load capacity prediction for SFLS design

6.5.7 Evaluation of choked flow at the seal exit

The following results were extracted directly from the SFLS coupled field model. Under ambient statics, investigation of the SFLS fluid film module analysis predicts the exit flow to become choked at 72 bar, with a discharge pressure of just over 1 bar. At this pressure and beyond, the exit velocity is predicted to be sonic. Although the exit velocity will not increase beyond the sonic value, the resultant pressure P^* at the seal exit will continue to increase above the ambient downstream pressure. At full operating conditions, of 300 bar and 293K, the calculated discharge pressure is 10.1 bar and a theoretical Mach number of 10.

Under full dynamic conditions of 12000 rpm and gas inlet temperature of 393K, the exit flow becomes choked at 45 bar, a lower value than under full pressure ambient statics. At full operating conditions of 12000 rpm, 300 bar and 393K, the calculated discharge pressure is 13.16 bar and a theoretical Mach number of 9.7.

At the inlet on the other hand, the flow never becomes choked under the conditions being considered, as is shown in Figure 89. The highest calculated velocity, found to be sonic occurs at the seal discharge.

6.5.8 Evaluation of seal entrance losses

The entrance losses in terms of temperature and pressure, are at their highest with the highest pressure. Modelling predicts the following losses, shown in Figure 89.

Full pressure ambient statics, 300 bar, 293K, 0 rpm	Full pressure & speed dynamics, 300 bar, 393K, 12000 rpm
Po_{eff} = 299.67 bar	Po_{eff} = 299.4 bar
$Temp_{eff}$ = 292K	$Temp_{eff}$ = 392K
U_o = 8.7 $m.s^{-1}$	U_o = 13 $m.s^{-1}$

Figure 89: SFLS seal predicted inlet conditions

6.5.9 Spiral groove end effect correction

From the formulation, it can be seen that the end effect correction is based primarily on the original groove geometry, and to a lesser degree, the mass flow rate through the seal. The influence of the end effect correction is to make the effective length of the groove less than the actual geometric value. In the case of the SFLS design under consideration, the value of R_g, the inner spiral groove radius, is 69.5 mm. For the given groove geometry, the model returns an effective inner groove radius, $R_{g\text{-}eff}$, of 70.78 mm.

6.6 SFLS GAS SEAL DESIGN TEST RESULTS

The following graphs show key results as recorded during experimental testing of the SFLS gas seal design concept, using the test facility and the test equipment described in section 4.

The first two graphs; Figure 90 and Figure 91 show the measured break out torque of the seals as a function of pressure. Breakout torque is by far the most effective means of measuring the point at which the seal faces have lifted off. From Figure 91 in particular, it can be seen that the breakout torque reaches a minimum asymptote value of just over 1 N.m between 2 and 3 bar of seal pressure. This confirms the point at which the seal faces have attained complete separation.

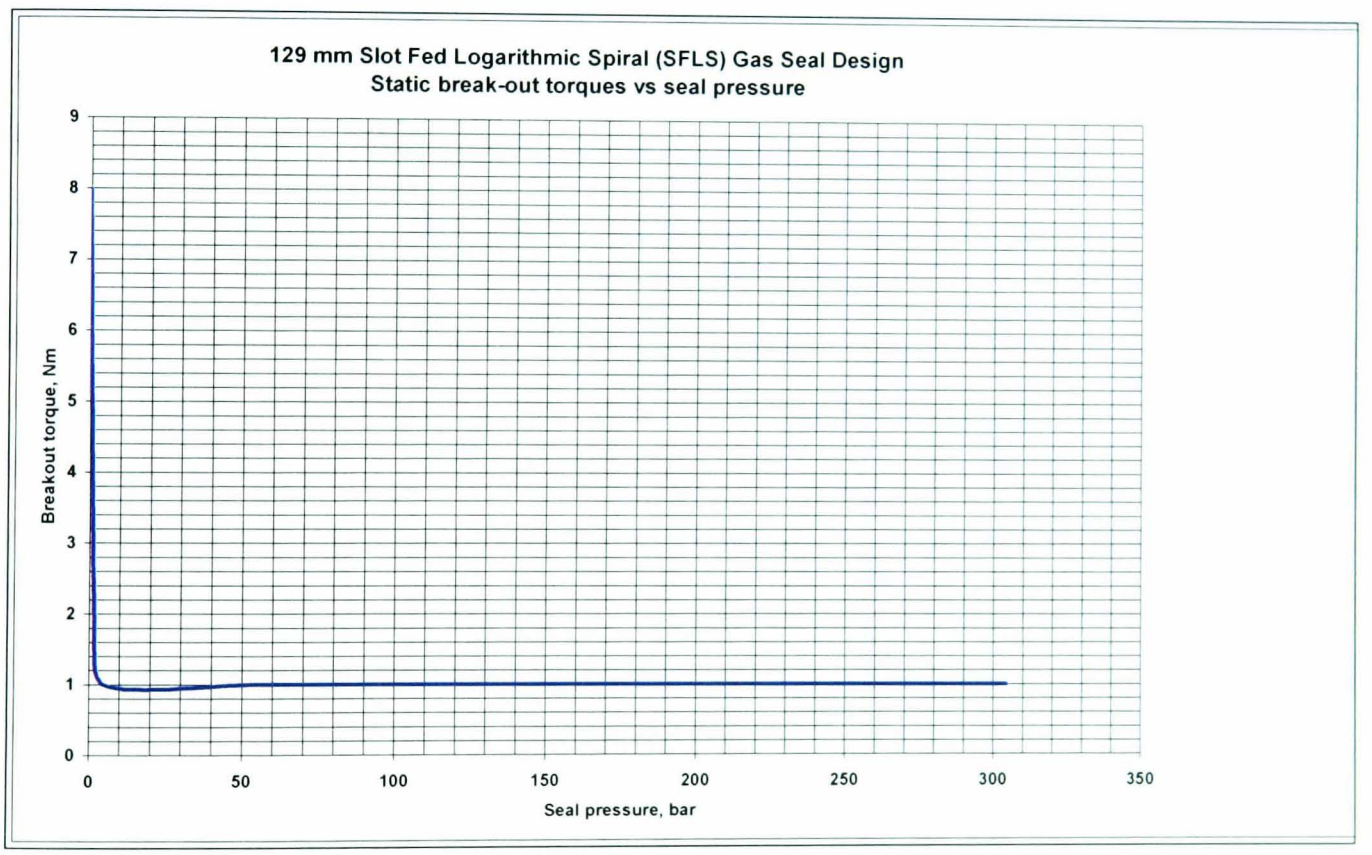

Figure 90: SFLS seal break out torque as a function of pressure

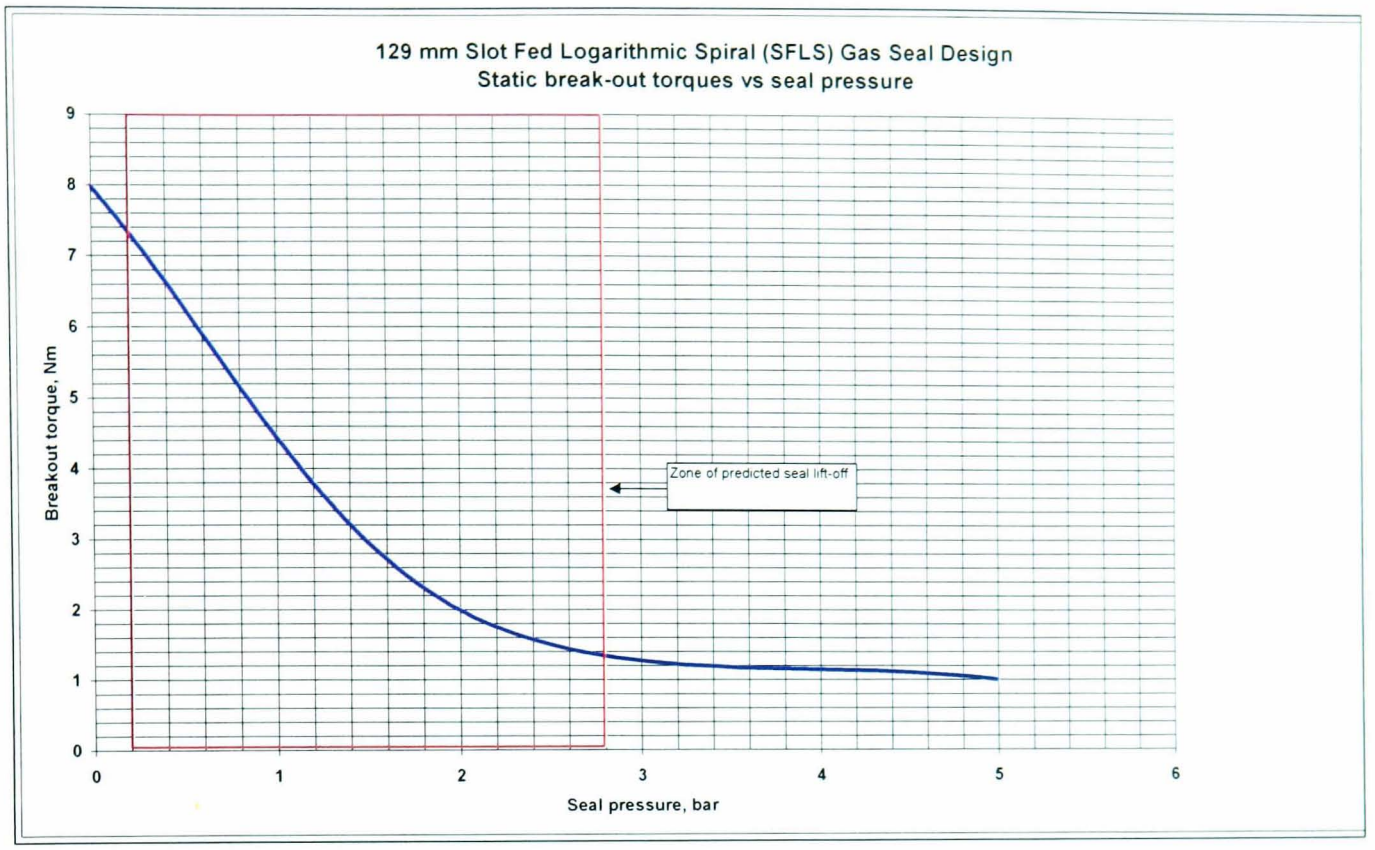

Figure 91: SFLS seal break out torque as a function of pressure – zoomed in

Figure 92 and Figure 93 show the measured seal performance in terms of static as well dynamic leakage at various key operating points across the performance envelope. On each of the graphs, the ordinate axis carries the seal pressure (in bar), the seal leakage in $l.min^{-1}$ and the operating temperature in deg C. The second ordinate axis on the right hand side carries the seal operating speed in rpm. The abscissa axis carries the time history of the test, in minutes.

For comparative evaluation, superimposed on these results graphs is the predicted seal performance from the SFLS coupled field computer model. Those prediction points are shown as blue dots on the graphs. The results are discussed in detail in section 6.7.

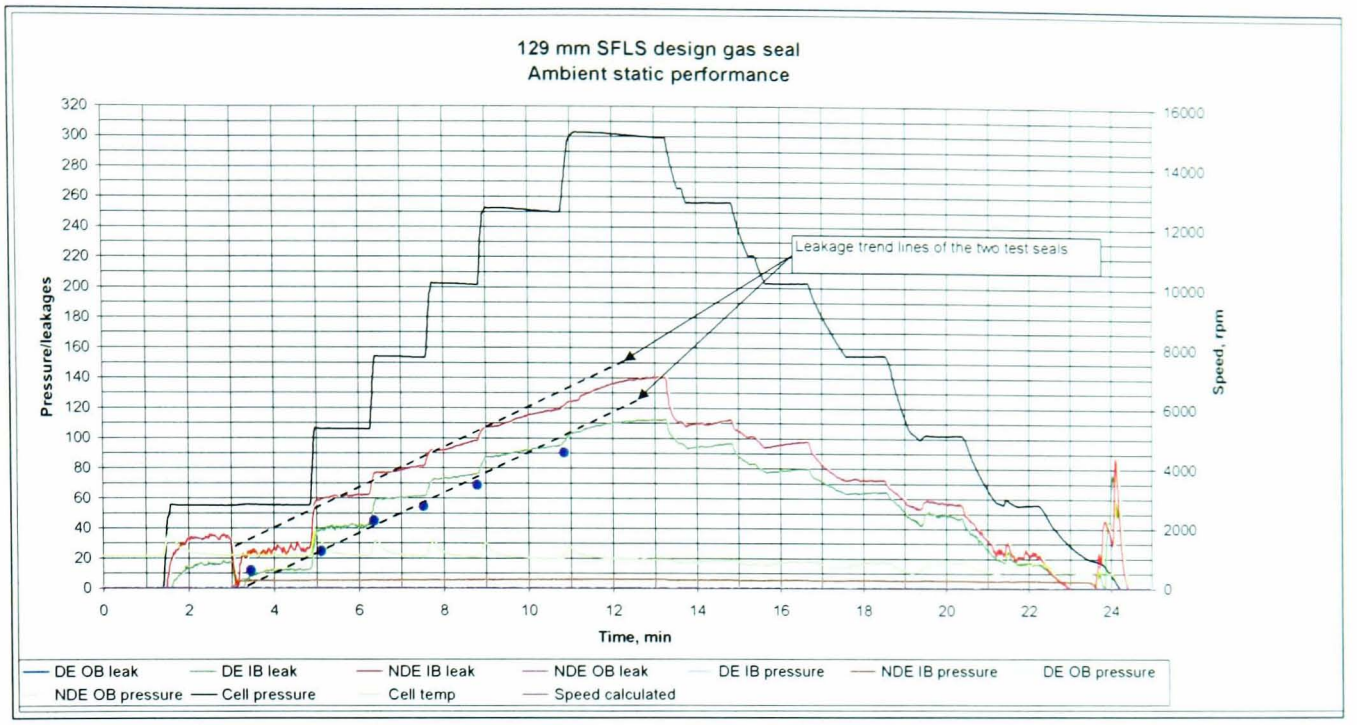

Figure 92: SFLS seal static leakage performance & correlation with model predictions (blue dots)

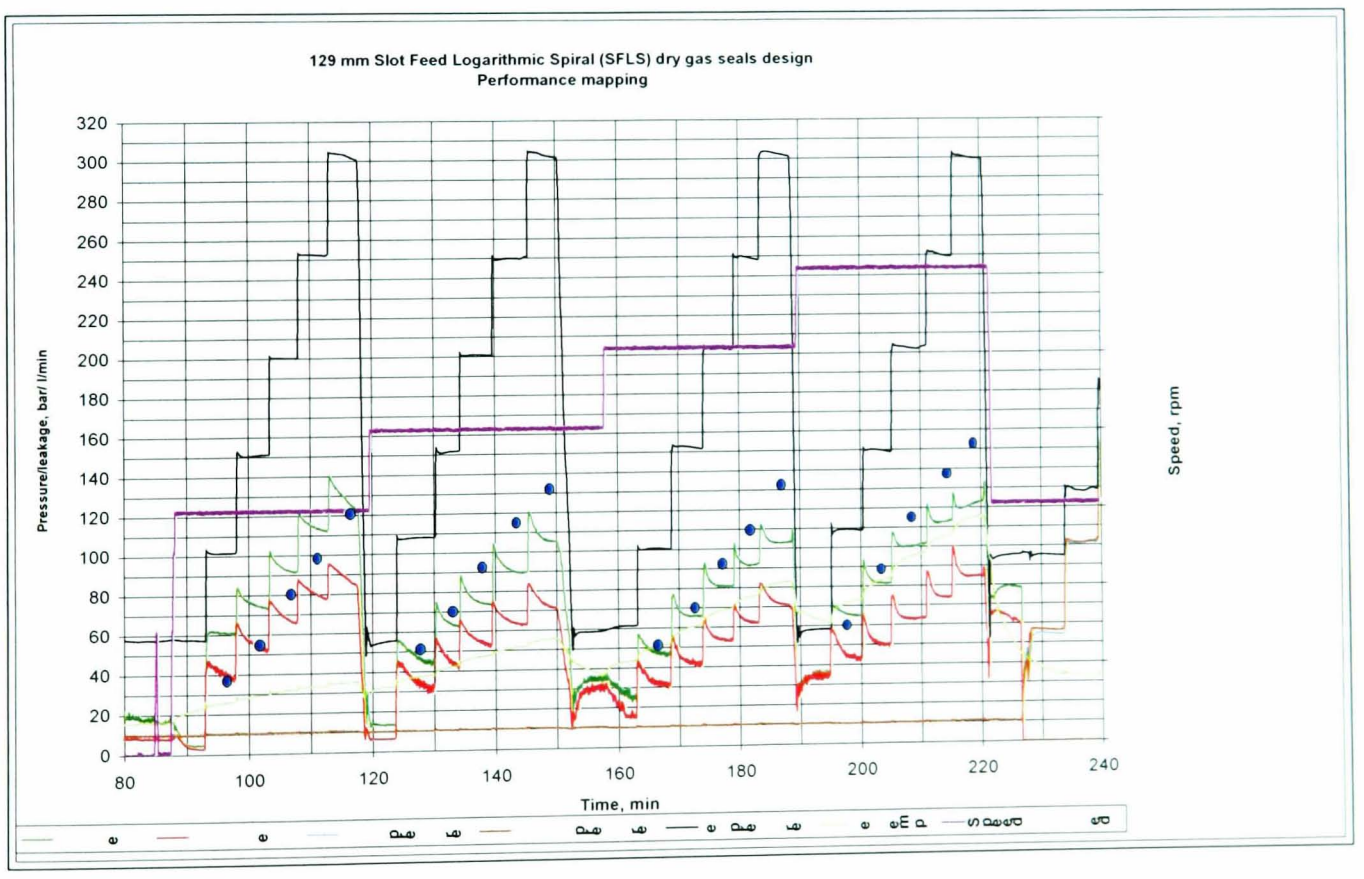

Figure 93: SFLS seal dynamic leakage performance and correlation with model predictions (blue dots)

Figure 93 shows a graph of the entire performance-mapping test for the concept seals. The speed range is from 6000 through to 12000 rpm, and the pressure range is from 50 through to 300 bar. Model predictions are shown for each pressure temperature point, as blue dots

6.7 DISCUSSION OF RESULTS

When it comes to non-contact mechanical gas seals, by far the most representative performance indicators are the seal leakage and the breakout torques. Above anything else these are the two values that bring one the closest to understanding as to what is happening at the operating seal gap, which is less than 2 μm wide.

6.7.1 Static leakage

With reference to Figure 81, the model predicts a near linear increase of leakage with pressure. One could argue that the usual expectation would be for more of a power law relationship. However, the model has full functionality for choked flow and this modelling consideration will predict lower leakage increase, particularly at higher pressures, compared to a model that does not take account of exit choking and sonic discharge.

For a detailed comparison, the modelling predictions have been superimposed onto actual test results. The first observation is that the modelling predictions closely follow the trends of static leakages, as the sealing pressure is progressively increased from zero to 300 bar, as shown by the two relevant trend lines. In each case, the model under-predicts the value of the static seal leakage by approximately 30 litres, regardless of the pressure. As the leakage discrepancy is independent of the sealing pressure, which would suggest it taking place through a very small opening, which has become choked at a much lower pressure than the primary seal zone. An ideal candidate for this could be one of the seven secondary seals surrounding the gas seal cartridge. Whether this is the case or not, the model predictions show very close and consistent correlation with the test results for static conditions.

At 300 bar, the seals are leaking an average value of 120 $l.min^{-1}$, where as the model predicts a maximum leakage of 90 $l.min^{-1}$. For a gas seal under static conditions, whose primary seal zone is bounded by seven secondary seals, all of which are potential leak paths in their own right, this is indeed a very close correlation between model and experiment.

6.7.2 Lift-off pressure

Figure 79 and Figure 80 show the predicted seal gap against pressure, indicating the pressure at which the seals are likely to lift off. If one was to apply the same logic as with the SF design, and assume that the waviness of the two faces is within the same tolerance of one light band (or 0.3 μm), one would expect the seal faces to lift off when the gas is between 0.2 and 0.6 μm. With reference to the graph of predicted seal gap against pressure (Figure 79) seal lift off should occur when the pressure is between 0.2 and 2.8 bar. It is worth noting that 0.2 bar is an extremely low figure and one that would be very difficult to measure. Never-the-less, this projected pressure band, over which the seals are expected to lift off, has been superimposed on the graph of experimental data measuring the seal break-out torque against sealing pressure (Figure 90 and Figure 91). The breakout torque starts at 8 Nm when the pressure is zero and the seal faces are in contact with each other. As the pressure is progressively applied from zero, the breakout torque drops rapidly until it reaches its minimum asymptotic value of 1 Nm, at around 2.6 bar. Thus there is complete correlation between the predicted lift-off pressure band and the actual values measured on test.

6.7.3 Dynamic leakage

The predicted leakage from Figure 82 and Figure 83, has been superimposed on the graph of actual experimental data shown in Figure 92 and Figure 93. The predicted leakage is shown as a series of blue dots at the corresponding pressures and seal speeds. The graph shows dynamic seal performance from 6000 to 12000 rpm and 50-300 bar sealing pressure. Taking the 6000-rpm speed run, it can be seen that the predicted leakage falls right on top of the actual leakages from the two seals, through the entire pressure range. The trends of predicted values versus actual follow each other very closely at the other speeds of 8000, 10000 and 12000 rpm. A further trend that is noticeable is that the seal model appears to over predict the leakages at the higher speeds. That level of over predictions appears to be the same for each speed point from 8000 to 12000 rpm. However, for a given speed run, the level of over prediction increases with increasing pressure. Thus, at 12000 rpm, and 100 bar, the model prediction is near enough on top of the actual result. However, at 300 bar the

model predicts a leakage of 150 $l.min^{-1}$ and the actual test leakage was measured at a range of 100-125 $l.min^{-1}$. One may argue that the difference is quite substantial, but it is not unusual to see such a variation in seal performance from build to build, much of this being attributed to variation in seal face curvature. Also, if one were to work out the change in seal gap necessary to produce such a change in leakage, it would be in the order of a few decimal points of a micrometer. What is important and encouraging is that the correlation between the two is close and consistent across the entire seal performance map.

6.7.4 Mesh density

The mesh density has been set at what is deemed to be an optimum value. Any further increase in mesh density would yield progressively diminishing returns. This is primarily because the mesh would be finer than the tolerance to which the parts can be physically made. Taking the mesh accuracy the other way, would in fact have a detrimental effect. Comparative modelling analysis shows that the model is very sensitive to the radial position of the feed orifice. The resultant orifice pressure, leakage and subsequent equilibrium convergence are all strongly affected by the feed orifice position. To ensure the model was representative, an appropriate mesh density was selected that enabled one to position the feed orifice within the physical geometric tolerance achievable in practice. The result of this was a mesh density of 40 in the radial direction.

6.7.5 Spiral groove end effect correction

It has already been established that the consequence of the end effects is to reduce the effective length of the spiral groove. In the case of the SFLS design, the effective length has been reduced by over 1 mm. The consequence of this consideration is to significantly lower the predicted leakage, as well as the operating gap and the convergence angle at which equilibrium is achieved. This effectively brings the predicted leakages closer to the experimental values, as expected and desired. The leakage reduction is in the order of 12-18%.

6.7.6 Inertial effects – entrance losses

The model considered the losses at the entrance to the seal interface. The calculated reductions in the seal pressure and temperature in that region at full operating conditions of 300 bar, 12000 rpm were quite small – less than 1 bar and 1 degree Kelvin reduction. However, the inclusion of this consideration alters the predicted leakage by approximately 8%. The mechanism for this reduction in predicted leakage is for the entrance losses to alter the opening force pressure profile shown in Figure 76 and Figure 77, which in turn altered the equilibrium convergence angle of the seal faces, hence the equilibrium gap and the leakage.

6.7.7 Choked flow

Modelling analysis predicts the onset of choked flow to occur at 45 bar, when the seals are running at 300 bar, 12000 rpm and 393K. In other words, the seals are choked for the major proportion of the operating envelope. The effect of choking on the predicted performance is to increase the seal discharge pressure above ambient condition. At the full dynamic condition mentioned above, the discharge pressure is calculated to be just over 10 bar. The altered pressure profile is shown in Figure 69. The effect of the altered pressure profile is to reduce the leakage, by altering the equilibrium convergence angle as well as resultant gap.

6.7.8 Other model considerations

The SFLS model takes full account of the heat transfer between the surrounding medium and the seal faces. As a reminder, to the theory, the convection coefficients are calculated within the fluid film module of the model, based on classical and empirical data. To take account of the fact that some of the seal regions experience high velocity gas flow and the others experience near stagnant gas flow conditions. two convection coefficient values are used. Nevertheless, it is recognised that this is probably the most important area where further improvements can and should be made. Subsequent paragraphs give a detailed presentation to this future work, as well as give some further background.

The greatest limitation of the calculations for the convection coefficients, is that the Reynolds numbers as defined by Re_D, because many seals and applications in fact

exceed the experimentally verified range of the Becker formula. Results of our analysis indicate Re_D value in the order of: $Re_D = 1.6x10^8$. when operating at 300 bar, 12000 rpm and 393 K. Furthermore, the rotation of a cylinder within a concentric cylindrical cavity, as is the case with a gas seal cartridge, creates complex flow patterns, known as Taylor vortices. It is quite possible that similar complex flow patterns would be present within a gas seal cartridge housing. However, no publications have been made on this. One would certainly expect some transitions between the types of vortices with varying speed. Hence, the relationship between the heat transfer coefficients and the seal speed is probably more complex than suggested by the Becker formula. The problem of flow between two concentric cylinders has been studied for general cases only, rather than for mechanical seals specific. Consequently, there is certainly a big question on whether the Becker formula is to be relied upon. Two things then have to be considered in attempting to justify its use. Firstly, some work has been done to validate Becker's workings. Lebeck [21] undertook some comparative work by comparing Becker's formula to a well-known formula for heat transfer in duct flow based on Reynolds analogy between heat and momentum transfer. The equations were found to be similar, as were the results. Also, work undertaken by Smith and Grief [35] shows agreement with the Becker formula. The author's own experience in this area lends some confidence to using the data. Finally, the author has not found any other documented work undertaken to pin down more accurately the convection coefficient values in mechanical seals. So at this moment in time Becker's work seems to remain the most relevant to mechanical seals.

The above knowledge gap certainly gives a pointer to what would be a very useful body of work to undertake in future, beyond the scope of this research. That is, to pin down more accurately the surface heat transfer coefficients likely to be experienced in gas seals. To achieve this, the author recommends that a modelling exercise be undertaken on the design in question. Probably the best way of doing this would be to utilise CFD techniques and carry out a coupled field analysis, on the gas seal design in question.

6.7.9 Laminar or turbulent flow

As has already been mentioned, three forces have been assumed in this modelling, which play a governing role in determining the flow within a gas seal. They are pressure forces, viscous forces and inertial forces. Now, the inertial forces are deemed to be negligible compared to the other two. This assumption is deemed to be usual in the theory of full film lubrication. If one were to investigate the accuracy of this assumption, then one would arrive at the following estimate.

For a unit volume, the ratio of the inertial force $\rho u \partial u / \partial x$ to the viscous force $\mu \partial^2 u / \partial z^2$ is approximately equal to:

$$(\rho u^2 / B)(h^2 / \mu U)$$

eqn. 6.109

Where u is the relative velocity of the bearing/seal surfaces, B is the length of the clearance gap in the direction of the fluid velocity, h is the film thickness, ρ is the fluid density and μ is its viscosity. As a basis, Muijderman [22] used the following dimensionless group in the analysis for the onset of turbulent flow.

$$\mathrm{Re}^* = (\rho U B / \mu)(h / B)^2$$

eqn. 6.110

This modified Reynolds number would normally be used when considering inertial forces in the lubricating film of a journal bearing. Now if Re* <<1, the inertial forces may be deemed negligible. If Re* ≈ 1, this is no longer the case, while if Re* increases further still, then the laminar and viscous flow disappears and is ultimately replaced by turbulent flow.

The difficulty with the original Re* equation was setting appropriate definition for the value of B in a spiral groove bearing. Should B be the spiral groove width or the radius r of the bearing/seal surface? It was again Muijderman [22] who suggested a way round this difficulty. He proposed estimating an order of magnitude of inertial forces by means of the Navier-Stokes equation written in polar co-ordinates. It then appears that the outer radius of the bearing and hence a gas seal is a suitable choice for B. So for a spiral groove seal we have:

$$\mathrm{Re}^*_{sgb} = (\rho \omega R_o R_o / \mu)(h_2 / R_o)^2$$

eqn. 6.111

If one still assumes that inertial forces start playing a role at Re*≈1, and then applies the operating conditions of a spiral groove gas seal. If we now consider our situation, of a gas seal with an outer face radius of 81.6 mm, running at 12000 rpm, with a maximum operating gap of 2 μm, and a sealed pressure of 300 bar, then the modified Reynolds number will be: Re*=0.05. Putting this another way, with $h_2/R_o \approx 2.5 \times 10^{-5}$, and air as the seal gas operating at 300 bar, then the following condition must be satisfied to ensure that Re*<<1:

$$\omega R_o^2 \leq 210$$

eqn. 6.112

where ω is in rad.s^{-1} and R_2 is in m. So a seal with a 81.6 mm outer radius, should begin to be affected by turbulence at ω ≈ 32000 rad.s^{-1}, which translates to 305000 rpm! One must remember that this only holds true for $h_2/R_o \approx 2.45 \times 10^{-5}$. If this ratio increases, then the onset of turbulence will occur at a lower speed. It can be seen from this relationship that the most influential variable is the gap. If that gap were to be an order of magnitude higher, at 20 μm, then:

$$\omega R_o^2 \leq 2$$

eqn. 6.113

And the onset of turbulence would occur at ω≈317 rad.s^{-1}, which translates to 3000 rpm. So for a given set of design parameters and the seal gas properties/conditions, the strongest factor by far, governing the onset of turbulence is in fact the operating gap.

So according to this theory the assumption of a laminar regime in the gas seal concept under consideration is valid; for the given seal design, operating parameters, and the designed operating gap.

In all this it must be noted that very little work has been done to establish experimentally the onset of turbulent flow and its relative location within a gas seal. We are thus left with the above analysis as the best approximation.

Taking into account all of the above considerations, the developed model has been found to show excellent correlations with experimental data, in terms of static and dynamic leakages. This very close correlation was also true for the all-important lift

off pressure predictions. . The model can indeed be used as an effective design. analysis and optimisation too.

7 DISCUSSION - COMPARISON OF THE TWO DESIGNS (THEORY AND PERFORMANCE)

The gas seal cartridges for both designs have proved to be very effective test vehicles for the entire test and evaluation program. The same applied to the test equipment as a whole, which also proved very effective at removing the necessary amount of heat from the system, thus enabling effective testing to be carried out.

In terms of overall performance under normal operating conditions, across the entire performance envelope, both designs performed extremely well in terms of all the key performance requirements. This is reviewed in the paragraphs below.

7.1 LEAKAGES

A summary table of leakages is given below

	SF design leakage, $l.min^{-1}$	SFLS design leakage, $l.min^{-1}$
Full pressure ambient statics: 300 bar, 0 rpm,293K	180	90
Full pressure dynamics 300 bar, 12000 rpm, 393K	140-170	120-150

Figure 94: Leakage summary between the two designs

Firstly in terms of static leakage, the SF design was found to leak more than the SFLS. In part that was due to the design, in setting the desired initial operating gap. In this, a minimum acceptable gap under static conditions had to be set, in the knowledge that the seal was not expected to have much, if any, hydrodynamic component. Thus, once the gap was set under statics by the seal face and the feed groove design, it would not alter much under dynamics, like for like. In fact, the dynamic gap would reduce due to the thermal effects in the fluid film. Conversely,

the SFLS is expected to, and does, have a significant component of hydrodynamic lift. This means that its operating gap under statics can be made to be lower, as was the design intent. The operating gap for this particular demonstrator was set to 1.4 μm at the full operating pressure of 300 bar (static). This was deemed to be acceptable in terms of adequate separation at full pressure - given that the seals are to be expected to be started at full pressure.

Dynamically, the two seals leak more or less on a par with each other. Not surprisingly, the minimum operating gaps of the two designs are very similar for a given set of operating conditions – 1.8 μm gap at the ID when running at 300 bar, 12000 rpm and 398K.

The SF model is significantly simpler than its SFLS counter part. Never the less its correlation to static leakage test data is very close at lower operating pressures, 150 bar and below. Above that, as expected, given the model assumptions, the correlation between theory and experiment deviates. However, that deviation is not massive. The deviation is due primarily to the assumptions made by this quite simple model. Under dynamics, the case is slightly better, but still shows some fluctuating deviation with modelled leakage being under predicted at one point and over predicted at another. Much of this would be to do with the fact that the SF model only predicts equilibrium in the fluid film. It its current form it is not able to predict seal face distortions, their effect on the fluid film pressure profile, and the resultant gap. That is, the model is not able to arrive at a coupled equilibrium condition between the fluid film and the structural/thermal deformations of the seal faces. This will certainly make the model lose significant accuracy as well as correlation consistency when the thermal effects start playing a more prominent role. Experimental results also show that the SF seal displays some hydrodynamic effects, with leakage rising, albeit by a small amount, as the seal speeds are increased. This effect is particularly prominent at the higher speed, but at its maximum, the leakage variation is in the order of 5%. However, the theoretical model could not predict any hydrodynamic effect. The only hydrodynamic effects it took account of was that of restricting the flow of gas into the rear feed slots due to the greater effects on the centrifugal force at higher speeds.

The design was found to perform very well across the entire operating envelope. However it found wanting on one particular scenario. This occurred under the

'artificial' interspace condition, simulating a failed IB seal stage. At this condition the OB seal stage was holding the entire pressure and the IB stage was seeing a small differential across it. At this condition it was found that the closing force on the IB seal increased beyond the value seen during the normal operating condition. The opening force generated by the fluid film was not adequate to sustain a large enough operating gap and the seal was found to contact. Although this occurred at an artificial condition, nevertheless, it is an unacceptable effect. An alternative and most novel design was proposed in the form of the SFLS concept. This design retained all the benefits of good hydrostatic lift, but had a greater hydrodynamic component, able to support the fluid film at those artificial interspace conditions.

The intent with the SFLS model was to develop an accurate and sophisticated design analysis tool for accurately predicting the performance of the design at all operating conditions. To achieve this, the model had to take account of the most important factors. These included the effects of entrance losses; flow choking at the seal discharge, groove end effects and full compressibility effects of real gases. Then finally and as important as all the rest, the model was designed to combine full coupled field capability between the fluid film and the structural response of the seals parts.

The SFLS model was found to show much closer correlation to the experimental results across the entire pressure and speed range of the performance envelope. At lower speeds the correlation was spot on. At higher speeds it tended to over predict the leakages. But the trends were found to be very consistent. Also, the low operating leakage values make this seal concept extremely competitive with the existing technology already in the field.

7.2 BREAK OUT TORQUES AND LIFT OFF PRESSURE

Both models gave very accurate predictions of seal lift off pressure, for their respective designs. The lift off pressure was predicted to occur at between 0.2 and 2.8 bar. Although the former of the two limiting values is hard to measure, experimental results indicate clearly that the seals achieved complete lift off between 2.5 and 3 bar. Beyond that the seals remained fully lifted off throughout their full operating range. As part of the test program, the seals underwent full pressure stop-

starts. Under these conditions, the presence of full and complete separation would be imperative to reliable speed start up. If the seals were not fully separated at this full pressure condition, then massive and severe face contact and damage would occur when the seal rotation commenced. On strip down, after full pressure stop-starts the seal face condition was excellent in every case. Prior to this, as with all other conditions, the sure indicators of robust seal performance are the break-out torques under statics and the leakages at all duty conditions. From the operational point of view, to achieve complete lift-off at such low pressures is an excellent result. Further more, for a design to maintain break-out torques at such low values, i.e. 1-2 N.m, throughout the entire pressure range is also a show of excellent performance.

7.3 INTERSPACE CONDITION AND SEAL LOAD CAPACITY

On the subject of the artificial interspace condition, firstly, the SFLS model predicted consistently that the seal gap would still be present. Secondly the prediction was successfully verified on test. Under this artificial condition, it is impossible to measure the seal leakage, hence, all one could go on was the sheer survivability of the IB seal. The seals survived every single test point.

Finally, given that the SFLS has both hydrostatic and significant hydrodynamic components, it makes for a much more versatile design. Further more, the nature of the design and the design variables provides extensive scope for fine-tuning these individual components

8 CONCLUSIONS AND RECOMMENDATIONS

The work carried out as part of this research has been extensive. The dedicated gas seals test facility was successfully engineered. It enabled the accurate measurement of all the important performance parameters at all key duty points with the necessary degree of accuracy. It enabled the effective completion of the entire test program for both seal concepts in a timely manner.

8.1 SLOT FED MODEL TESTS RESULTS, CORRELATION

An appropriate model was developed for the SF concept in order to predict its performance. The model was in effect a 1-D fluid film equilibrium model. It was based on compressible flow, but utilised ideal gas properties, ignoring all the inertia and choked flow effects. Finally the model did not incorporate any coupling between the fluid film analysis and the structural deformation of the seal faces. Those features although making the model deliberately quick and easy to use, also were its limitations to greater accuracy.

The slot fed (SF) gas seal design concept was successfully incorporated into an industry standard tandem cartridge configuration for experimental verification. The concept design performed well at every experimental duty point designed to simulate operational duty conditions. The leakages at full pressure ambient static conditions were in the region of 180 $l.min^{-1}$ and under full dynamic conditions of 300 bar, 12000 rpm, and 393K they were 140-170 $l.min^{-1}$. The predicted minimum operating gaps at dynamic condition was 1.8 μm.

The model gave reasonable correlation between its predictions and the experimental tests. One operational fault was discovered with the concept, associated with the simulated failure of the IB stage, where the OB seal stage was holding the entire process pressure. At this condition, the IB stage was found to undergo contact. Further analysis established that this was caused by the closing force exceeding the opening force, in turn reducing the film gap to an unacceptably low level, thus leading to contact. That is, the seal did not have adequate load carrying capacity at this condition to sustain the necessary operating gap. It was suspected that the absence of any effective degree of hydrodynamic lift was the cause of the inadequate load carrying capacity.

To improve on the above limitations, while retaining all the benefits of low leakage and breakout torque, a unique design concept has been created and developed by the author, incorporating the slot feed design with a modified logarithmic spiral groove geometry – the slot fed logarithmic seal concept (SFLS).

This is a totally novel and unique concept of gas seal design. A patent has been submitted by the author, in his name to both the to the European and the American patent offices for the novel slot fed logarithmic spiral lift concept for a gas seal.

As with the first design concept, an appropriate model was developed. The computer model developed to predict its performance is totally original and unique in every sense. In this particular case, the model is significantly more refined. The fluid film model was based on the finite difference technique. The model took account of full, gas compressibility, real gas properties, entrance losses, choked flow and spiral groove end effects. The model was fully coupled to the structural analysis of the seal faces. For this part, ANSYS Finite element analysis software proved to be a very effective platform.

Within the fluid film model, the developed method of superimposing the slot fed arrangement with the modified spiral groove proved to be very effective and efficient. The mathematical representation of the spiral groove and its use in allocating appropriate film gaps, together with automatic positioning of the slot feed arrangement and the corresponding mass flow calculation algorithm also proved to be very elegant modelling techniques. The model accuracy was refined to a level, which represented the geometric limitations of the design. No more refinement was necessary. Those features significantly enhanced the model accuracy.

The model gave very good correlation between its predictions and the experimental tests. At lower speeds the correlation was almost 100%. At higher speeds, across the pressure range, the model; over predicted the leakages by approx 20-30%. Overall, the predictions showed good consistency. The model could effectively be used as a reliable analysis and verification tool.

The seal performance was in fact better than the SF concept. The static leakages were lower: 90-110 $l.min^{-1}$ at 300 bar. They were also lower under dynamics, typically in the region of 120-150 $l.min^{-1}$ at 300 bar, 12000 rpm and 298K. The seals retained the characteristic of the very low lift off pressure (2.6 bar) and very low

breakout torques. These were typically 1-2 N.m right up to the full operating pressure of 300 bar.

The SFLS model has shown itself to be flexible and accurate. However, improvements can still be made. By far the biggest recommendation would be to undertake a detailed 3-D CFD modelling exercise. The core objective of this would be to map out in detail the surface heat transfer coefficients around the perimeter of the gas seal parts. It is quite possible that relationships will have to be formulated as part of the exercise. Once established and quantified, those convection coefficients, or their relationships can then be incorporated directly into the computer-based model. The model accuracy, at full dynamic conditions should increase significantly.

Another improvement could be made within the convergence algorithm to help speed up the convergence and the solution time. At the moment run times can be in the region of 3-6 minutes, with the model taking 2-5 iterations to converge to equilibrium. This can be achieved by adopting a more refined (albeit more complex) backward/forward stepping algorithm.

REFERENCES

1. ANSYS, V10, 2005, Finite Element analysis software and user reference manual.
2. ANSYS-CFX, V10, 2005, Finite Element analysis software and user reference manual.
3. Basu P., 1992, "Analysis of a Radial Groove Gas face Seal hydrodynamic", STLE Transactions, 35(1), pp. 11-20.
4. Becker J. M, 1963, "Measurement of Convective Heat Transfer from a Horizontal Cylinder Rotating in a Tank of Water", *International Journal of Heat and Mass Transfer*, **6**, pp. 1053-1062.
5. Cheng, H. S., Chow, C. Y., and Wilcock, D. F., 1968, "Behaviour of Hydrostatic and Hydrodynamic Non-contacting Face Seals", Journal of Lubricating Technology, April, pp. 510-519.
6. Corac Group, Sealing Technology Design Notes, 2000.
7. Ford, G. W. K., Harris, D. M. and Pantall, D., 1957, "Principles and Applications of Hydrodynamic Type Gas Bearings", Proc of the Institution of Mechanical Engineers, January, pp. 70-78.
8. FlowServe Corporation. . Mechanical Seal Company.
9. Gardner, J., F.,1973, "Recent Developments in Non-Contacting Face Seals", Lubrication Engineering, September, pp. 406-412.
10. Goldswain, I., M., 1993, "Mechanical Face Seal with Trapezoidal Shaped Grooves on a Sealing Face", US Patent no. 5,222,743. Assignee: John Crane International.
11. Gross, W. A., 1992, "Gas Film Lubrication", John Wiley & Sons. Inc.
12. James. D. D. and Potter, A. F., 1967, "Numerical Analysis of the Gas-Lubricated Spiral Groove Thrust Bearing-Compressor", Journal of Lubrication Technology. October. pp. 439-444.
13. John Crane International. Mechanical Seal Manufacturer.
14. Kaydon Ring and Seal Company. Patent number 5,066.026.

15. Kays, W. M. and Bjorlund, D. S., 1958 "Heat Transfer from a Rotating Cylinder with and Without Cross Flow", Transactions of ASME, vol. 171, No. 2, 1957, p. 93.

16. Key, W. E., Salant, R. F., Payvar P., et al 1989 "Analysis of a Mechanical Seal with Deep Hydropads", Tribology Transactions, vol. 32, No. 4, pp. 481-489.

17. Kouga T., Fujita, T., 1984, "The Hydrostatic Non-contacting Gas Seal Including Fluid Inertia Effects", ASLE/ASME Lubrication Conference in San Diego, California, 29(1), pp. 35-42.

18. Kouga T., Fujita, T., 1985, "The Hydrostatic Non-contacting Gas Seal", ASLE/ASME Lubrication Conference in Atlanta, Georgia, 29(4), pp. 505-514.

19. Laurenson I. T., O'Donoghue, J. P., 1978, "Preliminary Experiments with Slot Fed Hydrostatic Face Seals", 8th International Fluid Sealing Conference, BHRA Fluid Engineering, A4-41.

20. Laurenson I. T., O'Donoghue, J. P., 1978, "Hydrostatic Seal Design", Journal Mechanical Engineering Science, IMechE.

21. Lebeck E. A., 1992, Principles and Design of Mechanical Face Seals. John Wiley & Sons, Inc.

22. Muijderman, E. A., 1966, "Spiral Groove Bearings". Macmillan & Co. Ltd.

23. Neale Consulting Engineers, July 2000, "Dry Gas Seal Integrity", HSE Agrement No. D3819.

24. Pecht, G., Goldswain, I., 1994, "Using Advanced Numerical Techniques to Model Gas Lubricated Seals", STLE Annual Meeting, Pittsburg, PA.

25. Petrov, N. P., 1883, "Friction in Machines and the Effect of the Lubricant." Inzh. Zh. St. Petersburg, vol. 1, pp. 71-140.

26. PPDS, Real gas properties database. National Engineering Laboratory, 2001.

27. Rayleigh, Lord, Phil Trans., (1918) 35, pp. 1-12.

28. Reynolds, O., 1886, On the Theory of Lubrication and its Application to Mr Beauchamp Tower's Experiments. Philos. Trans. R. Soc. London Ser. A, vol. 177, pp. 157-234.

29. Sedy J., 1978, "Improved Performance of Film-Riding Gas Seals Through Enhancement of Hydrodynamic Effects". ASLE/ASME Lubrication Conference in Minneapolis, 23(1), pp. 35-44.

30. Sedy J., 1979, "A new Self-Aligning Mechanism for the Spiral Groove Gas Seal Stability", ASLE/ASME Lubrication Conference in Dayton. Ohio. 36(10). pp. 592-598.

31. Sedy J., 1980, "Self Aligning Spiral Groove Face Seal", US Patent no. 4,212,475, Assignee: John Crane International.

32. Sedy J., 1998, "Spiral Groove Face Seal", US Patent no. 5,722,665, Assignee: Flow Serve Corporation.

33. Shapiro, W., Walowit, J., and Jones, H. F., 1984, "Analysis of Spiral Groove Face seals for Liquid Oxygen", ASLE Transactions, 27(3). pp. 177-188.

34. Shimizu, T., 1995, "Seal Device of the Non-Contact Type", US Patent no. 5,398,943, Assignee: Nippon Pillar Packing Co.

35. Smith, R. N., Greif, R., 1971, "Turbulent Transport to a Rotating Cylinder for Large Prandtl or Schmidt Numbers", Journal of Heat Transfer, pp. 594-597.

36. Sneck, H. J., McGovern, J., F., October 1973, "Analytical Investigation of the Spiral Groove Face Seal", Journal of Lubricating Technology, pp. 499-510.

37. Stolarski T. A., and Xue Y., 1998, "Performance Study of a back –depression mechanical dry gas seal", Proceeding of the Institution of Mechanical Engineers, Volume 212, Part J.

38. Szeri, A. Z., 1980, "Tribology, Friction, Lubrication, and Wear", McGraw-Hill, New York.

39. Tournerie B., Huitric J., Bonneau, D., Frene, J., 1994, "Optimisation and Performance Prediction of Grooved Face Seals for Gases and Liquids", 14th International Conference on Fluid Sealing.

40. Victor J., 1995, "Contactless Pressurising-Gas Shaft Face Seal", US Patent no. 5,435,574, Flow Serve Corporation.

41. Whipple, R. T. P., 1949, "Herringbone Pattern Thrust Bearings", Atomic Energy Research Establishment. T/M 29.

42. Zuk J., Ludwig, P., Johnson, L., 1971, "Analysis of Rotational Effects on Compressible Viscous Flow Across Shaft Face Seals". NASA-Lewis Research 26th ASLE Annual Meeting, Boston, Massachusetts, 28(4). pp. 82-92.

43. Zuk J., Ludwig, P., Johnson, L., 1972, "Quasi-One-Dimensional Compressible Flow Across Face Seals and Narrow Slots", NASA Technical Note. DD-6668.